UNIVERSITY OF BIRMINGHAM

Numerical and Experimental Study of Spray Characteristics in the Gasoline Direct Injection Engine

By

Powen Tu

A thesis submitted to

The University of Birmingham

for the degree of

DOCTOR OF PHILOSOPHY

The University of Birmingham

School of Mechanical Engineering

Augest 2015

Abstract

In the recent development of the gasoline combustion engine, direct injection (DI) technology has been widely used to improve fuel economy and reduce exhaust emissions. Spray characteristics of the gasoline direct injection (GDI) injector are particularly important for engine developers with respect to optimization of air/fuel mixture preparation. Because of the limitation of experimental techniques, the transportation of fuel within the GDI injector nozzle hole and near-field spray is not well understood. In this study, computational fluid dynamics (CFD) modelling and direct coupling of the Euler in-nozzle flow model with the Lagrangian spray model are employed to investigate the effect of different nozzle geometrical designs on the GDI spray characteristics. In addition, several deposit case studies are performed to examine the comprehensive effect of deposit formation on spray characteristics and to identify the most prominent deposit location inside the nozzle and counterbore of the injector.

Euler modelling of the inside-nozzle flow reveals that a round nozzle inlet significantly increases the mass flow rate and nozzle exit velocity. However, the round inlet slows down spray atomisation because of less turbulent disturbance from the smooth nozzle inlet corner. A longer internal nozzle wall length results in a decrease in mass flow rate and larger droplet distribution in the nozzle near-field. The counterbore size of the GDI injector also affects droplet size distribution in the nozzle near-field due to air recirculation inside the counterbore.

At the nozzle exit, the nozzle flow parameters obtained from the Euler-based study are implemented as initial conditions for the subsequent Lagrangian-based spray model. The direct coupled Euler–Lagrangian approach is then compared with the Kelvin-Helmholtz-aerodynamic cavitation–turbulence (KH-ACT) model and the Max Planck Institute (MPI) model. Since the KH-ACT nozzle model does not consider the effect of nozzle inlet corner on

turbulent disturbances, resulting turbulent intensity values are low. However, in comparison to the KH-ACT model, the coupled Euler approach and the MPI model points out that the former is unstable in the calculation of mean droplet size.

The effects of injection and ambient pressure on spray characteristics are separately investigated by experimental and numerical approaches. Injection pressure greatly affects spray characteristics in the primary and secondary breakup regimes; however, the effect of ambient pressure becomes apparent only in the secondary breakup regime due to the increased droplet drag force with higher back pressure.

Three different fuels, iso-octane, DMF and ethanol, are investigated using the MPI-CAB model and experimental approaches in order to gain comprehensive insight into the effect of fuel properties on spray characteristics. This investigation shows that liquid density, surface tension and viscosity are dominant in affecting atomisation. Moreover, optimization of the injection strategy for these alternative fuels is studied with the goal of improving the in-cylinder air/fuel mixing in the GDI engine.

Acknowledgements

Firstly, I would like to express sincere thanks and gratitude to my supervisor **Professor Hongming Xu** for his great support during the research of this PhD. I also give my deepest thanks to my industrial supervisors **Dr. Cao Li** for his genuine and insightful consulting throughout this research.

I am grateful to **Dr. Weall Adam** from Jaguar Land Rover (JLR) for his support during the deposit project. Special thanks to all my best colleagues in **Future Power System** group, **Dr. Yanfei Li, Dr. Xiao Ma, Dr. Fan Zhang, Dr. Changzhao Jiang** and **Haichun Ding** to accompany me and support me during my PhD course. Also, I want to thanks **Janet Hingley** for her proofreading for my thesis

In the end, I would like to send my deepest gratitude to my **Parent and Family** for their assistances and supports.

I wish to dedicate this thesis to my family for their love and great support along the way

Contents

List of Abbreviations

ASOI	After Start of Injection
ATDC	After Top Dead Center
AMD (D10)	Arithmetic Mean Diameter
BTDC	Before Top Dead Center
BDC	Bottom Dead Center
CO	Carbon Monoxide
CI	Compression Ignition
CO_2	Carbon dioxide
CFD	Computational Fluid Dynamics
CAB	Cascade Atomization and drop Breakup
CFD	Computational Fluid Dynamics
CMC	Continuous Multi-Component
CB	Counter-Bore
CA	Crank Angle
DISI	Direct Injection Spark Ignition
DI	Direct Injection
DNS	Direct Numerical Simulation
DDM	Discrete Droplet Model
DDM	Discrete Droplet Model
DMC	Discrete Multi-Component
ECU	Electronic Control Unit
EVO	Exhaust Valve Open
EOI	End of Injection

EVC	Exhaust Valve Close
GDI	Gasoline Direct Injection
IC	Internal Combustion
IVO	Intake Valve Open
IVC	Intake Valve Close
KH-ACT	Kelvin Helmholtz-Aerodynamic Cavitation Turbulence
LES	Large Eddy Simulation
MPI	Max Planck Institute
MPI	Max Planck Institute
Nu	Nusselt number
NO_x	Nitrogen Oxides
PDPA	Phase Doppler Particle Analyzer
Pr	Prandtl number
PM	Particulate matters
RANS	Reynolds-Averaged Navier-Stokes
Re	Reynolds number
RI	Rounded Inlets
RT	Rayleigh-Taylor
SEI	sharp-Edge Inlet
SMD (D32)	Sauter Mean Diameter
SOI	Start of Injection
SGS	Sub-Grid Scale
Sh	Sherwood number
Sc	Schmidt number
TAB	Taylor-Analogy Breakup

TDC	Top Dead Center
TWC	Three-Way Catalyst
VVA	Variable Valve Actuation
VOF	Volume of Fluid
We	Weber number
Z	Ohnesorge number

List of Symbols

a	Radius of parent droplet
B_0	Breakup size constant in KH model
$C_{T,CAV}$	Constant parameter for KH-ACT model
C_c	Contraction coefficient
$\hat{J}$	Heat flux vector
K_{bu}	Breakup constant in CAB model
K_0	Initial turbulent kinetic energy
K_{bu}	Breakup constant in CAB model
l_n	Length of nozzle
$L_{c,grow}$	Liquid core length growth constant
L_{KH}	Breakup length scale in aerodynamically-induced model
L_{CAV}	Breakup length scale in cavitation-induced model
L_T	Breakup length scale in turbulence-induced model
$L_{c,steady}$	Liquid core length
$\dot{m}_{qp}$	Mass transfer from phase q to phase p
$\dot{m}_{pq}$	Mass transfer from phase p to phase q
n_b	Bubble number density
p_{vena}	The pressure in the vena-contracta
$\dot{Q}^c$	Source terms for chemical heat release
$\dot{Q}^s$	Source terms for Spray interaction
R_e	Mass transfer source from growth of vapor bubbles

R_c	Mass transfer source from collapse of vapor bubbles
R_B	Bubble radius
r_n	Radius of nozzle entrance
t_η	Duration of the smallest eddy structure
t_{bu}	Breakup time in CAB model
U_{vena}	Velocity in vena-contracta

Greek Symbols

ε	Average turbulent dissipation rate
ε_0	Initial dissipation rate
$\eta_{Kolmogorov}$	Kolmogorov length scale
k_{sgs}	Sub grid-scale kinetic energy
k	Turbulent kinetic energy
λ_{Taylor}	Taylor length
μ_t	Turbulent viscosity
$\bar{\tau}_{ij,t}$	Reynolds stress
τ	Breakup time in KH model
τ_{CAV}	Breakup time scale in cavitation-induced model
$\tau_{Collapse}$	Bubble collapse time scale
τ_{Burst}	Average time for bubble to reach the surface of liquid jet
τ_T	Breakup time scale in turbulence-induced model
ρ_m	Density for species m
Λ_{KH}	Wave growth rate

Ω_{KH}	Wave length

Subscripts and Superscripts

bu	Stands for breakup
c	Stands for liquid core
cav	Stands for cavitation
eff	Stands for effective
KH	Stands for Kelvin Helmholtz
l	Stands for liquid; laminar
m	Stands for species index
n	Stands for nozzle
seg	Stands for segment
sgs	Stands for sub grid-scale
T	Stands for turbulence
vena	Stands for Vena-contracta

List of Figures

List of Tables

List of Publications

SAE conference papers

Haiying Li, Li Cao, Xiao Ma, **Po-Wen Tu**, Hongming Xu, Shi-jin Shuai and Akbar Ghafourian, "Numerical Study of DMF and Gasoline Spray and Mixture Preparation in a GDI Engine," SAE Technical Paper 2013-01-1592

PoWen Tu, Changzhao Jiang, Haichun Ding, Cao Li, Hongming Xu, Akbar Ghafourian, Shi-jin Shuai "Investigation on the Spray Characteristics of DMF- Isooctane Blends using PDPA," SAE Technical Paper 2014-01-1408, 2014, doi:10.4271/2014-01-1408

PoWen Tu, Cao Li, Hongming Xu, Adam Well, Jens Krueger Venus, Dhananjay Kumar Srivastava, Karl Dearn, Daliang Jing " Numerical Investigation of GDI Injector Nozzle Geometry on Spray Characteristics" JSAE 201509061, SAE 2015-01-1906

Powen Tu , Daliang Jing , Cao Li ,Haiying Li , Hongming Xu "Numerical Study of the Nozzle Geometrical Effects on Spray Characteristics in primary and Secondary Breakup Regimes" The 13th Internal Conference on Liquid Atomization and Spray System, 2015

Papers to be submitted

Powen Tu, Hongming Xu, "Numerical Investigation of Deposit Effects on Spray Characteristics," Ready for Submission

Chapter 1

INTRODUCTION

1.1 Background

Since the 1860s, the Internal Combustion (IC) engine has been widely used in the engineering industry due to its convenience and high performance in terms of energy efficiency (Gupta 2012, Alagumalai 2014). It has also played a key role in the rapid development of the world's economy and has had a great effect on the daily lives of its population (Kalghatgi 2015). However, with the increasing concern about energy consumption and emission pollution, the improvements of the IC engine in fuel consumption and emission exhausts have gradually become an important issue for IC engine manufacturers (IMechE. 2013). Although, several new and creative technologies have been applied into the development of the new generation of IC engines such as hybrid engines or replacing the IC engine with as electric vehicles in recent years (Mwasilu 2014, Wesseling 2014), there are still several inevitable technical problems that need to be overcome such as the limitation of battery life, expensive research cost and charging technology (Hannan 2014). Thus, most of the vehicle manufacturers believe that the IC engine is still irreplaceable in the 21st century.

1.2 Energy Demand

With the continuous growth of global economic development and the world's population, the requirement for energy has witnessed an obvious increase and is gradually becoming a serious issue. An estimate of future energy production was proposed by British Petroleum (BP) to the

International Energy Agency (IEA). It indicates that the peak production of energy will be achieved in 2014-2015, due to lower oil prices, as Figure 1.1. However, all the types of energy production will decline simultaneously after this peak time. It is speculated that this will be the result of the global economic downturn and the cause of the adjustment of the energy company operations and their number of employees .

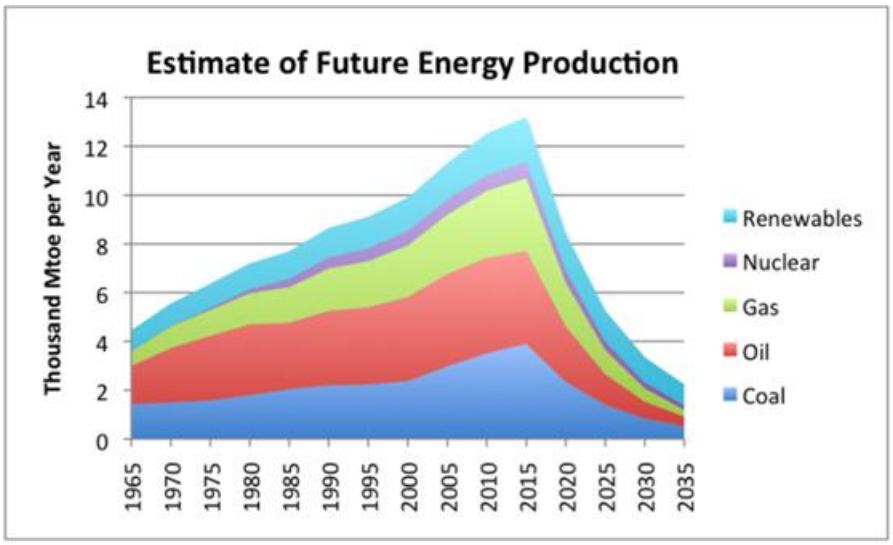

Figure 1.1 Estimate of production of future energy

However, another report from the Energy Information Administration (EIA) also points to the consumption of world energy and highlighted that consumption will increase by around 56 percent in 2060 as presented in Figure 1.2 (Sieminski 2013). Moreover, it shows that traditional energy such as coal, natural gas and crude oil will still be the major energy source for the whole world before 2040 and will account for up to 80% of world energy consumption. Thus, some new generational energy which include bio-fuels, solar and hydroelectrics will be required in order to decrease the dependence on traditional energy due to its shortage. Despite this, although the consumption of new generational energy gradually increases, there still shows an indication that traditional energy will occupy up to 60 % of world energy consumption in the

next three decades. This illustrates that traditional energy sources will still be irreplaceable in the future.

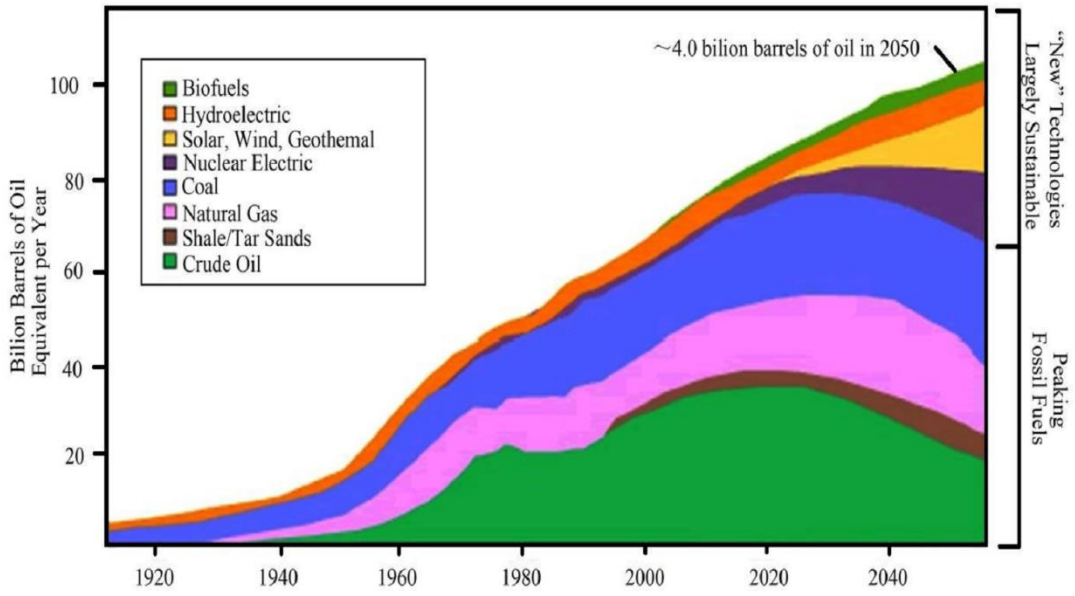

Figure 1.2 Estimate of consumption of future energy

The recent report into analysis of energy consumption from the EIA indicates that transportation occupied 28 % of world energy consumption which is as shown in Figure 1.3 . It shows that of all energy sources, petroleum consumption is the highest, i.e., 36% of the total energy sources, with approximately 71% used for transportation. Based on this analysis, it can be expected that transportation still will be the major consumer of petroleum over the next few decades. This study employs various approaches to explore spray characteristics under different nozzle designs, operating conditions and biofuel scenarios in an effort to improve fuel efficiency and therefore decrease fuel consumption in the transportation sector.

From Figure 1.1, the prediction of future energy production shows a decreasing trend. However, the future requirement of energy gradually increases. An energy crisis can be expected from the balance of energy production and consumption, as in Figure 1.2. Thus, several energy

policies and technologies have been applied in order to decrease energy consumption and increase energy production in different areas. Thus, in the vehicle industry, the topic of improvement of fuel efficiency and new application of energy have also been intensively studied and considered during engine development.

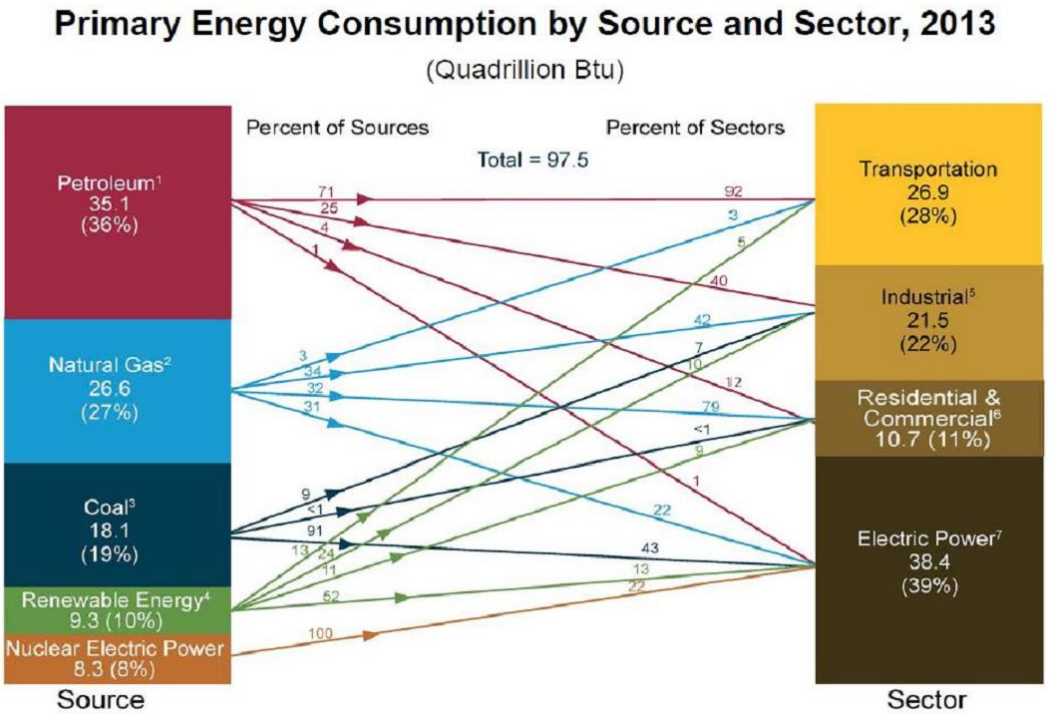

Figure 1.3 Distribution of primary energy consumption

1.3 Bio-Fuel and Emission

Because of the demands of environmental protection, regulations and legislation have been in place for decades to restrict vehicle exhaust emissions. The development of EU emission regulations for petrol cars is shown in Table 1.1, indicating a 46.7% decrease in CO emissions between 1992 and 2014. NOX emission was reduced by 60% between 2003 and 2014. Exhaust PM was regulated by mass starting in 2009 and by number starting in 2014.

Table 1.1 Development of EU emission regulation for petrol cars

Tier	Date	CO	THC	NMHC	NOx	HC + NOx	PM	P (#/Km)
Euro 1	1992	2.72	-	-	-	0.97	-	-
Euro 2	1996	2.2	-	-	-	0.5	-	-
Euro 3	2000	2.3	0.20	-	0.15	-	-	-
Euro 4	2005	1.0	0.10	-	0.08	-	-	-
Euro 5	2009	1.0	0.10	0.068	0.060	-	0.005	-
Euro 6	2014	1.0	0.10	0.068	0.060	-	0.005	6×10^{11}*

From the previous sections, due to the gradual increasing consumption of fossil fuels and stricter emission regulation, finding an alternative for them has become a new strategy for vehicle manufacturers when developing and designing their IC engines. The new applications of new energy sources in vehicles at present are hydrogen, electric and bio-fuels, which are currently being and have been in the past, examined by users. For the hydrogen vehicle, the problems of well to wheel efficiency and hydrogen storage, result in that it is still difficult for it to be accepted by drivers (Wang 2007). The same situation happens in the application of electric ehicles. Due to the high cost and recharging problem of battery and energy storage, electric vehicles are also still not universal at present. Therefore, the usage of bio-fuels is another common strategy which has been widely used in the industry.

The more common biofuel in the current market is ethanol. The advantages of ethanol are lower fuel price, anti-freeze, renewable source and lower emission. Sementa (Sementa 2012) has been pointed out that the HC, CO and NOx of ethanol showed the lower value than gasoline. However, due to the higher oxygen content of ethanol, it causes the higher CO2 emission. Another potential biofuel candidate is 2,5-dimethylfuran (DMF). To compare with ethanol, its energy density has 40% higher than ethanol which improve the problem of ethanol's limited cruise mileage. Moreover, the higher octane number of DMF (11.9) can allow to operate in higher compression ratio which increases the fuel consumption and engine performance. Therefore, the spray characteristics of these two different biofuels will be discussed in this research.

1.4 Development of Direct Injection Engine

Due to the above stricter exhaust emission regulation and higher concern of fuel economy, vehicle manufacturers have started to consider a new fuel injection system to replace the traditional Port Fuel Injection (PFI) system. Moreover, the improvement of engine performance gradually becomes an important issue for engine manufacturers which needs to be considered when the stricter emission regulation limits the engine performance. Thus, the Direct Injection Spark Ignition (DISI) system is proposed to solve both of these problems due to its accuracy of the dynamic air/fuel (A/F) ratio, and its application with the Variable Valve Actuation (VVA) and turbocharger (Clenci 2007).

The improvement of fuel efficiency and exhaust emission has been observed in the DISI engine which is compared with the Compression Ignition (CI) engine. Several advantages of the DISI engine are shown below:

- Fuel efficiency.

The specially designed control unit, i.e, Electronic Control Unit (ECU), in the GDI engine enables the control of the fuel injection strategy to achieve the best mixture preparation.

- Fuel injection.

The GDI injection system controls not only fuel quality but also injection timing. Different injection strategies can be applied to the DISI engine by adjusting the timing, duration, pressure and number of injections under different engine operating conditions.

- Engine performance.

Another advantage of the DISI engine is that the evaporation of injected fuel can lower the temperature of the in-cylinder charge and thus improve volumetric efficiency and reduce knock tendency. Because of the reduced knock tendency, the compression ratio of the GDI engine can be higher than other gasoline engines.

- Exhaust emission.

In the Gasoline Direct Injection (GDI) engine, the technology of the Three-Way Catalyst (TWC) can efficiently convert CO, HC and NO_x into the production of CO_2 and water (H_2O). However, as the PM emissions have been gradually limited by emission regulations, it can be observed from Figure 1.4 that the main source in the cause of the production of particulate formation is the spray interaction with the chamber piston and wall. Thus, the chamber wetting can be avoided by controlling the injection pressure and timing. Furthermore, the homogeneous air/fuel ratio can obviously decrease the exhaust emissions.

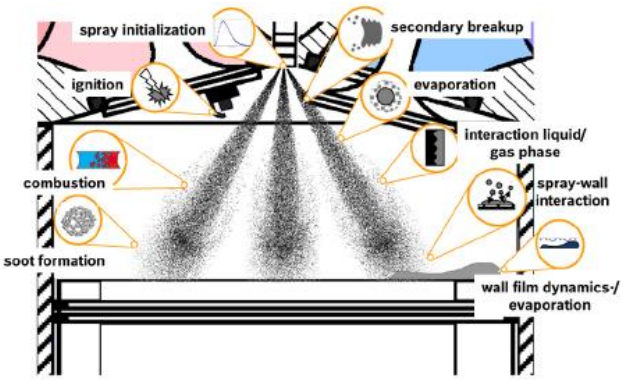

Figure 1.4 Formation of particulate in the combustion chamber (Kim 2013)

In the GDI engine, the spray atomization of injector is the one of the key issues to affect the engine performance and emission exhaust. The different nozzle's geometrical designs such as r/D, L/D and sac volume can directly affect the development of nozzle flow field and spray characteristics. For example, the reduction of sauter mean diameter (SMD) can improve the spray evaporation process because of the increase of overall surface area. This could be improve the problem of wall wetting form spray-wall impingement and further decrease HC emission.

1.5 Objectives

The objectives of this research are to understand the detailed effects of the GDI nozzle's geometrical designs on the spray characteristics in the primary breakup and secondary breakup regime. By using the above detailed analysis, the spray characteristics of several bio-fuels such as iso-octane, ethanol and 2,5-Dimethylfuran (DMF) are investigated by numerical and experimental methods in order to provide an accurate injection strategy for engine optimisation. The main objectives for this investigation are described as follows:

1. To study the effects of different GDI nozzle geometrical designs such as the different needle lift positions, r/D, L/D ratios and the size of counter-bore on spray characteristics to support the unknown spray behaviours in the nozzle near field.

2. To numerically analyse the breakup mechanism of the presented spray models to understand the effects of spray behaviours in the primary breakup regime on the entire spray development.

3. To numerically and experimentally study the spray characteristics under operating conditions such as different injection and ambient pressures in the nozzle near field and secondary breakup regime to examine and validate the capability and accuracy of the proposed spray models.

4. To numerically and experimentally study the effects of the different properties of biofuel on spray characteristics in the nozzle near field, secondary breakup regime and the mixture distributions in the GDI engine in order to understand the difference of the effects of different bio-fuels on engine performance.

5. To couple the nozzle flow simulation with a spray model in order to improve the accuracy of the numerical model.

1.6 Thesis Outline

This thesis is composed of nine chapters. A brief description for each chapter is given as below:

Chapter 2 - Literature Review

A literature review of presented GDI nozzle types and the spray numerical models, such as droplet breakup and evaporation models, is provided. In addition, the introduction of the foundation of spray characteristics is also included.

Chapter 3 - Research Methodology

This chapter provides the introduction of numerical and experimental methodology which is applied in this study. In the numerical approach, the detailed spray breakup theory and turbulent model using the Eulerian and Lagrangian approach are introduced. In the experimental approach, the experimental setups of the optical methods such as the Phase Doppler Particle Analyzer (PDPA) and high speed camera are described.

Chapter 4 - Modeling Validation of Nozzle Flow and Cavitation

The CFD software, Ansys-Fluent, is examined for its accuracy and its capability of calculation by validating it with experimental data. Moreover, the investigation of cavitation effects in the GDI nozzle is included.

Chapter 5 - Investigation of Nozzle Design in the GDI Injector

The effects of different GDI nozzle geometric designs on spray characteristics in the nozzle near field are discussed and compared by using the VOF-LES model. Furthermore, the detailed deposit case study is investigated, which not only can provide an insight for the deposit influences on spray characteristics, but also on the speculation of deposit formation.

Chapter 6 - Numerical Comparison of Spray Models

The spray characteristics are investigated under different breakup mechanisms and then the model initial parameters are improved by coupling the nozzle flow simulation results. In addition, the spray behaviours from two different spray breakup models are compared by using experimental data in order to examine their reliability and accuracy.

Chapter 7 - Influence of Operating Conditions in the GDI Injector

The spray characteristics from the proposed spray model were examined and validated by PDPA and a high speed camera system under different injection and ambient pressures. This can help to provide a complete understanding of the effects of an operating condition on spray characteristics in the primary and secondary breakup regime.

Chapter 8 - Influence of Fuel Properties on Spray Characteristics in the GDI Engine

The effects of different fuel properties on spray characteristics during the spray development process are investigated respectively by numerical and experimental methods. The study of mixture distribution in the GDI engine is also discussed to enable the engine manufactures to adjust the injection strategy.

Chapter 9 - Conclusions and Recommendations

The conclusions of the research results from Chapters 4 to 8 are presented and provides suggestions for future work are provided

Chapter 2

Literature Review

2.1 Introduction

The purpose of this chapter is to review the literature on the development of the GDI engine and its nozzle design and also on the fundamentals of fuel spray development which is related to the research in this thesis. It includes the spray characteristics in the primary and secondary breakup regime, CFD turbulent models, breakup models and its sub models. In the first part, the development of the GDI engine and nozzle design is introduced. Then, the literature relevant to the spray characteristics such as spray penetration length, spray angle and droplet size and velocity are discussed. In the third part, an overview of CFD modelling approaches for the simulation of spray development is provided. Finally, the application of bio-fuel in the IC engine is reviewed.

2.2 Overview of GDI Engines

Due to the increased emphasis on the exhaust emission and fuel consumption of the gasoline engine, improvement of the gasoline engine is necessary. In order to improve the horsepower output and fuel consumption of the gasoline engine, the direct injection (DI) engine has been gradually developed and applied from the 1930s. It shows the potential for higher power output and better fuel economy and advantages in minimising the knocking during the combustion process (Zhao 2010). The Gasoline Direct Injection (GDI) system was manufactured by Bosch

and was firstly applied on a two-stroke gasoline engine in 1952 by Goliath and Gutbrod. However, at well-known application of the GDI system was announced by Mercedes-Benz 300L in 1955. This was also the first application of the GDI system on a four-stoke engine. In this period, the development of the GDI engine aimed on increasing the performance of the vehicle and charging the cooling effect of the GDI system.

In the 1970s, the well-known research and development on the GDI engine was the "PROCO" (programmed combustion) system which was developed by the Ford Motor Company (Scussel 1978). It later used an injection and bowl design for the chamber position to achieve better combustion efficiency. However, the high cost and NO_x exhaust emission of this system forced the project to be stopped. The first successful application of the GDI system on the engine happened in 1996 when Galant/Legnum's 1.8L straight-4 which was announced by Mitsubishi Motors, was introduced into the Japanese market (Iwamoto 1997). Until 2001, the progress of the GDI engine was followed by other car manufacturers in Japan and Europe who developed their own GDI engines or obtained the license from Mitsubishi. The features of these GDI engines operated in the conditions of part load and low to medium operating speeds for stratified operation and high speeds and high loads for homogeneous operations. However, after 2001, because of the stricter emission mandate, the expensive and less efficient learn-burn NO_x after-treatment was used to comply with the emission legislation. This resulted in the GDI design of the engine being used at homogenous operating conditions only.

The later development of the GDI engine was carried out by Volkswagen (VW) and Audi. The technologies of turbochargers and superchargers were adopted aggressively into their GDI engines. The representative GDI engine with turbochargers and superchargers is the TSI 1.4

Litre GDI engine which shows an impressive power of density (90 KW/litre). This means the naturally aspirated engine was gradually replaced by a smaller turbocharged engine.

2.3 Types of GDI Injection and Combustion System

The development of the gasoline injection system has been continuous in modern vehicles. The injection system of gasoline engines has developed from using a carburetor to PFI injectors and then onto the new generation injector: the GDI injectors which is shown in Figure 2.1. These developments are driven by stricter emissions' standards, better fuel consumption and the enhancement of engine performance.

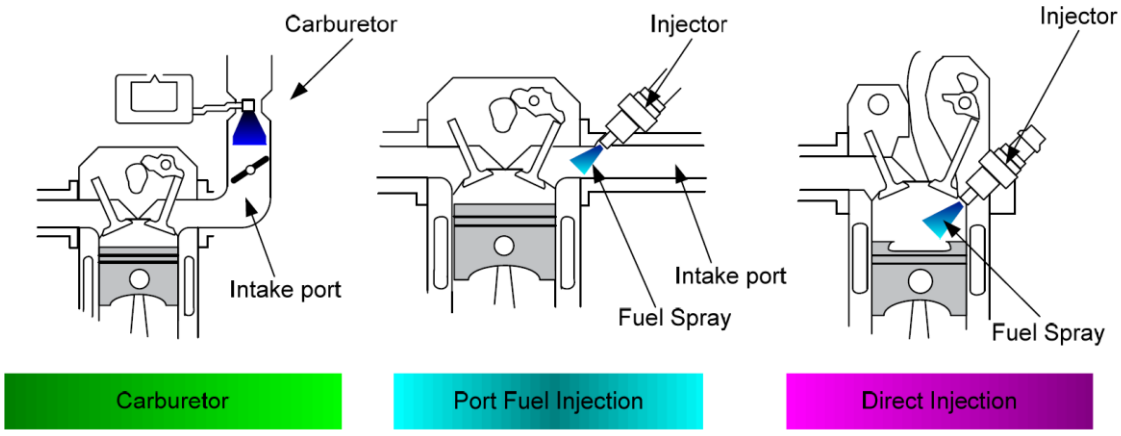

Figure 2.1 Mixture formation systems in GDI engines (Zhao 2010)

The GDI injectors have two advantages which cannot be found in PFI injectors and carburetors. Firstly, GDI injectors have an ability to control the amount of fuel injected into the engine chamber. This injection can allow industries to optimise the fuel amount in the engine in order to improve the fuel economy. Secondly, the cooling system of the GDI engine can avoid the occurrence of knocking when using a higher compression ratio, which can improve deposit accumulations.

During the development of the GDI injector, the fuel injector gradually becomes a key component because the GDI injector needs to provide the capability to operate on both homogenous and stratified charge combustion under different injection strategies. When the engine operates on homogenous charge conditions, a well-atomised and well-mixed dispersed fuel spray distribution is required under the conditions of early injection and low in-cylinder pressure. When the engine operates on stratified charge conditions, a well-atomised, compact and repeatable spray structure is required under higher in-cylinder pressure and late injection in order to obtain the fast mixture formation and controlled stratification. To fulfill the above requirements for the GDI engine, three different standard types of GDI injectors are widely used; their nozzle designs are shown in Figure 2.2.

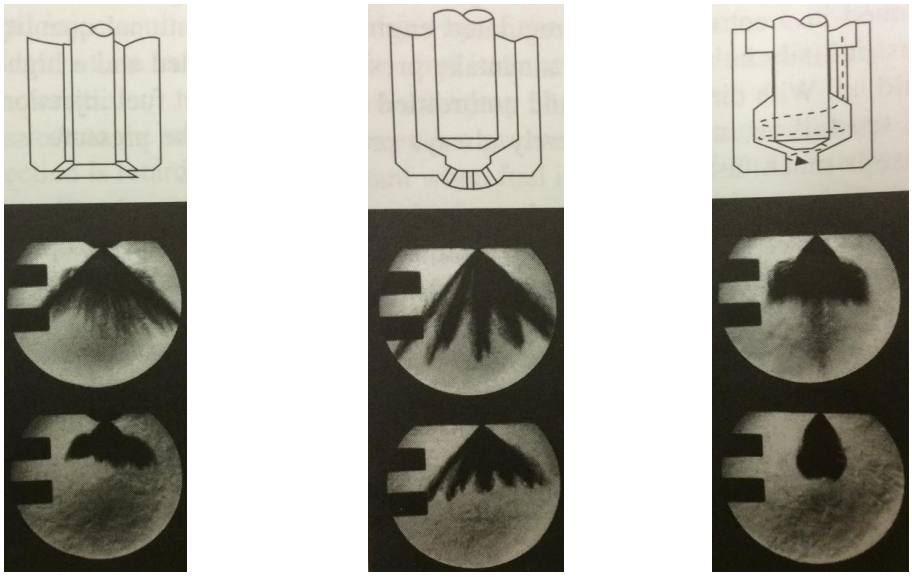

(a) Outward-opening nozzle (b) Multi-hole nozzle (c) Swirl nozzle

Figure 2.2 Types of GDI injector and their spray structure (Zhao 2010)

In Figure 2.2, the differences between the types of nozzle can be identified by the way in which they open and close. The injection mechanism for the outward-opening nozzle consists of liquid passing thorough the cross plane of the nozzle and producing a self-forming spray cone

angle when the valve opens. The multi-hole and swirl nozzle are designed as the inward-opening structure in order to generate swirl flow in the nozzle upstream for a better mixture. The characteristics of the multi-hole nozzle can be identified by its sharp and individual jet structure from Figure 2.2. By using the multi-hole nozzle, a partially homogenous mixture condition in the chamber can be established due to the insufficient spray atomisation quality. The distributions of the partially homogenous mixture contain an enriched mixture and lean mixture regions which result in different flame speeds during the combustion process. The flame speed accelerates in the enriched mixture region of each individual spray jet and then slows down in the lean region between each spray jet. To improve the lean mixture regions in the combustion chamber, increasing the number of nozzle holes and the hole's diameter are the common way to solve this issue. However, increasing the amount of hole numbers may result in a deposit formation and then cause higher hydrocarbon and soot emissions (Zhao 2010).

Currently, the swirl nozzle is widely used in the GDI engine due to its high quality of spray atomisation and spray flexibility. A characteristics of the swirl nozzle is its hollow cone angle to the spray structure which is strongly affected by the chamber pressure. This is a disadvantage for the swirl nozzle when the GDI engine operates at the various chamber pressures. It could influence the spray position in relation to the position of the spark plug.

To compare the outward-opening nozzle with the inward-opening nozzle, it can be seen that the advantage of the outward-opening lies in its production of a uniform structure of a hollow cone spray and also it is less affected from the chamber pressure for the spray angle. This allows the possibility of controlling the droplet size and injection mass flow rate by using multi-injection at a short injection duration time.

Three different combustion systems, i.e., spray-guided, wall-guided and air-guided, in the stratified operation GDI engine have been proposed, as shown in Figure 2.3.

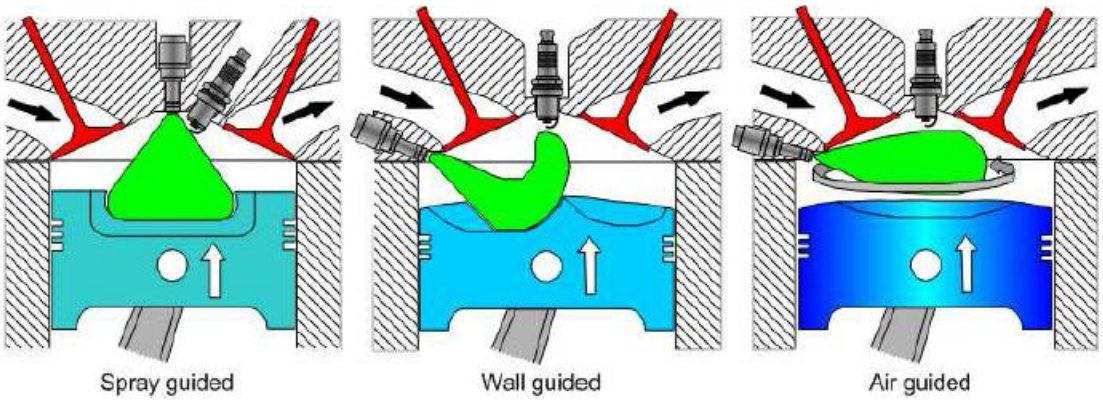

Figure 2.3 Spray, wall and air-guided combustion system at stratified charge (Stefan 2004)

- **Spray-Guided combustion system:** In this system, fuel is injected to the area near the spark plug and evaporated. Theoretically, the efficiency of spray-guided combustion system is higher than wall- and air-guided systems. This combustion system results in less wall wetting, lower row HC emission exhaust and lower sensitivity of air flow and cylinder-cylinder variation.

- **Wall-guided combustion system:** In this system, the fuel mixture is formed around the spark plug via specially designed combustion chamber geometry. The drawback of this combustion system is the increase in HC and CO emissions due to the incomplete evaporation of fuel.

- **Air-guided combustion system:** In this combustion system, the intake air flow guides fuel spray around the spark plug to achieve the stratification condition, greatly reducing wall wetting. The combination of air- and wall-guided combustion systems is widely used,

as shown in Figure 2.4. Fuel injected into the cylinder is directed by the effects of both wall-guided and air-guided bowls

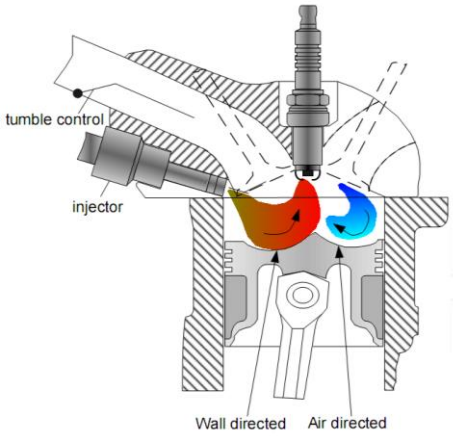

Figure 2.4 Spray, wall and air-guided combustion system at stratified charge (Giovanni 2013)

2.4 Multidimensional Models for a GDI Engine

2.4.1 Turbulence Modelling

Turbulent flows are characterised by diffusion, dissipation, fluctuating velocity fields and a high Reynolds number (Christensen and Johansson 2002). The turbulent flows are characterised by the time (turnover time) and eddy length scales (Reynolds 1980). The wide ranges of time scale are determined by the different flow structures such as laminar flow, turbulent flow and re-circulations. The definition of length scale in engine simulation can be expressed by the smallest Kolmogorov scale to the largest scale of engine geometry. For example, the rate of flame growth is directly affected by the varieties of turbulent distributions in spark ignition engines (Johansson 1996). Therefore, based on different turbulent eddy lengths and time scales, the turbulence model can be divided into three categories: the direct

numerical simulation (DNS), large eddy simulation (LES) and Reynolds-averaged Navier–Stokes (RANS).

The Navier–Stokes equations can be used to capture the effect of different scale of eddies, in order to solve the laminar and turbulent field flow in each computational cell without any turbulence models, a technique called direct numerical simulation (DNS)(Yokokawa 2002). It requires a fine enough mesh size to resolve the smallest length of flow problems including eddies in the flow field. The length of the smallest eddy in the flow field can be calculated by the Kolmogorov length scale (Kolmogorov 1941) which is presented below:

$$\eta_{Kolmogorov}[m] = \left(\frac{\nu^3}{\varepsilon}\right)^{\frac{1}{4}} \qquad \text{(Equation 2.1)}$$

Where ν is the liquid viscosity and ε is the average turbulent dissipation rate of kinetic energy. It can be observed that the Kolmogorov length scale decreases when the Reynolds number (*Re*) increases (ε increases). However, the current computer systems cannot afford the high total mesh number to calculate all the length scale in the high *Re* number condition due to the limitation of computational power. Therefore, the DNS method is not suitable for the high Re number, but it is useful to provide detailed information of the turbulent flow for the cases at a low Re number or simple computational geometry (Ferziger and Perić 2002).

With the fast development of computational capability and the limitation of the current computer power such as CPU for the DNS approach, another approach of the turbulent model, named the Larger Eddy simulation (LES) assumes that the turbulent flows are characterised by several ranges of eddies scale and LES only resolves the eddies in which their scale is larger than the mesh scale; the smaller eddies are solved by appropriate semi-empirical sub-models

(Ferziger and Perić 2002). This assumption indicates that the larger eddies' structure contains most of the turbulent energy and are more important in energy transport than smaller eddies. In the review of recent applications using the LES models, Rutland (Rutland 2011) indicated that the LES obviously deceases the computational time and improves the scenarios with the low *Re* number.

The LES approach determines the effects of different scales of eddies around a liquid jet (Figure 2.5). As a result, the LES approach has been widely used for the simulation of the nozzle flow, engines and spray (Rutland 2011, A. Lampa 2013, Wenjin Qina 2014, Lei 2015). For nozzle flow simulation, several studies (Befrui 2011, Delteil 2011, Befrui 2012, Befrui 2014) employed the LES approach to investigate the breakup mechanism of a liquid jet and the effects of different GDI nozzle geometric designs on primary breakup regimes for spray simulation, interactions between a liquid and gas are important. For example, the unsteady turbulent gas flow caused by high-speed sprays and other transient physical and chemical processes in a spray system can affect the turbulent flow field distribution and droplet dispersion. Because of the intensive interaction between a liquid and gas in the LES approach, liquid evaporation also affects the mixture distribution in the chamber (Lei 2015). In the application of the LES approach for engine simulation, additional flow structures, eddies and vortices that further affect the mixture and combustion distributions can be expected (Rutland 2011). Figure 2.5 shows a comparison of velocity vectors determined using RANS and LES approaches.

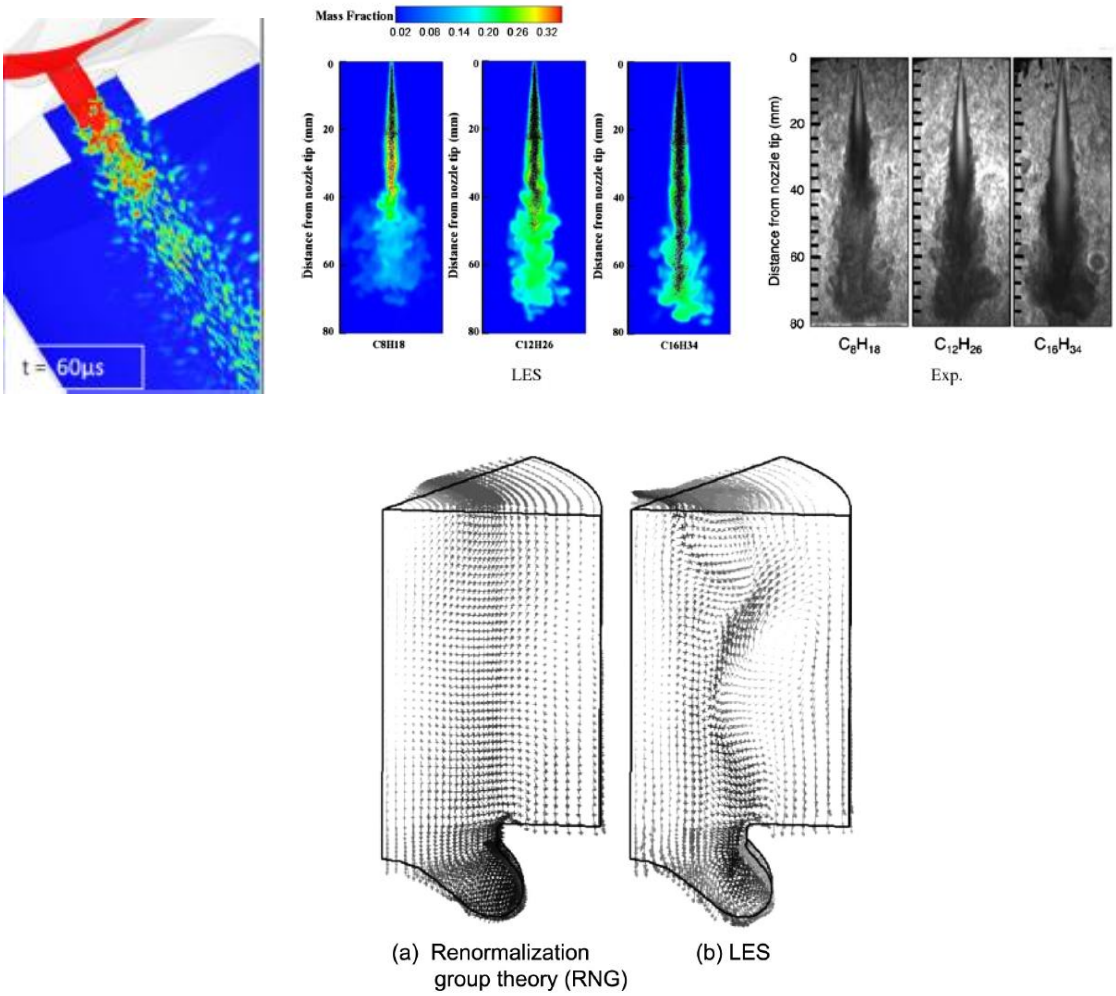

Figure 2.5 LES application on nozzle, spray and engine flow simulation (Rutland 2011, Befrui 2012, Lei 2015)

The third turbulent model, called the Reynolds-Averaged Navier-Stokes (RANS), firstly proposed by Osborne Reynolds (Reynolds 1894) has been widely used to solve engineering problems. This approach splits the instantaneous value of turbulent flow into a time-averaged value. Hence, RANS represents a macrocosm averaged for the ensemble range of turbulent fluctuation rather than a specific eddy variation. The two extra terms are added because of the averaging process; they are the Reynolds stress tensor and turbulent heat flux. According to the linear eddy viscosity model which is proposed by Boussinesq (Boussinesq 1877), the Reynolds stress can be modelled into an algebraic equation to turbulent viscosity which is shown in Equation 2.2.

$$\bar{\tau}_{ij,t} = \mu_t \left(\frac{\partial \overline{v_i}}{\partial x_j} + \frac{\partial \overline{v_j}}{\partial x_i} \right) - \delta_{ij} \frac{2}{3} \rho k \qquad \text{(Equation 2.2)}$$

Where μ_t is the turbulent viscosity and k is the turbulent kinetic energy.

In the approach of RANS, several different turbulent models such as the zero-equation model, one-equation model and two-equation model are proposed; they depend on the number of equations which are needed to be solved. The zero-equation turbulent model which is also named the Cebeci-Smith model was developed by Tuncer Cebeci and Apollo M. O (Smith 1967) in 1967. This model is suitable for the attached boundary layer like the simulation of airplane wing in the high speed flow field. However, this model cannot provide accurate numerical results for the cases with an obvious separated zone and curvature effects (Smith 1967). The one-equation model, also called the Mixing-Length Model and was proposed by Ludwing Prandtl (Wilcox 1988) in 1920. This model uses the mixing length, which defines the distance for a turbulent eddy, completely dispersed into the surroundings to be modified in terms of turbulent viscosity. The more common turbulent model which is used in the internal combustion engine is the two-equation standard *k*-*ε* model (Launder 1974). This model determines the two separate transport equations of turbulent kinetic energy *k* and the dissipation rate *ε* to solve the turbulent problems in the high Reynolds number with suitable boundary conditions (Rodi 1993). However, the weakest part of the standard *k*-*ε* model is its isotropy of turbulence and the calculation of the near wall flow field (Patel 1985). Thus, some modifications have improved the performance of the standard *k*-*ε* model. One of improving models which is called the Re-Normalisation Group (RNG) *k*-*ε* model (Yakhot 1992) is similar

in form to the standard *k-ε* model. This model adds the source term in the *ε* equation which can significantly improve the accuracy for stained and swirling flows (Yakhot 1992). Another improving model is called the realizable k-ε model and it has enhanced the accuracy of the standard *k-ε* model by using two important methods. Firstly, it includes a new formation to calculate the turbulent viscosity. Secondly, a new transport equation to calculate the dissipation rate *ε* of turbulence is applied by using a mean-square vortices fluctuation. The benefit of a realizable k-ε model is that it provides more accurate results for the flow field with rotation, separation and recirculation.

To combine the effects of the low Reynolds number and shear flow spreading, the k-ε model was developed by Wilcon (Wilcox 1998, Wilcox 2008); in which it showed a strong agreement in predicting the far wake, round and radial jets, wall-bounded and free shear flows. In addition, in order to enhance the calculating quality of the three-dimensional complex flows and anisotropic turbulent flow, Launder (Launder 1975, Popovac 2007) proposed Reynolds stresses model (RSM) which considers the effects of the Reynolds stress fields. However, due to the additional calculation for Reynolds stresses, the computational time is significantly longer than the standard *k-ε* model.

2.4.2 Spray Modelling

In GDI engines, the distributions of the air-fuel mixture strongly affects their combustion efficiency and exhaust emission. Moreover, with the gradual stricter emissions' requirements, the new generation bio-fuel and injection systems have been intensively investigated in order to match the stricter emissions' regulations. In order to decrease the research cost and increase the efficiency of research, the CFD approach has been widely applied to provide or support a

reference and an illustration for the experimental results. In the simulation of engine performance, several spray models had been proposed and developed in last few decades based on the different theories for the different operating conditions such as injection and ambient pressure.

However, the characteristics of engine spray are composed of a wide range of different droplet sizes and have a complex interaction with the surrounding gas. It results in the calculation of each spray droplet's behaviour becoming a big challenge due to the limitation of its computational capability. In order to overcome this challenge, an applicable way is proposed by using different sub-models to describe, respectively, its physical phenomenon during the development of the spray process. The physical phenomena in the spray development process generally includes nozzle flow, spray atomisation, evaporation, drop collision/coalescence, and spray/wall interaction (Reitz 1996) which are introduced in following sections.

The process of spray development, can be divided into two different regions: primary breakup and secondary breakup, which is shown in Figure 2.6.

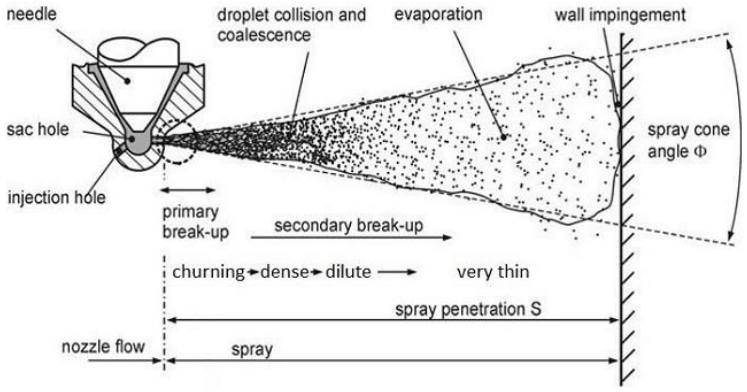

Figure 2.6 Sketch of physical phenomenon during spray development (Baumgarten 2006)

From Figure 2.6, the structure of spray can be divided into four different by calculating volume of the fluid which are respectively: intact corn and churning, dense, dilute and very thin zone.

The volume of the fluid can be calculated and compared with the volume of the air present within the spray edge. The volume fraction is a numerical parameter affected by the cell size. When liquid leaves from the nozzle exit, the incomplete atomisation results in the liquid still existing for a short distance from the nozzle hole and is presented by a jet shape which is called liquid breakup length or the intact core. This parameter is used to classify the primary and secondary breakup region. In this stage, some dense droplets and ligaments begin to disintegrate from the liquid jet body due to several different breakup mechanisms, such as aerodynamic and turbulent force; this is called the churning zone. In this zone, the percentage of the liquid phase is higher than that of the gas phase due to the intact core and dense distribution of ligaments.

After the zone of intact corn and churning, the spray structure develops into the dense zone due to the stronger liquid atomisation. The percentage of liquid phase is still higher than the gas phase, but it is lower than the churning zone. In the dense zone, the aerodynamic force and interactions between ligaments are the major factors causing the breakup. In the dilute zone, the percentage of liquid is smaller than the dense zone due to the droplet evaporation and the average space between each droplet is extended. However, because of the existence of the droplet-air-droplet effect, the aerodynamic force which is caused by other droplets is still affected by the droplet's behaviours. The far-field spray is called the very thin zone. In the very thin zone, because of the development of spray process, the zone spreads and larger than other zones. Because of atomisation, the number of droplets increases. However, despite this increase, the gas phase occupies most of this zone.

2.4.3 Primary Breakup Model

In the region of primary breakup, the mechanism of breakup can be caused by turbulence from the nozzle flow, the vapour bubble breakup from the cavitation effect and the aerodynamic force around the liquid jet surface (Arcoumanis 1997). When the liquid exits from the nozzle hole, the stronger turbulent effects are generated and accompanied by the liquid. This occurs because of the pressure drop inside the nozzle and the liquid velocity being accelerated by the gradually smaller nozzle hole area. Moreover, when the liquid passes through the sharp edge at nozzle entrance, it enhances the turbulent level and decreases the nozzle flow area due to the cavitation effects or wall separation. One of the breakup mechanisms from the liquid vapour bubble is caused by the generation of cavitation at the nozzle inlet corner. When the vapour bubble implodes inside the liquid, it increases the disturbances inside the liquid jet and then results in liquid disintegration (Stiesch 2003). These phenomena are described in Figure 2.7. The third mechanism of aerodynamic force is caused by the different velocity between the liquid and the surrounding gas and then the surface disturbance generates on the liquid surface results in the droplet detaching from the liquid jet.

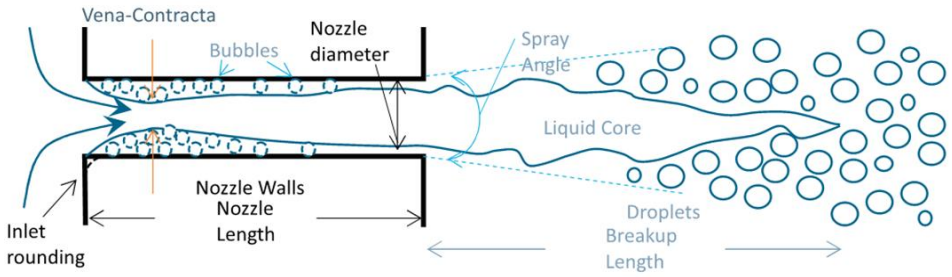

Figure 2.7 Illustration of primary breakup mechanism (Wang 2014)

In order to classify the breakup regimes, several researchers (Ranz 1959, Torda 1973, Reitz 1978, Reitz and Bracco 1986) proposed a classification description to analyse its breakup

phenomena by using the Reynolds number (*Re*), Weber number (*We*) and Ohnesorge number (*Z*) of liquid, which are defined as below:

$$Re = \frac{\rho_{air} V L}{\mu} \qquad \text{(Equation 2.3)}$$

$$We = \frac{\rho_{liquid} V^2 L}{\sigma} \qquad \text{(Equation 2.4)}$$

$$Z = \frac{\mu}{\sqrt{\rho \sigma d_{noz}}} \qquad \text{(Equation 2.5)}$$

Where v_{inj} is the liquid velocity, ρ is the liquid density, d_{noz} is the nozzle hole diameter, μ is the liquid viscosity and σ is the liquid surface tension.

In Figure 2.8, it shows the classification of the jet breakup regime by using *Re* and *Z* number and four different jet breakup regimes which can be classified: Rayleigh Breakup, First Wind-induced Breakup, Second Wind-induced Breakup and the Atomisation Regime (Reitz and Bracco 1982).

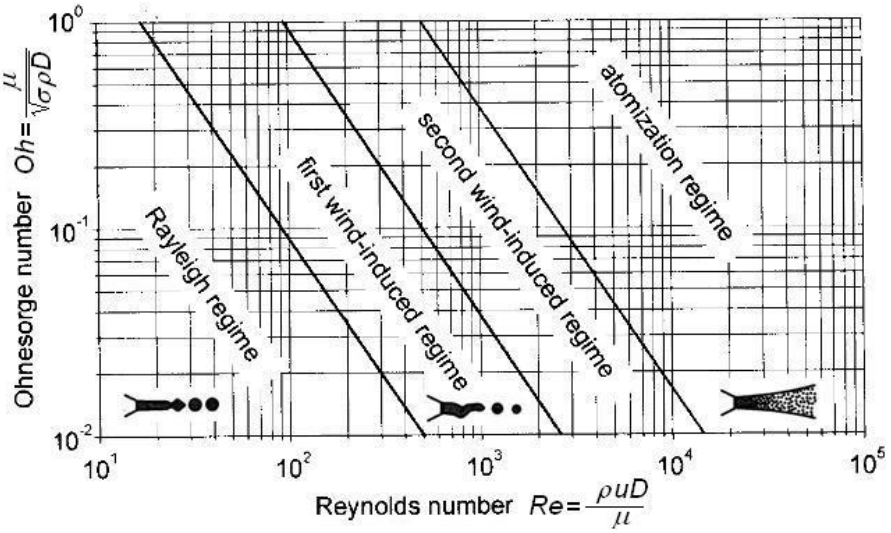

Figure 2.8 Distribution of jet breakup regime (Miesse 1955)

However, from Equation 2.3 and 2.4, it can be observed that the classification is defined by liquid properties such as liquid viscosity and surface tension and do not include the effects of

gas phase density. Experimental results point out that the gas density is one of the major factors to affect spray behaviours (Torda 1973). Thus, Ranz (Ranz 1959) proposed a modified classification by using the *We* number of the gas phase which considers the density of the gas phase and the surface tension of the liquid. However, this is not a comprehensive classification since the effects of liquid viscosity on jet breakup are not considered. Thus, Reitz (Reitz 1978) suggested a three-dimensional classification of jet breakup regimes which considers the gas to liquid density ratio, *We* and Ohnesorge number, in Figure 2.9.

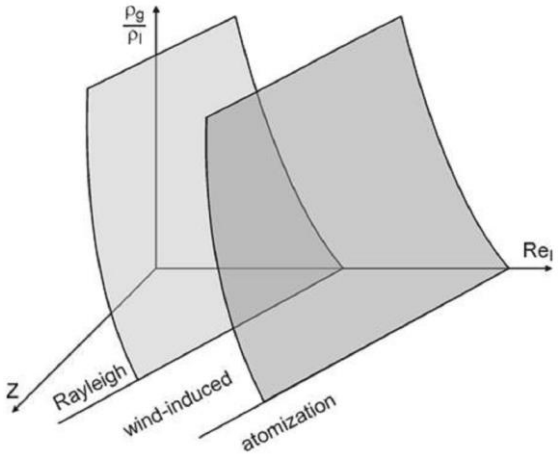

Figure 2.9 Schematic of three-dimensional classification for liquid jet breakup regimes (Reitz 1978)

The regime at a low injection velocity is called Rayleigh Regime and the breakup is primarily driven by the liquid oscillating force and its liquid surface tension force. In the regime ofwind-induced breakup, the increasing nozzle exit velocity results in the surface disturbance around the liquid jet surface; this is caused by the more intensive interaction between the liquid and gas phase, and leads to jet breakup. In the high density of the gas phase or high nozzle exit velocity condition, the atomisation regime is reached which is the breakup mechanism for the real spray situation in the direct injection engine.

Spray atomisation plays an important role in spray development. However, due to the limitation of experimental measurements in the high dense droplet zone, the investigation of detailed breakup mechanisms in the real size injector is incomplete. Therefore, different numerical models are used to predict the liquid breakup in this regime; they also consider the effects of turbulence and cavitation.

Due to the complicated gas-liquid two-phase flow, two different strategies are offered to solve the two-phase flow problem in the CFD approach, which are the Eulerian (Crowe 1982, Jiang 2010) and Lagrangian method (Gosman 1980) in Figure 2.10. In the Eulerian approach, the spray is considered as a continuous phase and solved by using the Eulerian assumptions. Moreover, the interface between the liquid and gaseous phase is tracked to calculate the variance of volume fraction. In the Lagrangian approach, the liquid droplets are treated as a 'particle' and the gaseous phase is solved by using Eulerian method. The 'particle' is assumed to include a number of droplets and they are given the same droplet size distribution and proprieties.

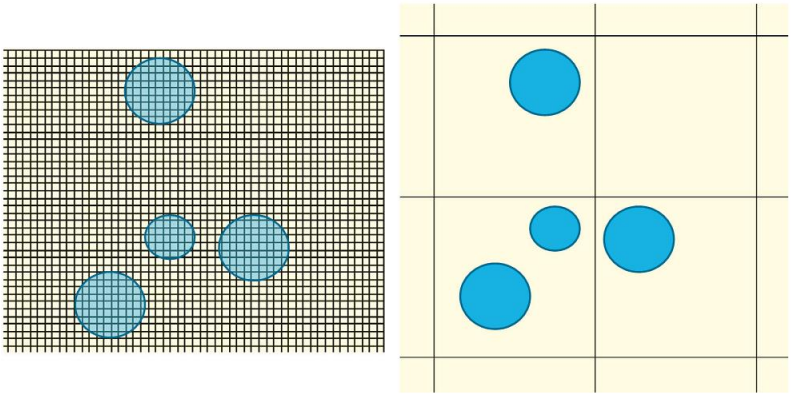

(a) Eulerian approach (b) Langrangian approach

Figure 2.10 Illustration of Eulerian and Langrangian approaches in the CFD method (Jiang 2010)

In numerical studies of spray development and droplet behavior, two different numerical approaches are widely used: Euler–Euler and Euler–Lagrange. In the Euler–Euler approach, the volume of fluid (VOF) (Hirt 1981) is often used in nozzle flow and near field simulation, whereas an interface tracking method is typically employed to study the interaction between the liquid and gas phase. The VOF approach can also be used to study the intensity of liquid atomisation in the primary breakup regime in nozzle simulation under different operating conditions. However, in order to capture the droplet's behaviors and the variances of the liquid surface, VOF requires a very small grid cell, shown in Figure 2.11 (Fuster 2009)

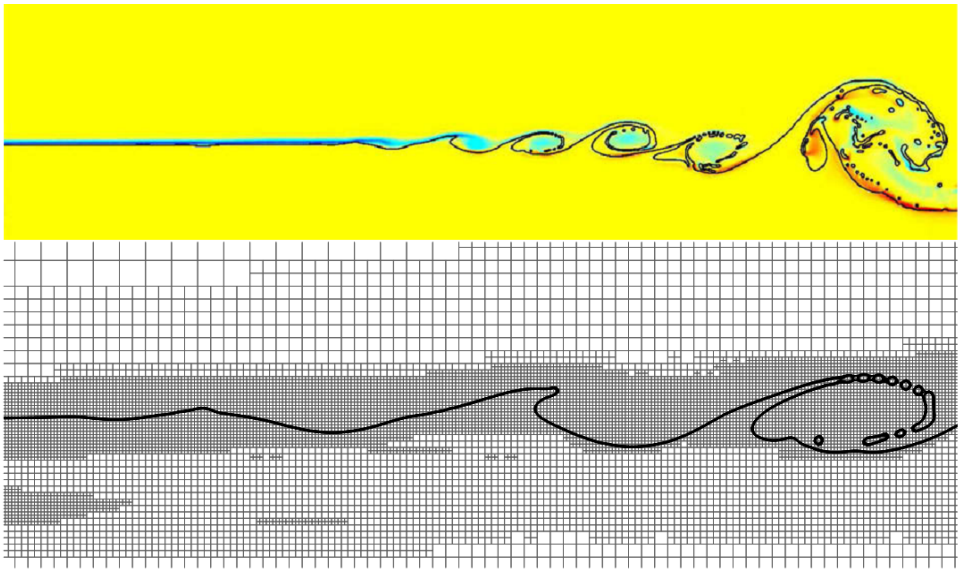

Figure 2.11 Mesh distribution on the liquid jet surface in the VOF approach (Fuster 2009)

In the Euler-Euler approach, both the liquid and gas phase are considered as continuous phases and each phase is solved respectively by using the Eulerian method (Sanjosé 2011). In the Euler-Lagrange approach, Discrete (Crowe 1982) Droplet Model (DDM) (Gosman 1980) approach is one of the approaches to be used widely to simulate the spray development. In the DDM approach, the fluid phase is considered as continuous phases and solved by Navier-stokes equations. The dispersed phase is solved by tracking a large number of particles, bubbles and droplet to calculate the their characteristics which is shown in Figure 2.12 (Gorokhovski 2008)

Figure 2.12 Illustration of the DDM approach (Gorokhovski 2008)

The VOF application on the primary breakup region is widely used with the LES model, which is called the VOF-LES method and has been intensively investigated in gasoline and diesel injectors (De Villiers 2004, Befrui 2011, Delteil 2011, Befrui 2012, Befrui 2014, Shost 2014). The capability of this method includes the effects from liquid surface tension, turbulence and aerodynamics which are the key factors that lead to fuel atomisation. Delteil (Delteil 2011) and Befrui (Befrui 2012)used the VOF-LES method to simulate primary atomisation and Rayleigh breakup of the liquid jet. They indicated that the VOF-LES method can provide an accurate prediction of the calculation of the breakup length and distribution of the droplet size. The applications of the VOF-LES method on the injectors are also used to predict the initial droplet size and velocity distributions in the nozzle near-flow field. E.de Villiers (De Villiers 2004) studied the mechanism of liquid disintegration by using the diesel injector. It indicates that the initial perturbation is driven by the inter-phase aerodynamic interaction. For gasoline injectors, Bizhan (Befrui 2011, Befrui 2014) investigated the internal flow and spray characteristic in GDI injectors by using the VOF-LES method. Moreover, the influences of different nozzle L/D ratios, counter-bore size and nozzle tapered geometry were also investigated by Bizhan (Befrui 2012). This study indicates that the tapered nozzle increases their breakup length due to the smoothness of the KH instabilities. Furthermore, the nozzle with a smaller L/D ratio presents a shorter breakup length due to the increase of vortices. Shost, et al (Shost 2014) compared two nozzle geometries with different L/D ratios. This study suggests that the nozzle with a smaller L/D ratio has a bigger spray plume angle.

The application of the DDM method is well known for the wave-breakup model which is also described as the Kelvin-Helmholtz (KH) model (Reitz 1987). The breakup mechanism of the KH model, was proposed by Reitz; and is dependent on the development of surface disturbance on the liquid jet surface which is driven by the aerodynamic force (Reitz 1987). This model is not only widely used in the primary breakup model but also for the secondary breakup model. To apply the KH model to simulate the high speed diesel jet, Reitz and Diwakar (Reitz 1987) introduced a “blob” theory into the spray model which is also called the Blob-injection model. This model assumes that the intact liquid is composed of several ideally spherical blobs with a constant density and has the same size of the nozzle hole diameter which can be seen in Figure 2.13. This model is used widely with the KH model. However, without considerations for the influences of the nozzle flow such as cavitation and wall separation effects, this model needs to be validated for its initial blob diameter with the experimental data (De Villiers 2004)

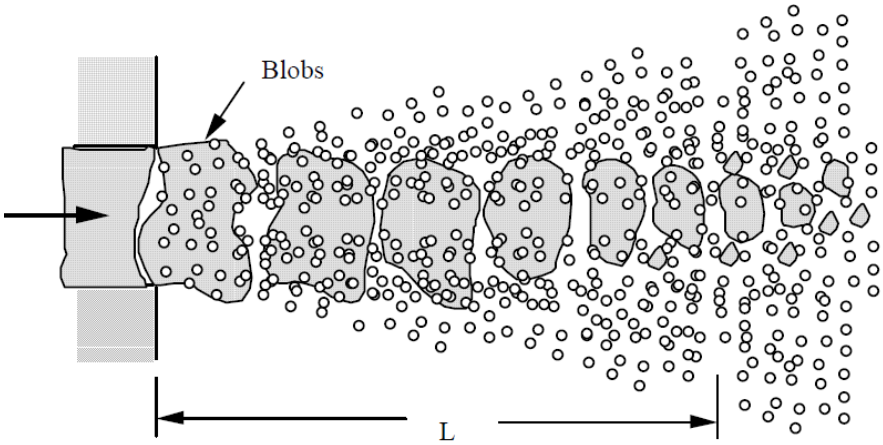

Figure 2.13 Schematic of Blob-injection method in the primary breakup region (Reitz 1987)

The above KH breakup model only considers the difference in the aerodynamic force from the velocity between the gas and liquid phase. However, due to the complicated breakup mechanisms, another two factors cause the liquid breakup which are the effects of turbulence and cavitation. A phenomenological model was developed by Huh et al. (Huh and Gosman

1991) which assumes that the turbulence and cavitation effects from the nozzle are the main source providing the perturbations on the liquid surface which then result in the liquid breakup. However, due to the crude calculation of the cavitation effects, the discharge coefficient number (*Cd*) needs to be corrected with the experimental data.

The cavitation phenomenon is well known as one of the important factors in nozzle design for automotive industries, and has also been a major issue for engineering due to the vibration and damage of the mechanical component. Cavitation is formed by the liquid vapor when the liquid static pressure is lower than the liquid vapor pressure. Due to the complexity of cavitation formation and its field flow, direct observation and numerical approaches are widely employed by researchers. Gavaises (Gavaises 2015) used visualization and numerical approaches to show the formation and development of a cavitation cloud, shown in Figure 2.14. The development of cavitation can be broken into six steps:

(1) A cavity forms from the nozzle turn due to the rapid acceleration of liquid.
(2) This cavity grows steadily.
(3) A re-entrant jet forms and pushes the cavitation back to the nozzle turn, which causes the cavity to start separating from the nozzle wall.
(4) The re-entrant jet causes the cavity to detach from the nozzle wall.
(5) The cavity completely detaches from the initial forming position, and the rear of the cavity transforms into a bubble cloud surrounded by significant vorticity due to the opposing direction of main flow.
(6) The detached cavity fully transforms into a bubble cloud and moves forward with following flow. In the nozzle turn, if the local pressure drops below the vapor pressure again, the cavity will form again in the nozzle turn and repeat the cycle from step 1 to 5.

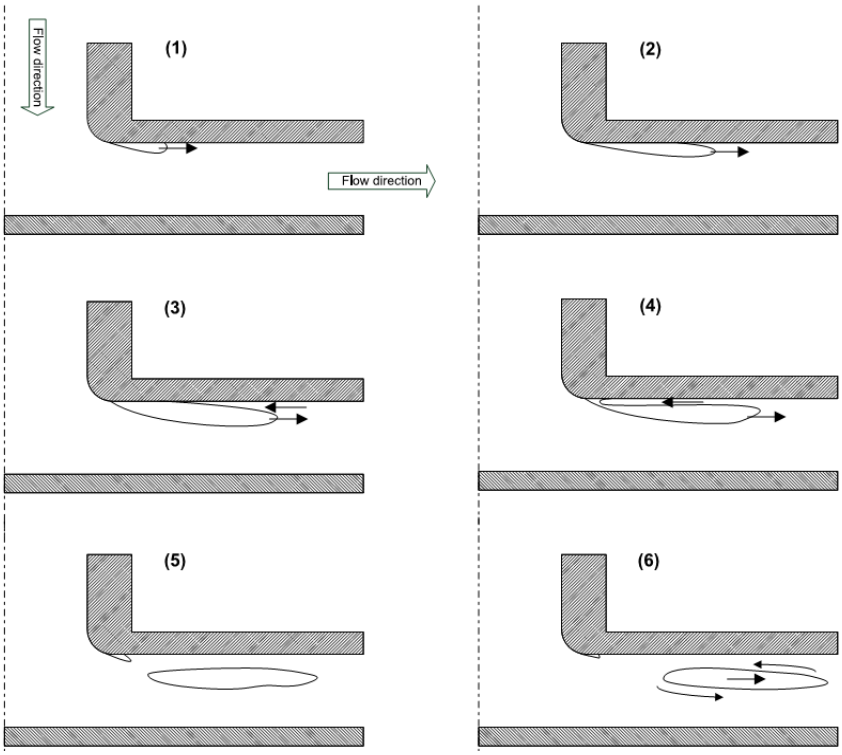

Figure 2.14 Formation and development of cavitation cloud (Gavaises 2015)

The formation of the cavitation in the nozzle is caused by several factors, including high injection pressure and the nozzle's geometric design. The influences of different nozzle geometry on cavitation formation have been studied experimentally by several researchers. Su et al. (Su 1995) investigated two different types of diesel injectors with rounded inlets (RI) and sharp-edge inlets (SEI) and observed that the spray generated from SEI injectors has a higher velocity, longer penetration length, smaller droplet size and larger spray angle. This is a result of the sharp-edge inlet causing greater flow contraction, which reduces the effective flow area at the nozzle exit. The influence of different nozzle geometries such as entrance curvature radius and orifice inclination angle has also been studied by Payri (Payri 2002) and He (He 2013). They recognised that changes of the curvature radius and inclination angle strongly influenced the distribution of pressure and cavitation inside the nozzle. The effect of different L/D ratios is also examined by Nouri. (Nouri 2012), who found that nozzles with larger L/D ratios show more developed and stable cavitating flow.

Unlike the high injection pressure for diesel, the average injection pressure of GDI nozzles is currently 100–200 bar. This means that the formation of cavitation in the GDI injector is not as obvious as in the diesel nozzle. Despite this, several authors used optical methods to study this cavitation in the GDI nozzle. Mirshahi (Mirshahi 2013) used a high-speed camera to observe the formation and development of cavitation in the 3D transparent six-hole GDI injector which is 15 times larger than real size GDI nozzle. It is found that the cavitation vortex directly changes the spray angle, and the effect of bubble collapse in the nozzle increases the instabilities of spray structure. Gavaises (Gavaises 2004) used high-speed video cameras to identify the effects of cavitation on the formation of string ligament/droplets at nozzle near-field under different needle lift conditions. They observed that two different phenomena, cavitation and air entrainment, occurred at different operating conditions. Furthermore, Nouri (Nouri 2012) discussed the effect of fuel temperature on cavitation development, pointing out that the lower viscosity and weaker molecular bounding caused by higher fuel temperature can enhance the cavitation effect. A study of the effect of fuel temperature on cavitation by Aleiferis (Aleiferis 2010) showed that fuel temperature higher than its boiling point can dominate atomisation.

In the development of numerical models for cavitation, Arcoumanis (Arcoumanis 1997) proposed a cavitation induced breakup model which uses the area ratio between the vapour bubble and liquid at the nozzle exit to calculate the initial blob size. However, the disturbance from the vapour bubble collapse is not considered in this model. Therefore, an improved cavitation model which includes the bubble's collapsed energy was presented by Nishimura (Nishimura 2000). This model transfers the collapsed energy from the cavitation vapour bubble into turbulent kinetic energy. Kuensberg (von Kuensberg Sarre 1999) developed a phenomenological nozzle flow model based on experimental data, to examine the effects of

different hole diameters, L/D and r/D ratios and summarised five different distributions of cavitation phenomenon inside the nozzle; as Figure 2.15.

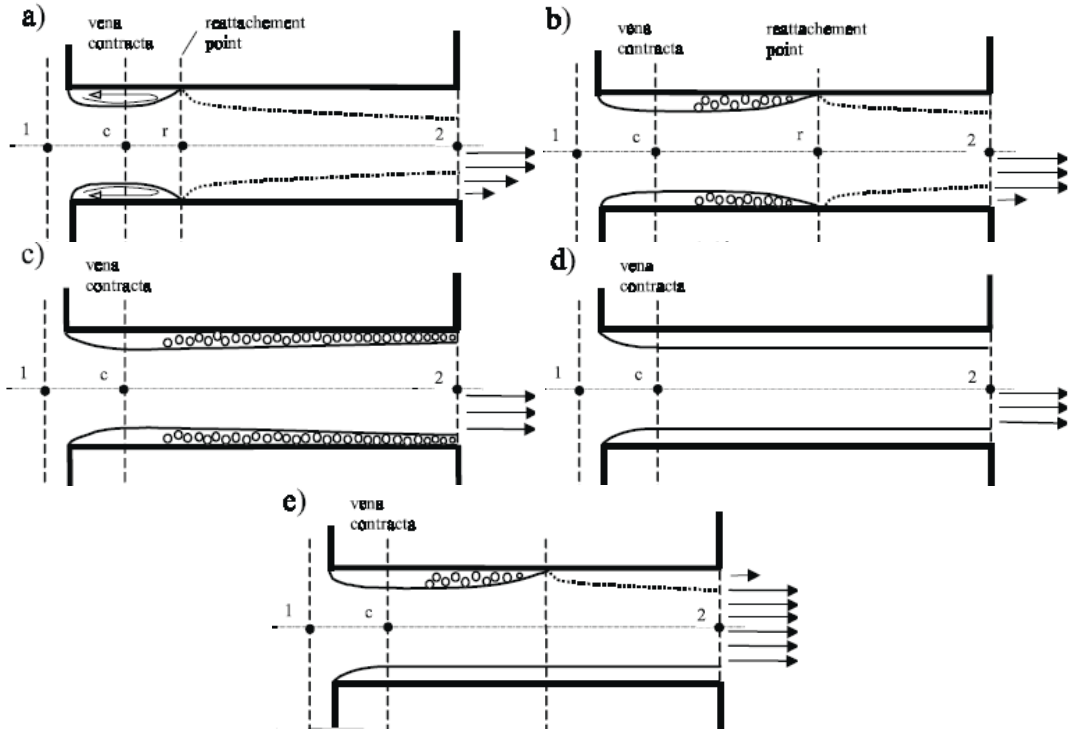

Figure 2.15 Distributions of cavitation regimes: (a) turbulent flow, (b) onset of cavitation, (c) super cavitation,(d) hydraulic flip and (e) partly reattached flow (von Kuensberg Sarre 1999)

According to the above cavitation regions, an improved blob injection method with the consideration of cavitation effects was developed by Kuensberg (von Kuensberg Sarre 1999) which is shown in Figure 2.16

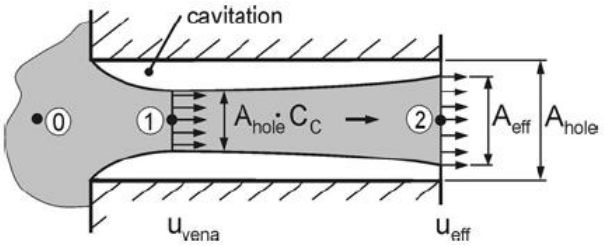

Figure 2.16 One dimensional cavitation model (Baumgarten 2006)

In this model, it is assumed that the injection effective velocity and initial blob diameter are directly influenced by different cavitation formation under different nozzle geometric designs,

such as: nozzle length, diameter and the radius of the nozzle inlet. However, the variation of turbulent kinetic energy which is caused by the implosion of vapour bubbles is not considered in this model. Another cavitation model based on the analysis of the boundary layer was introduced by Obermeier (Obermeier 1992, Obermeier 1993). It discusses respectively the cases of non-cavitating, cavitating flow and cavitating flow with reattachment by considering the cylinder pressure and the length of the cavitation region.

Recently, the improved primary breakup model which includes the major breakup mechanisms of aerodynamics, turbulent and cavitation effects was proposed by Som and is called the Kelvin Helmholtz-Aerodynamic Cavitation Turbulence (KH-ACT) model. (Som 2009, Som 2010). It assumes that the maximum ratio of the breakup length/ breakup time of each breakup mechanism dominates the liquid breakup process. In the calculation of the turbulent effects, the KH-ACT model calculates the initial kinetic energy and dissipation rate at the nozzle exit as the input parameters for the KH-ACT model which are calculated by the nozzle's geometrical design.

2.4.4 Secondary Breakup Model

When the liquid droplets detach from the liquid body jet, these droplets disintegrate into smaller droplets due to the aerodynamic force which is caused by the velocity difference between the droplet and the surroundings. The aerodynamic force results in an instable growing wave of the droplet surface and then leads to its disintegration when the aerodynamic force becomes larger than the surface tension force. Therefore, the droplet behaviours in the secondary breakup regime can be presented by the Weber number (*We*). According to the criteria of We number, Liu and Aoyama summarised breakup models from several studies. Secondary

breakup can be divided into five different regimes: vibrational, bag, shear or stripping, catastrophic and transitional breakup models, as in Figure 2.17 (Liu 1993, Aoyama 1996)

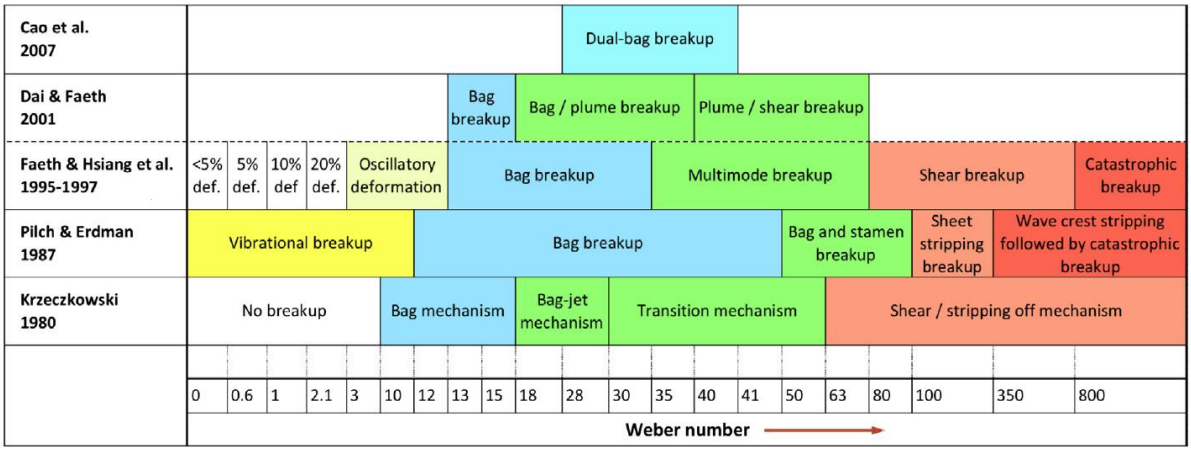

Figure 2.17 Sketch of the breakup model in the secondary breakup region (Jenny 2012)

Due to the different breakup models based on the different *We* range, it is impossible to use only one numerical breakup model to describe all the breakup regimes. Therefore, several numerical breakup models based on different theories and breakup assumptions have been proposed, such as: the Taylor-Analogy Breakup (TAB), Kelvin-Helmholtz (KH), Enhanced TAB (ETAB) and the Rayleigh-Taylor (RT) model.

The Taylor-Analogy Breakup (TAB) was developed by O'Rourke and Amsden (O'Rourke 1987) which is based on the theory of an oscillating force between a spring-mass system and a droplet, as in Figure 2.18.

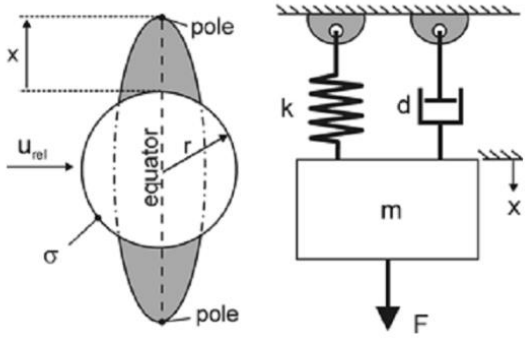

Figure 2.18 Sketch of the TAB model mechanism

In order to observe more realistic spray characteristics such as spray penetration, radius expansion and droplet size distribution, an Enhanced TAB model (ETAB) was developed by Tanner (Tanner 1997) to improve the accuracy in bag or stripping breakup. It is assumed that the droplet undergoes a process of cascade breakup until the child droplets reach a stable stage. The major difference compared with the TAB model is the calculation of child drop size and the number after the droplet breakup (Apte 2003). Furthermore, in order to extend the simulation range to a stronger droplet breakup with a higher *We* number, Tanner (Tanner 1997) reintroduced the Cascade Atomisation and drop Breakup (CAB) model. The most common secondary breakup model which is widely used is the Rayleigh-Taylor breakup (RT) model proposed by Su. et al (Su 1996). The breakup mechanism of the RT model assumes that the droplet is decelerated by the drag force and results in the development of the RT instabilities on the droplet surface (Patterson and Reitz 1998). In the recent applications, the KH-RT model (Beale and Reitz 1999, Lee 2002) is widely used in diesel spray in which the KH model is applied on the simulation of the primary breakup region and the combination of the KH and RT model is used in the secondary breakup region.

2.4.5 Other Spray Sub-Models

Drop Collisions and Coalescence

During the spray development, droplet collision frequently occurs in the dense spray region and the region near the spray axis in the high injection pressure condition. The effects of the drop collision directly affect the mean droplet size and its spatial distribution and further affect the spray combustion process.

The collision regimes can be divided into three main different regimes by using the collision We number and an impact parameter: permanent coalescence, bounce and temporary coalescence which is shown in Figure 2.19 (Munnannur 2007).

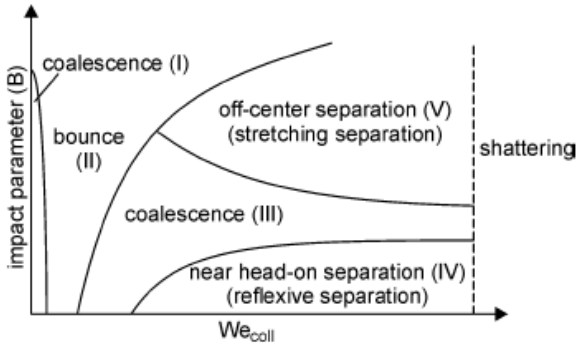

Figure 2.19 Regimes of droplet collision (Qian 1997)

The third collision regime (temporary coalescence) can be further divided into reflexive and stretching separation which depends on the different types of collision, as in Figure 2.20 .

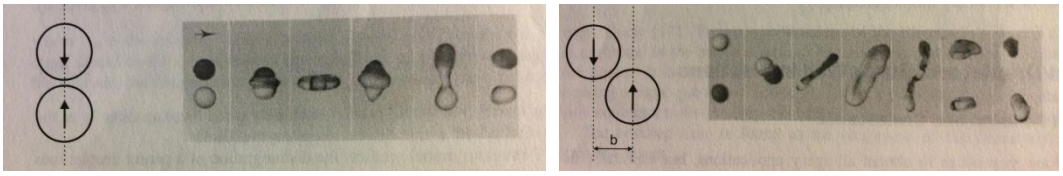

- reflexive separation (near head-on collision)
- (b) stretching separation (off-center collision)

Figure 2.20 Types of collision in temporary coalescence

Due to the difficult validation between the collision model and experimental spray data, there still are unknown mechanisms that occurred during the spray breakup and collision process. The classical standard collision model was developed by O'Rourke (O'Rourke 1981) and has been used widely in the present spray simulation. The O'Rourke model only investigates the regime of coalescence and the stretching separation (Amsden 1989). In order to extend the simulating capability in the collision regimes, several collision models for different collision regimes have been proposed (Tennison 1998, Estrade 1999, Georjon 1999). To provide a collision model with more simulating capabilities to couple the different collision regimes, Post (Post 2002) developed a collision which can predict the fragmentation behaviours in reflexive and stretching separation (Post 2002) and Munnannur (Munnannur 2007) introduced a collision model to account for all the collision regimes.

Drop Vaporisation

Evaporation is an important factor affecting the combustion rate and emission formation in the direct injection engine (Baumgarten 2006). This is because the air/fuel ratio is directly affected by the amount of vaporised fuel, and poor evaporation causes an increase in soot and unburned hydrocarbon emissions. Moreover, the rapid fuel evaporation causes an increase in nitrogen oxides in the diesel engine due to the rapid premixed combustion at high ambient temperatures.

Therefore, the robust evaporation model can provide a prediction for the overall distribution of mixture formation and further combustion development.

Most evaporation models treat fuel as single components. However gasoline and diesel are composed of hundreds of different components, thus single-component evaporation models are insufficient to predict droplet evaporation and behavior (Samimi Abianeh 2014). To increase prediction accuracy for evaporation rate, mixture distribution and emission for multi-component fuels, a multi-component fuel evaporation model is developed. Currently, there are two different approaches to the application of multi-component models: discrete multi-component (DMC) and continuous multi-component (CMC) approaches (Tamim 1995).

The DMC approach models fuel real distillation using a limited number of components; high accuracy of fuel surrogate properties such as thermal conductivity and heat capacity is not required. The DMC model has been examined by several authors, including Ra (Ra 2009), Torres (Torres 2003), and Abianeh (Abianeh 2012, Abianeh 2012). Smith (Smith 2007) used an experimental method to generate fuel distillation with limited components. Ra (Ra 2009) separately predicted the evaporation of diesel and gasoline using six and seven components, respectively, and the fuel distillation curve tracked closely with experimental measurement (Butts 2008)

Unlike the DMC model, the CMC model assumes that fuel composition is a continuous distribution of molecular weight, thus reducing the computational load. Tamim (Tamim 1995) developed a continuous thermodynamic vaporization model to describe the distribution of molecular weight for multi-component fuel using a gamma distribution. In addition, Wang and Chia-fon (Wang and Chia-fon 2005) used gamma distribution to develop a multi-component

wall-film vaporization model. However, when the CMC model is applied to the simulation of combustion or detailed chemical reactions, the description of the features of each component is limited, causing difficulties in calculating the consumption of each component.

The basic evaporation model uses the theory of *d2-law*, which assumes that the droplet diameter reduces linearly. However, this model does not consider variations in droplet surface temperature (Yan and Aggarwal 2006). In order to consider heat and mass transfer within fuel droplets, two different categories are discussed: infinite and finite diffusivity models."

Infinite diffusivity models assume a spherical and well-mixed droplet with temperature changing over time. These models can give a reasonable result for slow and fast droplet evaporation, in which the internal temperature and concentration profiles are not affected significantly by internal heat conduction and diffusion. Ra (Ra 2009) examined the evaporation of gasoline and diesel fuel droplets under different temperatures and pressures by using an infinite diffusivity model. However, several investigations indicate that the droplet interior temperature has spatial and temporal development (Chiang 1992, Sirignano 1993, Dwyer 2000), causing the underestimation of droplet evaporation rate, temperature and lifetime. Therefore, the finite diffusivity model is introduced, which assumes that the mass transfer within droplet employs surface and core layers. The transformation of heat and mass is modeled as shown in Figure 2.21.

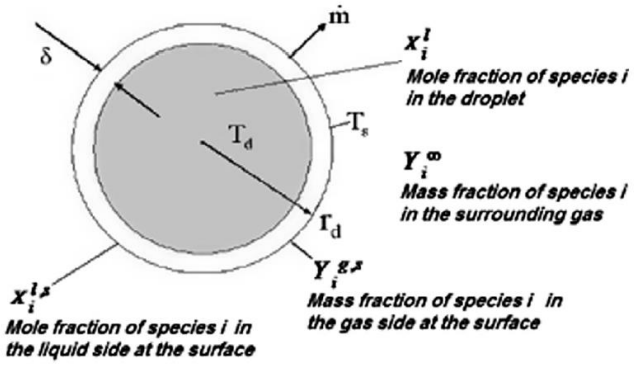

Figure 2.21 transformation of heat and mass of vaporation model (Samimi Abianeh 2014)

For computational efficiency, the evaporation model is established on Raoult's law which is based on the low-pressure simplification of the vapor-liquid phase equilibrium. In conditions such as the diesel engine, however, the effects of high pressure on drop evaporation must be considered. An alternative is to model real gas behaviors using various types of equations of state such as Redlich–Kwong (RK), Redlich–Kwong–Soave (RKS) and Peng–Robinson (PR). Hsieh (Hsieh 1991) solved the conservation equation using the RK equation of state to obtain the drop vaporization rate in high pressure conditions. Jia (Jia 1993) compared the RK and PR equations of state using a similar numerical approach to solve the evaporation of n-hexane in high-pressure nitrogen conditions and showed the advantage of the PR equation of state.

Spray-Wall Impingement

In the condition of high injection pressure, the spray-wall impingement is also a factor affecting the mixture's formation. The effects of spray-wall impingement could enhance the spray heating and evaporation because of the increase of liquid surface area on the cylinder wall. Another effect is the increase of burned hydrocarbon and soot emissions due to the insufficient mixture inside the combustion chamber.

The regime of the spray-wall impingement can be divided into stick, bounce, spread, boiling-induced breakup, breakup and splash, as in Figure 2.22.

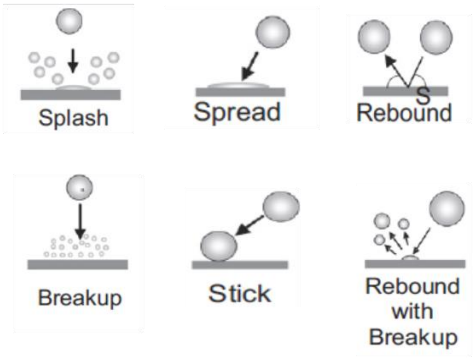

Figure 2.22 Schematic of regimes of spray-wall impingement (Bai 1995)

Figure 2.23 shows the criteria of these regimes by using the We number of droplets and wall temperature as proposed by Bai (Bai 1995), illustrating that more distinct regimes can be defined by different wall temperatures. For example, the boiling-induced breakup is observed between pure adhesion temperature (TPA) and Nukiyama temperature (TNU), and rebound is observed above Leidenfrost temperature (TLF). Ming (Jia 2008) reviewed a number of different sprayed wall-impingement models. Naber and Reitz (Naber 1988) proposed the first impingement model and considered the influence of wall conditions such as roughness in 1988. Wall-impingement can be divided into three modes: (1) stick mode, (2) reflect mode and (3) liquid jet mode. Reitz (Reitz 1995) used this wall impingement model to predict the combustion and emissions for a diesel engine. Watkins (Watkins 1990) proposed a spray/wall interaction model which assumed that the impinging of droplets on the wall can be classified into rebound or breakup by the incident energy. O'Rourke (O'Rourke 2000) developed a wall impinging model in KIVA3V which can include droplet rebound/spread/splash, film spreading and motion due to film inertia

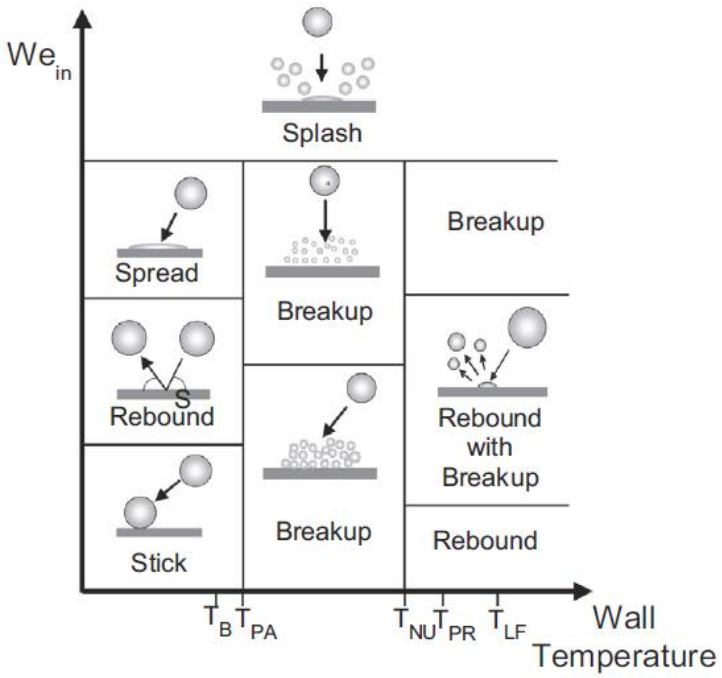

Figure 2.23 Criteria of regimes of spray-wall impingement (Bai 1995)

2.5 Developments of Bio-Fuel

Recently, bio-fuels have gradually become an important alternative fuel for gasoline and diesel; their use can significantly improve CO_2 emissions and engine efficiency. Bio-fuels can be obtained from vegetables and animals which can also reduce the production cost.

The most well-known biofuel, ethanol, is produced from sugar cane (Waldheim 2000) and widely used in engines today. In the study of ethanol's emission, it is shown that they are 40% lower than gasoline due to the lower flame temperature. The spray characteristics of ethanol and its blends have also been investigated by Changzhao and Guohong (Tian 2010, Jiang 2012). They pointed out that ethanol had a higher flame speed than gasoline and observed a larger droplet size distribution by using PDPA system.

Recently, the biomass-derived carbohydrate 2,5-dimethylfura (DMF) has been produced from glucose by a new catalytic strategy (Román-Leshkov 2007). The boiling point and energy density of DMF (36 and 37.8 MJ/L) are 20 degrees centigrade higher and 40% higher than ethanol (351 K and 24 MJ/L) respectively; Furthermore, its thermodynamic properties are close to gasoline, making it a more suitable replacement for gasoline than ethanol (Tian 2010). Hence, the spray characteristics such as the penetration length, cone angle, droplet velocity and size distribution of DMF and its blends need to be investigated in detail. Therefore, the spray characteristics of DMF and its blends under different operating conditions need to be studied by using optical methods in order to establish the guidelines (Tu 2014). Optical methods have been widely used to conduct a number of investigations on the spray characteristics of DMF and also its laminar flame characteristics; which were examined by using the Schlieren method (Wu 2011, Ma 2012). The results indicate that the laminar flame velocity of DMF is close to gasoline. Several research works have been conducted on testing DMF in engines and analyzing the effects of different cylinder pressures, injection pressures, and fuel composition (Daniel 2012, Daniel 2012, Jiang 2012, Wang 2012).

2.6 Summary

In this chapter, a literature review of GDI engine development and the types of GDI injectors has been introduced. Moreover, the detailed discussions of spray breakup mechanisms in the primary and secondary breakup regime are reviewed and the relevant CFD models during the spray development are also proposed by several investigations; which include the nozzle flow, primary breakup, secondary breakup and evaporation model. Finally, the recent developments and investigations of bio-fuels such as ethanol and DMF are discussed.

Chapter 3

Research Methodology

3.1 Introduction

In this study, the detailed investigations of spray characteristics are divided into two regions: primary breakup region and secondary breakup. Two different CFD software packages are used in this research; ANSYS-Fluent and KIVA3V release2.

In this section, the basic numerical equations such as the governing equations for mass and energy and momentum are introduced. Also, the sub-models such as cavitation models, turbulence models and spray breakup models are presented.

3.2 Ansys-Fluent

Two different CFD software package, ANSYS-Fluent and KIVA3V release2 are separately introduced. ANSYS- Fluent uses the Eulerian model to simulate nozzle flow and near field flow by solving two-phase flow, which also considers the different nozzle designs such as L/D ratio, counterbore size and r/D ratio. For KIVA3V release2, it uses the Lagrangian model to simulate the process of droplet primary breakup, secondary breakup, and droplet collision and evaporation.

3.2.1 Basic Conservation Equations

To solve the nozzle flow and near field flow, ANSYS-Fluent is set up to use Pressure-Implicit with the LES turbulence model and Splitting Operators (PISO) pressure-velocity coupling scheme which is based on the higher degree of the approximate relation between the corrections for pressure and velocity.

In the multi-phase model, The description of multiphase flow as interpenetrating continua incorporates the concept of phasic volume fractions, denoted here by α_q . Volume fractions represent the space occupied by each phase, and all phases are treated as continuous and solved separately for each phase.

The volume of phase q , V_q , is defined by

$$V_q = \int_V \alpha_q dV \qquad \text{(Equation 3.1)}$$

Where

$$\sum_{q=1}^{n} \alpha_q = 1 \qquad \text{(Equation 3.2)}$$

The governing equations for phase q is as below:

$$\frac{\partial \alpha_q \rho_q}{\partial t} + \nabla \cdot \left(\alpha_q \rho_q \vec{v}_q\right) = \sum_{p=1}^{n} \left(\dot{m}_{pq} - \dot{m}_{qp}\right) \qquad \text{(Equation 3.3)}$$

Where $\vec{v}_q$ is the velocity for phase q. $\dot{m}_{pq}$ is the mass transfer from p^{th} to q^{th} phase and $\dot{m}_{qp}$ is the mass transfer from q^{th} to p^{th} phase

$$\frac{\partial \alpha_q \rho_q \vec{v}_q}{\partial t} + \nabla \cdot \left(\alpha_q \rho_q \vec{v}_q \vec{v}_q\right) \quad \text{(Equation 3.4)}$$

$$= -\alpha_q \nabla P + \nabla \cdot \bar{\bar{\tau}}_q + \alpha_q \rho_q \vec{g}_q$$

$$+ \sum_{p=1}^{n} \left(\vec{R}_{pq} + \dot{m}_{pq} \vec{v}_{pq} - \dot{m}_{qp} \vec{v}_{qp}\right) + (\vec{F}_q + \vec{F}_{lift,q}$$

$$+ \vec{F}_{vm,q} + \vec{F}_{wl,q} + \vec{F}_{td,q})$$

In this equation 3.2, $\bar{\bar{\tau}}$ is the stress-strain of q^{th} phase

$$\bar{\bar{\tau}} = \alpha_q \mu_q \left(\nabla \bar{v}_q + \nabla \bar{v}_q^T\right) + \alpha_q (\lambda_q - \frac{2}{3}\mu_q) \nabla \cdot \bar{v}_q \bar{\bar{I}} \quad \text{(Equation 3.5)}$$

Here μ_q and λ_q are the shear and bulk viscosity of phase q, $\vec{F}_q$ is an external body force, $\vec{F}_{lift,q}$ is a lift force (described in Lift Force), $\vec{F}_{wl,q}$ is a wall lubrication force (described in Wall Lubrication Force), $\vec{F}_{vm,q}$ is a virtual mass force, and $\vec{F}_{td,q}$ is a turbulent dispersion force (in the case of turbulent flows only). $\vec{R}_{pq}$ is an interaction force between phases, and p is the pressure shared by all phases.$\vec{v}_{pq}$ is the interphase velocity.

3.2.2 Turbulent Model

The main theory for the LES model is to separate and calculate large eddy scales and small eddy scales individually. The establishment of governing equations for the LES model is done by filtering the time-dependent Navier-Stokes equation in the physical space. The standard for the equation to determine the eddy scale size is according to the mesh size. When the eddy scale size is larger than the mesh size, it will be resolved directly by Navier-Stokes equations.

However, for the small eddy scale size, they will be modeled by using a sub grid scale stress (SGS) model.

The sub grid scale stress turbulence model employs a Boussinesq hypothesis computing sub grid scale stress term τ_{ij} which can be expressed as

$$\tau_{ij} - \frac{1}{3}\tau_{kk}\delta_{ij} = -2\mu_t \bar{S}_{ij} \qquad \text{(Equation 3.4)}$$

Where μ_t is the subgrid-scale turbulent viscosity. The isotropic part of the subgrid-scale stresses τ_{kk} is not modeled in this equation, but it is calculated to filtered pressure term. The $\bar{S}_{ij}$ is the rate-of-strain tensor for the resolved scale which is defined by

$$\bar{S}_{ij} = \frac{1}{2}\left(\frac{\partial \bar{u}_i}{\partial x_j} + \frac{\partial \bar{u}_j}{\partial x_i}\right) \qquad \text{(Equation 3.5)}$$

The SGS model in this paper is a dynamic kinetic energy sub grid-scale model. The sub grid-scale turbulence can be modeled by accounting for the transport of sub grid-scale turbulence kinetic energy.

The definition of sub grid-scale kinetic energy can be expressed as below:

$$k_{sgs} = \frac{1}{2}\left(\overline{u_k^2} - \bar{u}_k^2\right) \qquad \text{(Equation 3.6)}$$

The sub grid-scale eddy viscosity, μ_t, is computed using k_{sgs} as:

$$\mu_t = C_k \rho k_{sgs}^{1/2} \Delta f \qquad \text{(Equation 3.7)}$$

LES models can consider the effect of smaller turbulent eddy from different nozzle designs such as r/D and L/D on liquid surface. When an RNS model is employed in this study, the effect of different nozzle designs become unobvious. In this thesis, the cavitation model is not considered due to the model limitation and the CFD model validation with experimental results.

3.2.3 Volume of Fluid Model

The principle of the Volume of Fluid (VOF) model is that two or more immiscible fluids can be modeled by solving a single set of momentum equations and tracking separately the volume fraction of the fluid in the domain. In each control volume, the volume fractions of all phases sum to unity. The fields for all variables and properties are shared by the phases and represent volume-averaged. The following three conditions are possible:

- $\alpha_q = 0$: The cell is empty of the q^{th} fluid
- $\alpha_q = 1$: The cell is empty of the q^{th} fluid
- $0 < \alpha_q < 1$: The cell contains the interface between the q^{th} fluid and one or more other fluids

The properties in the transport equation are calculated according to the presence of each component phase in each control volume.

The definitions of the mixture of thermo-physical properties are as below:

$$\rho = \alpha_f \rho_f + (1-\alpha_f)\rho_g \qquad \text{(Equation 3.8)}$$

In general, for an n-phase system, the volume-fraction-average density takes the following form:

$$\rho = \sum \alpha_q \rho_q \qquad \text{(Equation 3.9)}$$

3.3 KIVA3V Release 2

KIVA3V release 2 is a computational program which is written in FORTRAN. It allows the numerical modelling to a computer of the two-dimensional and three-dimensional transient field flow with spray in internal combustion engines. The first development of KIVA3V release 2 was done by Alamos National Laboratory on engine simulation. This software has been widely used by many industries and other academic units to simulate spray development, flow field in IC engines and combustion efficiency. This section presents the basic equations for mass momentum and energy and sub-models such as a breakup model and an evaporation model in KIVA3V.

3.3.1 Basic Conservation Equation

The basic equations for gas flow and liquid droplets include the conservation equation for mass, momentum and energy. The mass conservation equation for species m is presented:

$$\frac{\partial \rho_m}{\partial t} + \nabla \cdot (\rho_m \hat{u}) = \nabla \cdot \left[\rho D \nabla \left(\frac{\rho_m}{\rho}\right)\right] + \dot{\rho}_m^c + \dot{\rho}^s \delta_m \qquad \text{(Equation 3.10)}$$

Here ρ_m is the density for species m; ρ is the total mass density; $\hat{u}$ is the velocity vector of fluid; D is the turbulent diffusion coefficient; $\dot{\rho}_m^c$ and $\dot{\rho}^s$ represent separately the source term of chemical reaction and spray evaporation.

The momentum conservation equation is presented by:

$$\frac{\partial \rho \hat{u}}{\partial t} + \nabla \cdot (\rho \hat{u} \hat{u}) = -\nabla \mathrm{p} - \nabla \left(\frac{2}{3}\rho k\right) + \nabla \cdot \bar{\bar{\sigma}} + F^s + \rho \cdot \hat{g} \qquad \text{(Equation 3.11)}$$

The internal energy equation with chemical reaction and spray is

$$\frac{\partial \rho I}{\partial t} + \nabla \cdot (\rho \hat{u} I) = -p \nabla \cdot \hat{u} - \nabla \cdot J + \rho \varepsilon + \dot{Q}^c + \dot{Q}^s \qquad \text{(Equation 3.12)}$$

Where the specific internal energy is presented by $\boldsymbol{I}$; the heat flux vector is presented by $\hat{J}$ and ε is the turbulent dissipation rate; $\dot{Q}^c$ and $\dot{Q}^s$ are the source terms for chemical heat release and spray interaction source terms, respectively.

3.3.2 Turbulent Model

By solving the two transport equations for turbulent kinetic energy (k) and dissipation rate (ε), to calculate the effects of a small turbulent eddy, the standard $k-\varepsilon$ model is selected in the KIVA-3V

$$\frac{\partial \rho k}{\partial t} + \nabla \cdot (\rho \hat{u} k) = -\frac{2}{3}\rho k \nabla \cdot \hat{u} + \bar{\bar{\sigma}} : \nabla \hat{u} + \nabla \cdot \left[\left(\frac{\mu}{Pr_\varepsilon}\right) \nabla k\right] - \rho \varepsilon \qquad \text{(Equation 3.13)}$$

$$\frac{\partial \rho\varepsilon}{\partial t} + \nabla \cdot (\rho\hat{u}\varepsilon) = -\left(\frac{2}{3}c_{\varepsilon 1} - c_{\varepsilon 2}\right)\rho\varepsilon\nabla \cdot \hat{u} + \nabla \cdot \left[\left(\frac{\mu}{Pr_{\varepsilon}}\right)\nabla\varepsilon\right] + \frac{\varepsilon}{k}[c_{\varepsilon 1}\bar{\bar{\sigma}}: \nabla\hat{u} - c_{\varepsilon 2}\rho\varepsilon]$$

(Equation 3.14)

The parameters in Equation 3.23 and 3.24, such as $\mathrm{Pr}_{\varepsilon}$, Pr_{k}, $c_{\varepsilon 1}$, $c_{\varepsilon 2}$ and $c_{\varepsilon 3}$ are listed in Table 3.1.

In this study, the turbulence model utilized the RNG $k-\varepsilon$ model. The analytical derivation results in a model with constants different from those in the standard $k-\varepsilon$ model; and also an additional term and functions in the transport equations for ε , which improves the accuracy for rapidly strained flows. The ε equation of the RNG $k-\varepsilon$ model is given by:

$$\frac{\partial \rho\varepsilon}{\partial t} + \nabla \cdot (\rho\hat{u}\varepsilon) = -\left(\frac{2}{3}c_{\varepsilon 1} - c_{\varepsilon 2}\right)\rho\varepsilon\nabla \cdot \hat{u} + \nabla \cdot \left[\left(\frac{\mu}{Pr_{\varepsilon}}\right)\nabla\varepsilon\right] + \frac{\varepsilon}{k}[c_{\varepsilon 1}\bar{\bar{\sigma}}: \nabla\hat{u} - c_{\varepsilon 2}\rho\varepsilon] - \rho R$$

(Equation 3.15)

The definition of R is set as:

$$R = \frac{c_{\mu}\eta^{3}(1-\eta/\eta_{0})}{1+\beta_{t}\eta^{3}} \cdot \frac{\varepsilon^{2}}{k}$$ (Equation 3.16)

Here $\eta = S\kappa/\varepsilon, S = \left(2S_{ij}S_{ij}\right)^{1/2}$ is the magnitude of the mean strain $\bar{\bar{S}}_{ij} = \frac{1}{2}\left(\frac{\partial u_i}{\partial x_j} + \frac{\partial u_j}{\partial x_i}\right)$.

Table 3.1 Comparison of turbulence model constants between the two κ-ε models

	c_μ	$c_{\varepsilon 1}$	$c_{\varepsilon 2}$	$c_{\varepsilon 3}$	$1/\mathrm{Pr}_\kappa$	$1/\mathrm{Pr}_\varepsilon$	η_0	β_t
RNG κ-ε model	0.0845	1.42	1.68	Eq.3.12	1.39	1.39	4.38	0.012
Std. κ-ε model	0.09	1.44	1.92	-1.0	1.0	0.769		

By comparing the difference between the standard and RNG $k-\varepsilon$ model, it can be found that there is an additional term R in its ε equation in the RNG $k-\varepsilon$ model. The comparison of these two models has been investigated by Papageorgakis and Assanis (Papageorgakis and Assanis 1998) and shows the RNG $k-\varepsilon$ model presents more accurate and reliable results than the standard $k-\varepsilon$ model.

3.3.3 Fuel Spray Model-Cavitation Sub-Model

A phenomenological nozzle flow model in KIVA3V provides initial nozzle conditions at the nozzle exit, such as droplet initial size and velocity distribution for the following breakup models. This model considers the different nozzle geometrical parameters such as L/D, r/D ratio and hole diameter. Figure 3.1 shows the schematic diagram of the nozzle flow and the distribution of cavitation. The nozzle exit velocity, U_{eff}, and the initial droplet diameter, D_{eff}, are calculated as below:

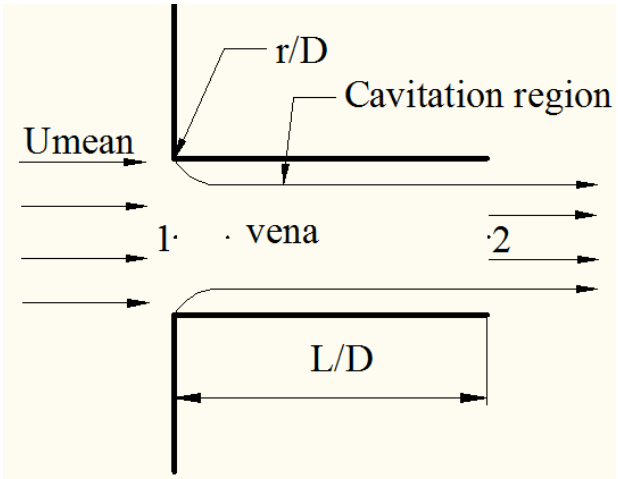

Figure 3.1 Schematic diagram of nozzle flow phenomena (Nurick 1976)

$$U_{eff} = U_{vena} - \frac{p_2 - p_{vapor}}{\rho_l \cdot U_{mean}}, \qquad D_{eff} = D\sqrt{\frac{U_{mean}}{U_{eff}}} \qquad \text{(Equation 3.17)}$$

In Equation 3.27, U_{vena} is the velocity in vena-contracta and is calculated by:

$$U_{vena} = \frac{U_{mean}}{C_c} \qquad \text{(Equation 3.18)}$$

Where C_c is the contraction coefficient which is dependent on the r/D ratio of the nozzle inlet.

The definition of C_c is described as below:

$$C_c = \left[\left(\frac{1}{C_{C0}}\right)^2 - 11.4 \cdot r/D\right]^{-0.5} \qquad \text{(Equation 3.19)}$$

Where Nurick (Nurick 1976) gives the value for C_{co} =0.62 for the sharp-edged orifices.

The pressure in the vena-contracta is determined by

$$p_{vena} = p_1 - \frac{\rho_l}{2} U_{vena}^{\ 2} \qquad \text{(Equation 3.20)}$$

3.3.4 Spray Breakup Models

Fuel Spray Model-Max Planck Institute (MPI) Primary Breakup Model

The assumption of the distribution of primary droplet size in the MPI model is that droplets are stripped off from the liquid core which is composed of several segments with the droplet diameter D_{seg}, as shown in Figure 3.2.

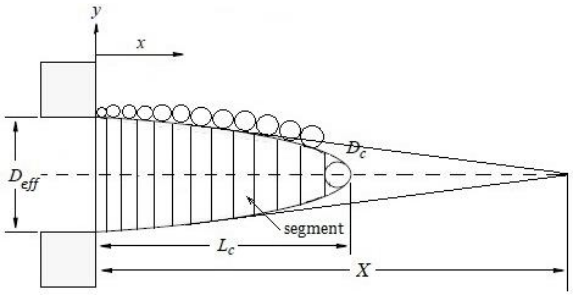

Figure 3.2 Schematic diagram of MPI primary breakup model

$$D_{seg} = D_{eff} - \left(D_{eff} - D_c\right) L_c \qquad \text{(Equation 3.21)}$$

Where L_c is the length of liquid core and D_c is the droplet diameter in the tip of the liquid core.

The definition of X in Figure 3.2 is given by

$$X = \frac{D_{eff}}{D_{eff} - D_c} L_c \qquad \text{(Equation 3.22)}$$

The relative axial velocity between the liquid core and the gas phase is presented by u_{rel} and its gradient normal to the injection direction is approximated by:

$$u_{rel} = \frac{U_{eff}}{2}\left(1 - \frac{3}{4}\frac{x}{X}\right) \qquad \text{(Equation 3.23)}$$

The assumption of radial velocity gradient is determined by :

$$\frac{du}{dy} = \frac{2u_{rel}}{1.2D_{eff} - D_{seg}} \qquad \text{(Equation 3.24)}$$

By combining Equation 3.33 and 3.34, the primary droplet diameter is calculated by presumed equilibrium of the lift force and the surface tension of the liquid. It is presented by the following relation:

$$d_p = \sqrt{52.34\frac{\sigma}{\rho_g u_{rel}\frac{du}{dy}}} \qquad \text{(Equation 3.25)}$$

Kelvin-Helmholtz-Aerodynamics-Cavitation-Turbulence Breakup Model

The KH-ACT model assumes that the mechanism of liquid breakup in the primary breakup regime is composed of the aerodynamic force, cavitation and turbulence which is shown in Figure 3.3.

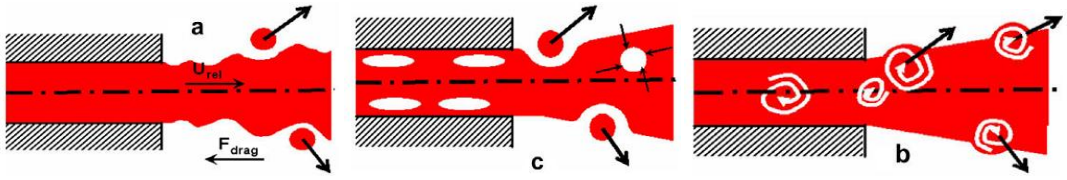

Figure 3.3 Schematic illustration of primary breakup mechanisms (a) aerodynamic force (b) cavitation induced and (c) turbulence induced (Som 2010)

To consider the effects of turbulence and cavitation on liquid atomisation, the Kelvin-Helmholtz-Aerodynamics-Cavitation-Turbulence (KH-ACT) model was proposed by Som et al (Som 2010). In the primary breakup regime, the KH-ACT model calculates respectively the instantaneous length of aerodynamic breakup; the length scale of the vapour bubble from cavitation and the relevant length of turbulence and the breakup time scale of the aerodynamically induced breakup; the time for bubble collapse and burst of cavitation and the relevant time scale of turbulence. The calculation of length and time scale for each breakup mechanism is expressed as below:

Aerodynamically induced breakup

$$L_{KH} = r - r_{KH} \quad \text{(Equation 3.26)}$$

$$\tau_{KH}(\textit{Breakup time}) = \frac{3.276 B_1 r}{\Omega_{KH}\Lambda_{KH}} \quad \text{(Equation 3.27)}$$

where r is the radius of parent droplet; r_{KH} is the radius of the newly formed droplet; B_1 is the constant parameter of the KH model; Λ_{KH} is the wavelength and Ω_{KH} is the maximum growth rate.

Cavitation induced breakup

$$L_{CAV} = R_{CAV} = r_{hole}\sqrt{(1 - C_a} \quad \text{(Equation 3.28)}$$

$$\tau_{CAV} = \min(\tau_{Collapse} : \tau_{Burst}) \quad \text{(Equation 3.29)}$$

where C_a is the coefficient of area reduction; $\tau_{Collapse}$ is the bubble collapse time and τ_{Burst} is the average time for the bubble to reach the surface of the liquid jet.

Turbulence induced breakup

$$L_T = C_\mu \left(K(t)^{1.5} / \varepsilon(t) \right) \quad \text{(Equation 3.30)}$$

$$\tau_T = C_\mu \left(K(t) / \varepsilon(t) \right) \quad \text{(Equation 3.31)}$$

where C_μ is the turbulence model constant and $K(t)$ and $\varepsilon(t)$ are the instantaneous turbulent kinetic energy and dissipation rate which are expressed as below:

$$K(t) = \left[\frac{(K_0)^{C_\varepsilon}}{K_0(1 + C_\mu - C_\mu C_\varepsilon) + \varepsilon_0 t(C_\varepsilon - 1)} \right]^{1/(1-C_\varepsilon)} \quad \text{(Equation 3.32)}$$

$$\varepsilon(t) = \varepsilon_0 \left(\frac{K(t)}{K_0} \right)^{C_\varepsilon} \quad \text{(Equation 3.33)}$$

where C_ε is the turbulence model constant and K_0 and ε_0 are the initial turbulent kinetic energy and dissipation rate at the nozzle's exit.

The KH-ACT model assumes the strongest effects of the three different breakup mechanisms which dominate the droplet breakup. Thus, the largest ratio of length and time scale for each breakup mechanism is used to determine the dominant mechanism during the droplet breakup process, which is as shown below:

$$\frac{L_A}{\tau_A} = \max\left(\frac{L_{KH}(t)}{\tau_{KH}(t)}; \frac{L_{CAV}}{\tau_{CAV}}; \frac{L_T(t)}{\tau_T(t)}\right) \quad \text{(Equation 3.34)}$$

If the aerodynamically induced breakup shows the dominant role in the primary breakup process, the calculation of droplet breakup in the primary breakup regime uses the KH breakup model. If the cavitation or turbulent effects become the dominant role in the primary breakup regime, its change rate of parent droplet radius will be presented by :

$$\frac{dr}{dt} = -C_{T,CAV}\frac{L_A}{\tau_A} \quad \text{(Equation 3.35)}$$

where $C_{T,CAV}$ is the constant parameter for the KH-ACT model.

Kelvin-Helmholtz (KH) Secondary Breakup Model

The assumption of the KH model is a cylindrical liquid jet with radius (a) which penetrate into a incompressible surrounding gas. The velocity difference between the liquid surface and the surrounding gas results in the growth of instability waves developing on the liquid surface (Figure3.4)

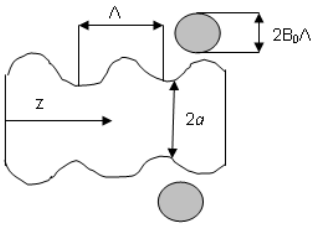

Figure 3.4 Schematic growth of surface perturbation in the KH model

The change rate of the parent droplet is calculated by wave growth rate Λ_{KH} and the wave length Ω_{KH}, as given below:

$$\Omega\left(\frac{\rho_l a^3}{\sigma}\right)^{0.5} = \frac{0.34 + 0.38We_g^{1.5}}{(1+Oh)(1+1.4Ta^{0.6})}, \quad \text{(Equation 3.36)}$$

$$\frac{\Lambda}{a} = 9.02\frac{(1+0.45Oh^{0.5})(1+0.4Ta^{0.7})}{(1+0.87We_g^{1.67})^{0.6}} \quad \text{(Equation 3.37)}$$

Where a presents the radius of the parent droplet or blob and We_g and We_l are the Weber number of the surrounding gas and liquid, $We_g=\rho_g U^2 a/\sigma$ and $We_l=\rho_l U^2 a/\sigma$. Oh is the Ohnesorge number, $Oh = We_l^{0.5}/Re_l$, where $Re_l=\rho_l U a/\mu_l$. Ta is the Taylor number, $Ta = OhWe_g^{0.5}$.

The child droplets are assumed to be produced from parent droplets. The radius of the child droplets is given as below:

When $B_0\Lambda \le a$

$$r = B_0\Lambda \quad \text{(Equation 3.38)}$$

When $B_0\Lambda > a$

$$r = \min\left[(3\pi a^2 U/2\Omega)^{1/3}, (3a^2\Lambda/4)^{1/3}\right] \quad \text{(Equation 3.39)}$$

Here, B_0 is the breakup size constant. The change rate of the parent droplet radius is as according to Equation 3.40,

$$\frac{d\mathrm{a}}{dt} = -\frac{a-r}{\tau} \ , \ r \le a \qquad \text{(Equation 3.40)}$$

Where τ is the breakup time which is given as below

$$\tau = 3.788 B_1 \frac{a}{\Lambda\Omega} \qquad \text{(Equation 3.41)}$$

Where B_1 is the breakup time constant related to the injector configuration.

Cascade Atomization Breakup (CAB) Secondary Breakup Model

The theory of the CAB model is based on an analogy between droplet oscillation and deformation, which is similar to the Taylor Analogy Breakup (TAB) model. However, the CAB model provides a new strategy to describe the droplet process. The droplet breakup is modelled by an exponential law which is based on the relation between mean child droplet size and the breakup time of the parent droplet.

The expression of mass conservation between parent and child droplet is given as below:

$$\frac{d}{dt}\bar{m}(t) = -3K_{bu}\bar{m}(t) \qquad \text{(Equation 3.42)}$$

Where $\bar{m}(t)$ is the average mass of the child droplet and K_{bu} is the breakup constant which is depends on the regimes of the droplet breakup. The drop breakup regimes K_{bu} are divided respectively to three regimes, bag, stripping and the catastrophic breakup regime. The definitions of K_{bu} are expressed as below:

$$K_{bu} = \begin{cases} k_1\omega & if \quad 6 < We \le 80 \\ k_2\omega\sqrt{We} & if \ 80 < We \le 350 \\ k_3\omega We^{0.75} & if \quad 350 < We \end{cases} \qquad \text{(Equation 3.43)}$$

The value of k_1 needs to be determined by experimental data. The calculation of the constants k_2 and k_3 is dependt on the continuity of K_{bu} at the transition of various breakup regimes.

Moreover, due to the assumption of the equal droplet size distribution of the child droplet, Equation 3.42 changes to

$$\frac{r}{a} = e^{-K_{bu}t_{bu}} \qquad \text{(Equation 3.44)}$$

Where a presents the radii of parent droplets; r are the radii of child droplets; and t_{bu} is the breakup time.

The calculation of the radial velocity component of the child droplet is based on the energy conservation between parent and child droplets.

Other Sub-Models

For the spray model, two important parameters, liquid core length and spray cone angle, need to be calculated to provide the classification of breakup regime and initial spray condition. The liquid core length is the key parameter to distinguish the region of the primary and secondary breakup model. According to the Hiroyasu/Arai model (Hiroyasu and Arai 1990), the liquid core length is related to the ambient gas pressure. The calculation of steady liquid core length is defined as below:

$$L_{c,steady} = HD_{eff}\left(1+0.4\frac{r_n}{D_n}\right)\left(\frac{p_g}{\rho_l U_{eff}^2}\right)^{0.05}\left(\frac{l_n}{D_n}\right)^{0.13}\sqrt{\frac{\rho_l}{\rho_g}} \qquad \text{(Equation 3.45)}$$

In Equation 3.45, r_n is the radius of the nozzle entrance, D_n is the hole diameter of the nozzle; l_n is the length of the nozzle and H is the equation coefficient which is defined by:

$$H = H_0 + H_{\ln}\ln\left(\frac{p_g}{1atm}\right) \qquad \text{(Equation 3.46)}$$

Where H_0 and H_{ln} are constants. The linear growth rate for the liquid core length is also defined by Hiroyasu. It is given as below

$$\frac{dL_c}{dt} = L_{c,grow}U_{eff} \qquad \text{(Equation 3.47)}$$

Where $L_{c,grow}$ is the liquid core length growth constant.

For the calculation of the spray cone angle, the model from Naber-Siebers (Naber and Siebers 1996) considers the effects of ambient pressure, which is presented as below:

$$\theta = 2\tan^{-1}\left[C_\theta\left(\frac{\rho_g}{\rho_l}\right)^{0.19}\right] \quad \text{(Equation 3.48)}$$

Here, C_θ is the constant.

3.4 Drop Evaporation Model

The process of droplet evaporation involves the transfer of heat, mass and momentum between the gas and the liquid phase. The change rate of droplet radius due to droplet evaporation is defined by the Frossling correlation (Lefebvre 1988) and shown in the following:

$$\frac{dr}{dt} = -\frac{\rho D}{2\rho_1 r}\frac{Y_1^* - Y_1}{1 - Y_1^*}Sh \quad \text{(Equation 3.49)}$$

Where D is the mass diffusivity of liquid vapour, Y_1 and Y_1^* respectively present the vapour diffusivity of liquid in the air, where $Y_1 = \rho_1 / \rho$; and the mass fraction of liquid at the droplet surface. The definition of Y_1^* is obtain from

$$Y_1^*(T_d) = \frac{W_1}{W_1 + W_0\left(\frac{p}{p_v(T_d)} - 1\right)} \quad \text{(Equation 3.50)}$$

Where W_1 is the molecular weight of liquid (fuel) and W_0 is the average of the molecular weight of all species except liquid vapour. The assumption of Equation 3.50 is defined as the partial pressure of liquid vapour at the droplet surface was the same as the equilibrium vapour pressure.

The definition of the Sherwood number (*Sh*) is given by

$$Sh = (2.0 + 0.6\,\mathrm{Re}_d^{1/2}\,Sc^{1/3})\frac{\ln(1+\frac{Y_1^* - Y_1}{1-Y_1^*})}{\frac{Y_1^* - Y_1}{1-Y_1^*}} \qquad \text{(Equation 3.51)}$$

Where *Sc* is the Schmidt number and given by $Sc = \mu_{air} \big/ \rho D$, here, μ_{air} is presented as the dynamic viscosity of air.

In energy conservation, the latent heat of evaporation and the heat conduction of the droplet are considered. The changing rate of droplet temperature was given by:

$$\rho_l \frac{4}{3}\pi r^3 c_l \dot{T}_d - \rho_l 4\pi r^2 \frac{dr}{dt} L(T_d) = 4\pi r^2 Q_d \qquad \text{(Equation 3.52)}$$

Where the latent heat of vapourization is given as $L(T_d)$, c_l presents the liquid specific heat. The heat conduction rate Q_d is defined by the Ranz-Marshall correlation.

$$Q_d = \frac{\psi(T - T_d)}{2r} Nu \qquad \text{(Equation 3.53)}$$

Where the Nusselt number (*Nu*) and Prandtl number (*Pr*) respectively, are presented as below:

$$Nu = (2.0 + 0.6\,\mathrm{Re}_d^{1/2}\,\mathrm{Pr}^{1/3})\frac{\ln(1+\frac{Y_1^* - Y_1}{1-Y_1^*})}{\frac{Y_1^* - Y_1}{1-Y_1^*}} \qquad \text{(Equation 3.54)}$$

$$\Pr = \frac{\mu_{air}}{\rho \psi} \qquad \text{(Equation 3.55)}$$

3.5 Summary

In this study, numerical and experimental methods are used to examine the spray characteristics in the primary and secondary breakup regimes. In this chapter, the basic numerical models in this study are introduced. The VOF-LES model in ANSYS-Fluent is used to simulate the GDI nozzle flow field and jet breakup in the nozzle near field. The KIVA-3V is used for the simulation of the droplet development process in the primary and secondary breakup regime such as droplet breakup and evaporation. Finally, this chapter also provides a fundamental knowledge for the present spray models.

Chapter 4

Experiment Setup and model Validation

4.1 Introduction

CFD models provide an efficient and low cost method to examine a number of physical problems which cannot be observed by experiments. However, these models need to be examined and validated with experimental results, in order to firstly examine the reliability and accuracy of the CFD models.

This chapter introduces the verification of cell size of nozzle flow and validations of the mass flow rate with the experimental data under different injection pressures using a real size GDI injector.

4.2 Experiment Setup and Data Analysis

The common method to measure spray characteristics uses optical techniques. Several optical techniques such as Particle Image Velocity (PIV), use of a high speed camera and the Phase Doppler Particle Analyzer (PDPA) system can directly measure spray patterns such as spray angle, penetration length, the distributions of droplet size and velocity. Therefore, these two techniques were used to validate the spray models in the following chapters.

The testing injector uses a Bosch 6-hole gasoline direct injection injector which is shown in Figure 4.1. The hole position of each is not symmetric due to the optimization for the combustion chamber. The fuel injection system is composed of GDI injector and fuel accumulator and is driven by a nitrogen bottle. The fuel injection amount, timing and frequency of this injection system are controlled by an Electronic Control Unit (ECU).

Figure 4.1 6-hole gasoline direct injection injector

PDPA System

A Dantec PDPA system consisting of a high power CW laser, transmitting optics, photon detector, signal processer and traverse system is used for the spray measurements. The main laser beam, after travelling through the transmitting optics, is divided into a pair of beam with different polarity and they are intersected at the measuring location forming a measuring volume. When droplets pass through the measuring volume, the droplets disperse the laser and produce signals. Then, the photon detector senses these signals which are processed to translate into parameters for each droplet such as droplet size and velocity. The measuring location is changed by moving the PDPA system via a 2D transverse system.

The schematic of the PDPA system is presented in Figure 4.2. The fuel is pressurized in an accumulator tank by a nitrogen bottle equipped with a pressure regulator. The pressurized fuel is fed to the GDI which injects the fuel into a vessel, shown in Figure 4.2. By adjusting the pressure regulator on the nitrogen bottle, the injection pressure could be varied from 1 bar to 200 bar. Also, to study the effects of the ambient pressure on spray characteristics, the pressure vessel is connected to another nitrogen bottle. In order to control the injection duration time, the GDI injector is connected to an injector trigger which drives the injector and controls its duration. The injection duration is kept constant at 1.0 ms. Each signal from the trigger drives the injector to inject four times.

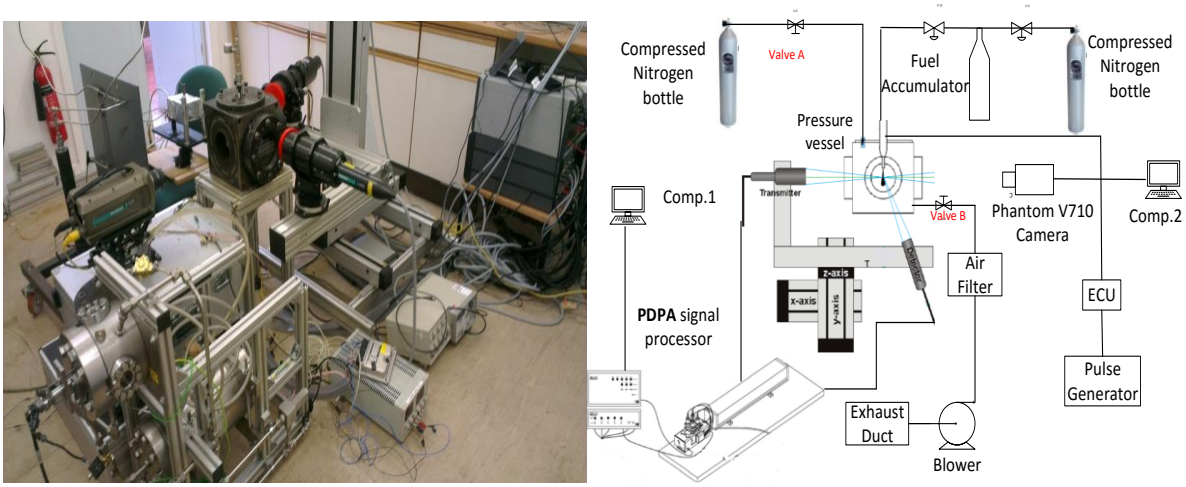

Figure 4.2 Schematic of the PDPA system

The pressure vessel into which injections are made and is purged with nitrogen after each test by using two valves A and B. Valve A supplies fresh nitrogen and valve B provides the passage to the exhaust duct, Figure 4.2. The exhausted gas is filtered and collected by a blower to keep the test room and environment clean. To investigate the effects of ambient pressure on the spray characteristics, valve A is opened and nitrogen from the nitrogen bottle through a pressure regulator is allowed into the vessel while valve B is kept closed.

High-Speed Camera

A high-speed camera, a Phantom V710 in Figure 4.3, is used for the macroscopic study of the spray. The images are taken and recorded at a rate of 18003 kHz and a resolution of 608x800 pixels. A 500W xenon lamp coupled with a lens group and a pin hole generated the point light source for the imaging experiments.

Figure 4.3 High speed camera, Phantom V710

4.3 Data Processing

The selected points for the PDPA measurements are presented in Figure 4.4. Due to the asymmetric development for 6 sprays, PDPA measurements are made for only one of the sprays which has the least interaction with the other sprays, indicated in Figure 4.4(a) by a white line. From this spray, droplet size and velocity are measured at different distances from the nozzle for 55 points, as shown in Figure 4.4(b). The number of points increases with the distance from the nozzle (18.2, 27.3, 36.4, 45.5 and 54.6 mm) due to the spray pattern, as shown in Table 4.1. By using the information from these measuring points, droplet size distributions at different operating conditions can be compared and studied.

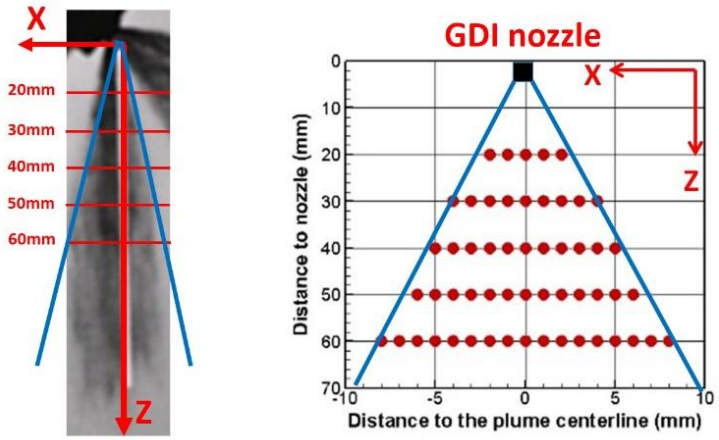

(a) (b)

Figure 4.4 (a) The selected spray for measurements, (b) The location of 55 measuring points

Table 4.1 Location of measuring points

Distance to the nozzle (mm)	Distance to the plume centerline (mm)
20	-2,-1,0,1,2
30	-4,-3,-2,-1,0,1,2,3,4,
40	-5,-4,-3,-2,-1,0,1,2,3,4,5
50	-6,-5,-4,-3,-2,-1,0,1,2,3,4,5,6
60	-8,-7,-6,-5,-4,-3,-2,-1,0,1,2,3,4,5,6,7,8

For this analysis, the measurement volume size of PDPA system is as follows:

dX=0.04767 mm (Green beam)

dY=0.04734 mm (Blue beam)

dZ=0.3989 mm (Length of measurement volume)

To ensure the statistical accuracy of the data, each measuring point includes 20,000 validated data points. The validation rate is approximately 65%–75% at different measurement positions, and points for which the data rate is low are dismissed. The measuring range of droplet size is from 0 to 40.66 micrometer. Due to the nature of PDPA measurement, the experimental error

is determined by the error span of the phase plot between the first detector and subsequent detectors. Droplets outside the span are rejected. Thus, the measurement error for the PDA measurement is quantified by the phase error, which is ±15% for this experiment.

The macroscopic information such as penetration and spray angle for the spray pattern can be obtained from the high speed images. Due to the three dimensional nature of the spray structure and its relative angle to the high-speed camera, the spray length in the images is not the real spray length. To calculate the real length of the spray, some correcting calculations are done. The calculations of penetration and spray cone angle development with time are done by using the consecutive images from the high speed camera. Figure 4.5. (a) shows the image of sprays taken from the bottom relative to the injector and the sketch on the right-hand side, Figure 4.5. (b), shows the view angle correction required for calculating the real length. The real spray length and edge development calculations are done by using a MATLAB code, in Figure 4.6. The MATLAB code uses the luminance level of the spray images and development (Figure 4.6. (a)) for the binarisation of the high-speed images and calculates the spray length including the view angle correction, as in Figure 4.6.b. Tangent lines enveloping the spray images are used to measure the spray angles.

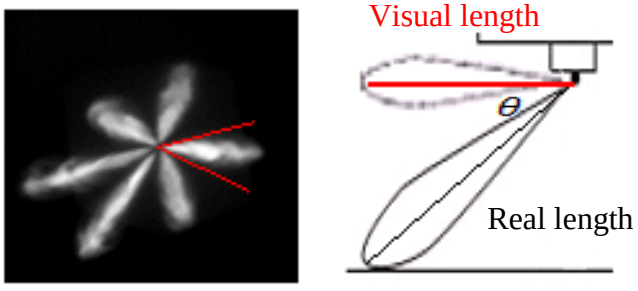

(a) (b)

Figure 4.5 (a) Spray image taken from the bottom relative to the injector, (b) View angle correction for calculation of spray length

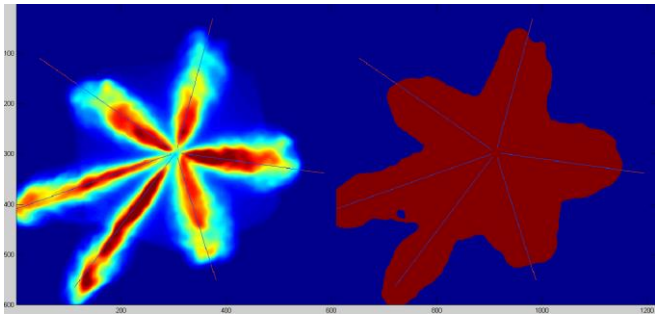

(a) (b)

Figure 4.6 (a) The luminance levels in a spray image analysis, (b) The binarisation of the same spray image

To validate the accuracy of penetration length measurements using the MATLAB code, several thresholds were examined on spray images. Figure 4.7 shows the sensitivity analysis of the threshold on the measurement of spray penetration length. Thresholds ranging from 10% to 50% are employed to examine the spray penetration length of iso-octane under 150 bar injection pressure and 1 bar back pressure at a room temperature of 20o C. From the comparison, it can be observed that the lower value of spray penetration length is measured by using the higher threshold. However, the influence of threshold on spray penetration length is not significant. For example, there is only a 4%–5% difference in spray penetration length at the end of injection for thresholds between 10% and 50%. The difference between 15% and 20% threshold is only 1% at the end of injection. The spray penetration length in this study is set to a 20% threshold, at which the boundary of the spray in other directions is clearly indicated.

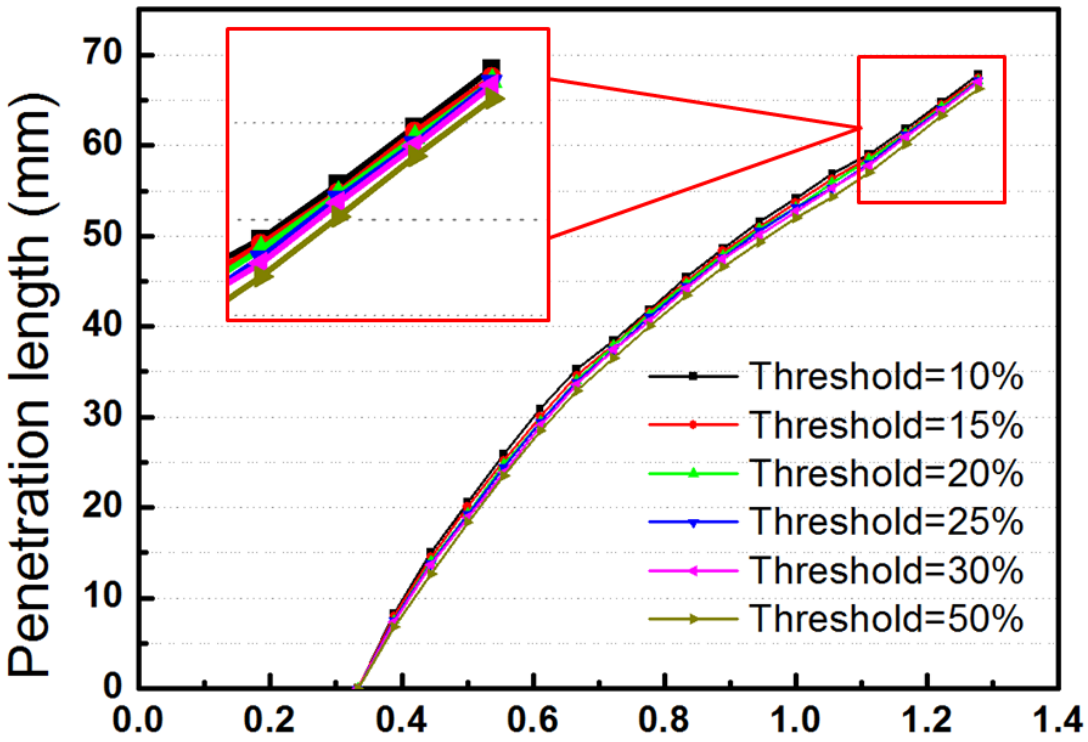

Figure 4.7 Effect of different thresholds on the penetration length measurement

4.4 Measurement of Mass Flow Rate and Fuel Properties

4.4.1 Experimental Setup

Due to the limitations of measuring techniques, the details of nozzle flow and near-field are difficult to obtain. Therefore, the measurement of mass flow rate for the testing injector is used as the basic reference for the validation of CFD models. Figure 4.8 shows the experimental setup for the mass flow rate test. The testing Bosch six-hole injector is connected to a fuel accumulator and an ECU is used to control injection time and duration. During injection, the injector is installed into a transparent container in order to collect all the injection fuel. From the scale monitor, the total amount of injection fuel can be observed.

.

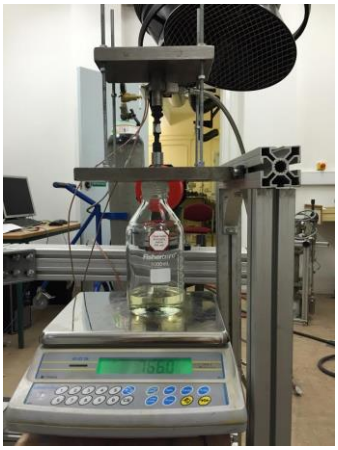

Figure 4.8 Experimental setup of mass flow rate

4.4.2 Test Conditions and Fuel Properties

The mass flow rate is examined by using different injection durations (1, 2 and 3 ms) at 150 bar injection pressure and 1 bar ambient pressure in order to examine the consistency and stability of mass flow rate and avoid the effect of needle movement. The injection time is set to 500 for each injection duration. Test conditions can be found in Table 4.2.

Table 4.2 Testing conditions for numerical and experimental method

	Test Conditions
Test Fuel	**Iso-octane, DMF, Ethanol**
Injection Pressure	**150 bar**
Ambient Pressure	**1bar**
Injection Duration	**1, 2, 3 ms**
Fuel Temperature	**293K**
Ambient Temperature	**293K**
Injection Time	**500**

In order to examine the effect of different fuel properties, three different testing fuels, iso-octane, DMF and ethanol, are used in this measurement. The fuel properties of these test fuel are shown in Table 4.3.

Table 4.3 Fuel properties of bio-fuels

	Iso-octane	DMF	Ethanol
Molecular Formula	C_8H_{18}	C_6H_8O	C_2H_6O
H/C Ratio	**2.25**	**1.333**	**3.0**
O/C Ratio	**0**	**0.167**	**0.5**
Density @293K (kg/m^{-3})	**702.6**	**889.7**	**789**
Molar Mass (g/mol)	**114.2**	**96.13**	**46.07**
Vapour Pressure@293K (pa)	**5500**	**4728**	**6539**
Viscosity@293K(k Pa s)	**$5.028x10^{-7}$**	**$6.503x10^{-7}$**	**$1.149x10^{-6}$**
SurfaceTension@293K (N/m)	**0.01816**	**0.02603**	**0.02406**

Figure 4.9 shows the average mass flow rate divided by total injection time for different test fuels at different injection durations. The average mass flow rate for each injection durations has shown the similar value. This ensures the average mass flow rate from experimental test has less influence from the needle movement and can be used to validate the nozzle flow model.

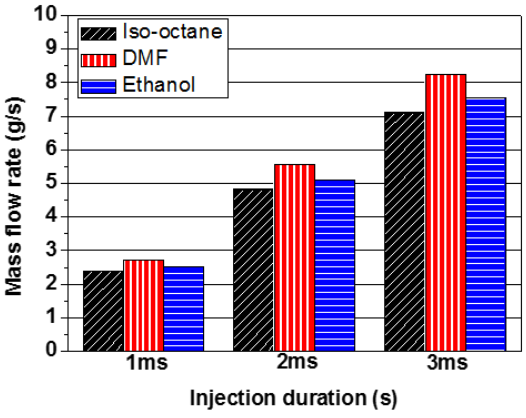

	Iso-octane	DMF	Ethanol
1 ms	2.53 g/s	2.72 g/s	2.41 g/s
2 ms	2.55 g/s	2.77 g/s	2.41 g/s
3 ms	2.51 g/s	2.74 g/s	2.37 g/s

Figure 4.9 Experimental setup of mass flow rate for different fuels

A second bench test examines the variation of mass flow rate of iso-octane at different injection pressure (50,100 and 150 bar) using the same experimental method and setup described above. The average mass flow rate at different injection pressure is shown in Figure 4.10.

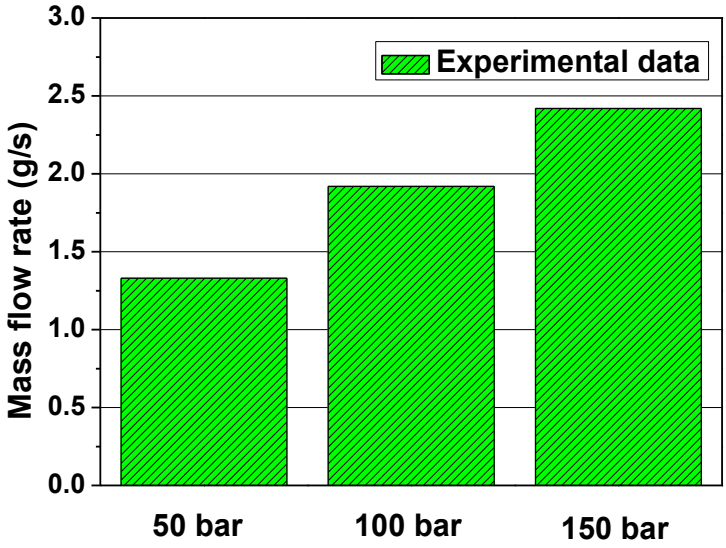

Figure 4.10 Experimental setup of mass flow rate for different injection pressure

4.5 Computational Domain and Grid Validation

The testing nozzle is a six-hole Bosch GDI injector. Figure 4.11 shows the cutting plane for the real Bosch GDI injector and the CFD nozzle domain which is established by measuring the geometrical scale.

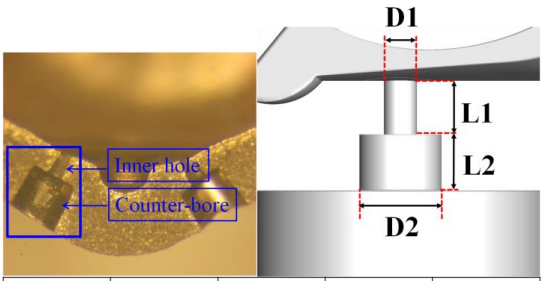

Inner hole diameter	Counter-bore diameter	L1/D1	(L1+L2)/D1	D2/D1
D1	D2	1.66	3.389	2.5

Figure 4.11 Distributions of nozzle geometry and parameters

In order to examine the mesh size sensitivity on the nozzle mass flow rate, the nozzle geometry is established as Figure 4.12. In this examination, the consideration of ambient is ignored in order to reduce the amount of total mesh. The movement trajectory of the injector needle is not considered due to the limitations of high computational expense and the high mesh quality required for the moving mesh. The needle motion will change the aspect ratio of the grid which could cause numerical divergence during calculation.

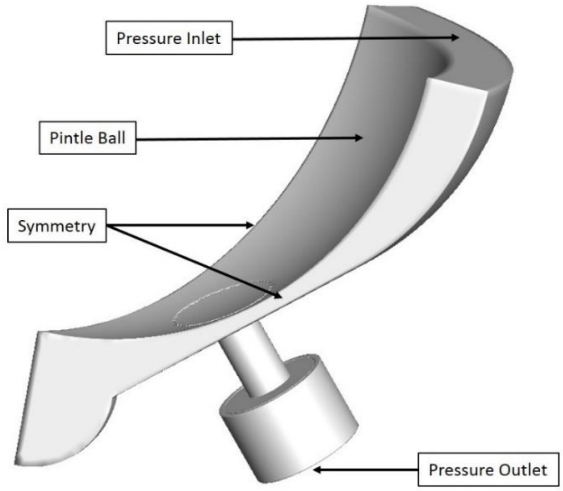

Figure 4.12 Nozzle geometry of mesh sensitivity

In order to provide the basic test condition of mesh sensitivity, Table 4.4 presents the range of length scale (eddy scale) under different injection pressures which can provide a guide to establishing the mesh resolution in order to capture the turbulent effects and small eddies. From Table 4.4, the smallest eddy scale can be estimated as η which is called the Kolmogorov length while the largest eddy scale is estimated as L. Another turbulent length scale is the Taylor length, λ, which offers a calculation for the fluctuating strain rate field.

Table 4.4 Nozzle flow turbulence length scales and time scale

Injection pressure	150bar	100bar	50bar
$\eta_{Kolmogorov}[m]=\left(\frac{v^3}{\varepsilon}\right)^{\frac{1}{4}}$	**1.42E-07**	**1.66E-07**	**2.16E-07**
$\lambda_{Taylor}[m]=\left(\frac{15vu^2}{\varepsilon}\right)^{\frac{1}{2}}$	**1.46E-05**	**1.68E-05**	**2.02E-05**
$L_{\mathrm{int}egral}[m]=\eta\,\mathrm{Re}^{\frac{3}{4}}$	**0.000353**	**0.000363**	**0.000365**
$t_\eta[s]=\left(\frac{v}{\varepsilon}\right)^{\frac{1}{2}}$	**2.51E-08**	**3.46E-08**	**5.86E-08**

According to Table 4.4, in the test of mesh sensitivity, the mesh size in the research zone (internal area, counter-bore area) is examined by 2.5, 4.5 and 9 μm. For the remaining computational domain, the mesh size is up to 10 μm. Moreover, the time scale for the smallest eddy is estimated as t_η which means the duration of the eddy structure. According to t_η from Table 4.4, the time step size of the CFD model is set as $1e^{-8}$. The test conditions of mesh sensitivity is shown in Table 4.5.

Table 4.5 Test conditions of mesh sensitivity

Injection Pressure	150 bar
Injection Duration	1ms
Ambient Pressure	1 Bar
Fuel	Iso-octane
Fuel Temperature	293 K
Ambient Temperature	293 K
Mesh size in research Zone	2.5, 4.5 ,9 μm

The two main parts of a stepped hole GDI injector are the inner hole and the counter-bore. Figure 4.13 shows the locations of measuring planes in the computational domain used to compare the change of mass flow rate at different measure planes in the CFD model:

- Inlet: initial mass flow in
- A-A: the internal hole exit plane,
- B-B: the counter-bore exit plane,

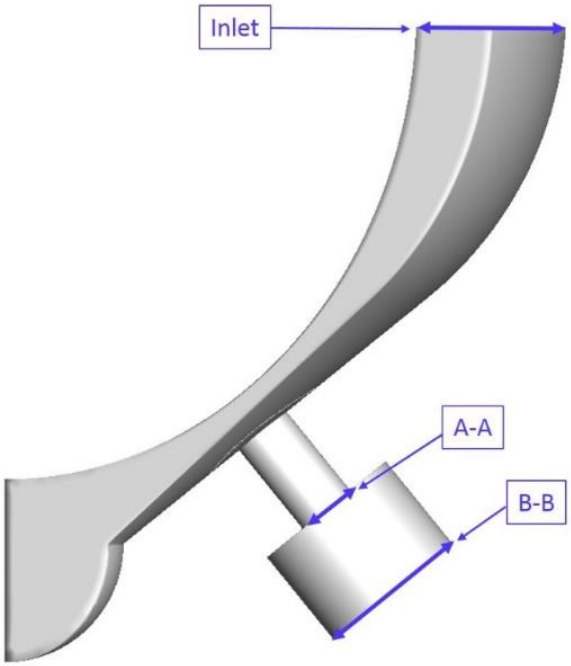

Figure 4.13 Location of measuring planes

The comparison of mass flow rate under different mesh size is shown in Figure 4.14. It shows the trend of each mesh size are all similar at different measuring planes (Inlet, A-A and B-B). The trend between different measuring planes, inlet and A-A, is similar. However, the trend at measuring plane, B-B, presents the fluctuation on their distribution of mass flow rate. This is due to the aerodynamic force and turbulent effect inside counter-bore cause the fluctuation on the liquid surface. For the further detailed validation, the average mass flow rate is used to

compare the difference of mesh size and mass conservation at different measuring planes. In order to calculate the average static flow rate value, the average value of mass flow rate is calculated from 20 to 50μs which is the flow field become steady. From Figure 4.14, average mass flow rate of all mesh size present the same value at the different measuring planes.

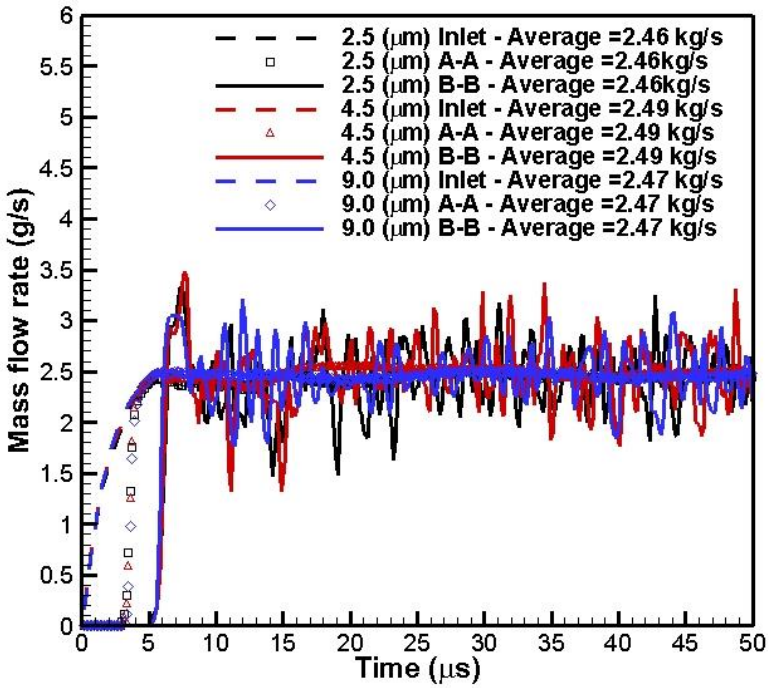

Figure 4.14 Mass flow comparison of different mesh size

From the above average mass flow rate data, the difference between different mesh size is not so significant. However, the comparison of mass flow trend at measuring plane, B-B, shows the 9.0 mm cell has smaller fluctuation on its mass flow rate distribution. This is because of the larger mesh size cannot catch the effects of smaller eddies on flow field which causes the simulation result of mass flow become more steady. The difference between average mass flow rate and its distribution between 2.5 and 4.5 μm is similar. Therefore, in order to increase the computational efficiency, the mesh size of 4.5 μm is used in the following computational domain.

Another mesh vlaidation is to examine the dribution of droplet size at the exist of counterbore (plane B-B) which is shown in Figure 4.13. The mean droplet size is calculated by measuring the ratio of the liquid area to its perimeter in the liquid jet cross plane. Figure 4.15 is a cross plane image for VOF=0.5 which indicates the red region as liquid and the blue region as air. The calculation of droplet size is as below:

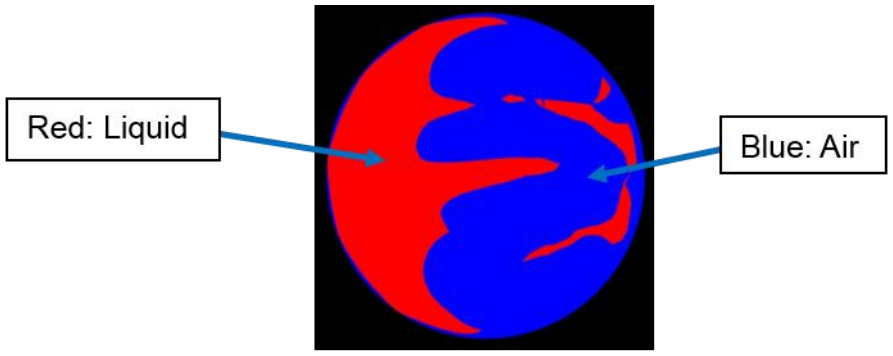

$$Droplet\ diameter = 2 \times \frac{area\ of\ liquid\ (red)}{perimeter\ of\ \ liquid\ (red)}$$

Figure 4.15 Methodologies to analyse droplet size

Due to the transient simulation of the LES model in this study, the distribution of droplet size is varied at different flow times. Therefore, in order to compare the droplet size for different mesh sizes, the mean value of droplet size at different flow times (20, 25, 30 and 35 μs) is used which is shown in Figure 4.16.

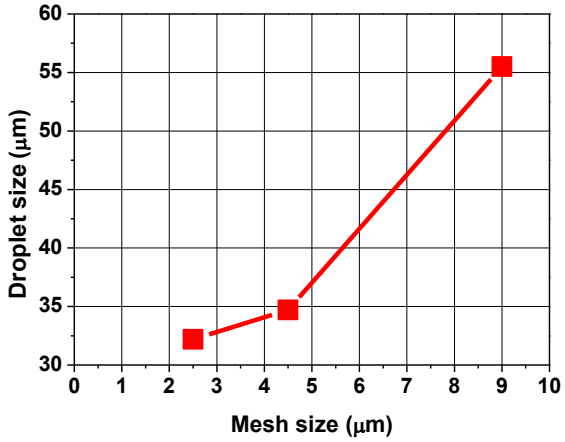

Figure 4.16 Comparison of average droplet size at different mesh size at plane B-B

Figure 4.16 shows the average droplet gradually decreased when the mesh size becomes smaller. It illustrates that the distribution of droplet size has a strong sensitivity with mesh resolution. This is because of the interaction between liquid surface and air cannot be accurately simulated when the droplet size is larger than the mesh size. The detailed distribution of liquid jet inside the conterbore area at 25 μs is shown in Figure 4.17. It is obvious to observe the difference of liquid jet surface. When the mesh size become larger, liquid jet surface become smoother.

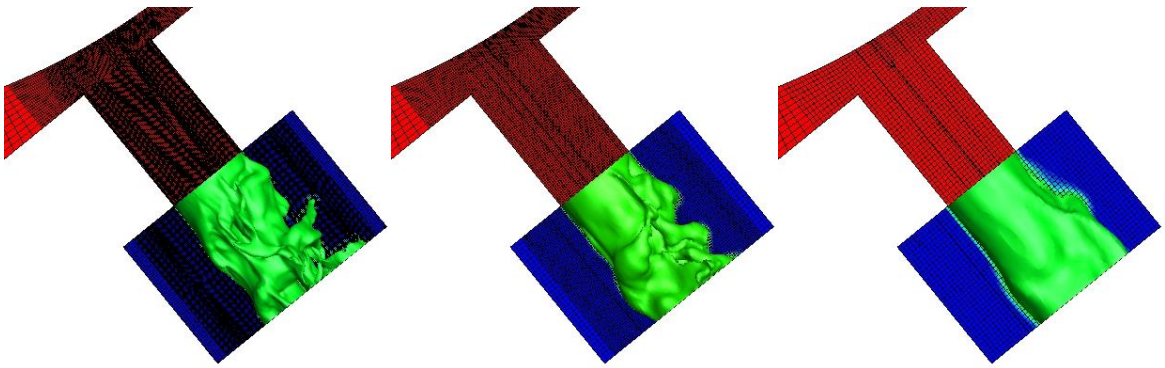

2.5μm 4.5μm 9.0μm

Figure 4.17 Distribution of liquid jet surface at different mesh resolution

The above results point out the average value of droplet size between 2.5 and 4.5μm has a similar value (32.2 and 34.7 μm). To consider about the calculating efficiency in this study (the following nozzle design will include the ambient domain), the mesh size, 4.5 μm, is used on this study.

In the validation of CFD model, the independent of time step also needs to be examined. Therefore, the average droplet size at three time steps, 0.005, 0.01 and 0.05 μs, are used to examined their difference at mesh size 4.5 μm which is shown in Table 4.6.

Table 4.6 Test conditions of time step independent

Injection Pressure	150 bar
Ambient Pressure	1 Bar
Fuel	Iso-octane
Fuel Temperature	293 K
Ambient Temperature	293 K
Mesh size in research Zone	4.5 μm
Time Step	0.005,0.01,0.05, μs

Figure 4.18 shows the comparison of average droplet size at three different time steps. It is observed that the average droplet size is between 34 and 36 μm at different time steps. Therefore, in order to decrease computational time, the time step, 0.05 μs, is used in the following studies.

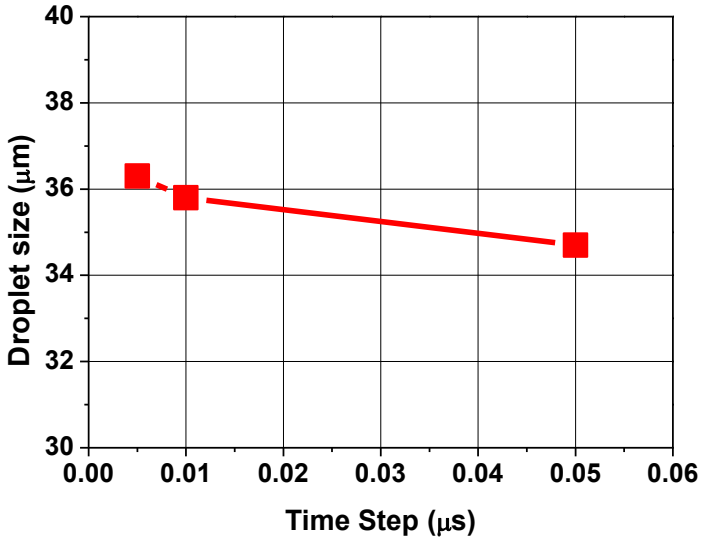

Figure 4.18 Distribution of liquid jet surface at different time steps

4.6 Validation of the Nozzle Model

Figure 4.19 presents a three dimensional GDI geometry and computational mesh used in the CFD simulation which includes the valve -group flow region, counter-bore and near-field region. In this section, the ambient section is included in this computational domain.

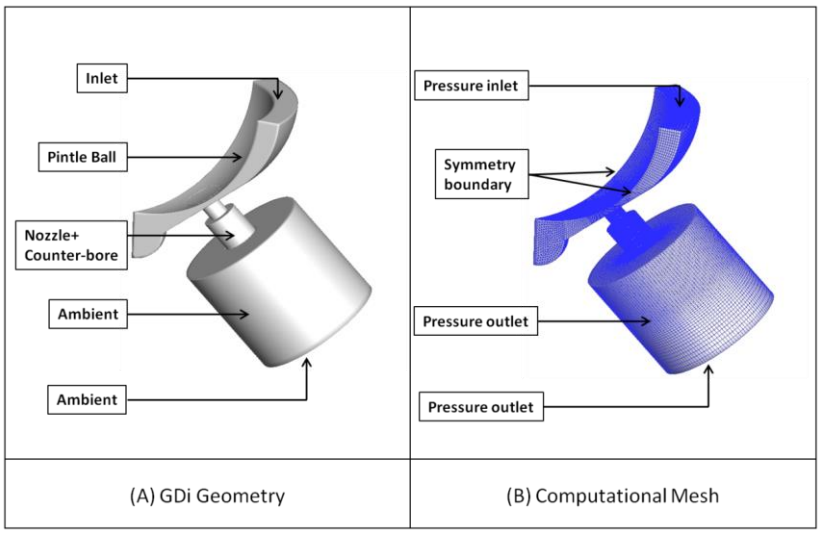

Figure 4.19 Boundary conditions and computational mesh

To match the real test conditions, the inlet boundary condition is given the same injection pressure and the same ambient pressure experimental test which is shown in Table 4.7. The movement of needle is also not considered in this research.

Table 4.7 Test conditions of different injection pressure

Injection Pressure	50, 100, 150 bar
Ambient Pressure	1 Bar
Fuel	Iso-octane
Fuel Temperature	293 K
Ambient Temperature	293 K
Mesh size in research Zone	4.5 μm
Time step	0.05 μs

According to last section, the mesh size, 4.5 μm, and time step, 0.05 μs, are used in the research zone. The area of research zone includes GDI nozzle, counter-bore and near-field which is shown in Figure 4.20. To decrease the total mesh amount, in remaining domain, the mesh size is set to 10 μm and computational mesh consists of approximately 3 million cells.

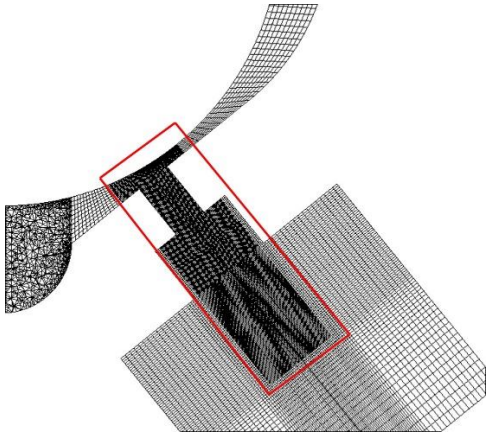

Figure 4.20 Definition of research area

Therefore, the injector static flow rate measured from a flow test bench from pervious section is used for comparison with the predicted flow rate from the CFD model. In order to measure the changes of spray characteristics inside the nozzle and its near field flow, Figure 4.21 shows the locations of measuring planes in the computational domain used to analyze the simulated flow field data:

- A-A: the internal hole exit plane,
- B-B: the counter-bore exit plane,
- C-C: the cross plane at 0.2 mm from the counter-bore exit plane,
- D-D: the cross plane at 0.4 mm from the counter-bore exit plane.

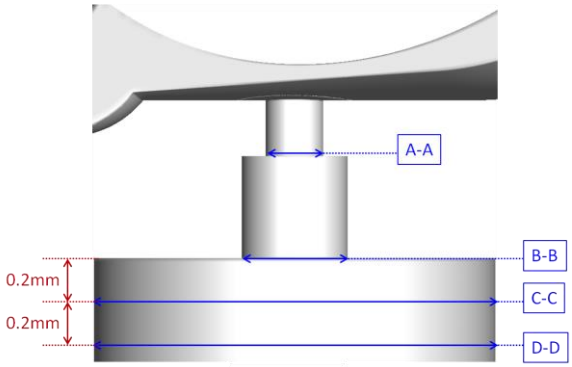

Figure 4.21 Location of measuring planes

In this research, the near field is also an issue to be discussed. Therefore, in order to examine the law of mass conservation of this nozzle model, Figure 4.22 shows the variation of mass flow rate at different measuring planes. It shows the trend of mass flow rate at plane B-B, C-C and D-D is fluctating due to the aerodynamic force and turbulent effets from ambient. The mass flow rate between plane A-A and B-B shows the same vlaue. The difference of mass flow rate between different measureing planes in the nozzle (Plane A-A nad B-B) and in the ambient (Plane C-C and D-D) is only 1.6 %. This is due to the more intensity fluctation happens in the ambient area which causes the measuring difference.

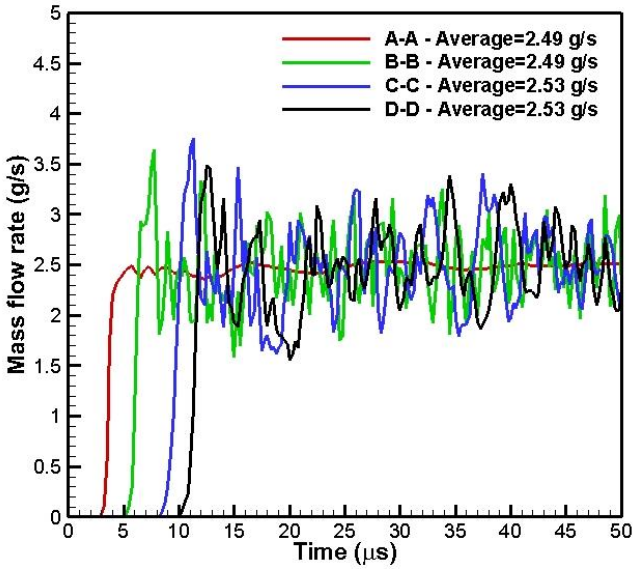

Figure 4.22 Variation of mass flow rate at different measuring planes

To compare the simulation result with experimental result, the CFD model calculates the liquid flow through plane A-A at different calculated times and averages the value from 20 to 50μs. Figure 4.23 shows a comparison between the experimental data and CFD results at different injection pressures (50 bar, 100 bar and 150 bar). From this comparison, the errors between experiment and simulation are 6% for 50 bar, 7.2% for 100 bar and 2% for 150 bar. Moreover, from this comparison between experimental data and simulation result, it can be observed that the experimental data at different injection pressures are all lower than simulation results. This could be the effect of needle movement on mass flow rate. From these results, although the effect of needle movement is observed, the error between them is not significant (2 to 6.5%) which shows the ANSYS-Fluent CFD model has the capability to simulate the nozzle flow in terms of mass flow rate.

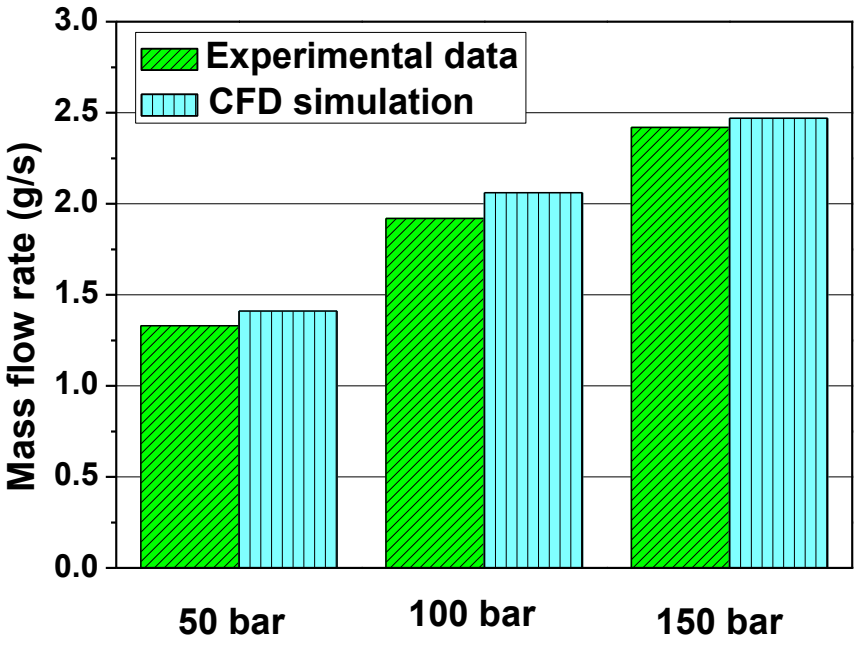

Figure 4.23 Validation of mass flow rate

4.7 Validation of Lagrangian spray model

In this study, Lagrangian spray model uses the output data from nozzle flow simulation to be the initial conditions to simulate the effects of different nozzle geometrical designs and fuel properties on the spray characteristics in the secondary breakup region. Therefore, this section examines the sensitivity of mesh and time step of Lagrangian spray model.

The CFD domain in Lagrangian spray model is designed as a cylinder to simulate the spray development which is shown in Figure 4.24. The radius of this cylinder is 30 mm with the length of 140 mm.

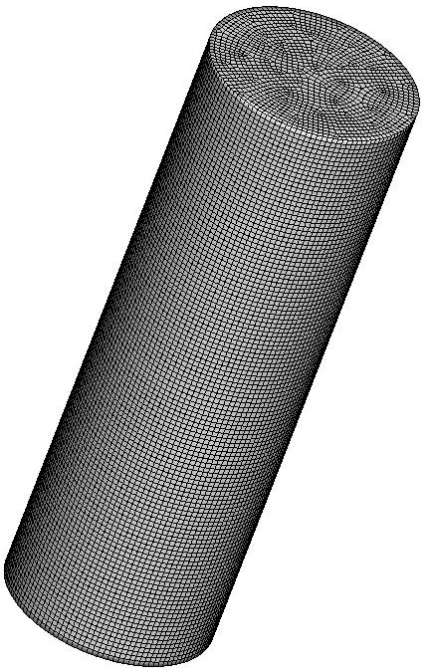

Figure 4.24 CFD domain of spray model

The test conditions in this sensitivity are shown in Table 4.8. The injection amount used in this test is based on the pervious experimental data of 150 bar injection pressure.

Table 4.8 Test conditions of mesh sensitivity

Testing Fuel	Iso-octane
Injection pressure	150 bar
Ambient pressure	1.0 bar
Injection duration	1.0 ms
Injection flow rate	2.53 g/s

The conditions of sensitivity of mesh size are shown in Table 4.9. The testing mesh size is examined separately by 0.5, 1.0, 2.0 and 4.0 mm (Figure 4.25) by using $1e^{-6}$ time step in the CFD model, shown in Table 4.9.

Table 4.9 Case distribution of different mesh sizes

Mesh size	CFD Time Step
0.5 mm	$1e^{-6}$ s
1.0 mm	$1e^{-6}$ s
2.0 mm	$1e^{-6}$ s
4.0 mm	$1e^{-6}$ s

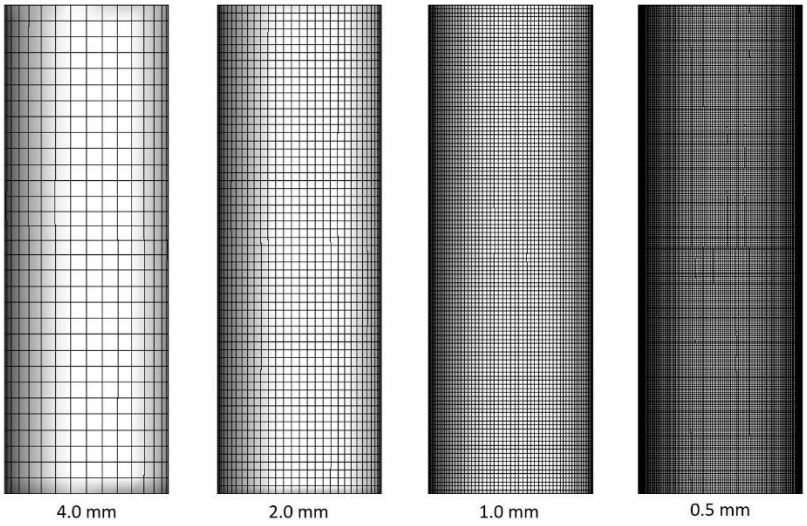

Figure 4.25 Mesh distribution of different sizes

Figure 4.26 shows the comparison of spray penetration length between different mesh sizes. It can be observed that the penetration length of 0.5 and 1 mm mesh size are almost similar and the penetration length decreases when the mesh size becomes larger. This comparison illustrates that the larger mesh size causes an obvious effect on spray simulation and calculation due to numerical diffusion. Due to the concern of efficiency of calculation and the comparison results of penetration length, the mesh size of 1.0 mm is used in Lagrangian spray model to continue further discussion.

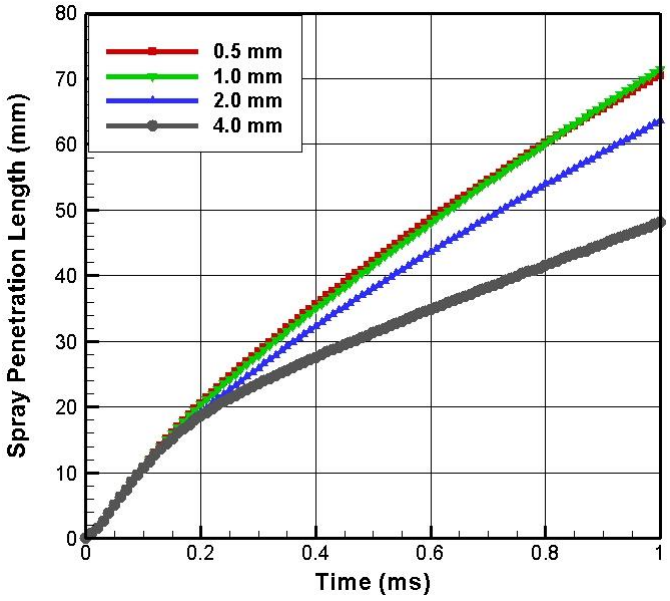

Figure 4.26 Comparison of spray penetration length at different mesh sizes

The parameter of time step in CFD model is also an important factor to affect directly numerical results. Hence, three different time steps, $5e^{-6,}$ $1e^{-6}$ and $1e^{-7}$, are examined in 1 mm mesh size CFD domain. The detailed description of test conditions is shown in Table 4.10.

Table 4.10 Case distribution of different time steps

Mesh size	CFD Time Step
1.0 mm	$5e^{-6}$, $1e^{-6}$, $1e^{-7}$ s

Figure 4.27 shows the comparison of spray penetration length at different time steps in CFD model and indicates that the difference of penetration length between each time step is unobvious. Therefore, according to the comparison of different mesh size and time step, the 1mm of mesh size and $1e^{-6}$ of time steps are used in the Lagrangian spray model in the following chapter.

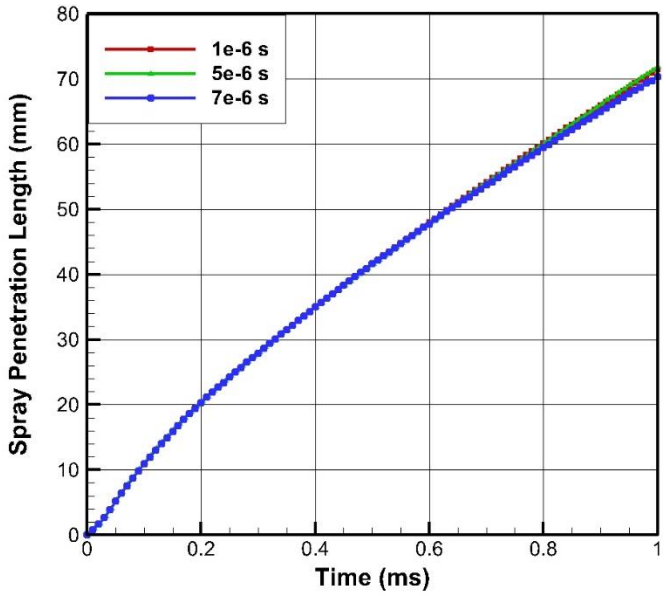

Figure 4.27 Comparison of spray penetration length at different time steps

4.8 Summary

This chapter introduces the experimental methods and setup such as PDPA and high speed camera which are used in this research. Also, in order to ensure the cell size can provide an accurate result in the GDI nozzle model, the mesh sensitivity has been examined by using three different cell sizes and time steps. The different measuring planes in the GDI nozzle and its near field show the CFD model still follows the law of mass conservation in this simulation. Finally, the comparison of mass flow rate show the numerical model shows a strong agreement with experimental results at different injection pressures.

Chapter 5

Numerical study of nozzle design in Nozzle flow

This chapter introduces the effects of different nozzle designs such as r/D, L/D and counterbore size on spray characteristics in the primary breakup region using the Eulerian model and a two-phase flow model in ANSYS-Fluent.

5.1 Introduction

The improvement of fuel atomisation in the GDI nozzle is a major issue into enhance engine combustion development. The common strategy to increase spray atomisation is by changing the operating conditions such as the injection pressure and ambient pressure. The effects of different injection and ambient pressures are mentioned in the following chapter. Another way to improve spray atomisation is to consider the nozzle design in the GDI injector.

This chapter investigates the different spray characteristics under different r/D ratio, L/D ratio and counterbore size by using three dimensional GDI nozzle geometry. In this study, the movement of the injector needle is not considered, because of the high mesh quality required by a LES model. However, the mass validation from the last chapter shows the effect of needle movement does not show a significant effect on the variation of mass flow rate. Another two important factors which have been widely discussed are the r/D ratio and L/D ratio. For the GDI injector, these two factors have been rarely studied as only slight cavitation effects can

happen. However, the r/D and L/D ratio not only affects cavitation formation but also the spray characteristics.

The unique counterbore design of the GDI injector is used to alleviate the accumulation of deposits in the inner hole and avoid the damage caused during the installation process. However, the influences of the counterbore diameter on spray characteristics are extremely rarely investigated. Several reviews indicate that counterbore can affect spray characteristics. Kazour et al (Kazour 2014) reported that the counterbore of the GDI injector affects the spray penetration length. The spray characteristics of GDI injectors with and without a counterbore are also compared in the work of Befrui et al (Befrui 2014) who finds that the counterbore introduces more vortices into the spray flow pattern. Moreover, the effects of the deposit on spray characteristics inside the nozzle have been intensively studied in industry. The deposit effects on spray patterns have been measured by several optical methods. The existence of such deposits increases penetration length and droplet size and reduces the spray angle.

This chapter examines the specific influences from different geometric features and deposit designs on the near flow field of a production GDI injector by using a VOF-LES model. Furthermore, the initial jet breakup characteristics such as droplet size, spray angle and velocity are compared between different injector designs in order to investigate the detailed influences of the different nozzle geometries. The other objective of the study is to provide accurate initial boundary conditions to Lagrangian models to improve the accuracy of fuel spray simulations.

5.2 Analysis Methodology of Fuel Spray Characteristics

This section introduces the methodologies used to analyse the data from the flow field simulations. To estimate the intensity of atomization, three parameters are used in this discussion, spray angle, breakup length and droplet size. Figure 5.1 presents the method which is applied to measure the spray angle and breakup length. The spray angle is used to define the droplet spatial distribution in the combustion chamber. The breakup length represents the liquid core length with which the liquid jet remains intact before it begins to break up into ligaments and droplets.

The spray angle is defined as the angle of liquid dispersion, which is measured from the nozzle entrance to the edge of the downstream liquid distribution. Liquid breakup length is measured as the liquid length of VOF=0.5 (the common value for VOF model to represent liquid) from the exit of an internal nozzle to the end of the liquid jet.

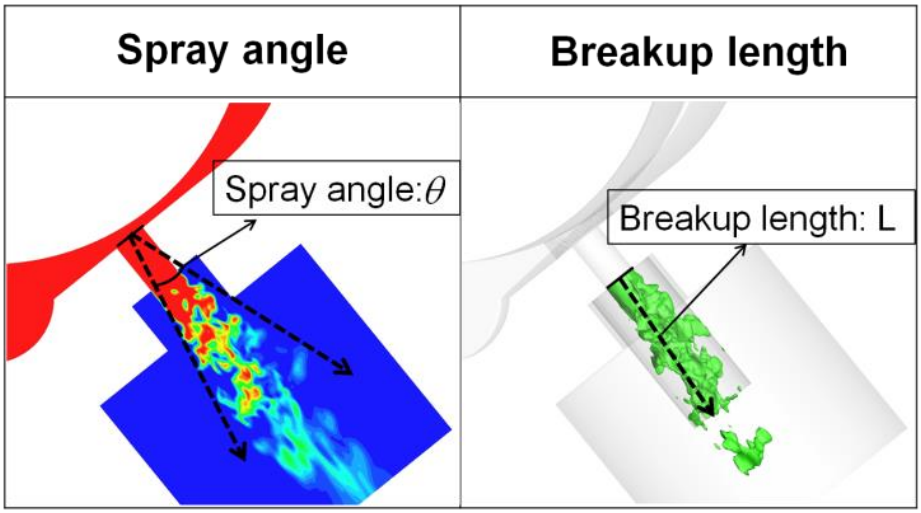

Figure 5.1 Methodologies to analyse spray angle and breakup length

Spray angle and liquid length are measured at different flow times after the flow field stabilizes. Several values of breakup length and spray angle from different times are averaged in order to calculate mean breakup length and spray angle under different operating conditions.

The near field spray characteristics are very important parameters for gaining insight into the primary breakup mechanism. In this analysis, four measuring planes, which are shown in Figure 4.20, are set up to analyse droplet size at the internal exit, counterbore exit and near field which provide a better understanding of the distributions of the droplet size. In the region of primary breakup, the liquid is formed with both liquid jet and liquid ligaments, but the latter are used instead of droplets.

5.3 Effects of Nozzle Design

5.3.1 r/D Ratio

In this section, detailed discussions of the influence of different r/D ratios on spray characteristics are introduced. The definition of the r/D ratio in this section is shown in Figure 5.2. The orifice entrance curvature radius is set as r and the nozzle hole diameter is D. The curvature radiuses in the nozzle's upper wall and at the bottom are the same value. Moreover, the testing conditions are shown in Table 5.1.

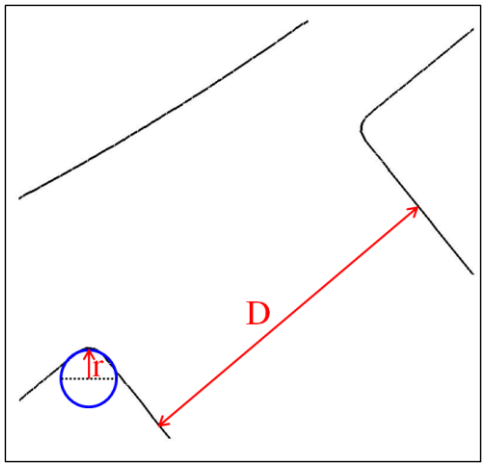

Figure 5.2 Definition of r/D ratio in the GDI nozzle

Table 5.1 Testing conditions and r/D ratio

	Test Conditions
Test Fuel	**Iso-octane**
Injection Pressure	**150 bar**
Ambient Pressure	**1 bar**
Testing Range of r/D	**0.0, 0.05, 0.1**

When the injection pressure is 150 bar and the ambient pressure is 1bar, for a different r/D ratio (0.0, 0.05 and 0.1) of the GDI nozzle at the needle lift, H, the distribution of the velocity and the streamline in the nozzle are shown in Figure 5.3. It can be seen that the velocity around the upper inlet corner gradually decreased when smoothing the inlet corner shape from r/D=0.0 to 0.1. In addition, the distributions of the streamline show that a smaller vortex takes place in the nozzle upper wall in r/D=0.0. However, when r/D increases to 0.05 and 0.1, the vortex disappears and the flow field becomes smooth. This is due to the smooth nozzle inlet corner (increase of r/D) decreasing disturbances from the sudden flow direction change in the nozzle.

These disturbances in the fluid may accelerate the droplet breakup in the downstream and then decrease the spray angle and liquid breakup length.

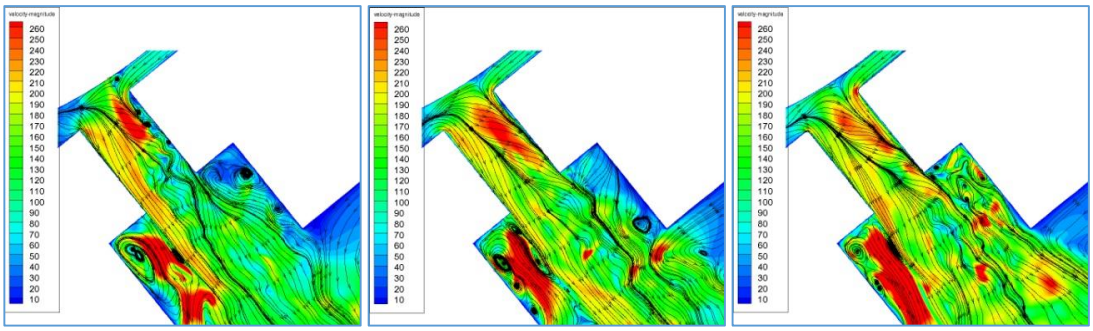

(a) r/D=0.0 (b) r/D=0.05 (c) r/D=0.1

Figure 5.3 Distributions of velocity and streamline at different r/D ratios at 30μs

The comparison of average mass flow rate at the inner hole nozzle exit at different r/D ratios points out that the effects of different r/D ratios on mass flow rate are significant and direct in Figure 5.4.(a). When r/D changes from 0.0 to 0.005, the mass flow rate is increased by 14.57% and increased by 22.67% from 0.0 to 0.1. In Figure 5.4.(b), the discharge coefficient (C_d) for r/D=0.1 is up to 0.85. It can be observed that smoothing the orifice entrance curvature radius can improve the fuel injection amount.

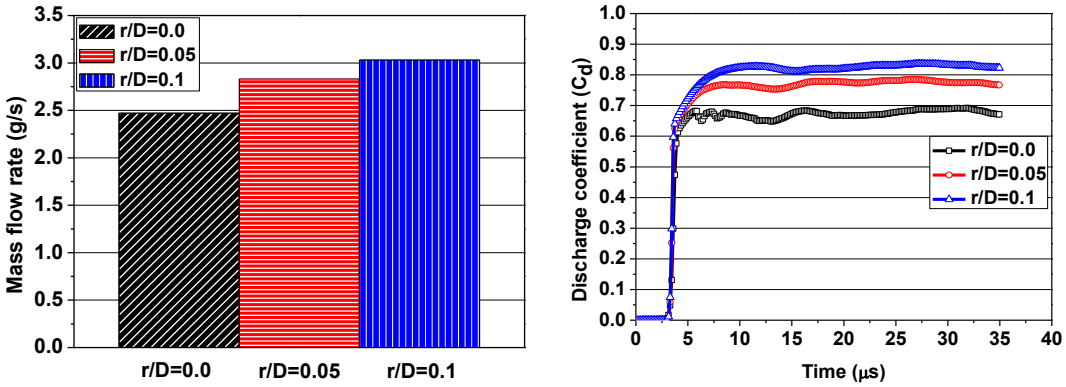

(a) (b)

Figure 5.4 Average mass flow rate and variation of Cd at different r/D ratios

Figure 5.5 compares the average value and variation of nozzle velocity and the distribution of velocity at the nozzle exit. Due to the decrease of drag force from the orifice entrance angle, the nozzle exit velocity is increased to 183m/s at r/D=0.1 which is 20% higher than r/D=0.0 in Figure 5.5.(a). In Figure 5.5.(b), compared with Figure 5.5.(a), the velocity distribution of r/D=0.0 reaches a peak velocity at the nozzle exit; due to the sharp inlet corner causing a greater recirculation zone.

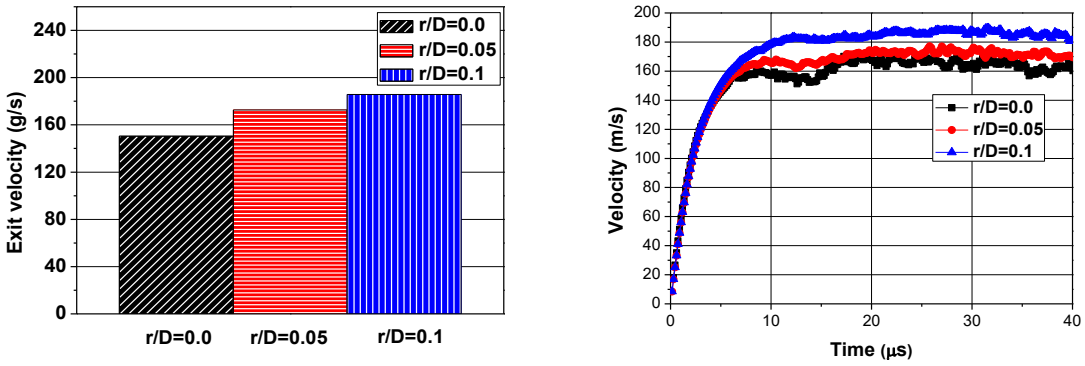

(a)

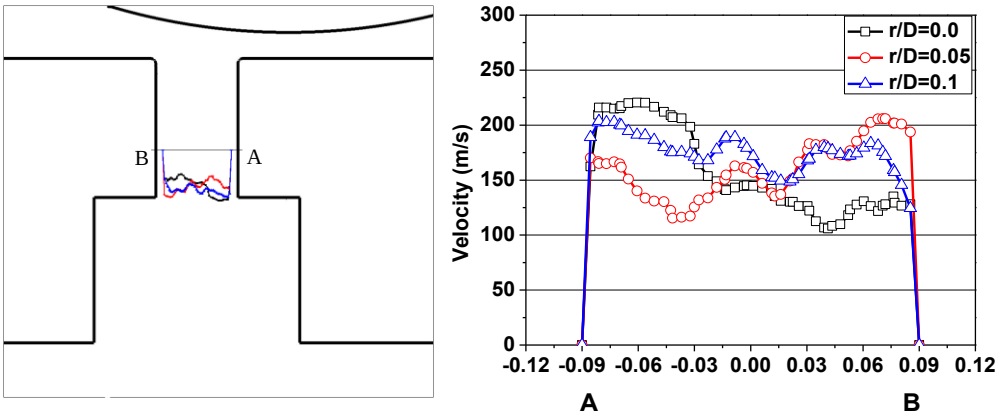

(b)

Figure 5.5 Velocity and the distribution of velocity at the nozzle exit at 30 μs

This results in the nozzle area decreasing and then accelerating the field velocity. However, to compare with r/D=0.05 and 0.1, it can be observed that the nozzle exit velocity is more uniform

than r/D=0.0. The difference between peak value and the lowest for r/D=0.0 is up to around 100 m/s. when the r/D ratio increased, the difference dropped by 50%.

Opposite results are shown in turbulent kinetic energy. The mean turbulent kinetic energy is calculated and averaged from each cell at plane A-A at different time steps and the mean value from different time steps are averaged again to calculate the mean value of kinetic energy for the whole simulation result. The trend is gradually decreased when the nozzle velocity increases (r/D ratio increase), as shown in Figure 5.6(a). This is due to the smooth entrance corner, causing liquid to flow into the inner hole without a large direction angle change and then decreasing the turbulent disturbances. The distribution of turbulent kinetic energy in the nozzle flow also indicates that the turbulent kinetic energy is significantly decreased when the r/D ratio increases, as shown in Figure 5.6(b).

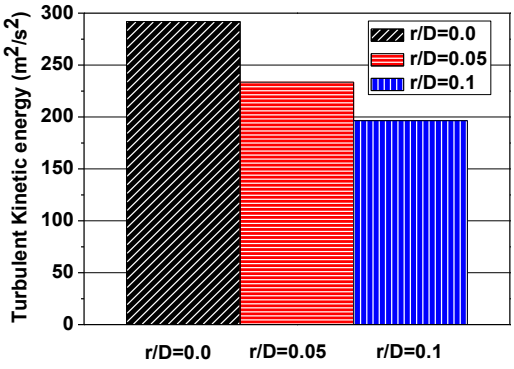

(a)

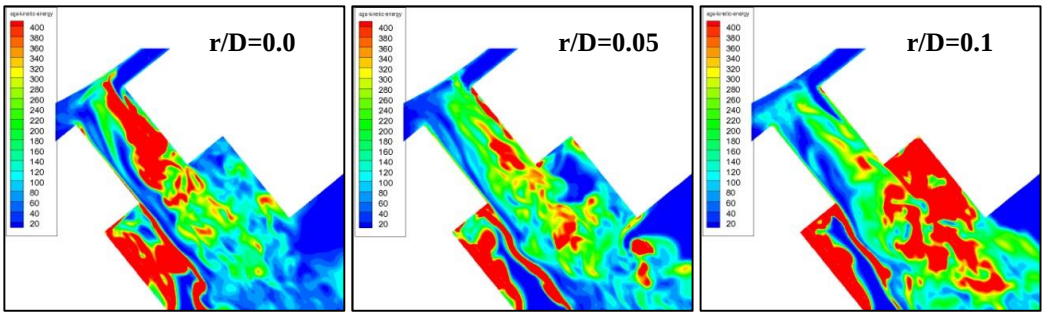

(b)

Figure 5.6 Average kinetic energy value (a) and the distribution of kinetic energy at different r/D ratio at 30 μs

Figure 5.7 shows the value of VOF distribution in each cell, with red color indicating 100% liquid and blue color representing 100% air. Therefore, when the liquid (red color) enters the ambient air (blue color) from the nozzle hole, the disturbance around the liquid jet causes some liquid to detach from the jet body. This causes the mixing of air and liquid in some cells around the liquid jet edge. For example, if the value shows 0.25 in the cell, then this means 25% of liquid and 75% of air. Although the exit velocity has obvious differences for different r/D ratios, the spray angle and jet breakup length show a similar value in Figure 5.8. The liquid distributions of different r/D ratios at 30 μs are presented in Figure 5.7. By measuring the spray angle and jet breakup length, it indicates that the spray angle slightly increases when the r/D ratio increases as in Figure 5.8 a). However, the differences between them are around 2-3 degrees. These similar results show up in the breakup length which is around 0.42-0.45 mm in Figure 5.8 b). These results illustrate that spray angle and liquid breakup length are not obviously affected although the nozzle exit velocity increased, because turbulent disturbances decrease when velocity increases.

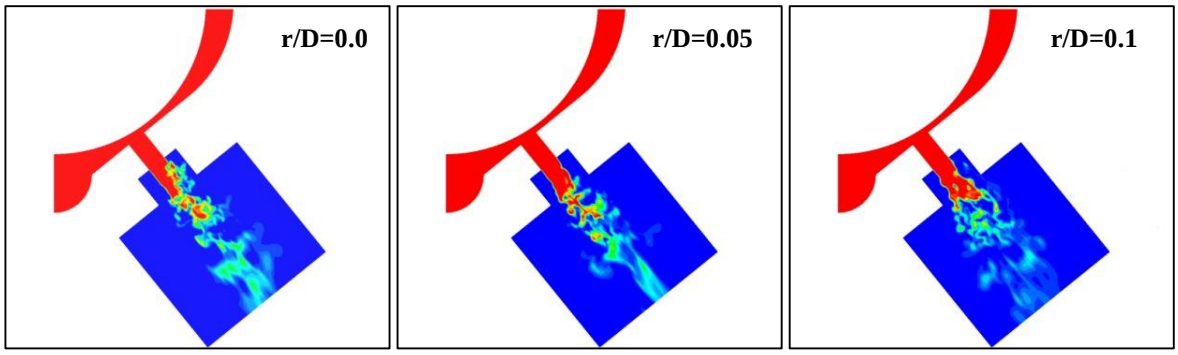

Figure 5.7 Distribution of liquid at 30 μs

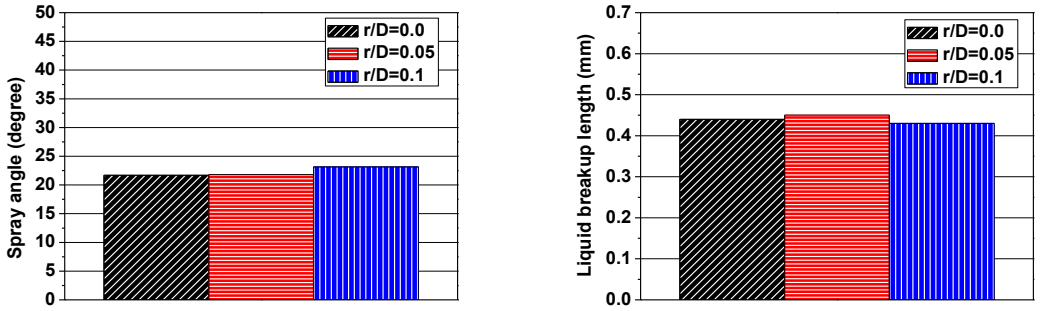

(a) **(b)**

Figure 5.8 Average value of spray angle and breakup length at different r/D ratio

The distribution of VOF at plane B–B is shown in Figure 5.9. In the primary breakup regime, it is difficult to compare the effect of different nozzle geometries on the spray characteristics due to the existence of only liquid jet and ligaments. Thus, by employing numerical approaches, the trend of spray characteristics for different nozzle geometry designs and operating conditions can be revealed. In the Euler approach, the blob model describes the liquid jet, assuming several different sizes of blob.

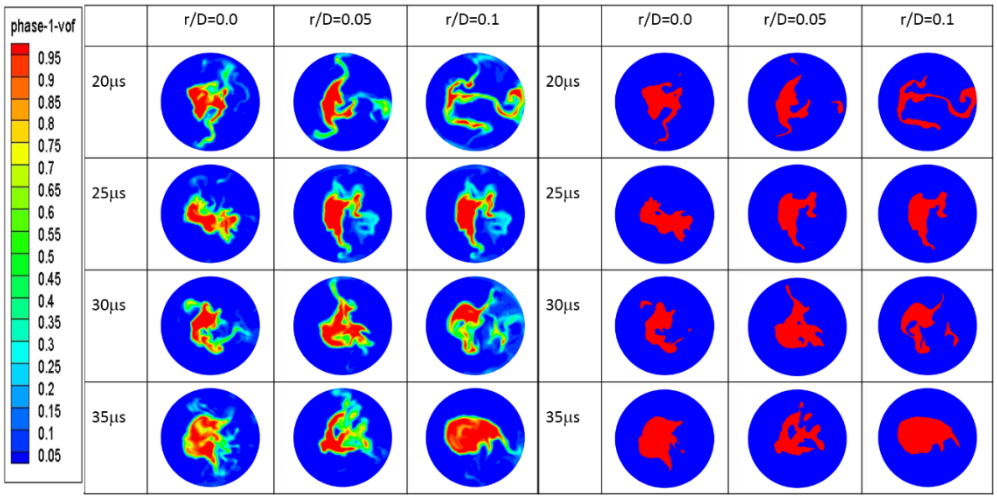

Liquid distribution VOF=0.5

(a) (b)

Figure 5.9 Distribution of liquid and VOF=0.5 at measuring plane B-B at 30μs

In Figure 5.9, blob size calculated from liquid jet is used to compare the effect of different operating conditions and nozzle designs on the spray characteristics in primary breakup regime.

Then, by using the methodology from Figure 4.14, Figure 5.10 shows a comparison of average droplet size at different measuring planes which is an average value between 20 to 35 μs. At the inner hole exit (plane A-A), the droplet size for different r/D ratios provide the same value which equalizes with the inner hole diameter. At the counterbore exit (Plane B-B), although a higher r/D ratio presents a higher exit velocity, the droplet size of the higher r/D ratio still has a larger average droplet diameter. This is due to the less turbulent kinetic energy in the liquid slowing down liquid jet breakup instead of the aerodynamics from the high exit velocity.

At plane C-C and D-D, the differences between the r/D ratios become insignificant, but a higher r/D ratio still has a larger droplet size. When the liquid jet leaves from the counterbore, more factors affect the liquid jet breakup. From Figure 5.6 (a), it shows that the average turbulent kinetic energy in the inner hole is decreased when the r/D ratio increases. However, the larger turbulent kinetic energy distribution takes place on the right-hand side of the counterbore due to the higher velocity from the larger r/D ratio. This could cause stronger turbulent effects on jet breakup in the downstream. Another factor could be that the aerodynamics play a leading role in liquid jet breakup in the downstream.

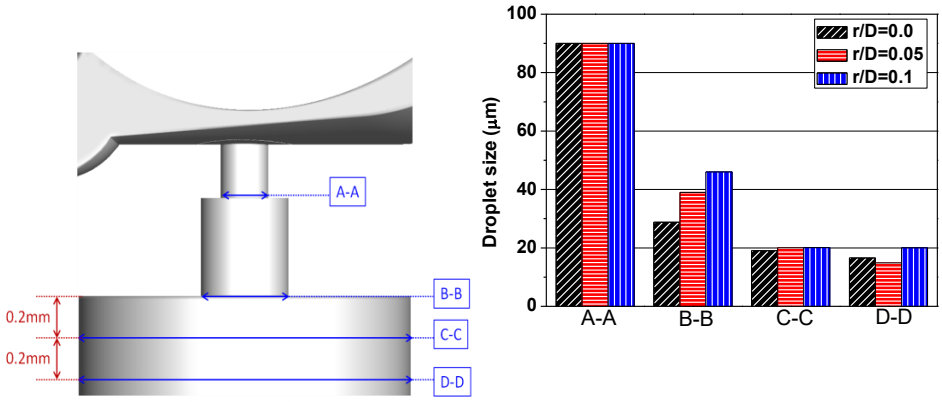

Figure 5.10 Distribution of average droplet size at different measuring planes

The recent investigations concerning of r/D ratio and nozzle flow examine the formation of cavitation at different r/D ratios in diesel nozzles. Most research show that the increase of r/D ratios decreases the nozzle exit velocity in the diesel nozzle, because the increasing r/D ratio decreases the recirculation zone (decrease cavitation effects); which is followed by an increase in the nozzle effective exit area. This causes lower nozzle exit velocity and slower liquid breakup. On comparing the cavitation effects between diesel and gasoline injectors, it is found that there are fewer or no-cavitation effects in the gasoline injector. This could be the reason behind the different results between diesel and gasoline injectors under different r/D ratios.

5.4 L/D Ratio and Counterbore Diameter

A range of different nozzle geometries were investigated using a sensitivity analysis approach. In total nine cases are modelled, with different L/D ratios and d/D ratios as given in Figure 5.11. In order to investigate the influences from different L/D ratios and counterbore sizes, three different L/D ratios are discussed separately 1.0, 1.3 and 1.6, with different d/D ratios of 1.85, 2.0 and 2.15.

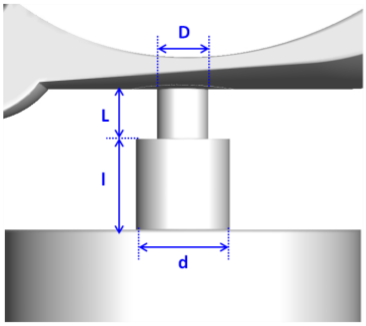

	L/D	(l+L)/D	d/D
Case 1	1	2.8	1.85
Case 2	1.3	2.8	1.85
Case 3	1.6	2.8	1.85
Case 4	1	2.8	2.0
Case 5	1.3	2.8	2.0
Case 6	1.6	2.8	2.0
Case 7	1	2.8	2.15
Case 8	1.3	2.8	2.15
Case 9	1.6	2.8	2.15

Figure 5.11 Case distribution of different L/D and d/D ratios

The boundary conditions applied for in this paper are described as follows:

- Inlet: The fuel injection pressure is set to 200 bar for the sensitivity study.
- Outlet: At ambient pressure, the length of the ambient domain is designed to be 10 time the diameters which can provide enough distance for jet development and avoid the reflection of pressure disturbance from the wall as much as possible
- Test fuel: Iso-octane is used in all simulations at ambient temperature.

The dimensional effects of the two main parts of a stepped hole GDI injector, namely: the inner hole and counterbore, on the injection characteristics such as the mass flow rate, velocity, spray angle, breakup length and droplet size are presented and discussed in this section. For the purpose of simulations, the dimensional parameters of the inner hole and counterbore are considered as non-dimensional parameters of L/D ratios for the inner hole and d/D for the counter bore, as shown in Figure 5.11. However, the inner hole diameter and counterbore length are kept constant. In the analysis of the results, the two parameters used are the L/D ratio and counterbore diameter.

The distributions of VOF at 30 μs for the cases investigated are presented in Figure 5.12. These images are used to provide a better understanding of flow patterns inside the counterbore. Moreover, Figure 5.13(a) shows that the liquid distribution occurs at the counterbore exit plane (B-B) 30μs from the start of the fuel entering the nozzle. Figure 5.13(b) is the distribution of VOF=0.5 which is used to calculate the droplet size at plane B-B. With an increased L/D ratio at the inner hole (from case 1 to case 3, case 4 to case 6, and case 7 to case 9 as shown in Table 5.1), the liquid wall impingement and wall attachment are decreased as shown in Figure 5.13

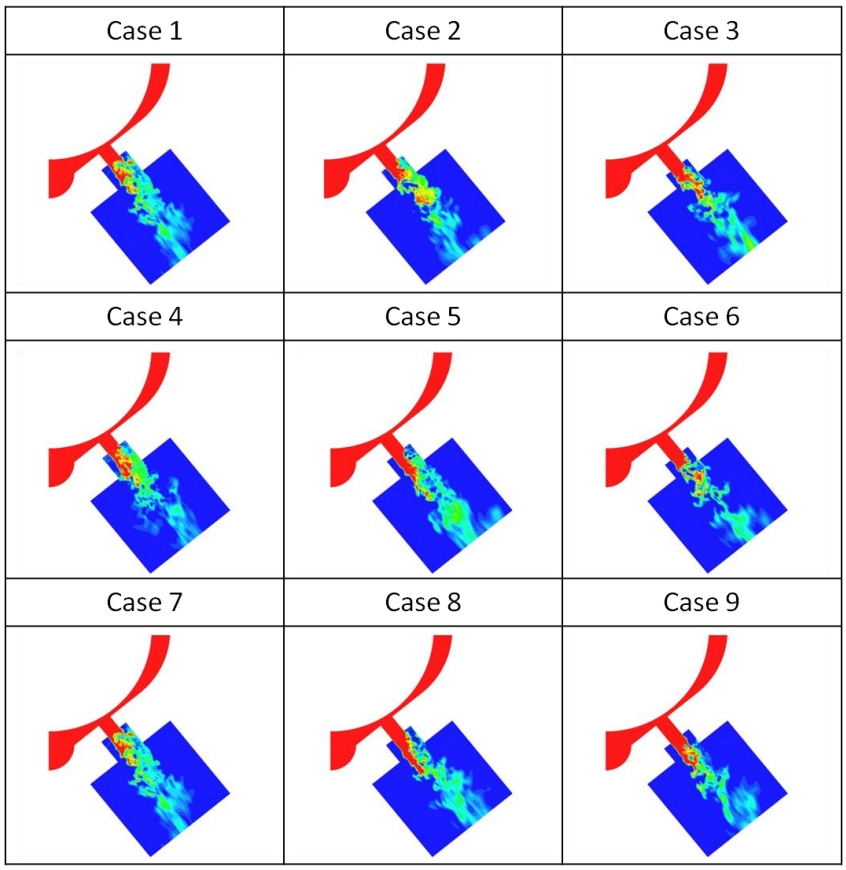

Figure 5.12 VOF distribution at 30 μs for different cases

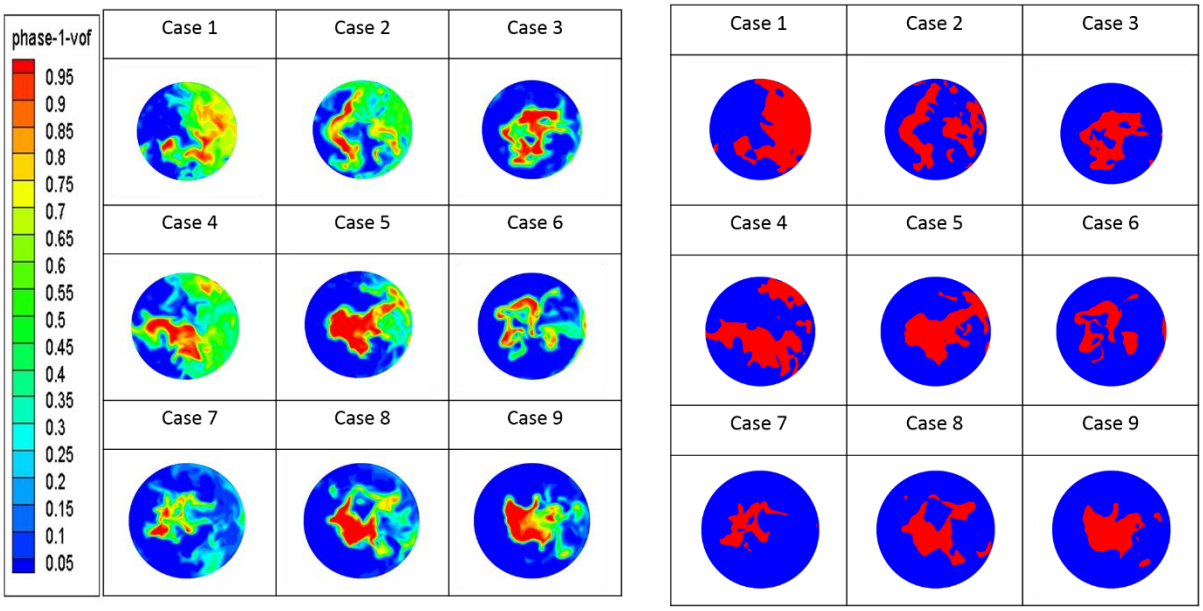

(a) (b)

Figure 5.13 Comparison of liquid distribution (a) and VOF=0.5 (b) used for droplet size calculation at the B-B plane at 30 μs from the start of fluid flow into the nozzle

5.5 Inner Hole L/D Ratio

Mass flow rate variations for cases 7, 8 and 9 with respect to time are calculated at the A-A plane and are presented in Figure 5.14. The mass flow rate of case 7 appears less steady compared to the other two cases with larger L/D ratios. It is highly likely this is due to the combined effects of numerical instability caused by using the LES model which produces slightly different results each time it is executed; and also the physical nature of the in-nozzle reattachment flow downstream from the recirculation region. This flow instability is reduced by increasing the inner hole length, since the reattached flow becomes more stable further away from the recirculation zone, caused by the sharp entrance edge rim.

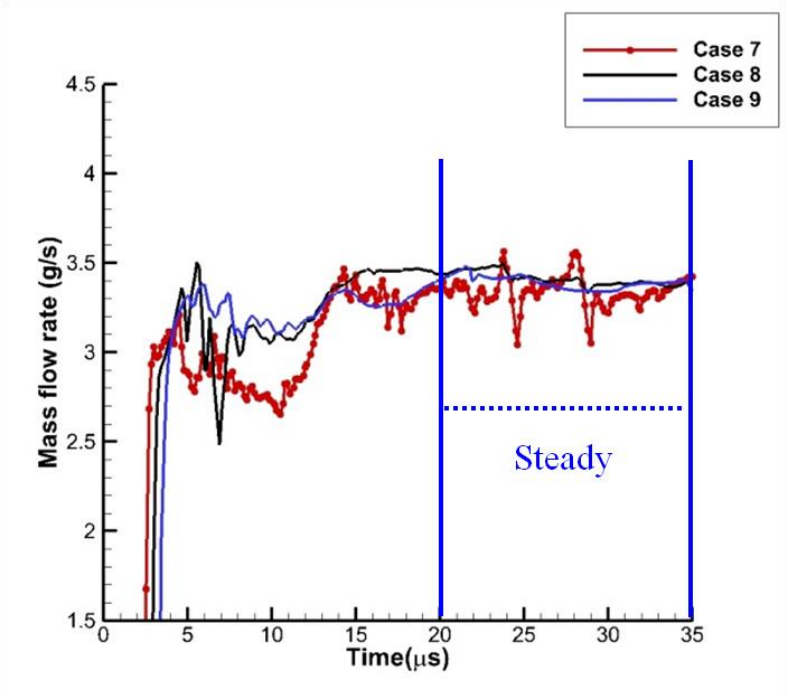

Figure 5.14 Mass flow rates with respect to time for cases 7, 8 and 9

In order to compare the differences between the mass flow rates for different L/D ratios, average mass flow rates are calculated over the time interval of 20 to 35μs which is after the initial transition time, as shown in Figure 5.14. Simulated mass flow rates for the different L/D ratios are presented in Figure 5.15.(a). The nozzle holes with smaller L/D ratios produced higher mass flow rates, indicating a smaller restrictive effect on the average mass flow rate as the L/D decreased. The small discrepancies in effect of L/D on the averaged simulated mass flow rates for different d/D values is within the range of LES error. Moreover, Figure 5.15.(b) also points out that the smaller L/D ratio has a bigger discharge coefficient (C_d) than the larger L/D ratio; since the latter ratio has to process larger friction from the longer nozzle wall.

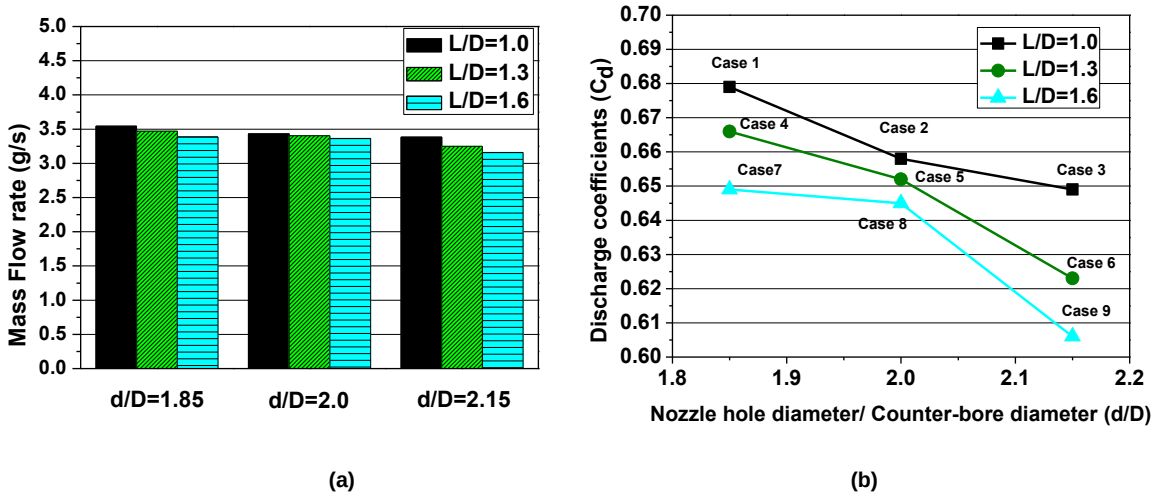

Figure 5.15 Average mass flow rates and discharge number for different L/D and d/D ratios

Cell based averaging of the liquid velocity at the A-A plane for the same three cases is presented in Figure 5.16. The flow rate consistently reduces as the L/D increases. For L/D=1.3 and 1.6, the exit velocities are more stable with exit velocities of 180 m/s for L/D=1.3 and 172 m/s for L/D=1.6. The exit velocity for L/D=1.0 is unstable and varies from 185 to 194 m/s reflecting its three dimensional nature.

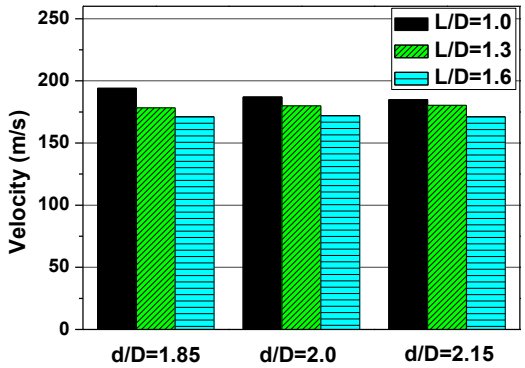

Figure 5.16 Exit velocities at A-A plane for different L/D and d/D ratios

The effects of the L/D ratio on spray angle are presented in Figure 5.17. The spray angles were measured and averaged at five different times after the mass flow had become steady. The smallest L/D ratio results in the largest spray angle and the spray angle tended to decrease as the L/D ratio increased. Higher exit velocities at the A-A plane associated with smaller L/D

ratios led to more intensive interactions between air and the liquid in the counterbore region, resulting in better breakup of the liquid jet into droplets and wider spray angles. In shorter inner holes, the reattached flow cannot be fully developed into one directional flow when it exits the inner hole and its original three-dimensional nature leads to wider spray angles.

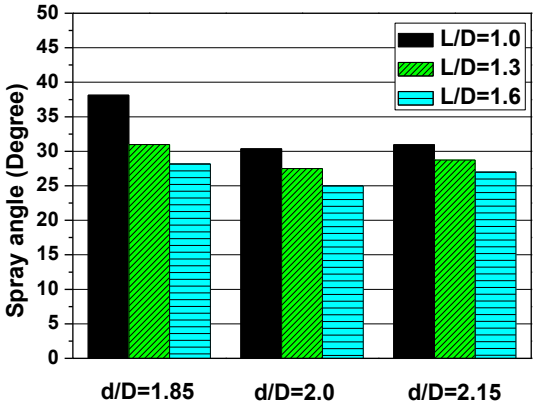

Figure 5.17 Exit spray angles for different L/D and d/D ratios

Figure 5.18 presents a comparison of breakup lengths for different L/D ratios. The VOF-LES model is used to simulate the transient flow field and the average breakup lengths are calculated for different times. It is shown that the average breakup length tended to increase with the L/D ratio except for case 5 (L/D=1.3, d/D=2.0) which followed a dissimilar trend. This could be due to the competing effects of the liquid jet's turbulent intensity versus the damping of the aerodynamic force by the doughnut shape recirculation zone. A higher liquid jet turbulent level (low L/D) results in shorter breakup length. A stronger recirculation zone (larger d/D) reduces the velocity difference of the ambient and the liquid jet which reduces the aerodynamic force and increases the breakup length. Case 5 appears to be the condition where the damping effect of the recirculation zone had a dominant effect compared to the other cases. However, by reviewing all the trends, the results indicate that smaller L/D ratios give rise to improved jet atomisation with decreased breakup lengths.

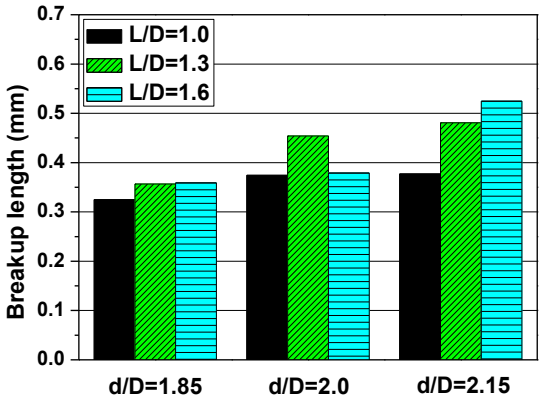

Figure 5.18 Breakup lengths for different L/D and d/D ratios

The method used to determine nominal droplet sizes is based on calculating the ratio of the liquid area to its circumference along any cross-section as described previously, although it cannot distinguish between droplets and ligament. However, it is a reliable indicator of atomisation quality. The estimated droplet size at the internal hole exit (plane A-A) for different L/D ratios is presented in Figure 5.19. The initial droplet size for L/D= 1.0 is the smallest (84 to 96 μm). The upstream geometry of the injector forces the flow to make a sharp right turn to enter the internal hole, resulting in a region prone to flow detaching on the upper right side of the internal hole wall. For small L/D ratios, the liquid does not reattach to the wall before it exits the internal hole (plane A-A), resulting in the reduction of the effective exit area and thus, higher exit velocities and smaller droplet sizes. For the longer nozzle length (L/D=1.6), the initial droplet size is almost equal to the hole diameter indicating full attachment of the liquid jet to the internal hole wall.

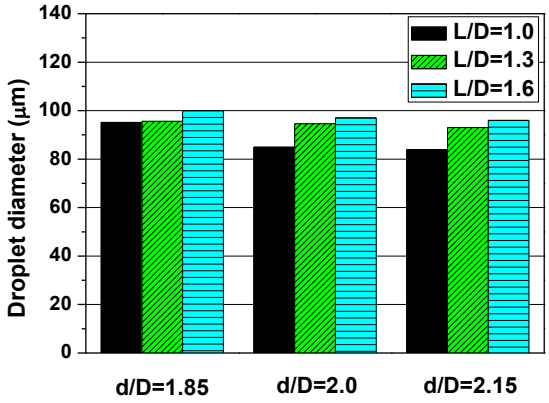

Figure 5.19 Droplet sizes at plane A-A for different L/D and d/D ratios

Figures 5.20, 5.21 and 5.22 present droplet sizes at different measuring planes. Droplet sizes all decrease when the measuring plane is moved away from the inner hole exit plane. Comparing Figures 5.20 and 5.21, the droplet size at counterbore exit at plane B-B is bigger than that at plane C-C, 0.2 mm downstream of the counterbore exit.

For case 1 with L/D=1.0, its droplet sizes are larger than those for cases 2 and 3. However, the droplet sizes for case 1 have a larger size reduction (40%) as they move from plane B-B to plane C-C than for cases 2 and 3, which are reduced by only 25%. This is another indication of stronger atomisation for shorter L/D ratios caused by higher jet velocity, air entrainment and possible cavitation effects. For the cases with L/D=1.3 and 1.6, trends of droplet size increases are observed when the L/D ratio is increased. The comparison of droplet sizes at different measuring planes indicates that the inner hole length directly affects the droplet size; smaller L/D ratios have smaller droplet sizes. This is caused by the shorter nozzle length not providing enough length for the three dimensional flow to fully develop, resulting in a higher liquid turbulent level at the exit plane and stronger liquid atomisation.

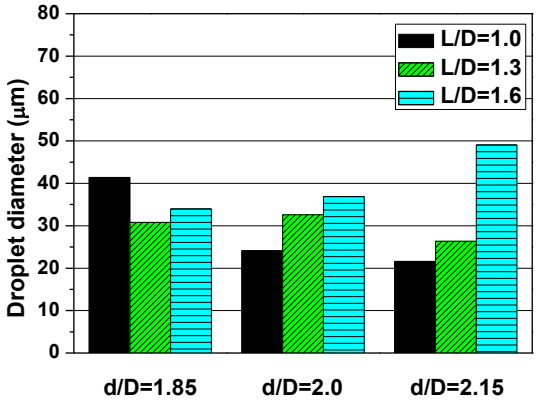

Figure 5.20 Droplet size at measuring plane B-B for different L/D ratios

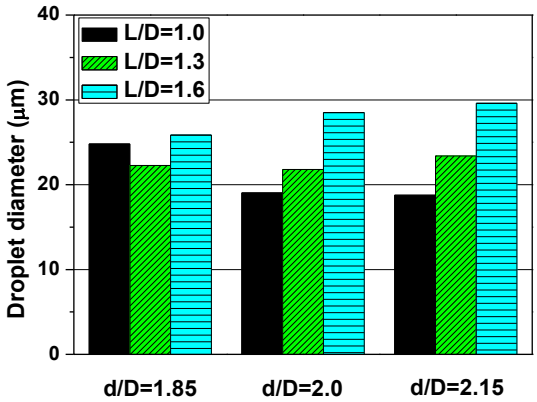

Figure 5.21 Droplet size at measuring plane C-C for different L/D ratios

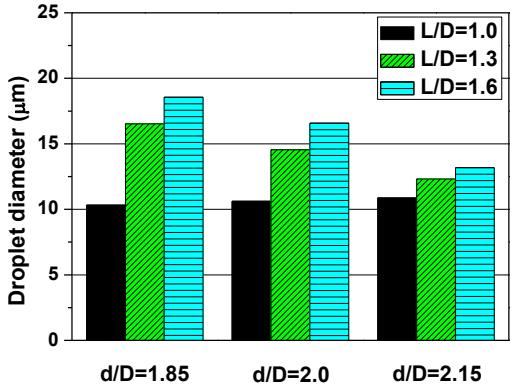

Figure 5.22 Droplet size at measuring plane D-D for different L/D ratios

5.6 Counterbore Diameter

The influences of different counterbore dimensions on spray characteristics such as droplet velocities, diameters, spray angle and breakup length are presented and analysed in this section. The comparison of mass flow rates and the discharge coefficient for different counter-bore dimensions has been presented in Figure 5.15. Injectors with smaller counterbore diameters have higher mass flow rates. This observation can be explained by the fact that a liquid jet flowing through the counterbore produces a positive circulating air flow inside the counter-bore cavity which reduces the flow resistance and increases the total mass flow rate from the inner hole,as in Figure 5.23.

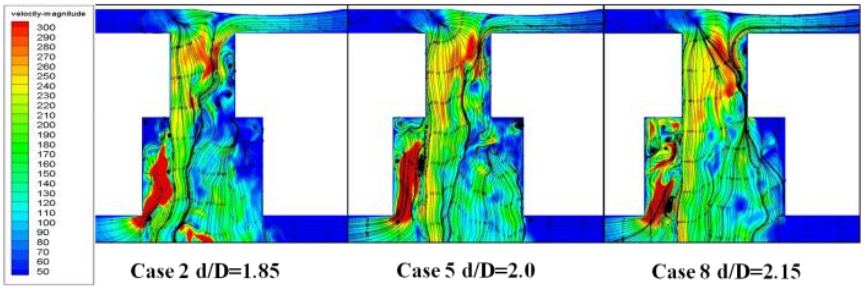

Figure 5.23 Distribution of velocity and streamline at different d/D ratios

However, when the counterbore diameter is increased, the amount of air into the counterbore cavity is increased this reduces the recirculation velocity and its positive effect on the flow rate of the liquid jet.

The velocities at the inner hole exit (plane A-A) for different counterbore diameters are presented and compared in Figure 5.16. The effects of the counterbore diameter on the inner hole exit velocity at plane A-A are less pronounced for larger L/D ratios. A clear reduction of the exit velocity is observed for L/D=1 with an increased counterbore diameter. This reduction

can be explained by the fact that in larger counterbore sizes more air is entrained into the counterbore cavity and it is thus harder to generate a positive circulation. However, the influences from different counterbore diameters are negligible for the L/D=1.3 and 1.6 cases. Since the recirculation zone is induced by the velocity difference of the liquid jet and the ambience, for longer L/D with lower jet velocity, the induced recirculation zone became weak and consequently has less effect on the exiting jet. Therefore, the exit jet velocity and the recirculation zone feed each other and a certain level of jet velocity is required to induce a strong enough recirculation zone to result in measurable differences in both mass flow rates and atomisation quality.

Exit velocities at the counterbore exit plane B-B are presented in Figure 5.24. The exit velocity at plane B-B which is decreased with the reduction of counterbore diameter for L/D=1 because the corresponding spray angles are larger, and for small counterbore diameters, sprays impinge on the counterbore wall results in a loss of momentum and exit velocity at plane B-B. However, for L/D=1.6 the spray angles are smaller and they could pass through the counterbore without impinging on the wall.

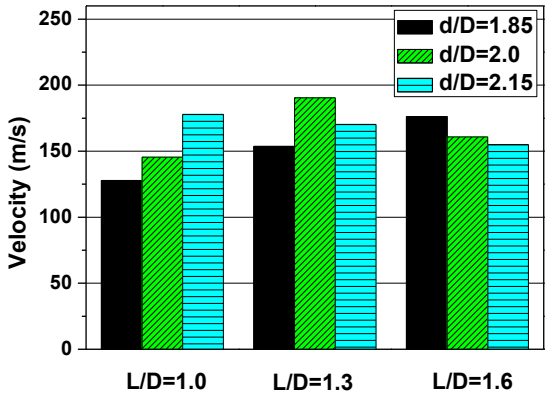

Figure 5.24 Comparison of inner hole velocity at B-B for different d/D and L/D ratios

However larger counterbore diameters have more entrained air and weaker recirculation which has an adverse effect on the droplet velocities, as shown in Figure 5.24. For L/D=1.3, spray angles are believed to be in a range that would result in intermittent impingements and thus, there is no clear trend observed for the exit velocity with different counter bore sizes.

A comparison of velocity reduction as fluid passes through the counterbore with different diameters has been provided and the results are presented in Figure 5.25. In accordance with the previous observation for L/D =1 which produces large spray angles, the velocity reduction through the counterbore with a small diameter (d/D <2) is very high (>30%) indicating the significant effect of wall impingement on both velocity and momentum. For the same case of L/D=1.0, increasing the counterbore diameter (d/D=1.85 to d/D=2.15) substantially reduces the velocity loss by as much as 90%; which indicates that for this case there was little wall impingement. For the highest L/D ratio (L/D=1.6) which produces the smallest spray angles, increasing the counter bore diameter resultes in an increased velocity drop for the droplets passing through the counterbore, indicating the adverse effect that the air entrained into the counterbore cavity has on the spray flow rate. Velocity drops observe for the case of L/D=1.3 are small but have a decreasing trend with the increased counterbore diameter; which indicate the possibility of slight wall impingement, but with a substantially smaller effect on velocity loss.

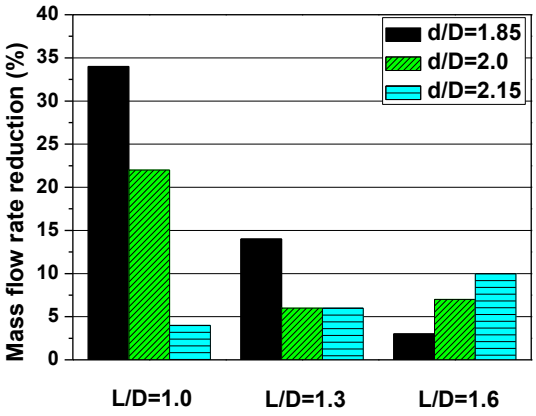

Figure 5.25 Velocity reduction from the inner hole exit A-A to the counterbore exit B-B

Effects of the counter bore diameter on the spray angle variation for different L/D ratios can be observed from Figure 5.17 For all cases of L/D ratios investigated, the spray angles are initially reduced when the counterbore diameter is increased (from d/D=1.85 to d/D=2.0) because of the spray velocity reduction caused by the entrained air and establishment of a torus shape recirculation zone, as shown in Figure 5.26.

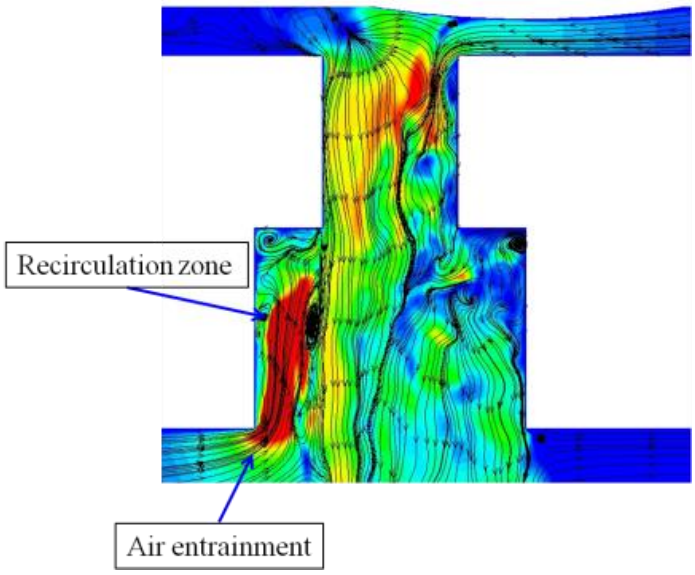

Figure 5.26 Schematic of air entrainment and recirculation zone in the counterbore

However, a further increase of the counterbore diameter (from d/D=2.0 to d/D=2.15) does not affect the spray angles which indicates that a larger counterbore does not increase the strength of the recirculation zone and its influence on the spray.

Another important spray parameter to consider when investigating the counterbore effects on spray is the breakup length, as shown in Figure 5.18. For all cases considered, breakup lengths increase with increases in counterbore diameter (d/D=1.85, 2.0 and 2.15). Increasing the counterbore diameter increases the amount of air entrained into the counterbore cavity resulting in liquid flow velocity reduction which is accompanied by weakening of the atomisation process. A weak atomisation process produced larger droplets and increased the volume ratio of ligaments to droplets. Many of these ligaments are interconnected and go through deformation and further breakup (secondary breakup) with an overall effect of increased breakup length.

Figures 5.27 to 5.30 provide the results for the comparison of droplet sizes for different counterbore diameters at different measuring planes. From Figure 5.27, an increased counterbore diameter produced very little effect on the droplet sizes at plane A-A which is expected since the counterbore diameter has a downstream effect on the exiting jet at plane A-A and upstream of this plane is mostly liquid (incompressible) whereas the flow downstream is mostly gaseous (compressible). Careful analysis of Figure 5.27 reveals that the increased counterbore diameter has a stronger effect on reducing the droplet size for L/D=1 than for the other two cases of L/D=1.3 and 1.6; this is due to the increased resistance caused by the increased air entrained into the counter bore.

At counterbore exit plane B-B, droplet sizes are decreased by increasing the counterbore diameter for L/D=1, as shown in Figure 5.28. This occurs because the short L/D ratio - the exiting liquid jet from the inner hole, is less developed and has a stronger three dimensional nature with a short breakup length, which makes it more vulnerable to the resistance caused by the increased entrained air. For L/D=1.3, the more developed the exiting jet became from the inner hole, makeing the liquid body in the counterbore cavity, the more resistancet it has to the entrained air and almost no changes in the droplet size diameter are observed with the increased counterbore diameter. On the other hand, droplet sizes for the larger L/D=1.6 with lower velocities (Figure 5.16) increase with the increasing counterbore diameter, because the increased entrained air further reduced the jet velocity and weakened the atomisation.

Droplet sizes at the two locations - plane C-C and D-D downstream of the B-B plane, are presented in Figures 5.29 and 5.30 respectively. Since plane C-C is only 0.20 mm away from the counterbore exit plane B-B, the droplet size variation pattern with the changing counterbore diameter is similar to plane B-B, except that droplet sizes are reduced due to further breakup. Downstream at the D-D plane, droplet sizes are further reduced. The cases with the largest droplet size at plane C-C have the greatest size reduction at plane D-D. The relative distance from D-D to the inner hole exit plane is more than 3 inner holes in diameter which makes ligament breakup (secondary breakup) a justifiable reason for the observed size reductions, as seen in Figure 5.11.

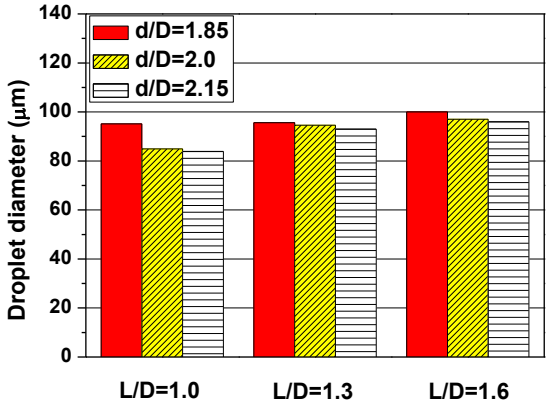

Figure 5.27 Comparison of droplet sizes at measuring plane A-A

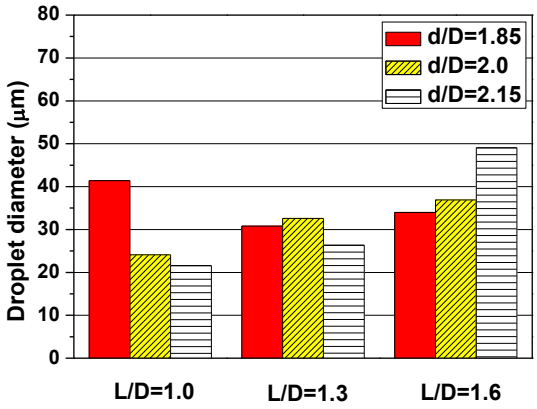

Figure 5.28 Comparison of droplet sizes at measuring plane B-B

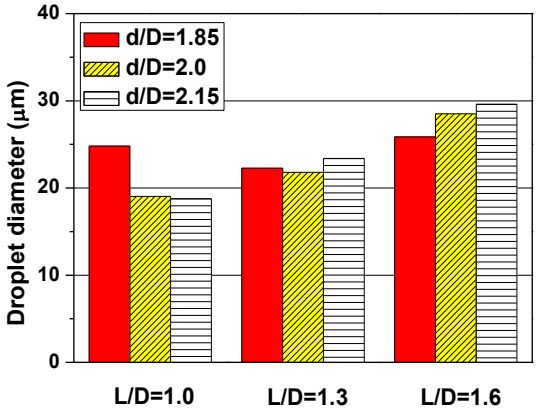

Figure 5.29 Comparison of droplet sizes at measuring plane C-C

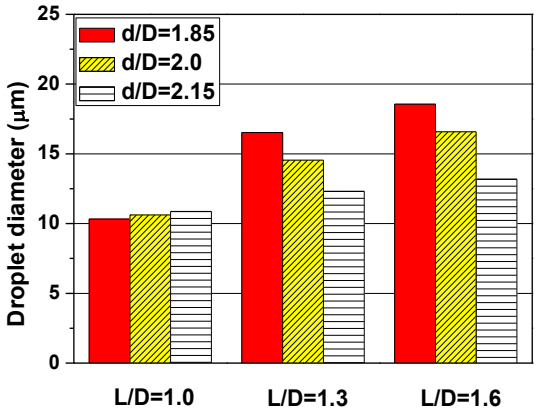

Figure 5.30 Comparison of droplet size at measuring plane D-D

5.7 Effects of Deposit Design

An expanding investigation on deposit formation in the GDI nozzle has been intensively studied due to the different fuel qualities around the world as well as fuel components. After a long time of the engine running, the deposit gradually accumulates inside the nozzle and affects the spray characteristics. In this section, the case studies of different deposit designs in the GDI nozzle are used to compare with PDPA data and high speed images. This comparison can provide more understanding about the deposit effects on the spray characteristics and the mechanism of deposition formation. The same GDI injector investigated for the mass flow rate, PDPA measurements and high speed imaging is split to gain clear visual access to the geometry of the deposit formation inside. Its cross section that includes the inner hole, counterbore and deposit formation is shown in Figure 5.31

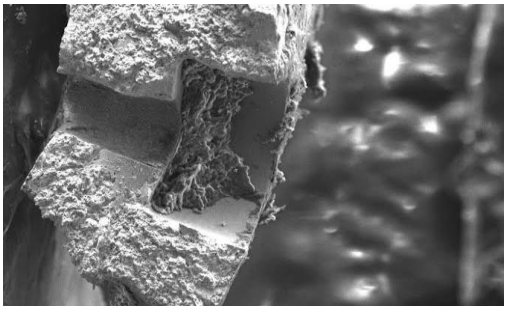

Figure 5.31 A cross section of the GDI injector with deposit formation

The splitting process of the injector could have damaged or broken off some of the deposit and the deposit's structure shown in Figure 5.31, it may not provide a complete view of the deposit formation inside an injector, but it shows that the deposit accumulated mostly on the counterbore surface. The actual dimensions of the deposit's structure grow and change with time as the injector is used. Based on visual observations of foul injectors, several deposit shapes are selected and they are shown in Figure 5.32. It is assumed that there is no deposit inside the inner hole and outside of the counterbore, and for the deposit structure to have either a cylindrical or half cylindrical shape covering the entire counterbore circumference or half of it, respectively, as provided in Figure 5.32.

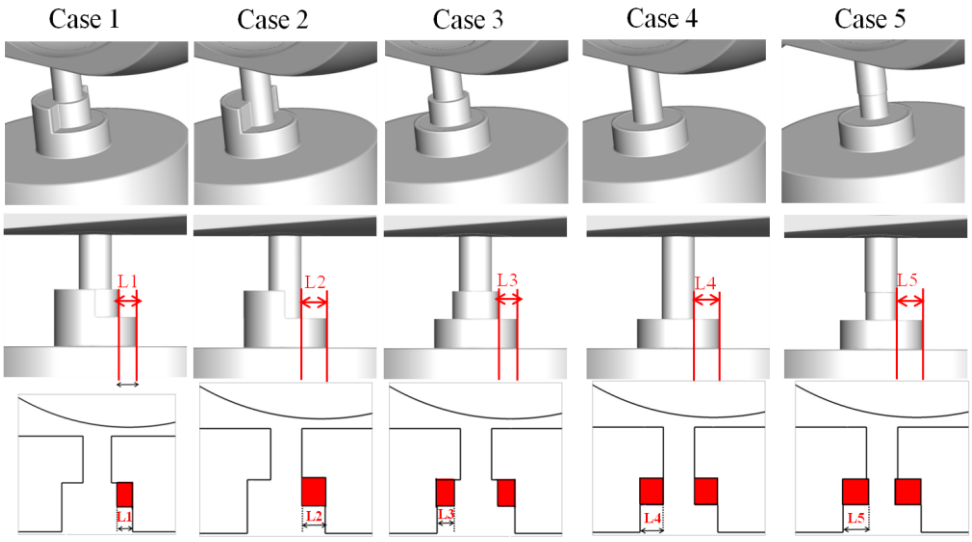

Figure 5.32 Description of deposit design

From the deposit image of Figure 5.31, it is observed that the deposit length is up to almost half way from the bottom of the counterbore to its outer rim. Thus, the deposit lengths for all cases are assumed to occupy half of the counterbore length. Five different shapes of deposit structures are investigated. Cases 1 and 2 have half of the cylindrical deposit structures with different thicknesses, 0.75L and L, as shown in Table 5.2. Cases 3 and 4 have full cylindrical deposit structures inside the counterbore with thicknesses of 0.75L and L, again in Table 5.2. Case 5 has a full cylindrical deposit with a thickness of 1.05L. For case 5, the deposit thickness is larger than L in order to study the possible effect of the deposit obscuring the flow passage. This comparison is examined by 150bar injection using iso-octane.

Table 5.2 Description of deposit thickness

	Case 1	Case 2	Case 3	Case4	Case 5
Thickness	L1=0.75L	L2=L	L1=0.75L	L4=L	L5=1.05L
	L=D-d, where D= radius of counter-bore and d=radius of inner hole				

Averaged mass flow rates for different deposit shapes, cases 1 to 5 and their comparison with the mass flow rate of a clean injector are presented in Figure 5.33.

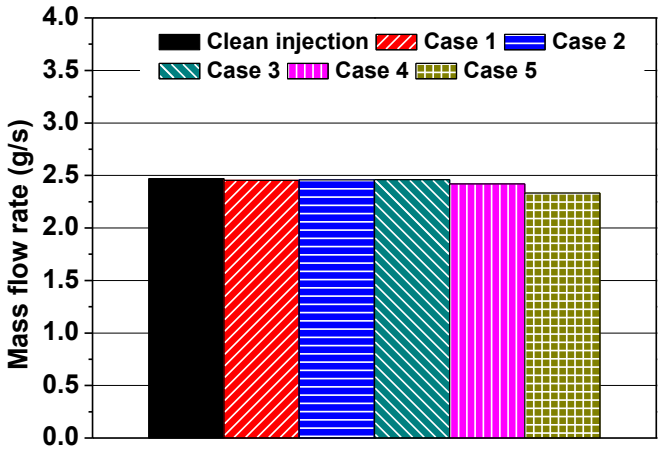

Figure 5.33 Comparison of calculated average mass flow rates for different deposit shapes

Cases 1 to 3 have almost the same mass flow rates as the clean injector with variations of less than 1%. These results indicate that for the injection pressure used, 150 bar, the counter bore geometry has little influence on the mass flow rate. For case 4, the deposit shape makes it an extension of the inner hole and is treated as an injector of the larger L/D ratio. Case 4 shows slightly more reduction of mass flow rate due to the higher friction from the longer inner hole wall. For case 5, the mass flow rate is decreased more than the other cases; by as much as 5.6% due to the inner hole's exit area being reduced by the deposit's structure.

Experimental mass flow rates are measured by using the same injector as in Table 5.3. When the injector is clean, its mass flow rate is measured for the injection pressure of 150 bar. The same injector is used in the engine test and after it is fouled, its mass flow rate is measured again. As a clean and fouled injector, it is examined by 1.5 and 1.65 ms pulse widths at 150 bar injection pressure and it shows only around 2% mass flow rate loss which can be attributed to measurement errors.

Table 5.3 Experimental mass flow rate for clean and fouled injector

150 bar injection pressure	Clean injector	Fouled injector	Flow rate loss
1.5ms	**10.2 gm**	**10.02 gm**	**2.04%**
1.65ms	**11.3 gm**	**11.12 gm**	**2.21%**

The extent to which the injector is fouled can be seen in Figure 5.31 which shows the cross section of one of its holes after it is fouled. Considering the injector's geometry and its dimension, it is not possible to split all its holes to verify the deposit formation structure inside hole. However, based on the observation of Figure 5.31, it is assumed that the inner hole has no deposit inside it and the deposit in the counterbore does not obscure the passage in the counterbore for the injection pressure used. It should be noted that it has been observed at

higher injection pressures and injection velocities, the counterbore's geometry plays a more significant role in determining the mass flow rates.

Figure 5.34 shows images captured by the high speed camera for the clean and fouled injector. From the experimental images, it can be seen that the spray angle of the fouled injectors becomes smaller. The spray angles calculated from the different cases simulated are presented in Figure 5.34 (c). Furthermore, the simulation results indicate that the five cases of fouled injectors have smaller spray angles. Spray angle reductions for the fouled injector cases can be justified by a detailed study of the flow field in the counterbore which is provided in the following discussion. In addition, the deposit structure in the counterbore can act as an obstacle in the path of the exiting jet from the inner hole and consequently divert the spray flow to a narrower region. For case 5, it has the smallest spray angle because a portion of the inner hole exit area is covered by the deposit and the exit hole area is decreased.

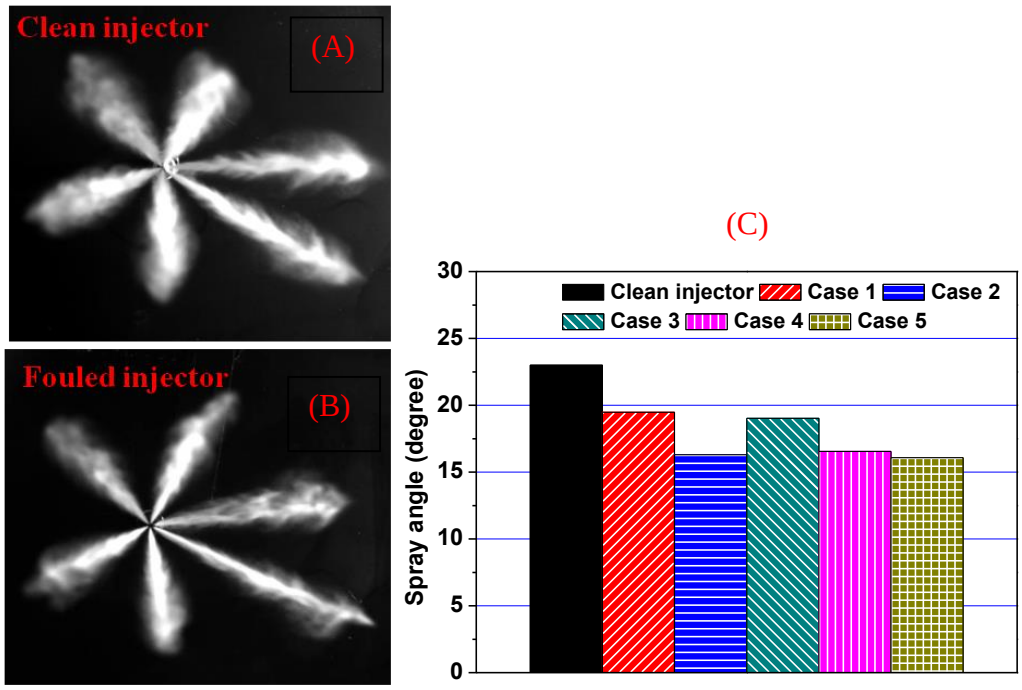

Figure 5.34 (A) Spray from the clean injector, (B) Spray from the same injector when fouled, (C) Spray angles calculated from simulation results

Spray penetration lengths are measured from the high-speed images, shown in Figure 5.35(a). The same injector, when fouled, has longer spray penetration lengths than when it is clean. The comparison of numerical simulation results between clean injectors and different deposit cases also shows similar trends for liquid breakup length, as shown in Figure 5.35(b). In cases 1 to 4, the liquid breakup length increases only slightly. In case 5, the liquid breakup length is significantly longer. These increases in the breakup length observed in the simulations are also due to the flow field structure inside the counterbore (see simulated flow field results given below)

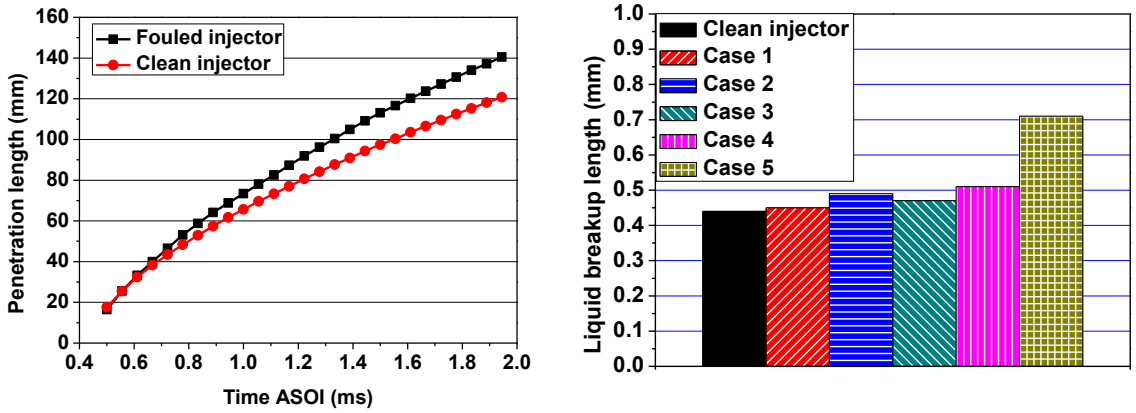

(a) (b)

Figure 5.35 (a) Experimental penetration length (b) Liquid breakup lengths calculated from simulation results

Spray droplet sizes at different distances from the injection plane were measured for both the clean and fouled GDI injectors by the PDPA system. Droplet sizes at each distance were averaged and are presented in Figure 5.36 (a). It was observed that on average, the SMD increased by as much as 16% when the injector was fouled. To compare the trend with the simulation results, averaged droplet sizes for the clean injector and the five cases investigated were calculated at different distances from the injection plane as presented in Figure 5.36.(b). The simulation results produced the same trend in which the fouled injectors of the five cases had higher averaged droplet sizes than the clean injector. All cases had the greatest effect on

the averaged droplet size at plane B-B and least at plane C-C. Since plane B-B is located at the counterbore's exit plane, it is exposed to both entrained air flow from its downstream and recirculation flow at its upstream. Case 5 resulted in the highest increases of average droplet sizes which can be attributed to the reduction of mass flow rate by the deposit structure obscuring the inner hole.

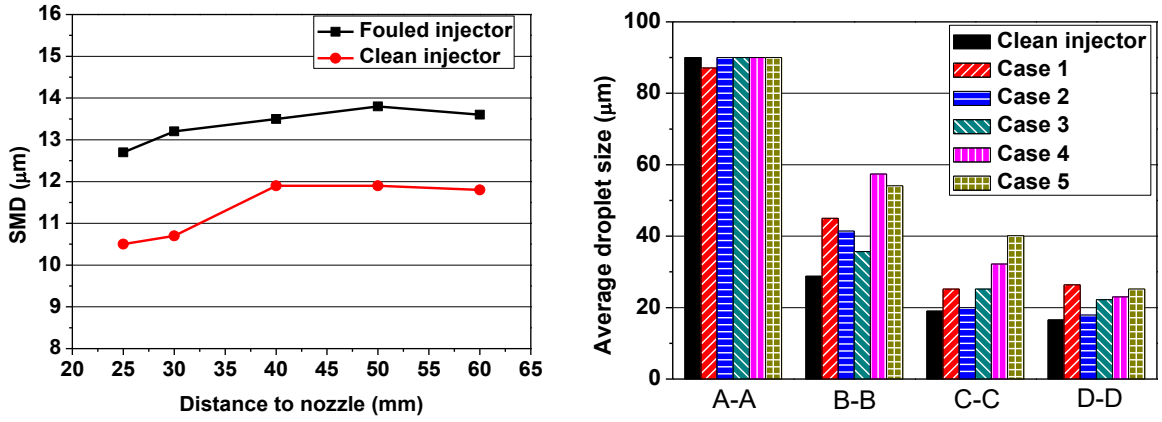

(a) (b)

Figure 5.36 (a) Experimental SMD of the clean and fouled injector (b) Averaged droplet size calculated from simulation results

According to these results, it can be summarized that the deposit in the counterbore does not change mass flow rate if the deposit's thickness does not cover the nozzle hole. However, deposits inside the counterbore affect the spray characteristics.

The results of the five case studies are presented in Figure 5.37. The streamlines at 30 μs for cases 1 to 5 are presented in Figure 5.38. It is observed that the flow entrance into the inner hole is extremely turbulent in three dimensions and is asymmetrical, affected by the needle geometry. The inner hole flow has strong vortex structures pushing to the right side of the flow due to the strength of the left hand side flow in the inner hole. The three dimensional flow of

the inner hole emerges into the counterbore to form a non-axisymmetric spray which expands and exits the counterbore at plane B–B.

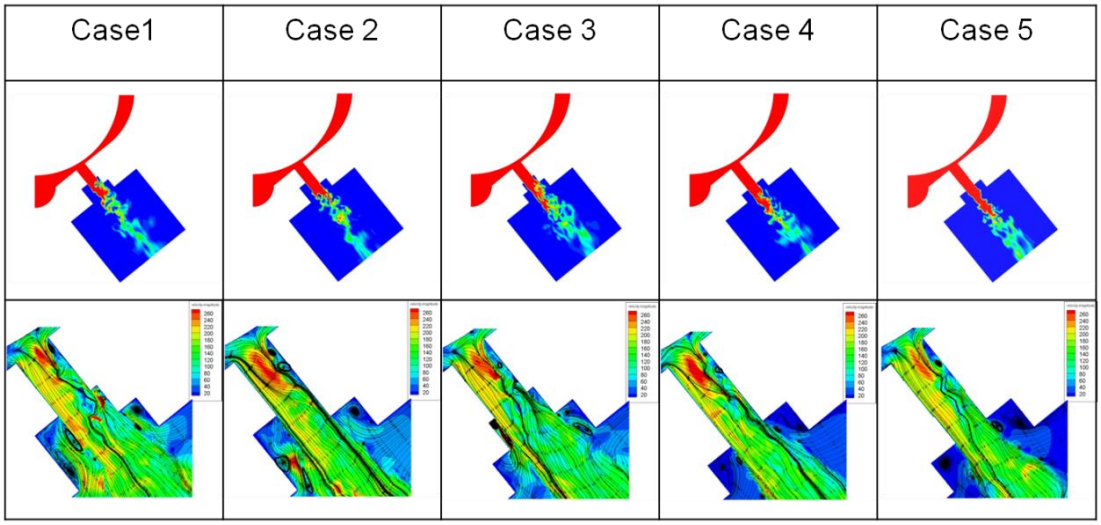

Figure 5.37 Distribution of VOF and streamline at 30 μs

For the cases in which sufficient space is available around the liquid jet flow inside the counterbore, recirculation flow zones are observed which surround the liquid jet flow, and air is entrained into the counterbore from downstream and is fed into the recirculation zones. The recirculation zones are stronger when larger cavities are available in the counterbore. The flow of strong recirculation entangled with the liquid jet inside the counter-boar can lead to increased spray angles, reducing breakup lengths and droplet sizes. The smallest amounts of entrained air and recirculation are observed for case 5, followed by case 4.

Simulation results for the liquid jet flow for the five cases are presented in Figure 5.38. Impingement of the spray with the deposit structure as a boundary can interfere with spray expansion patterns. In cases 1 and 3, the liquid spray angle is limited by the deposit on the right hand side of the counterbore. For cases 2 and 4, the deposit thickness is such that it can be

treated as an extension to the inner hole; this caused the velocity development to become more stable inside the nozzle with less turbulent disturbances and resulting in a smaller spray angle. Therefore, the deposit's structure shape and size can influence the spray characteristics.

5.8 Summary

This chapter examines the effects of different nozzle geometries on spray characteristics in the nozzle flow and near flow by using numerical methods. The detailed variations of nozzle flow at different needle lift positions show its effects on mass flow rate change and the location of the recirculation zone. The effects from changing the r/D and L/D ratio in nozzle geometry also indicate the changes between nozzle exit velocity, turbulent kinetic energy and spray characteristics. The case studies with different deposit thickness and design provide the information for the deposit influences on spray characteristics. According to this information, some key findings which have added value and importance for future applications of injector flow simulation and its geometrical design are:

- Increasing the r/D ratio can increase the nozzle exit velocity and improve the recirculation inside the nozzle. However, due to the decrease of turbulent kinetic energy, the spray atomisation is slowed down. Moreover, the existence of cavitation inside the nozzle can have different results on the nozzle exit velocity.

- The L/D ratio variation of the inner hole had more significant influences on the spray characteristics than the counterbore's diameter variation. Reducing the L/D ratio effectively increases the mass flow rate, velocity, spray angle and reduces the droplet size and breakup length. The increased spray angle results in wall impingements inside the counterbore's cavity, particularly for L/D=1 which can potentially lead to increased injector deposit build up.

- Increasing the counterbore's diameter has an overall adverse effect on the spray characteristics exiting the counterbore and further downstream from it. Flow rates and spray angles are decreased and droplet sizes are increased with increased counterbore diameters for any given L/D ratio. However, the positive recirculation inside the counterbores with small diameters improves the mass flow from the inner hole. A summary of the influence of different design parameters used in the sensitivity study are shown in Table 5.5.

Table 5.4 Summary of the influence of different L/D ratios and CB diameters

	L/D increase	CB increase
Mass flow rate	↓	↓
Exit velocity	↓	Similar
Breakup length	↑	↑
Spray angle	↓	Similar
Droplet size	↑	Discuss

- The deposit inside the counterbore directly affects the spray characteristics due to the effects of the flow field in the counterbore area. However, although the spray characteristics are affected by the deposit, less influences are shown on mass flow rate (>1%). The mass flow rate will be changed when the deposit thickness covers the inner hole

Chapter 6

Numerical comparison of spray models

In this chapter, two different spray models with different primary and secondary breakup models are compared with the experimental results. Moreover, the spray characteristics such as the mass flow rate, turbulent kinetic energy and dissipation rate of different nozzle's geometrical design discussed in the last chapter are used to combine with the spray model to investigate its reliability.

6.1 Introduction

The atomisation of spray is an extremely important process which directly influences further combustion efficiency and exhaust emission. Therefore, it is necessary to investigate the development of spray atomisation. Recently, experimental methods such as the PDPA system and the use of a high speed camera can provide an insight into the spray's characteristics such as: the droplet velocity, mean droplet size and the distribution of SMD in the secondary breakup regime. Therefore, according to these experimental data, several spray breakup models with different breakup theories can be validated with the experimental data to provide more detailed information into spray atomisation which cannot be obtained from the experiment.

The spray breakup can be divided into a primary and secondary breakup regime. In these two different breakup regimes, their breakup mechanisms are not the same. For example, the primary breakup regime can be affected by the aerodynamic force, cavitation effects and the

nozzle's geometric designs. However, in the regime of secondary breakup, the only factor which affects spray's characteristics is the aerodynamic force. Therefore, in the numerical calculation, these two different regimes respectively use different models to simulate the spray's atomisation.

In this section, the KH-ACT is compared with its original calculation of turbulent effects and the coupling model with nozzle flow simulation by using the Lagrangian model (from last chapter). Following this, the MPI primary breakup model is compared with the above models in the experimental data.

6.2 Kelvin-Helmholtz-Aerodynamics-Cavitation-Turbulence (KH-ACT) Model

The detailed breakup mechanism of the KH-ACT model can be illustrated as in Figure 6.1. The criterion to define the regime of primary breakup and secondary breakup uses the liquid jet breakup length. When the breakup process takes place in the primary breakup regime, the KH-ACT model will be applied to simulate the breakup process. When the droplet detaches from the liquid jet body and it is still in the primary breakup regime, its breakup process will be simulated by the KH model. When droplets are in the secondary breakup regime, all the droplets breakup behaviour will be simulated by the KH-RT model. The detailed computing process of the KH-ACT model is presented in Figure 6.2.

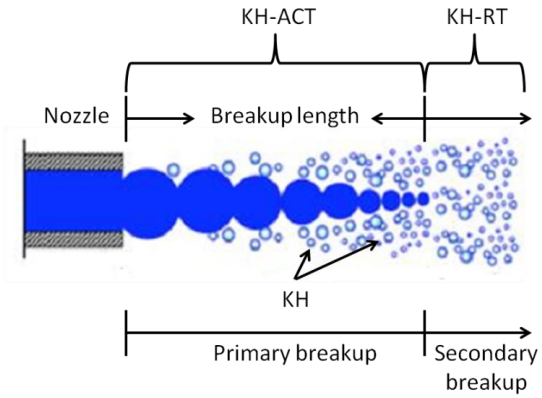

Figure 6.1 Schematic illustration of KH-ACT model

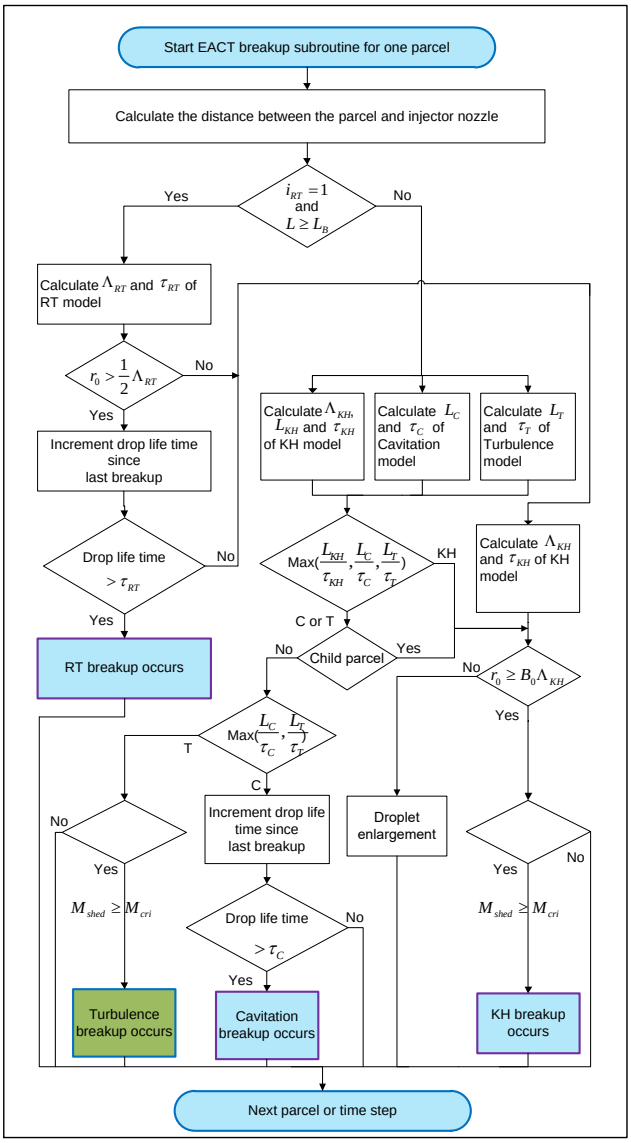

Figure 6.2 Flow chart of KH-ACT model

6.3 Testing Cases and Conditions

In this chapter, the comparison of different breakup models is investigated. Several breakup models are examined for their spray characteristics such as spray penetration length, droplet mean size, droplet velocity and SMD with the data from the optical experiment. The breakup models which are used in this comparison are as below:

- KH-RT
- KH-ACT-RT
- KH-ACT-RT+ Nozzle flow simulation
- KH-ACT-CAB
- MPI-CAB

From the above breakup models, the KH-ACT-RT is compared with the original KH-RT to observe the difference when the effects of cavitation and turbulence are considered. Due to the lack of calculation of the turbulent effects, in the original KH-ACT model, its calculations of turbulent kinetic energy and dissipation rate are provided according to Bianchi (Bianchi and Pelloni 1999) as below:

$$K_0 = \frac{U_{inj}^2}{8\left(L/D\right)}\left(\frac{1}{C_d^2} - K_c - (1-S^2)\right) \qquad \text{(Equation 6.1)}$$

$$\varepsilon_0 = K_\varepsilon \frac{U_{inj}^3}{2L}\left(\frac{1}{C_d^2} - K_c - (1-S^2)\right) \qquad \text{(Equation 6.2)}$$

where $K_\varepsilon = 0.27$, $K_C = 0.45$, $S = 0.01$, L is the nozzle length and D presents the hole diameter. However, from the above Equation 6.11 and 6.12, it can be observed that the calculation of kinetic energy and dissipation rate does not consider the influences from the nozzle's geometrical design such as the r/D ratio and the existence of the counterbore. Therefore, the original KH-ACT model is compared with the KH-ACT model combined with nozzle flow simulation in this chapter. The initial conditions such as mass flow rate, average kinetic energy and dissipation rate and initial droplet size are provided by the GDI nozzle flow simulation to be used as input parameters for the KH-ACT model which is shown in the flow chart in Figure 6.3.

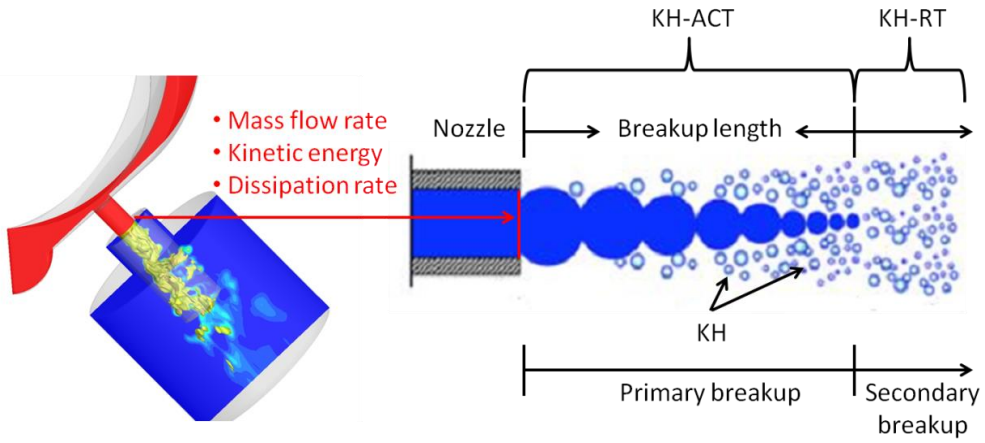

Figure 6.3 Schematic illustration of KH-ACT model coupled with GDI nozzle simulation

Lastly, another breakup model, the MPI-CAB, is compared with the original KH-ACT-RT and the KH-ACT-RT model coupled with GDI nozzle flow simulation by using an optical method to examine their simulation results.

The optical methods used in this study involve using a PDPA system and a high speed camera to observe spray characteristics. The test conditions for this experiment are shown in Table 6.1. The testing injector uses a Bosch GDI injector and is examined by the injection pressure 150bar with a pulse time of 1.0 ms and 1 bar ambient pressure. The test fuel uses iso-octane its fuel properties are similar to those of gasoline and it is widely used in numerical studies to replace gasoline.

Table 6.1 Testing conditions for the optical experiment

	Test Conditions
Test Fuel	Iso-octane
Injection Pressure	150 bar
Ambient Pressure	1bar
Ambient Temperature	293 K
Fuel Temperature	300K

6.4 Comparison of the KHRT Model and the KH-ACT Model

As mentioned above, the KHRT hybrid model has been widely used for the spray breakup simulations. However, the breakup mechanism of the KH model does not consider the cavitation and turbulent effects from the nozzle in the primary breakup regime. In this section, the original KH-ACT-RT model which includes the breakup mechanism of cavitation and turbulence is used to evaluate with the KH-ACT model in order to compare the different breakup theories on the spray characteristics. Spray penetration is one of the important spray characteristics and directly affect the following mixture distribution in the cylinder. The comparison of spray penetration length at 150 bar injection pressure for the KH-RT model and the original KH-ACT-RT model with the experimental data from the high speed images is shown in Figure 6.4.

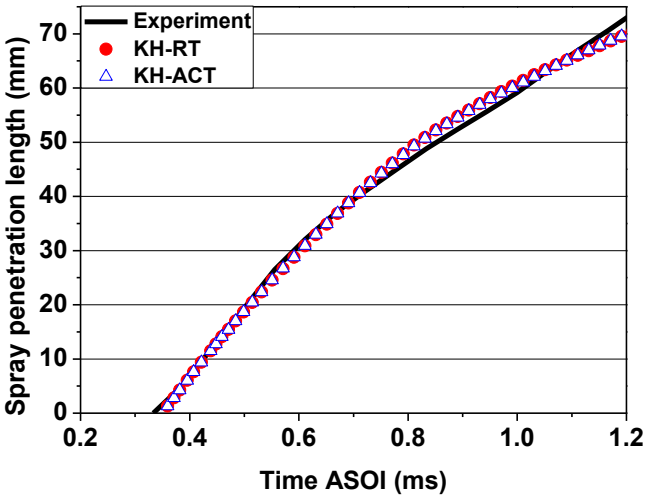

Figure 6.4 Comparison of penetration length for the KH-RT and the original KH-ACT-RT model

The comparison shows that the penetration results from the KH-RT and the original KH-ACT-RT model all have good agreement with the experimental penetration length. The difference between the KH-RT and the original KH-ACT-RT model is small, however, the penetration length of the KH-RT model is slightly longer than that of the original KH-ACT-RT model. This is due to the droplet size of the KH-RT model which showing a larger SMD value than the original KH-ACT-RT model, as seen in Figure 6.5.

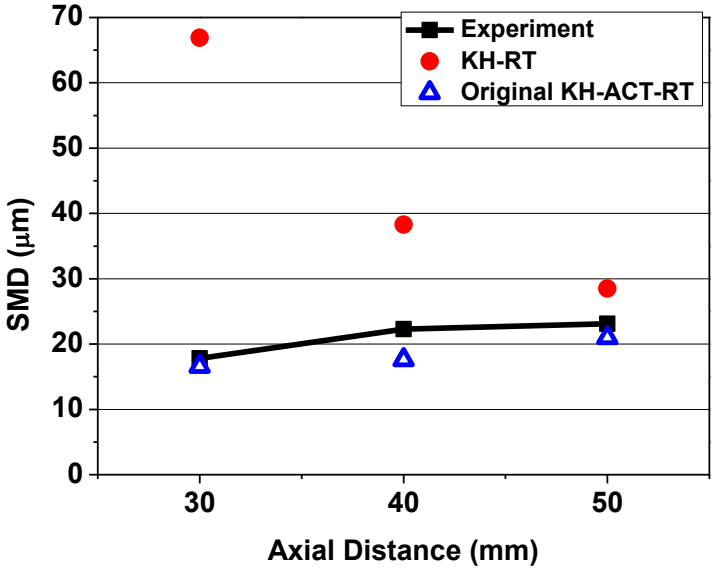

Figure 6.5 Comparison of SMD for different breakup models

The validation range of the experimental data from the PDPA system is recommended after 30 mm from the nozzle hole. This is due to the fact that the high density of the droplet number before 30mm can result in a measuring error. From the SMD results from the PDPA system, the SMD gradually increases from the measuring point at 30 mm to 50 mm because of the smaller droplets which evaporate and the existence of the larger droplets. From the comparison of the SMD, it can be observed that the KH model predicted a high SMD value at different measuring points. This can explain how the incomplete breakup mechanism of the KH model causes a smoother process of droplet breakup in the primary breakup regime. For the results of the KH-ACT-RT model, the extra two breakup mechanisms of cavitation and turbulence accelerated the speed of the droplet breakup and then presented a smaller SMD value than the KH-RT model and a better agreement with the experiment. Moreover, when comparing the droplet mean diameter (D10) for the KH-RT model and the original KH-ACT-RT model (Figure 6.6), the mean diameter of the original KH-ACT-RT model presents an extremely low value which can not compare with the experimental data. This is due to the KH-ACT model producing many small droplets which affected the calculation of the droplet mean diameter.

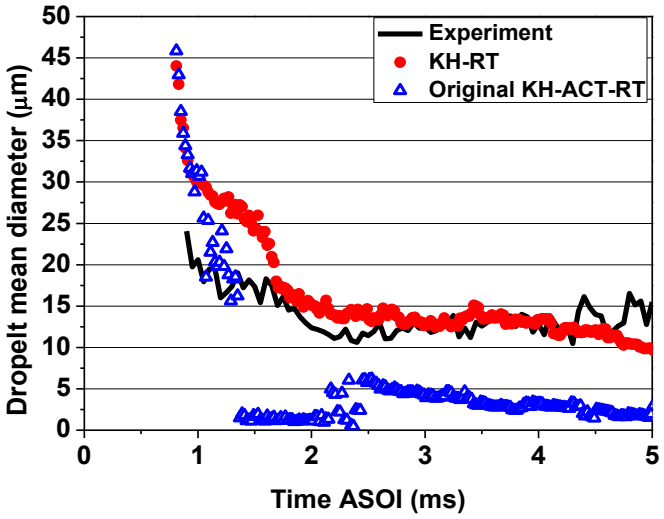

Figure 6.6 Comparison of droplet mean diameter for different breakup models

On comparing the droplet average velocity at a measuring plane of 50 mm from the nozzle hole, the droplet average velocity of the KH-RT and the KH-ACT-RT models is similar and has a strong agreement with the experimental data as shown in Figure 6.7. From the above comparison of spray penetration length, droplet size and velocity, it can be observed that the different breakup mechanisms of the breakup model strongly affect droplet size distribution and have less influence on spray penetration and droplet velocity.

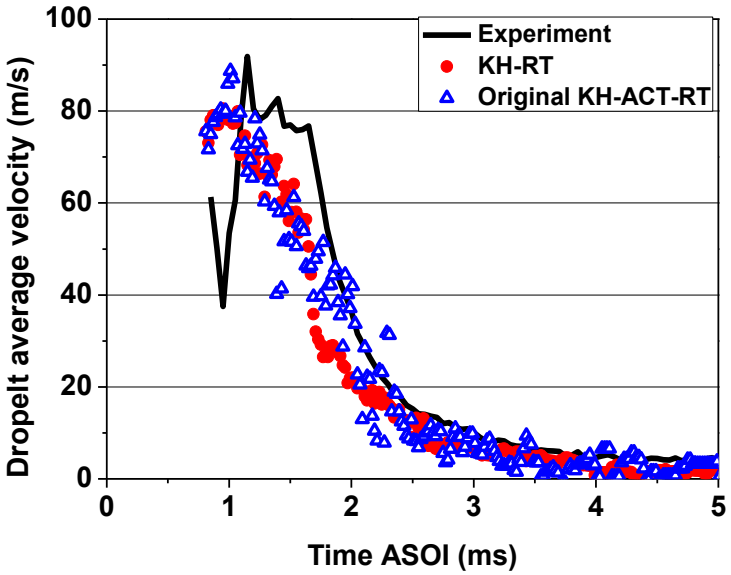

Figure 6.7 Comparison of droplet average velocity for different breakup models

To analyze the breakup mechanism during spray breakup, one counter code is written into the KIVA program, which records the time utilized by different breakup mechanisms. This analysis shows which mechanism (aerodynamic force, cavitation effect or turbulent effect) will majorly dominate droplet breakup. Breakup numbers for all mechanisms of the KH-RT and original KH-ACT-RT models are shown in Figure 6.8. For the KH-RT model, the KH model initially leads the breakup before 0.3 ms and then switches to the RT model. For the original KH-ACT-RT model, the aerodynamic force does not exhibit the dominant role, as with the KH-RT model. During original KH-ACT breakup, it can be observed that spray breakup caused

by turbulence is more significant than the other two mechanisms. Moreover, the breakup mechanism of cavitation does not join this breakup process. Figure 6.9 shows the total breakup number for these two models. It can be seen that the total breakup number of the KH-RT model is higher than the original KH-ACT-RT model. This can illustrate why the droplet mean diameter was very small due to the great number of small droplets. Intensive spray breakup of the original KH-ACT-RT model results in the parent droplet breaking up into several small child droplets quickly and decreases the total breakup number. Moreover, the difference between the KH-RT and the original KH-ACT-RT model in the total breakup number is the turbulent breakup mechanism in the original KH-ACT model happened earlier than the KH effects in the KH model, as in Figure 6.9.

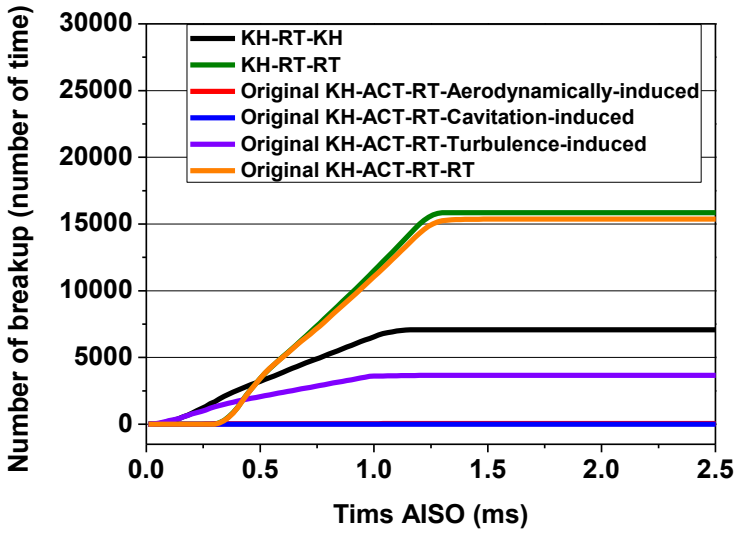

Figure 6.8 Breakup statistical analysis for different breakup models

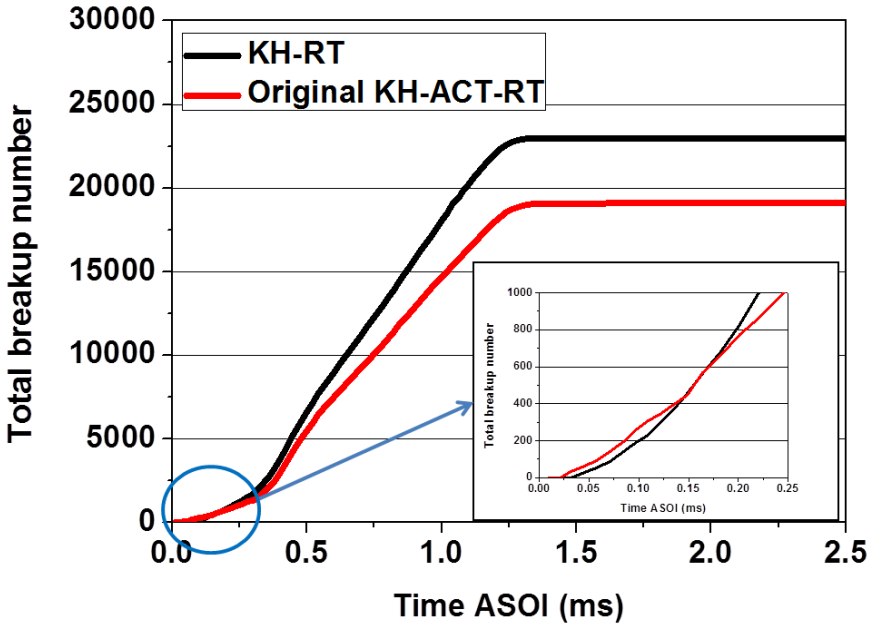

Figure 6.9 Breakup statistical analysis for different breakup models

6.5 KH-ACT with and without Nozzle Simulation

The turbulence calculation of the original KH-ACT model used in Equations 6.1 and 6.12 was proposed by Bianchi (Bianchi and Pelloni 1999) to provide the initial turbulent kinetic energy and dissipation rate to be used as an initial parameter for the KH-ACT model. However, in Equations 6.1 and 6.2, they only consider the L/D ratio of the nozzle. In this section, the detail of the nozzle flow simulation in the GDI nozzle includes the effects of L/D, r/D and counter-bore design and provides detail on the initial conditions such as the initial droplet size, mass flow rate and turbulent kinetic energy and dissipation rate to the KH-ACT model (Figure6.3).

To compare the difference between the calculation of turbulent kinetic energy and dissipation rate, Figure 6.10 shows the average value from the Bianchi equations and GDI nozzle flow simulation. It can be observed that the turbulent kinetic energy and dissipation rate from the GDI nozzle simulation all show a higher value than the Bianchi equations.

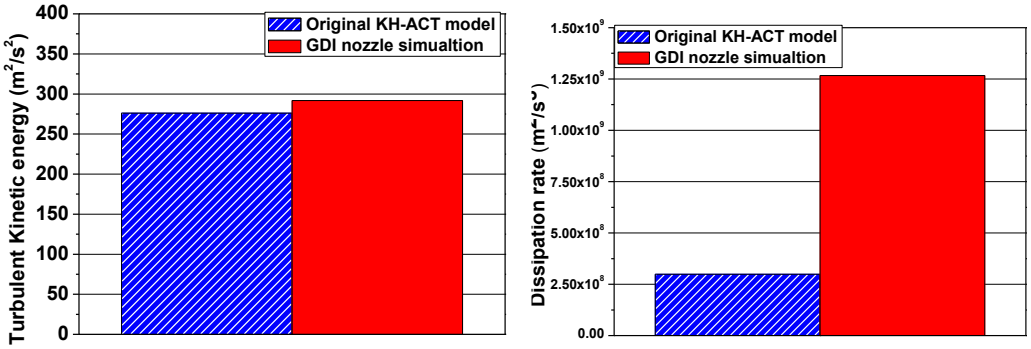

(a) Turbulent kinetic energy (b) Dissipation rate

Figure 6.10 Comparison of (a) Turbulent kinetic energy and (b) Dissipation rate

This significant difference is mainly caused by the sharp nozzle inlet corner which is shown in Figure 6.11. From the results of the previous chapter, it is indicated that the nozzle inlet corner increases the disturbances due to the sudden direction change in the nozzle flow. These disturbances in the fluid may accelerate the droplet breakup downstream. However, the equations proposed by Bianchi did not consider the disturbances from the nozzle inlet corner.

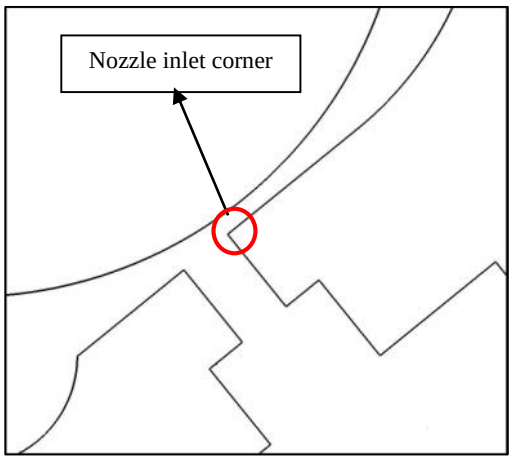

Figure 6.11 Schematic illustration of the nozzle inlet corner

In the comparison of spray penetration, both of the models show an agreement with the experimental data which is calculated from the high speed images, as in Figure 6.12. The spray penetration length of the KH-ACT-RT with nozzle simulation model is shown to be slightly longer than the original KH-ACT-RT model after After Start of Injection (ASOI) at 0.7ms. However, the overall value of these two models was similar.

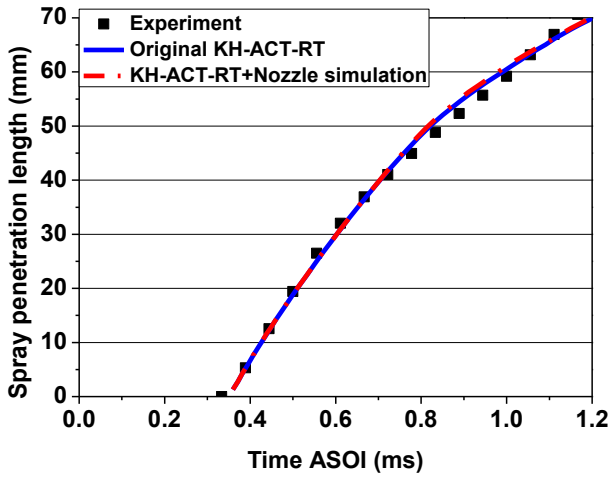

Figure 6.12 Comparison of spray penetration length

From the analysis of each breakup mechanism number (Figure 6.13), it can be seen that the number of the total breakup number for the KH-ACT model with nozzle simulation is increased by 13%. This is due to the higher turbulent dissipation rate from the GDI simulation, which causes the breakup speed in the primary regime to slow down although it has a higher turbulent kinetic energy. Moreover, it can be found that the turbulent breakup number of the KH-ACT model with nozzle simulation is decreased by 23% and this then resulted in the increase of aerodynamic breakup number. This appears more reasonable compared to the original KH-ACT model. Moreover, the cavitation breakup mechanism does not join this spray breakup process.

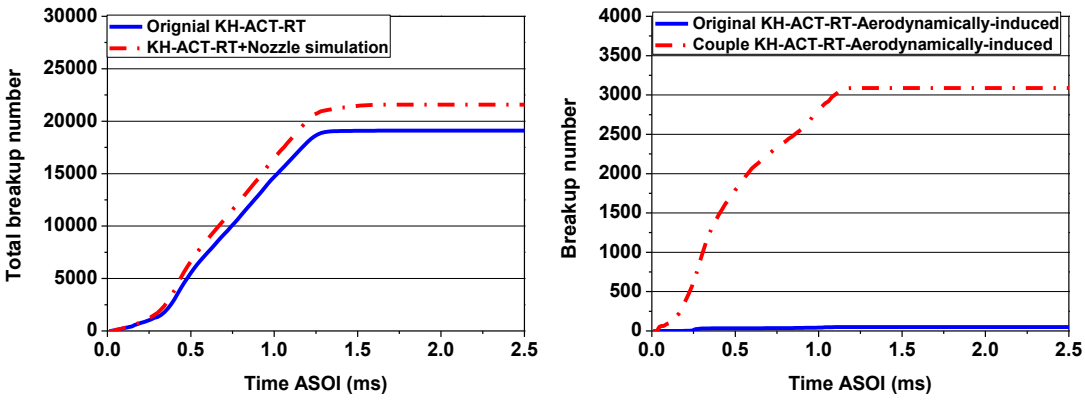

(a) Total breakup number (b) Aerodynamica breakup

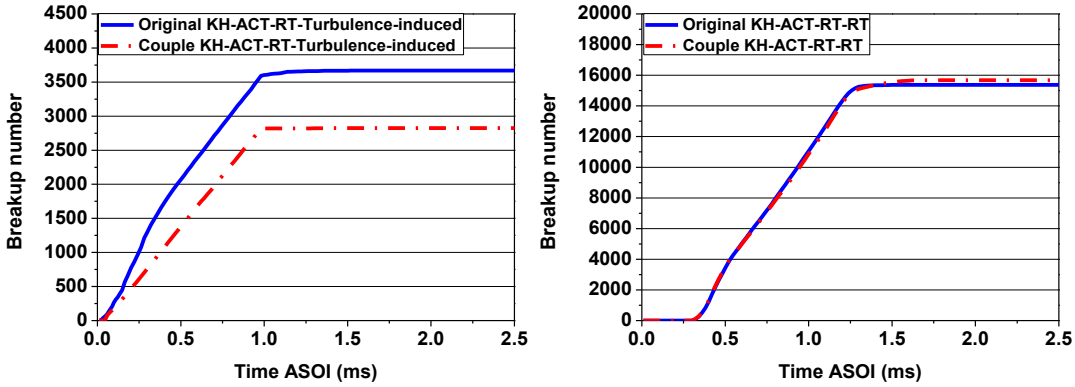

(c) Turbulent breakup (d) RT breakup

Figure 6.13 Analysis of the breakup mechanism

The comparison of the SMD distribution also shows the difference between these two models which is shown in Figure 6.14. The SMD distributions of the KH-ACT-RT model with nozzle simulation show a lower value than the original KH-ACT-RT model. This is due to the low breakup speed of the droplets in the primary breakup regime which cause more intensive droplet breakup processes such as the KH and RT effects during the secondary breakup regime.

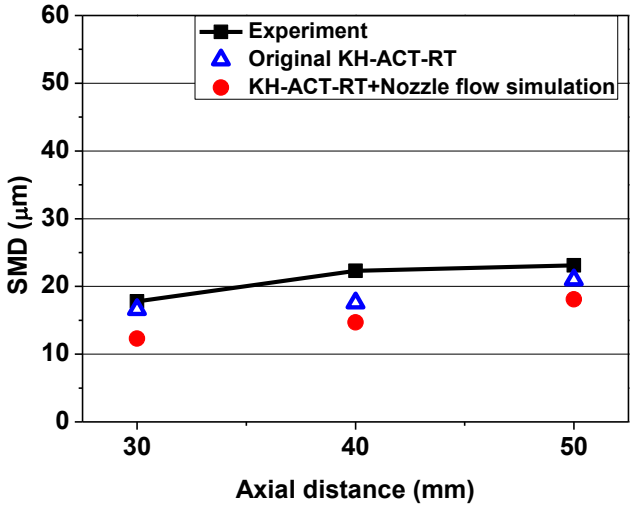

Figure 6.14 Comparison of SMD at different measuring planes

From the comparison of the droplet mean diameter D10 at a measuring plane 50 mm from the nozzle hole, as in Figure 6.15, it can be seen that the droplet mean diameter of the KH-ACT-RT model with the nozzle simulation significantly increases. This is due to the decreased number of the small child droplets from the KH-ACT-RT model with nozzle simulation. From a comparison of these two models, it is indicated that the turbulent breakup mechanism causes a more intensive breakup process or higher breakup speed compared with other two breakup mechanisms and also causes a generation of small child droplets.

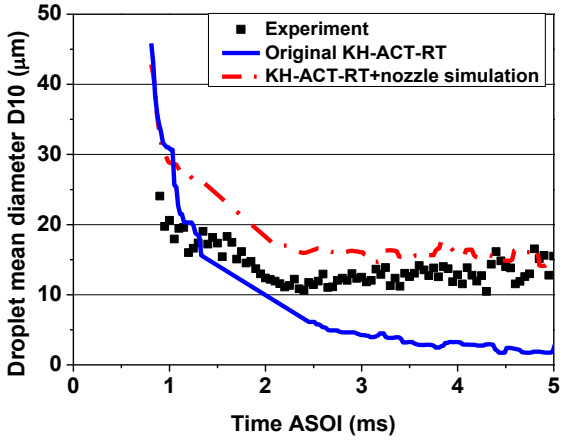

Figure 6.15 Comparison of droplet average velocity at 50mm from the nozzle hole

Figure 6.16 shows the comparison of average droplet velocity for each breakup model at 30, 40 and 50 mm respectively from the nozzle hole. It can be observed that the droplet average velocity at 30 and 40 mm is higher than the original KH-ACT model because of the larger droplet mean size in Figure 6.15 and also the lower amount of small droplets generated from the KH-ACT model with nozzle simulation which results in the increase of the droplet average velocity in the velocity calculation. At 50 mm, the droplet average velocity of these two models becomes similar and has a strong agreement with the experiment; this is due to the most of the droplet breakup processes having been completed at this distance and droplet behaviour is dominated by the drag force from the ambient density. This can also explain why the SMD at 50 mm from the nozzle hole for these two breakup models is closed which is shown in Figure 6.14.

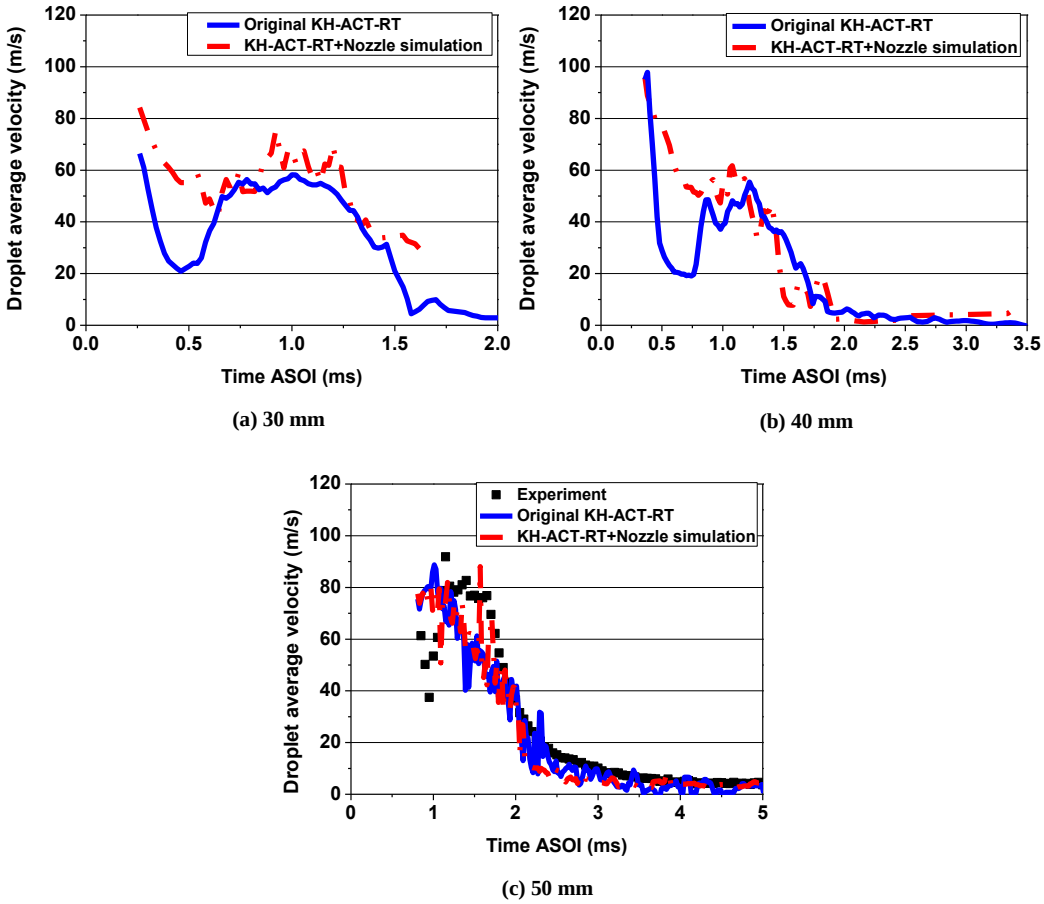

Figure 6.16 Comparison of droplet average velocity at 50mm from nozzle hole

6.6 Spray Modelling with Nozzle Flow Simulation at Different Nozzle Designs

In this section, the KH-ACT-RT model was compared with the MPI-CAB model for different GDI nozzle designs. In Chapter 5, the different nozzle geometrical designs such as nozzle L/D and r/D ratio were investigated for their spray characteristics and nozzle exit conditions in the primary regime. It indicated that the nozzle geometrical design can directly affect its mass flow rate, exit velocity and initial droplet distributions and these parameters directly affect the development of the spray.

The KH-ACT model combined with the GDI nozzle simulation has shown better and more reasonable results in the breakup mechanism analysis than the original KH-ACT model. In order to include the effects from the nozzle designs, the nozzle exit parameters from more detailed nozzle design simulations are combined with the KH-ACT-RT model and compared with the MPI-CAB model. In the MPI model, its phenomenological nozzle flow model provides the initial nozzle conditions at the nozzle exit such as droplet initial size and velocity distribution for the breakup model. This model considers the variations of cavitation effects and nozzle flow field from different nozzle L/D and r/D ratios.

From Chapter 5, the GDI nozzle simulations show the mass flow rate, turbulent kinetic energy and dissipation rate for different r/D ratios nozzles with L/D =1.66 which is shown in Table 6.2. It can be found that a bigger r/D ratio increases the mass flow rate and also decreases turbulent kinetic energy and dissipation rate. This is due to fewer disturbances from the smooth nozzle inlet corner.

Table 6.2 Comparison of nozzle exit conditions from different r/D ratios

L/D=1.66	Mass flow rate	Kinetic energy	Dissipation rate
r/D=0.0	2.47 (g/s)	291.84 (m^2/s^2)	$1.266*10^9$ (m^2/s^3)
r/D=0.05	2.80 (g/s)	246.36 (m^2/s^2)	$1.039*10^9$ (m^2/s^3)
r/D=0.1	2.96 (g/s)	208.25 (m^2/s^2)	$8.495*10^8$ (m^2/s^3)

Furthermore, the discussion of different L/D ratios is presented in the previous chapter and it pointed out the importance of the nozzle L/D ratio as a factor to influence the cavitation formation and spray characteristics. In this section, two different real sized GDI injectors with different L/D ratios which are widely used in the GDI injection system are investigated. Figure 6.17 shows their nozzle's geometrical parameters. It can be observed that the two different GDI nozzles have the same diameter for the inner hole and counter-bore, but with different L/D ratios for the internal nozzle (1.11 and 1.66) and counter-bore (0.89 and 0.69). In Table 6.3, it shows the comparison of the mass flow rate, turbulent kinetic energy and dissipation rate for the GDI nozzles A and B. The mass flow rate between GDI nozzle A and B is similar; however, its turbulent kinetic energy and dissipation rate show obvious differences because the shorter nozzle length (L/D=1.11) cannot provide enough nozzle length for the three dimensional flows to fully develop to a one dimensional flow in the nozzle. This results in a higher liquid turbulent level.

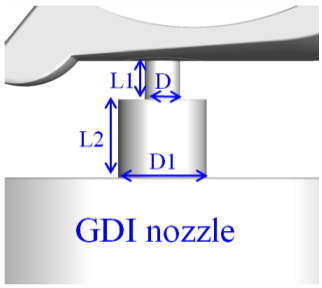

	Nozzle diameter	Counter-bore diameter	L1/D ratio	L2/D1 ratio
GDI nozzle A	D	D1	1.11	0.89
GDI nozzle B	D	D1	1.66	0.69

Figure 6.17 Schematic distribution of nozzle geometrical parameters

Table 6.3 Comparison of nozzle exit conditions from different L/D ratios

r/D=0.0	Mass flow rate	Kinetic energy	Dissipation rate
L/D=1.11	2.49 (g/s)	323.83 (m^2/s^2)	$1.707*10^9$ (m^2/s^3)
L/D=1.66	2.47 (g/s)	291.84 (m^2/s^2)	$1.266*10^9$ (m^2/s^3)

The analysis of the nozzle exit parameters from different r/D ratios and L/D ratios is used as the initial conditions for the KH-ACT and MPI models to further predict the droplet behaviour. The following sections introduce the effects of nozzle geometric design on the calculation of the KH-ACT-RT and MPI-CAB models in order to compare the advantages and drawbacks.

6.6.1 r/D ratio comparison

The effects of different r/D ratios at the nozzle inlet have been observed to be the obvious differences in the spray characteristics in the primary breakup regime and nozzle exit conditions by using the Eulerian approach in previous chapter. Thus, more detailed investigations of the effects of the r/D ratio on spray characteristics are studied by the Lagrangian approach.

The two different spray models, the KH-ACT-RT and MPI-CAB model, are examined by combining the nozzle exit parameters from Table 6.1 in their own phenomenon model. Figure 6.18 shows the comparison of spray penetration length in (a) the KH-ACT-RT and (b) MPI-CAB model.

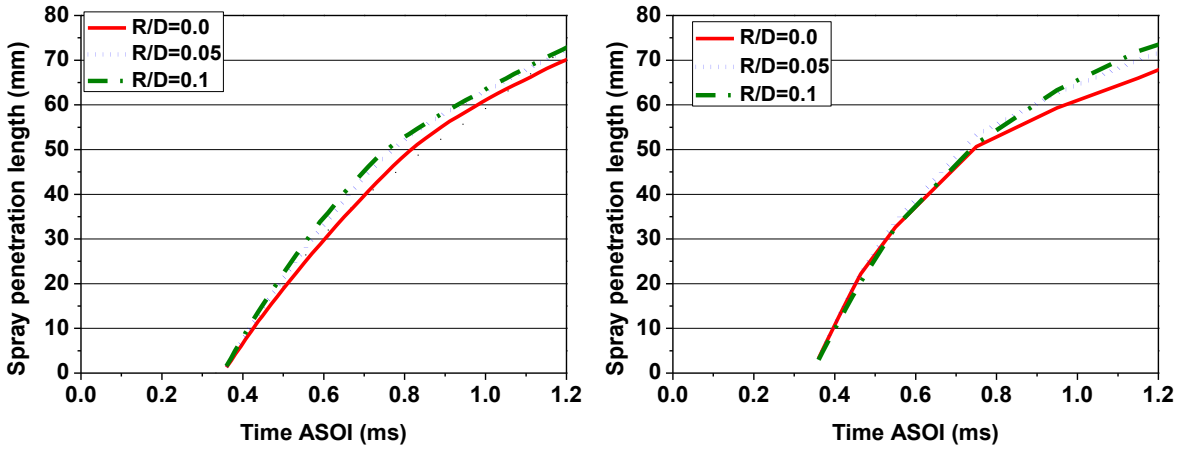

(a) KH-ACT-RT model (b) MPI-CAB model

Figure 6.18 Effects of r/D ratio on spray penetration by using KH-ACT-RT and MPI-CAB model

The overall trend of spray penetration length from these two spray models shows that the longer penetration length takes place when the r/D ratio increases because the nozzle exit velocity increased by 20% from r/D=0.0 to 0.1 and then resulted in a longer spray penetration length for a larger r/D value.

The comparison of the SMD is shown in Figure 6.19. The KH-ACT-RT model predicts a lower SMD value than the experimental data from the PDPA system and can not present clearly the difference for the different r/D ratios. This could be due to the faster droplet breakup speed of the KH-ACT model which results in the amount of smaller child droplets generated causing in the error of SMD calculation. For the MPI-CAB model, the larger SMD value is predicted at 30 mm from the nozzle exit and the closed results with experimental data at 40 and 50 mm. For the effects of the r/D ratio, the MPI-CAB model shows the decreasing trend of the SMD value when the r/D ratio increases.

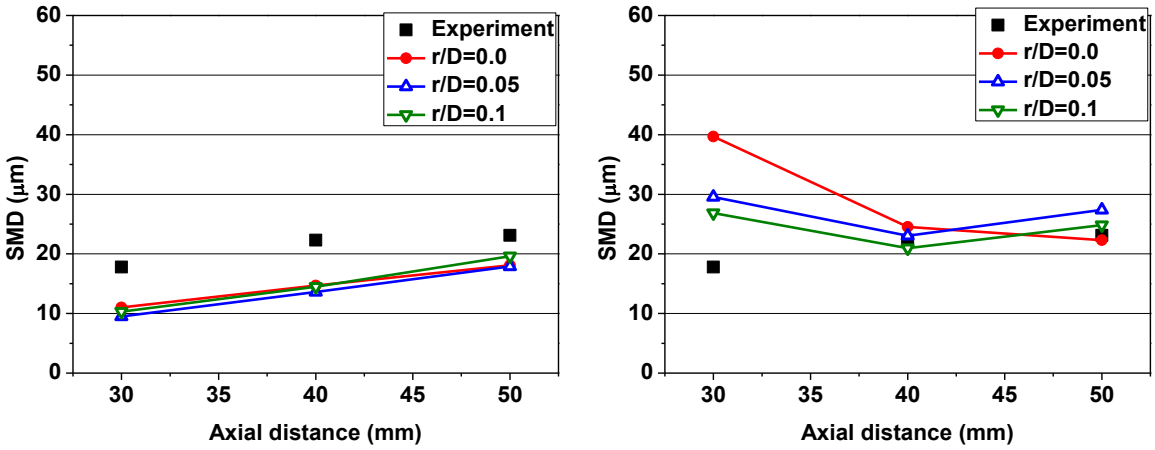

(a) KH-ACT-RT model (b) MPI-CAB model

Figure 6.19 Effects of r/D ratio on SMD by using the KH-ACT-RT and the MPI-CAB model

Comparing these results with the variation of droplet size in the primary breakup regime, the opposite trend is shown in the droplet size distribution in the primary and secondary breakup regimes. In the primary breakup, although there is a higher injection velocity from a larger r/D value, the lower turbulent kinetic energy decreases the intensity of the droplet breakup and generates a larger droplet size. However, when the droplet process experience secondary breakup, the aerodynamic force becomes a dominant factor in the secondary breakup regime and the higher droplet velocity results in a smaller droplet size from the larger r/D (higher injection velocity). This illustrates why the decreased trend of the SMD takes place when the r/D ratio increases.

The comparison of droplet average velocity at 50 mm from the nozzle hole is shown in Figure 6.20.

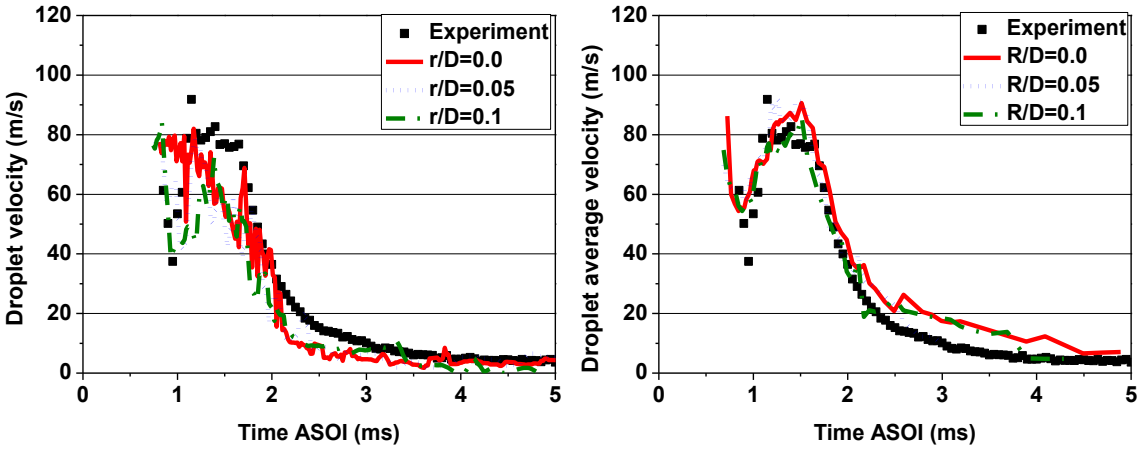

(a) KH-ACT-RT model (b) MPI-CAB model

Figure 6.20 Effects of r/D ratio on droplet average velocity at 50 mm from the nozzle by using the KH-ACT-RT and MPI-CAB models

The KH-ACT-RT model shows more unsteady droplet average velocity distributions than the MPI-CAB model. This is also caused by the amount of smaller child droplets. In the comparison of the r/D effects on droplet average velocity, both of these models illustrate that the droplet average velocity decreases when the r/D ratio increases. This is due to the larger droplets from the larger r/D ratio having a higher kinetic energy than smaller droplets. However, the difference of droplet average velocity is not obvious in this measuring point due to the droplets of the SMD from different r/D ratios being similar, as in Figure 6.19.

To analyse the breakup mechanism of the KH-ACT-RT model, Figure 6.21 (a) shows the distribution of aerodynamically-induced, turbulence-induced and RT breakup during the spray development. For the aerodynamically-induced breakup mechanism, the breakup number of the larger r/D value has a higher breakup number than the smaller r/D value. This is due to the higher injection velocity resulting in a larger difference of the relevant velocity between the droplet and ambience.

In Figure 6.21 (b), the analysis of the turbulence-induced numbers indicates the smaller r/D value which results in the intensive turbulent breakup mechanism during the spray breakup process. According to Figure 5.7 (a), the turbulent kinetic energy is gradually decreased when the r/D ratio increases because the smooth entrance corner makes the liquid flow enter the inner hole without a large direction angle change and then decreases the turbulent disturbances. As a result, the higher turbulent kinetic energy from the smaller r/D value causes a higher amount of turbulent breakup. In the analysis of the RT breakup mechanism in Figure 6.21 (c), the droplets with a larger size produced from the smaller r/D ratio experiences more drag force from atmosphere and results in a greater amount of RT breakup. In the analysis of the cavitation-induced breakup, it does not join in this breakup process. This is due to less cavitation affecting the gasoline nozzle which has been studied in the previous chapter.

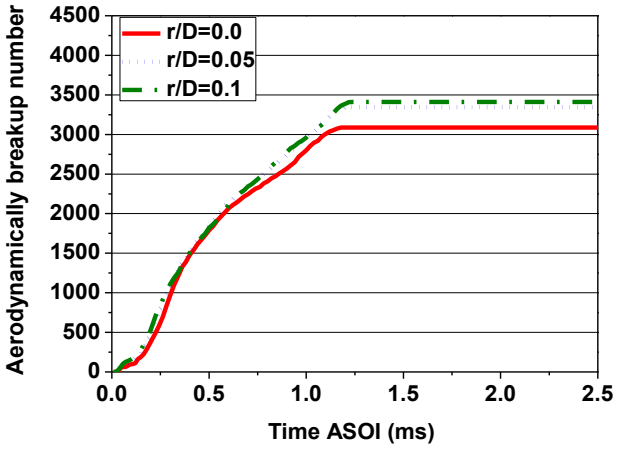

(a) Aerodynamically-induced Breakup

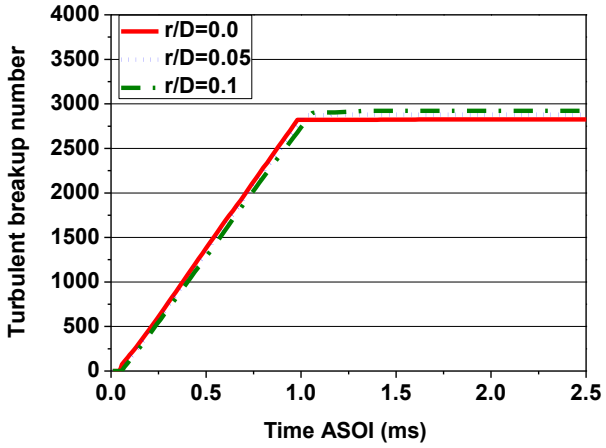

(b) Turbulence-induced Breakup

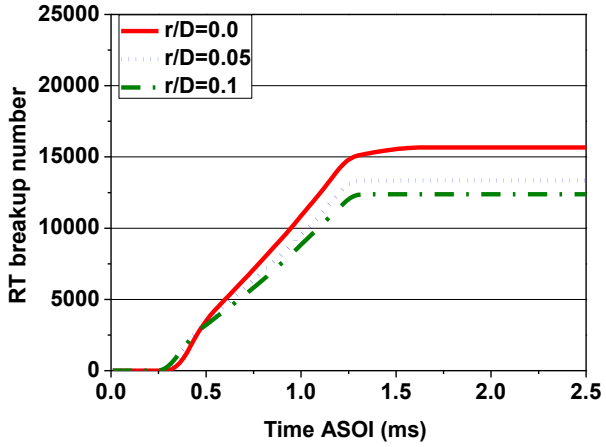

(c) RT breakup mechanism

Figure 6.21 Breakup number of different breakup mechanisms in the KH-ACT-RT model

In Figure 6.22, the different spray images from different r/D ratios and spray models at 0.5 and 0.7 ms are shown. By comparing the spray images from these two models, it can be seen that the spray angle of the MPI-CAB shows a wider angle than the KH-ACT-RT model. Furthermore, from the droplet distribution of the KH-ACT-RT, the droplet number is obviously higher than in the MPI-CAB. This is illustrated again by the breakup speed of the KH-ACT model which is faster and resulted in a great number of child droplets.

0.5ms

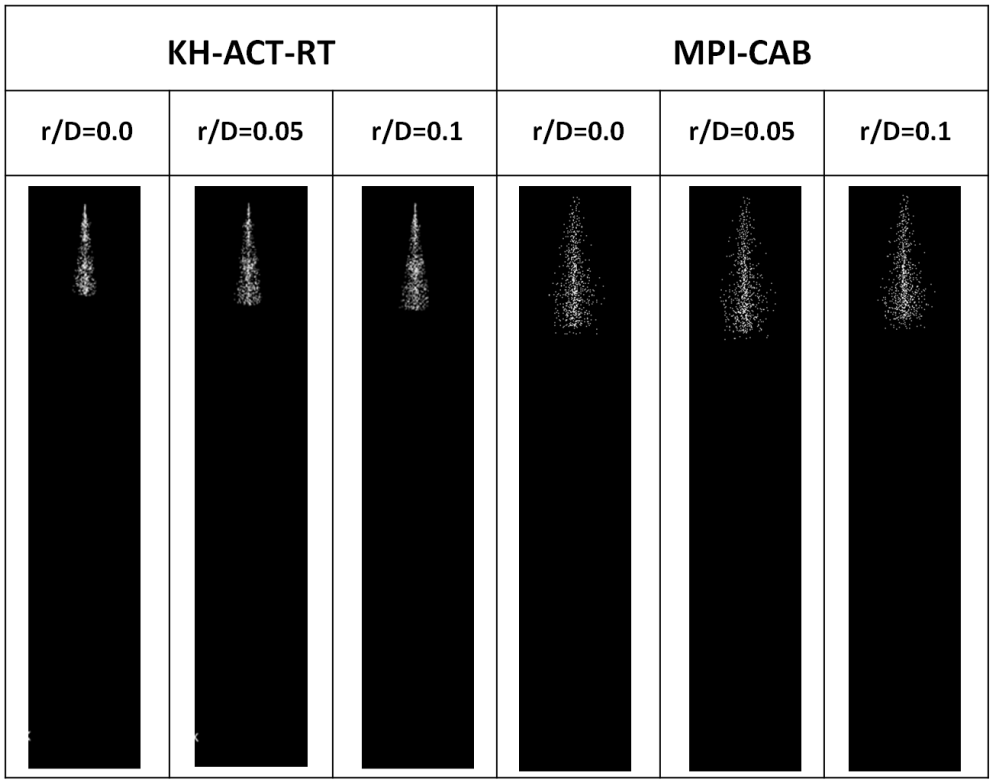

0.7ms

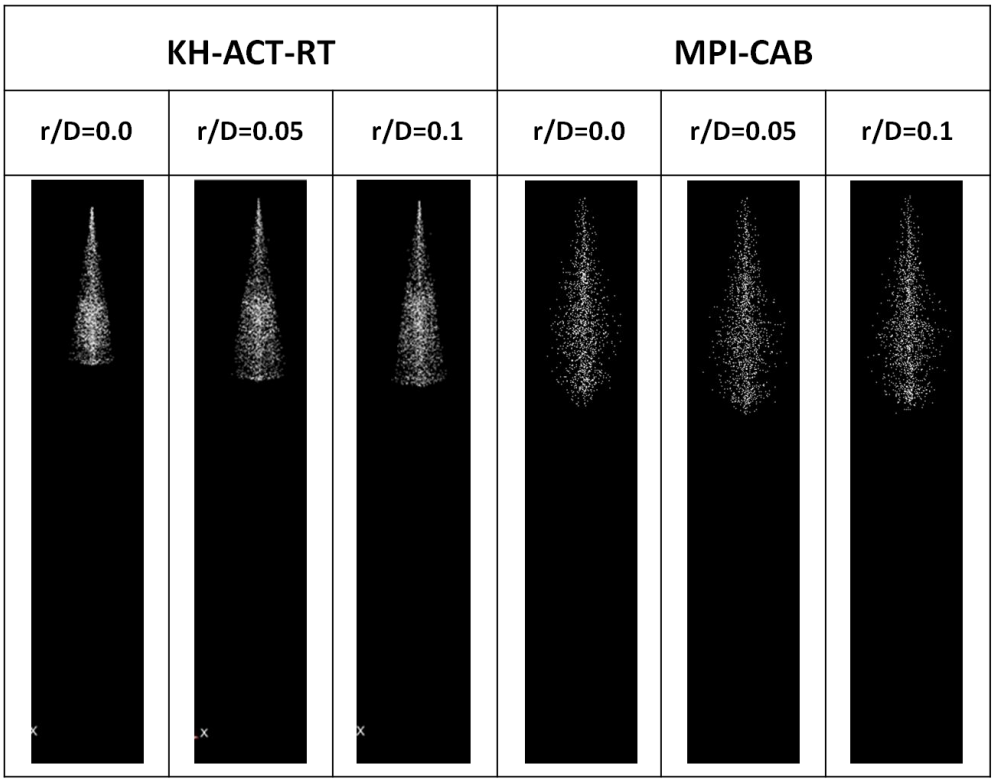

Figure 6.22 Development of spray structure at different r/D ratios

6.6.2 L/D ratio comparison

Another nozzle geometrical parameter which is also investigated intensively is the L/D ratio of the nozzle. In the previous chapter, the effects of different L/D ratios on spray characteristics such as mass flow rate, exit velocity, droplet size distributions and spray angle in the primary breakup regime were examined. In this section, the effects of various L/D on spray characteristics in the secondary breakup regime are examined respectively by the KH-ACT-RT and MPI-CAB models.

Figure 6.23 shows spray penetration length of different L/D ratios from the KH-ACT-RT and MPI-CAB models. It can be observed that both of the models show the effects of various L/D ratios on spray penetration length to be very low. To compare with the results from the previous chapter relating to various L/D ratios, it is important to note that the significant effects from the various nozzle L/D ratio needs to be examined by a higher injection pressure such as 200 bar injection pressure. This is necessary because of the larger friction from a longer nozzle length which decreases the velocity distribution as located near the nozzle wall. Thus, the higher injection results in more obvious differences of velocity distribution between the nozzle centre and edge.

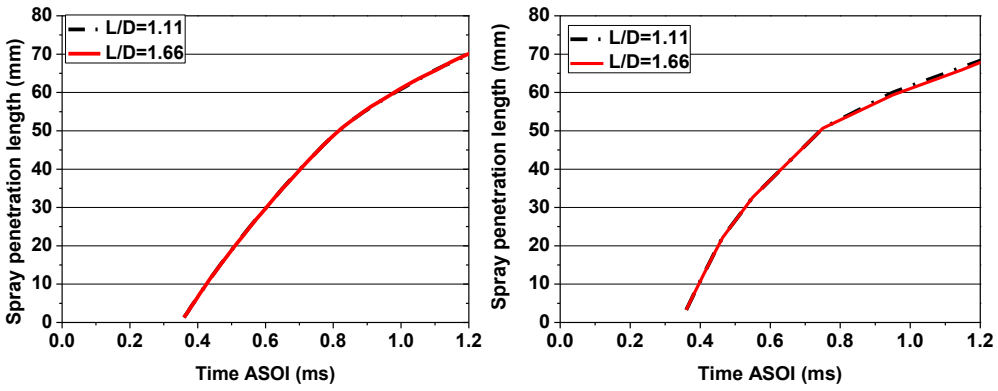

(a) KH-ACT-RT model (b) MPI-CAB model

Figure 6.23 Spray penetration length of different L/D ratios

In the KH-ACT-RT and MPI-CAB models, the simulation results of the spray characteristics all indicated that the effects of various nozzle L/D ratios are not obvious in the spray penetration length. On comparing the droplet average velocity at 50 mm from the nozzle (Figure 6.24), the KH-ACT-RT model shows a similar trend of droplet velocity. However, the MPI-CAB model shows that the droplet average velocity for smaller L/D ratios has a slightly higher value than the longer nozzle length because of the higher friction from the longer nozzle wall decreases the nozzle average exit velocity. To compare the droplet velocity trend, it can be observed that the MPI-CAB can accurately predict at the similar velocity distribution to the experimental data from the PDPA system. This occurs because there was a small group of droplets with a larger droplet size in front of the sprays main body which also can be seen in Figure 6.24. This again illustrates that the KH-ACT model predicts the smaller droplet size distribution due to the fast droplet breakup speed.

Figure 6.25 compares the SMD distribution from these two models. It can be found again that the various nozzle L/D ratios still show few effects on the spray characteristics in the secondary regime. This is due to the different breakup mechanisms between the primary breakup regime and secondary breakup regime. In the primary breakup regime, the droplet breakup is affected by turbulent effects, cavitation bubble collapse and the aerodynamic force between the liquid surface and atmosphere. Thus, the effects of various nozzle L/D ratios are more obvious in the primary breakup regime. In the regime of secondary breakup, the droplet breakup mechanism was mainly dominated by aerodynamic force; this is why the effects of the L/D ratio are hard to observe. From the numerical study of spray images in Figure 6.26, the spray structure at different L/D ratios does not show clear differences for the KH-ACT-RT and MPI-CAB models.

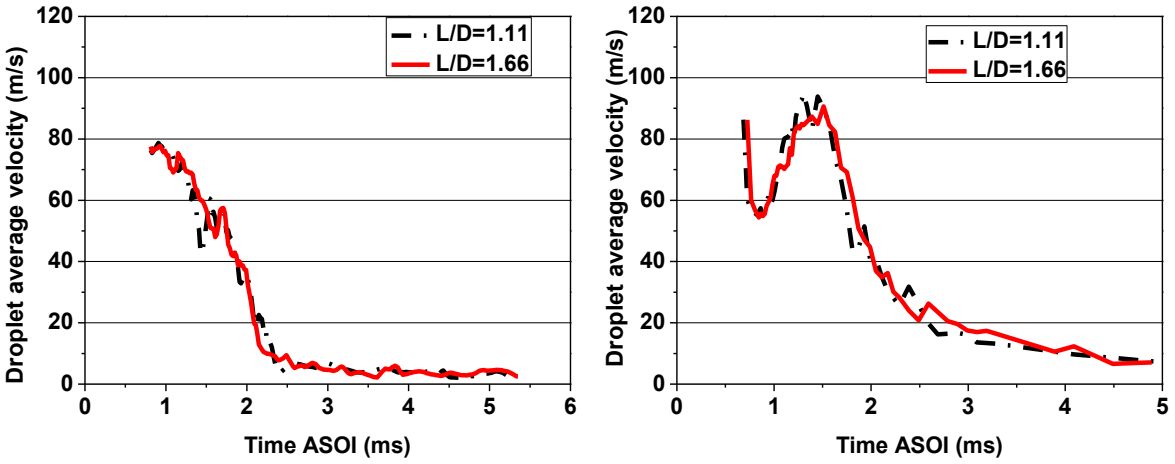

(a) KH-ACT-RT model (b) MPI-CAB model

Figure 6.24 Distribution of droplet average velocity for different L/D ratios at 50mm from the nozzle

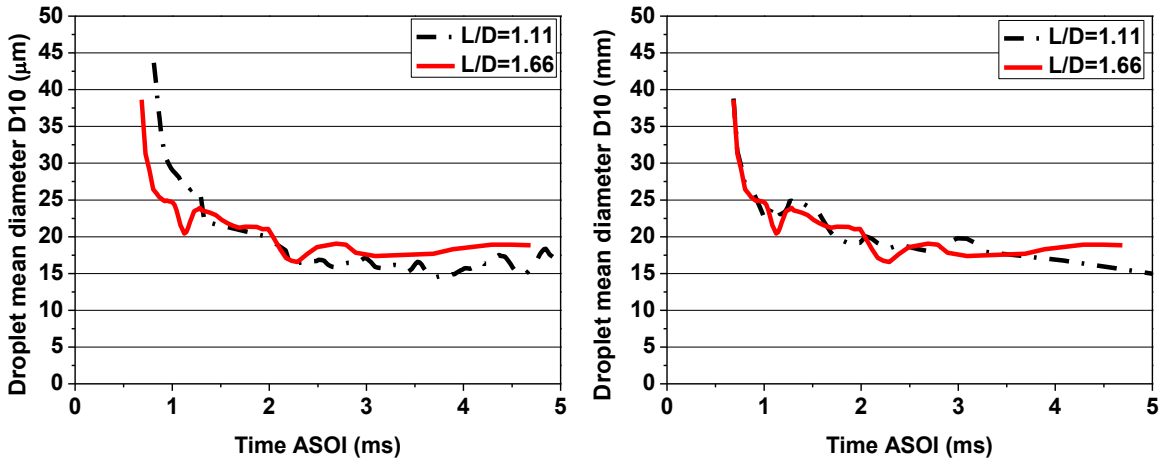

(a) KH-ACT-RT model (b) MPI-CAB model

Figure 6.25 Distribution of droplet mean diameter at 50 mm from the nozzle

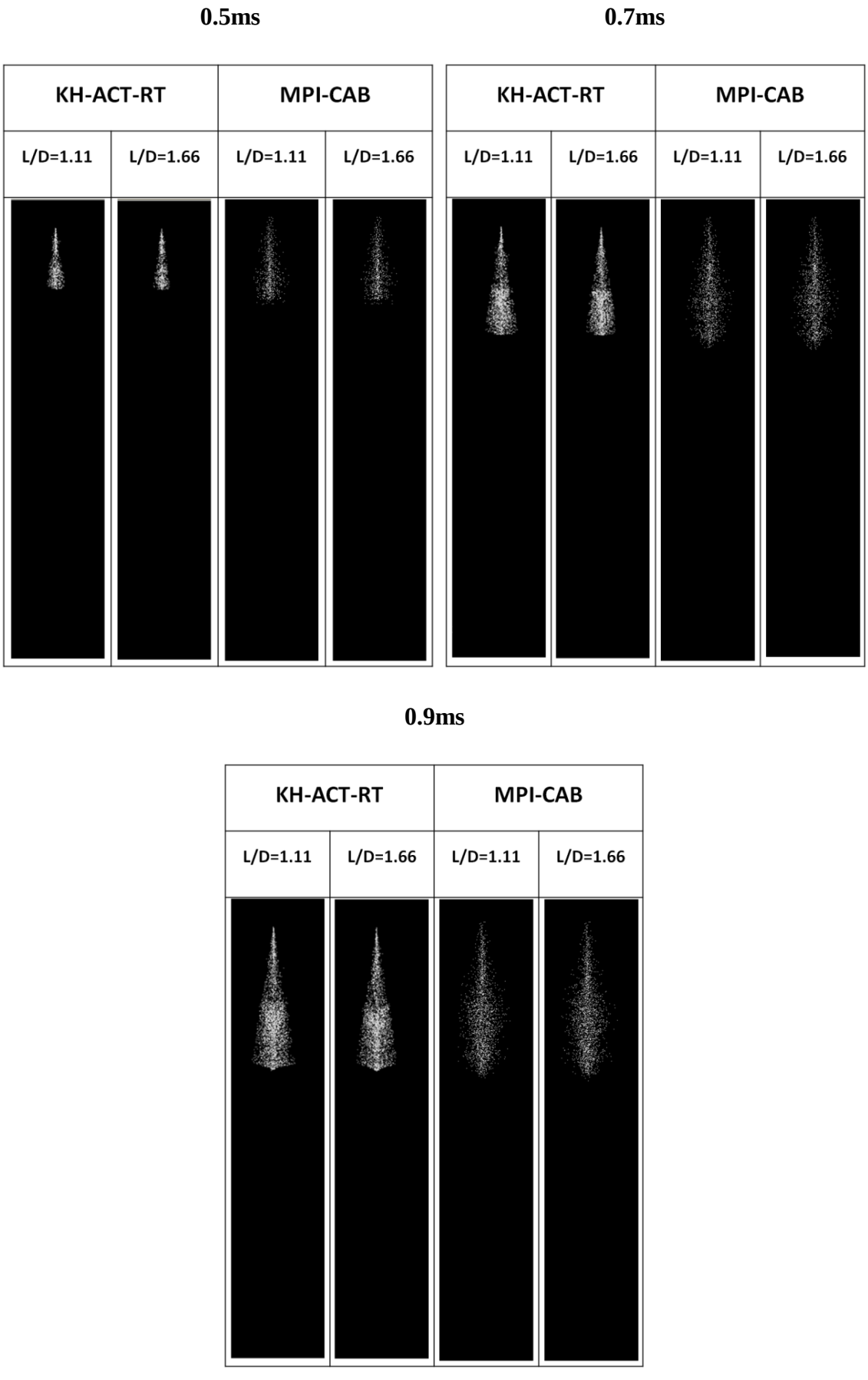

Figure 6.26 Numerical study of spray structure and development at different L/D ratios

6.7 Summary

The sensitivity of the main spray characteristics on the different r/D and L/D ratio of a GDI fuel injector has been investigated numerically using an Eulerian approach. Two different spray breakup models are also discussed for their spray characteristics of different nozzle geometrical designs. Influences of different r/D and L/D ratios on the spray characteristics and the breakup mechanism in the secondary breakup regime have also been analysed. The key findings which have added value and importance for future applications in injector flow simulations and its geometrical design are:

- The comparison of the KH-RT and KH-ACT-RT models indicates that the uncompleted assumption of the breakup mechanism of the KH model results in a higher SMD than that of the KH-ACT model. However, the intensive breakup process of the KH-ACT-RT model causes a faster breakup speed and a great amount of small child droplets.

- The calculated value of the turbulent kinetic energy and dissipation rate from the Bianchi equations presented a lower value. This is due to the assumption that the Bianchi equations do not consider the effects of the r/D ratios on turbulent disturbances. Compared to the result of the Bianchi equations, both the turbulent kinetic energy and dissipation rate from the nozzle simulation shows higher values. Moreover, the comparison of the original KH-ACT-RT; and the KH-ACT-RT with nozzle flow simulation shows improvements in the mean droplet diameter.

- The effects of the r/D ratio not only influence the spray characteristics in the primary breakup regime but also in the secondary breakup regime. The numerical study indicates that a larger r/D ratio increases the spray penetration length due to higher nozzle exit

velocity and resulted in a smaller droplet size in the secondary breakup regime, which is opposite to the nozzle flow simulation. This is due to the aerodynamic force becoming a dominant role in the secondary breakup regime and higher nozzle exit velocity which results in a more intensive breakup process.

- In the secondary breakup regime, a clear difference in the spray characteristics between different L/D ratios cannot be seen by using the KH-ACT-RT and MPI-CAB models. Although the clear differences can be observed by nozzle flow simulation, the L/D ratio has less effect on spray characteristics in the far-field because the aerodynamic force plays a dominant role in the secondary breakup regime.

- The analysis of the breakup mechanism shows that the turbulence induced breakup firstly takes the place of the initial breakup process in the primary breakup regime and then the aerodynamically induced breakup plays a dominant role in the secondary breakup regime.

The comparison of the KH-ACT-RT and MPI-CAB models shows the features of each breakup model. However, the KH-ACT-RT shows a more unstable trend and lower value in droplet velocity due to the great amount of small child droplets. To compare with the KH-ACT-RT model, the MPI-CAB shows a better agreement and similar trend with the experimental data. Thus, the MPI-CAB model will be used to simulate the following studies.

Chapter 7

Experimental and Modelling studies of spray characteristics

This chapter investigates the near field flow and spray characteristics for iso-octane under various operating conditions using the LES-VOF model and optical methods. The effects of different injection pressures and ambient pressures on the exit velocity, spray angle, breakup length and droplet size are discussed.

7.1 Introduction

Due to the limitations of optical methods, it is difficult to measure the changes in the spray characteristics in the nozzle near field under different operating conditions. For example, the PDPA system can only provide reliable data after 30mm from an injector tip because the high density of the droplet number near the injector tip causes a measuring error. To solve this problem, the CFD method provides an efficient and a low-cost way to study the nozzle flow and near field flow. Several CFD models have been established to simulate nozzle flow in order to provide initial conditions such as the exit velocity and initial droplet size to the spray model for spray simulations. However, due to the complex calculations, some initial conditions and physical problems are simply assumed. For example, the initial droplet size is assumed to the whole diameter and the exit velocity is calculated according to the mass flow rate in the spray model.

This chapter introduces the changes of spray characteristics at the primary and secondary breakup regions. For the primary breakup region, spray characteristics are simulated by the ANSYS-Fluent VOF-LES model to investigate the nozzle flow and near field flow which considers the influences from nozzle geometry such as: L/D ratio and counterbore design under different injection and ambient pressures. It provides more accurate initial conditions to the Lagrangian model to simulate spray development at different injection pressures and ambient pressures. Moreover, the differences of spray characteristics under different operating conditions in the primary breakup region can be investigated. In the secondary breakup region, more detailed spray characteristics are studied by applying optical methods such as the PDPA system and use of a high speed camera for different injection pressures and ambient pressures. According to these experimental data, the spray model in KIVA-3V is validated to examine its reliability.

7.2 Modelling of Nozzle Flow and Primary Breakup

7.2.1 Test Conditions and Boundary Conditions

The Bosch GDI injector is used as the testing GDI injector, which is the same as in Figure 4.1. From the previous chapter, the reliability of the LES-VOF model and GDI nozzle has been validated by the mass flow rate from the experiment. As concluded from the previous chapter, these nozzle flow simulations do not consider the cavitation effects inside the nozzle.

The testing conditions of different operation conditions are shown in Table 7.1. The influences of different injection pressures on spray characteristics are investigated by 100, 150 and 200 bar in the ambient pressure which are the common injection pressures used in GDI engines.

The effects of different ambient pressures on the spray characteristics are investigated in 1, 3 and 7 bar by using 150 bar injection pressure. The testing fuel used iso-octane. The fuel properties are shown in Table 4.3

Table 7.1 Testing conditions for different injection pressure and ambient pressure

	Test Conditions
Test Fuel	**Iso-octane**
Injection Pressure	**100, 150, 200 bar**
Ambient Pressure	**1bar, 3bar, 7bar**
Ambient Temperature	**293 K**
Fuel Temperature	**293K**

7.2.2 Modelling the Effects of Injection Pressure

The common strategy to improve fuel atomisation is by increasing injection pressure. Higher injection pressure produces higher exit velocity and stronger turbulences which cause faster liquid breakup. The detailed spray characteristics in the primary breakup process are discussed as well as the influences of different injection pressures on mass flow rate, exit velocity, breakup length, spray angle and the distributions of droplet size.

Mass flow rate is one of the main factors affecting the spray's behaviour. The calculation of mass flow rate is conducted by averaging the mass flow rate data when it arrives at a steady state which is the same calculating method as Figure 4-8. The comparison of mass flow rate at a different injection pressure is shown in Figure 7.1. The average mass flow rate increases when the injection pressure rises from 100 to 200 bar. The mass flow rate increases by

approximately 20% from 100 to 150 bar and 16% from 150 to 200bar. This is due to the higher injection pressure producing high exit velocity and causing a raise in the mass flow rate.

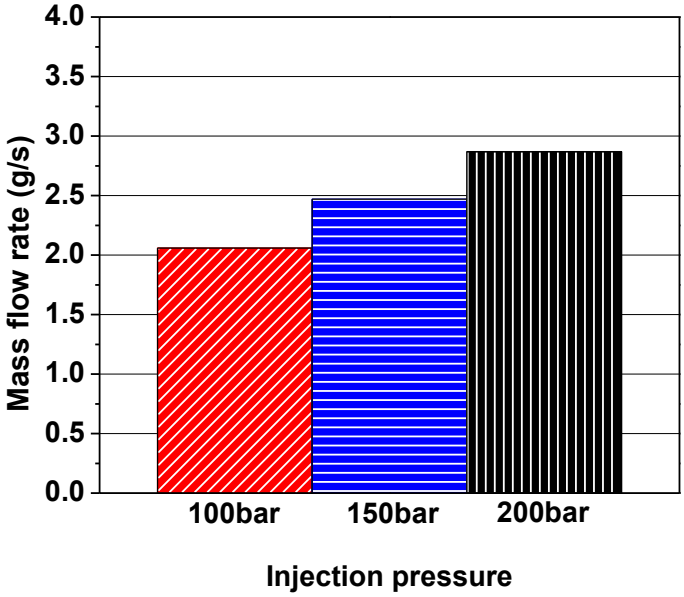

Figure 7.1 Comparison of mass flow rate at different injection pressures

The cell-based averaging of liquid velocity at the nozzle exit (plane A-A is shown in Figure 5.2) is shown in Figure 7.2 which portrays the changes of velocity at different flow times. For 150 and 200 bar, the velocity range for the highest and lowest values is around 8 %. For 100 bar, the difference between the highest and lowest is 6%. It can be explained that the lower injection pressure has smaller turbulent effects inside the liquid which provides a steadier exit velocity. From the comparison of the average value for exit velocity, the same trend is shown as the mass flow rate at different injection pressures in Figure 7.3 (a); the higher injection pressure shows the higher velocity. For injection pressure of 100 bar, its nozzle exit velocity is around 125m/s and increases by 20% to 150 bar and 16% from 150 to 200bar. Figure 7.3.(b) shows the distribution of the average velocity along the nozzle exit at plane A-A. It can be observed that the higher velocity distribution presents a higher injection pressure. Furthermore, the value of the left side shows a higher average value than the right-hand side, resulting from the sharp-edged corner at the nozzle entrance accelerating the liquid velocity.

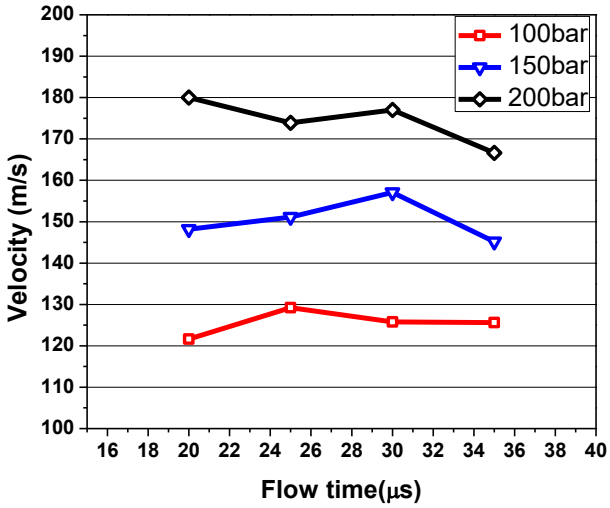

Figure 7.2 Comparison of mass flow rate at different injection pressures at different flow times

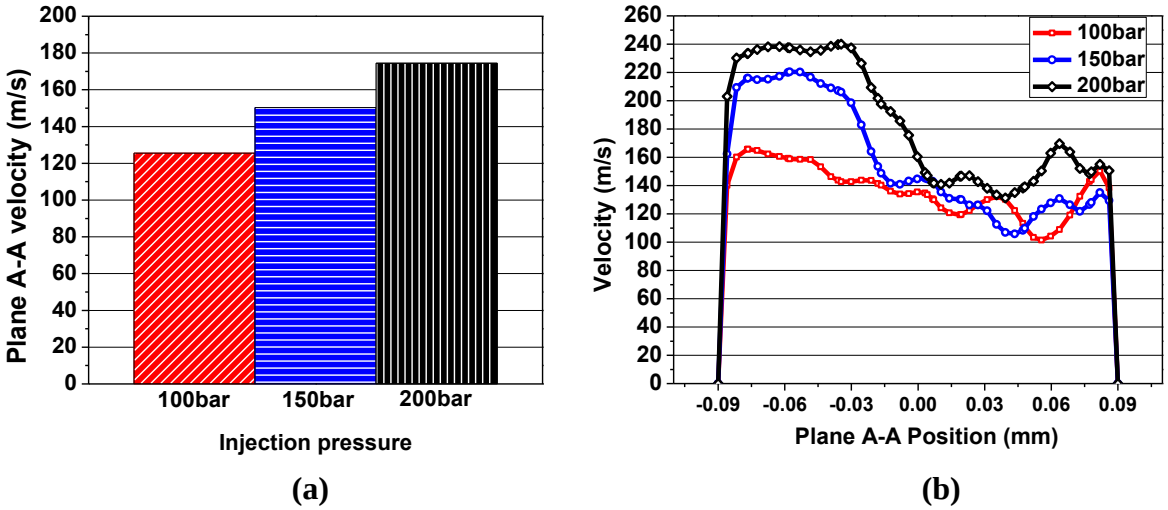

Figure 7.3 (a) Comparison of exit velocity (b) Distributions of velocity along nozzle exits at different injection pressures (Plane A-A)

From Figure 7.4, it can be observed that a higher injection pressure causes a higher flow velocity at the nozzle inlet and produces a stronger vortex inside the counterbore. This is due to the larger mass flow rate leaving from the counter-bore area and causing more air to flow back into the counterbore.

	100bar	150bar	200bar
m/s	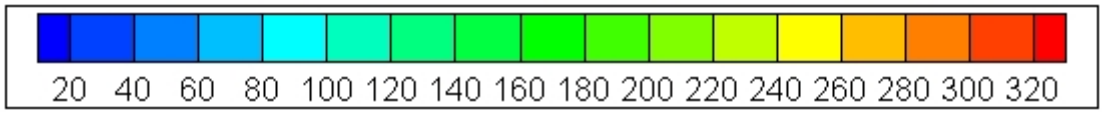		
20μs	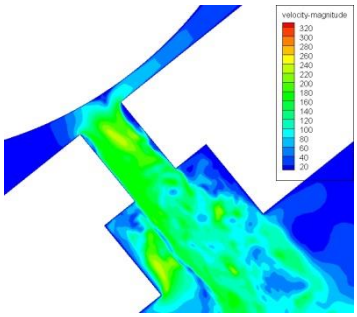	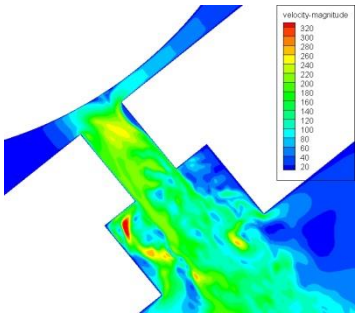	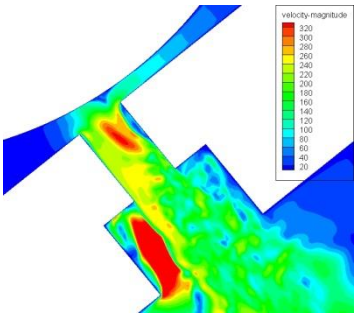
25μs	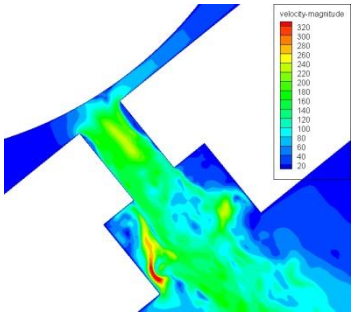	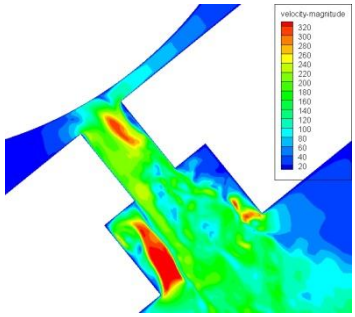	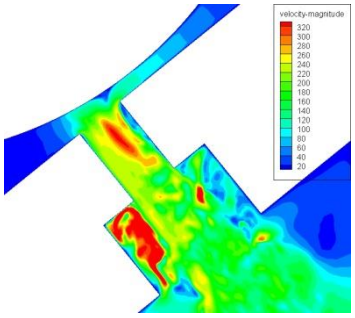
30μs	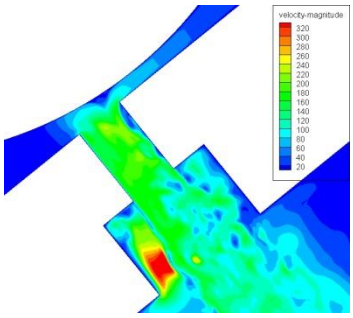	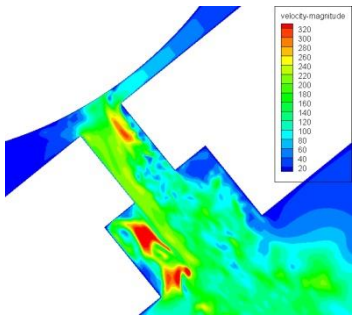	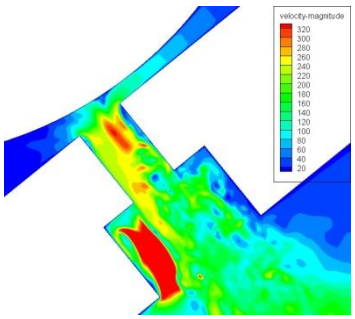
35μs	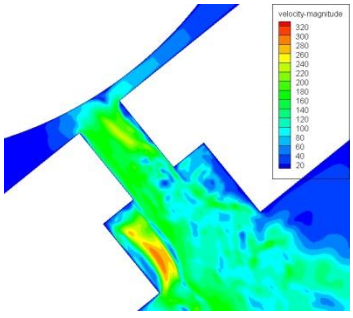	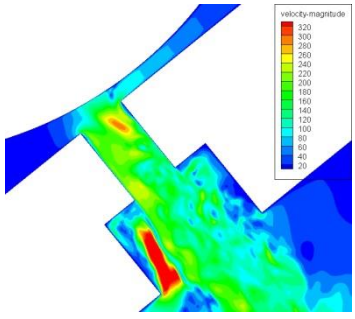	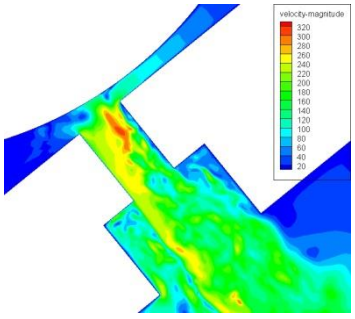

Figure 7.4 Distributions of velocity field at different flow time and injection pressures

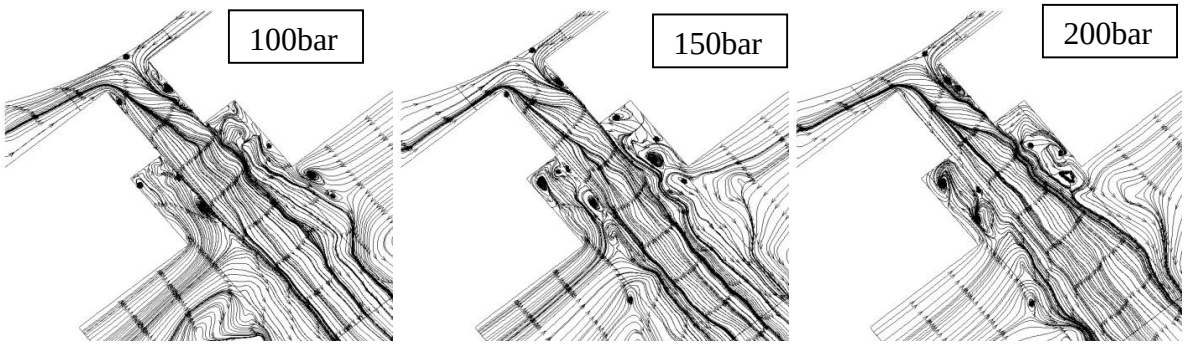

Figure 7.5 Distributions of streamline injection pressures at 25 μs

Figure 7.5 shows the distribution of streamline under different injection pressures at 25 μs. To compare velocity distribution at 25μs from Figure 7.4, it can be projected that the stronger vortex is produced at a higher injection pressure. To understand the turbulence effects, the turbulence kinetic energy is investigated. In the fluid dynamics, turbulence kinetic energy is the mean kinetic energy per unit mass associated with eddies in turbulent flow. The comparison of turbulence kinetic energy is shown in Figure 7.6.

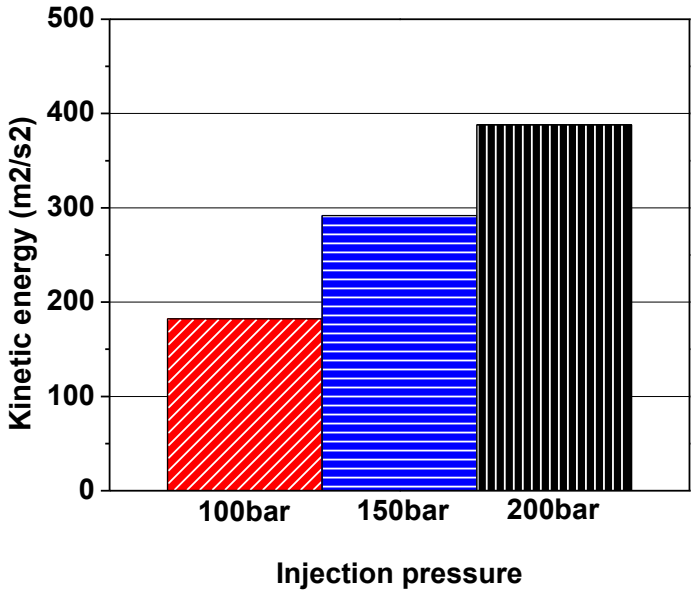

Figure 7.6 Comparison of kinetic energy at different injections

Another spray characteristic in the primary region which estimates the liquid breakup speed is the measurement of liquid breakup length. Due to the different nozzle designs such as the existence of a counterbore for the GDI nozzle, the liquid breakup length is difficult to measure in the GDI injector. Measuring the liquid jet breakup length for GDI injectors presents complications due to the counterbore design. Figure 7.7 compares the average liquid breakup length at different injection pressures. It can be observed that the higher injection pressure decreases the liquid breakup length due to the stronger atomisation because of stronger turbulences around the liquid and the kinetic energy inside the liquid. From Figure 6-9, the breakup length decreases from 0.48 mm to 0.38 mm when the injection pressure increases from 100 to 200 bar.

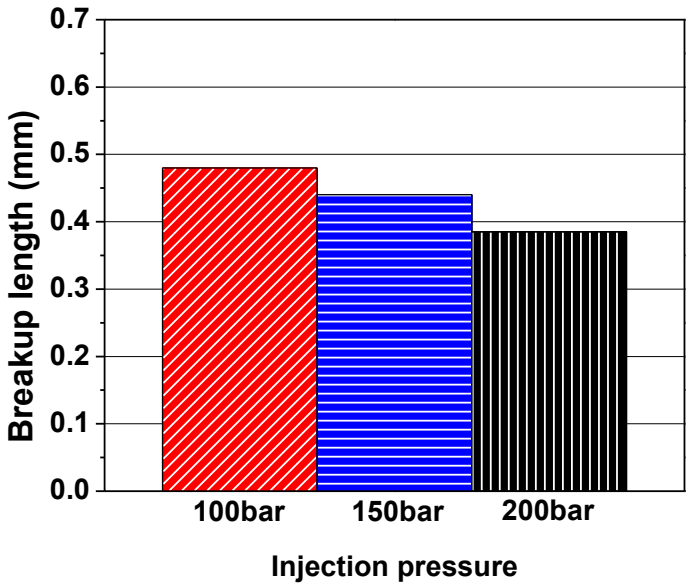

Figure 7.7 Comparison of kinetic energy at different injection pressures

The spray angle of different injection pressures is shown in Figure 7.8. When the injection pressure increases, the spray angle increases due to better fuel atomisation. This can be observed in the comparison of liquid breakup length. Due to the higher injection pressure producing stronger turbulence and higher exit velocity, the liquid break up becomes easier and

quicker which causes more droplets to be detached out from the liquid jet increasing the spray angle. From Figure 7.8 and 7.9, the average spray angle of 100 bar is around 18° and increases from 14.5 % to 150 bar and 30.6% to 200 bar. Figure 7.10 shows the VOF distribution of liquid at different injection pressures at different flow times. It can be seen that the liquid breakup length for 200 bar is shorter than the others and has a more intensive liquid breakup.

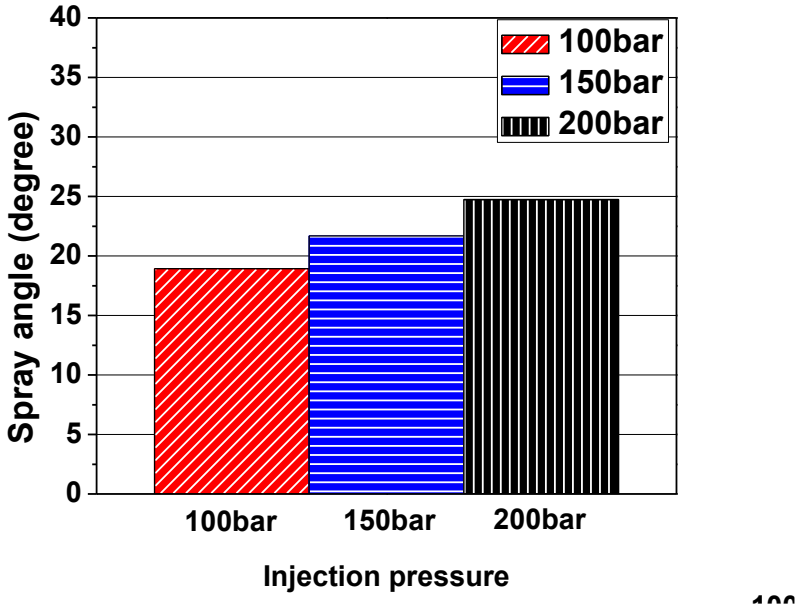

Figure 7.8 Comparison of spray angle at different injection pressures

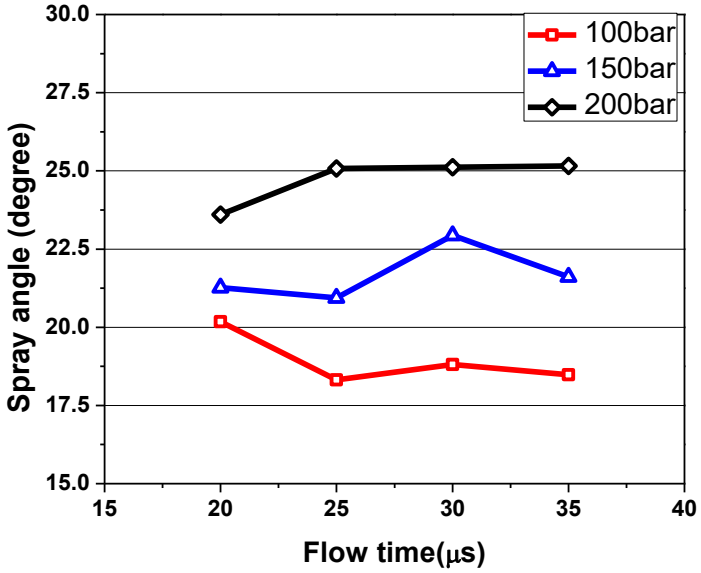

Figure 7.9 Comparison of spray angle at different injection pressures at different flow time

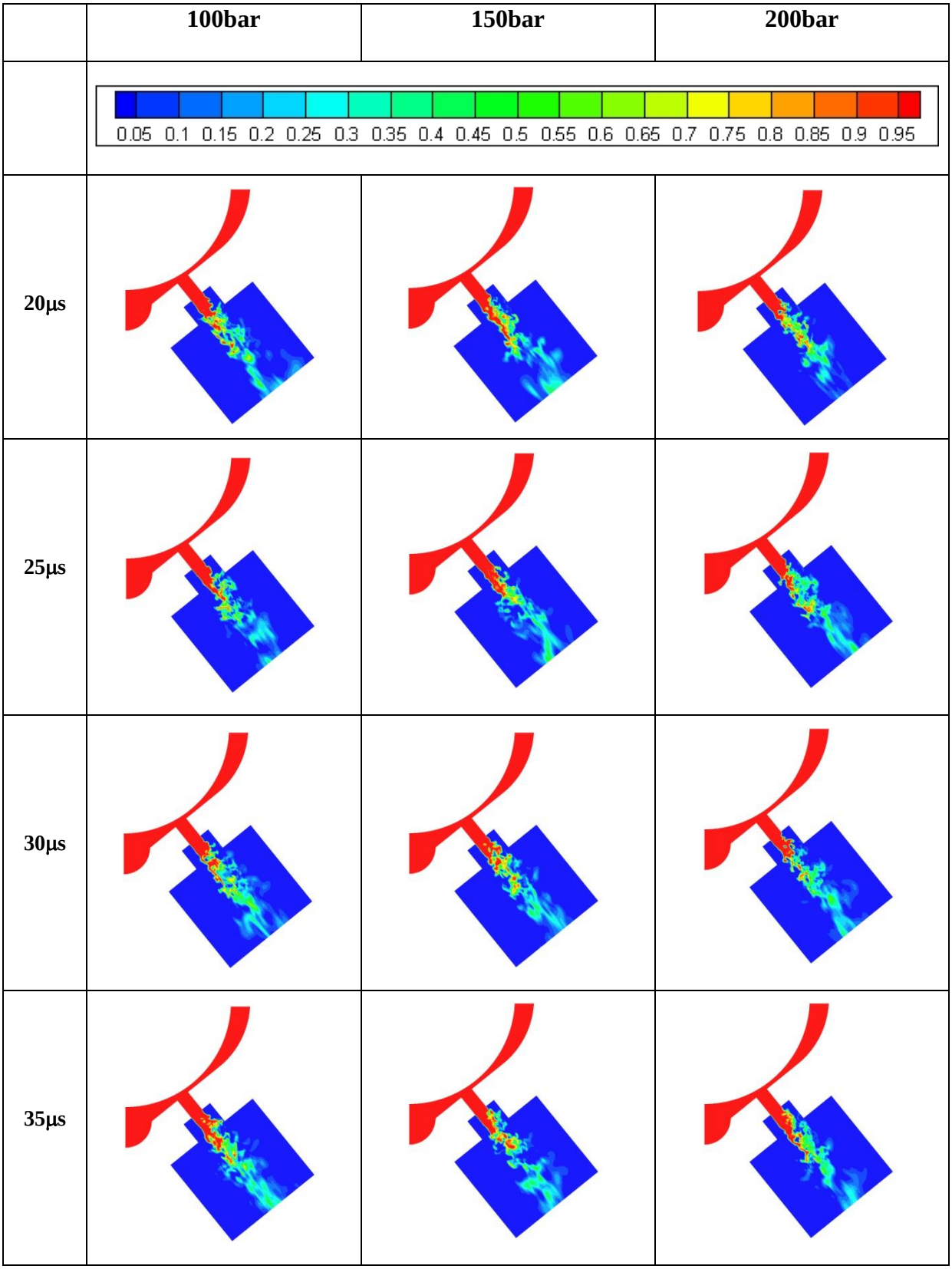

Figure 7.10 Distribution of liquid at different flow time and injection pressures

Figure 7.11 displays the average droplet diameter at different measuring planes (Figure 5.2) and different injection pressures. In the nozzle exit (plane A-A), the droplet diameter at different injection pressures is the same which is equal to the nozzle hole diameter. This illustrates that the length of cavitation or wall separation did not arrive at the GDI nozzle exit. In the counterbore exit (plane B-B), the average droplet diameter dropped by 67 % from the nozzle exit to the counterbore exit. This is due to the intensive interactions with air which then cause primary breakup to take place inside the counterbore. The influences of different injection pressures on droplet size are not significant at this distance. However, at the plane C-C and D-D, the effects of different injection pressures influence droplet diameter significantly. The average droplet diameters at a higher pressure become smaller after the liquid leaves from the counterbore exit (plane B-B). Figure 7.12 shows the distributions of VOF=0.5 at 30μs under different injection pressures. It can be seen that the red area of 200 bar has more broken regions than the others.

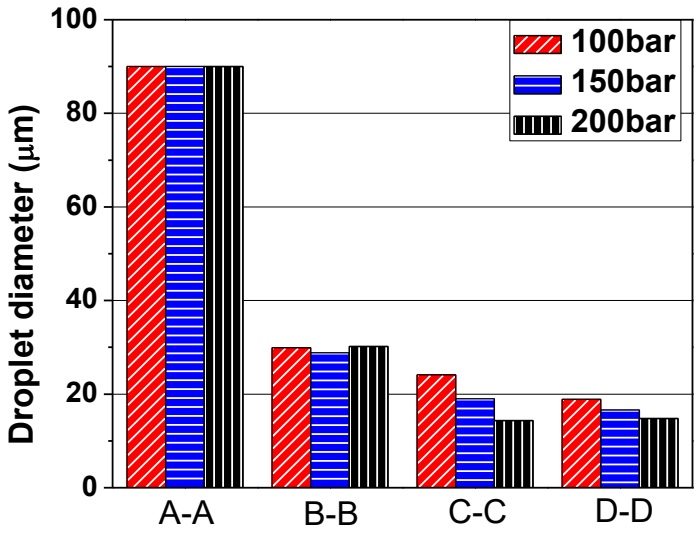

Figure 7.11 Average droplet diameters of different measuring planes at different injection pressures

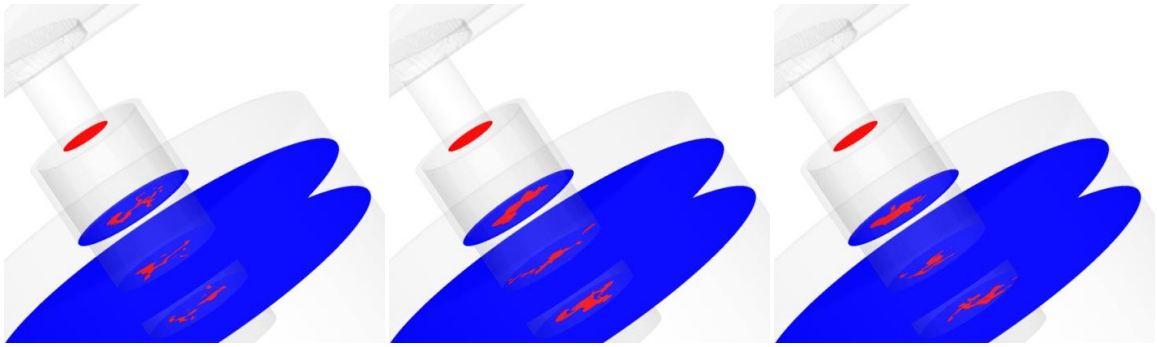

(a)200bar (b)150bar (c)100bar

Figure 7.12 Distributions of VOF=0.5 at different measuring plane at 30 μs under different injection pressures

7.2.3 Modelling the Effects of Ambient Pressures

This section discusses the influences of different ambient pressures on the spray characteristics in the primary breakup region. The ambient pressures are examined by 1, 3 and 7 bar at 150 bar injection pressure. The testing fuel was still iso-octane.

Figure 7.13 provides the average value of mass flow rate at different ambient pressures which was measured at the nozzle exit plane A-A. The mass flow rate at 1 and 3 bar ambient pressure has similar mass flow rate data. At 7 bar ambient pressure, the mass flow rate decreased by around 3%. From this comparison, it can be observed that increasing ambient pressure has very limited effects on mass flow rate because the ∇P between the nozzle entrance and exit only has 2 bar and 6 bar for 3 bar and 7 bar.

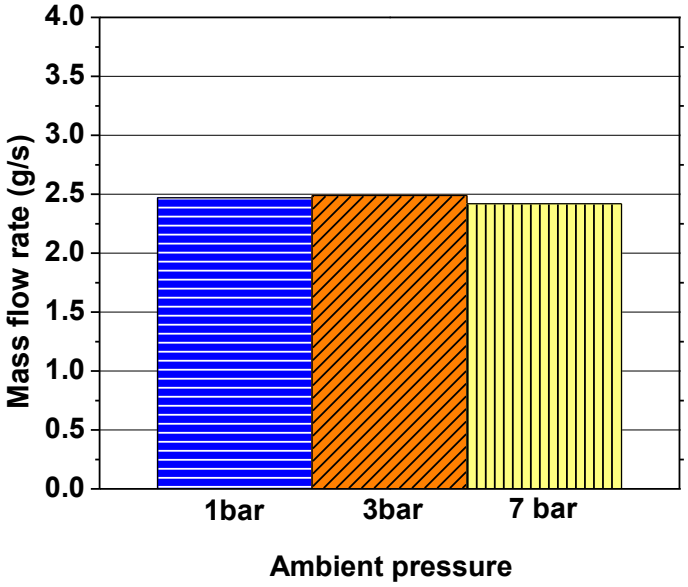

Figure 7.13 Comparison of mass flow rate at different ambient pressures

There were similar results for the mass flow rate in the comparison of nozzle exit velocity at plane A-A, as in Figure 7.14. The exit velocity was around 150m/s under different ambient pressures at the nozzle exit; which can explain why the mass flow rate is similar at the plane A-A. However, at the counterbore exit plane B-B, the influences of ambient pressure decreased the velocity. The velocity at the counterbore exit dropped separately by 4 % for 3 bar and 7 % for 7 bar. This is due to the ambient density increasing by raising the ambient pressure which increases the drag force on the liquid breakup. At the nozzle exit plane A-A, the effects of ambient pressure were not as significant as expected. However, when the liquid jet goes forward into ambient, more drag force decreases the velocity. Figure 7.15 shows the comparison of turbulence kinetic energy at the nozzle exit and counterbore exit under different ambient pressures. The effects of ambient pressure not only decrease the kinetic energy at the nozzle exit but also at the counterbore exit. Figure 7.16 shows the velocity field at different ambient pressures. It is found that a weaker vortex happens in the lower part of the counterbore when the ambient pressure gradually increases from 1 bar to 7 bar.

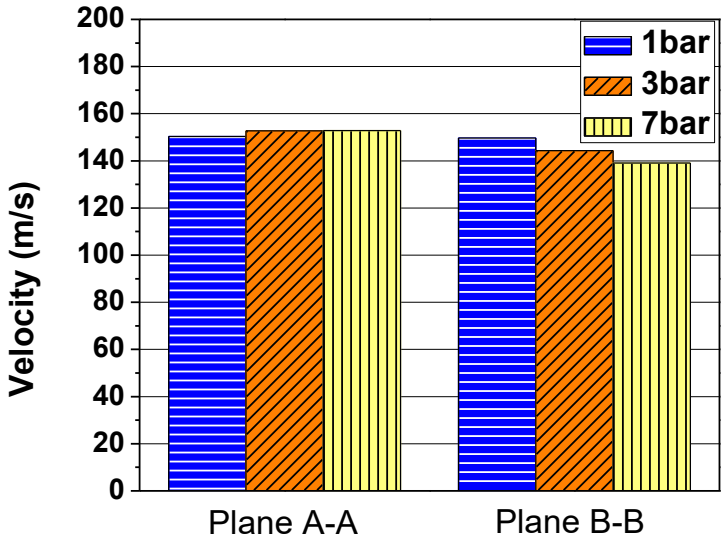

Figure 7.14 Comparison of velocity at different measuring planes under different ambient pressures

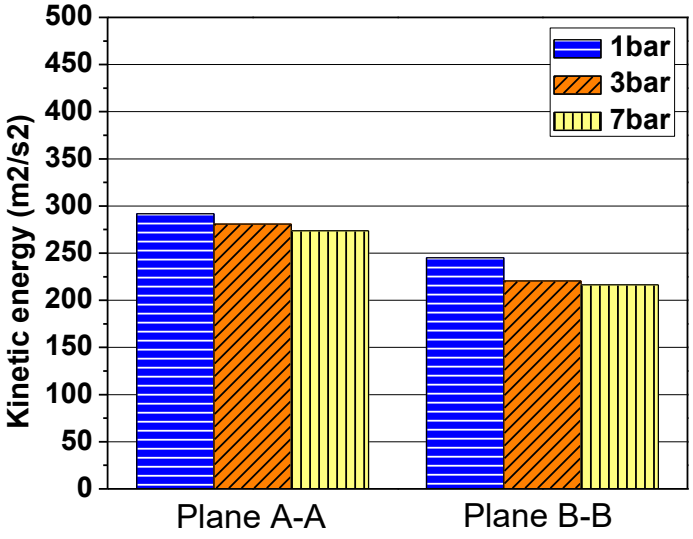

Figure 7.15 Comparison of turbulence kinetic energy at different measuring planes under different ambient pressures

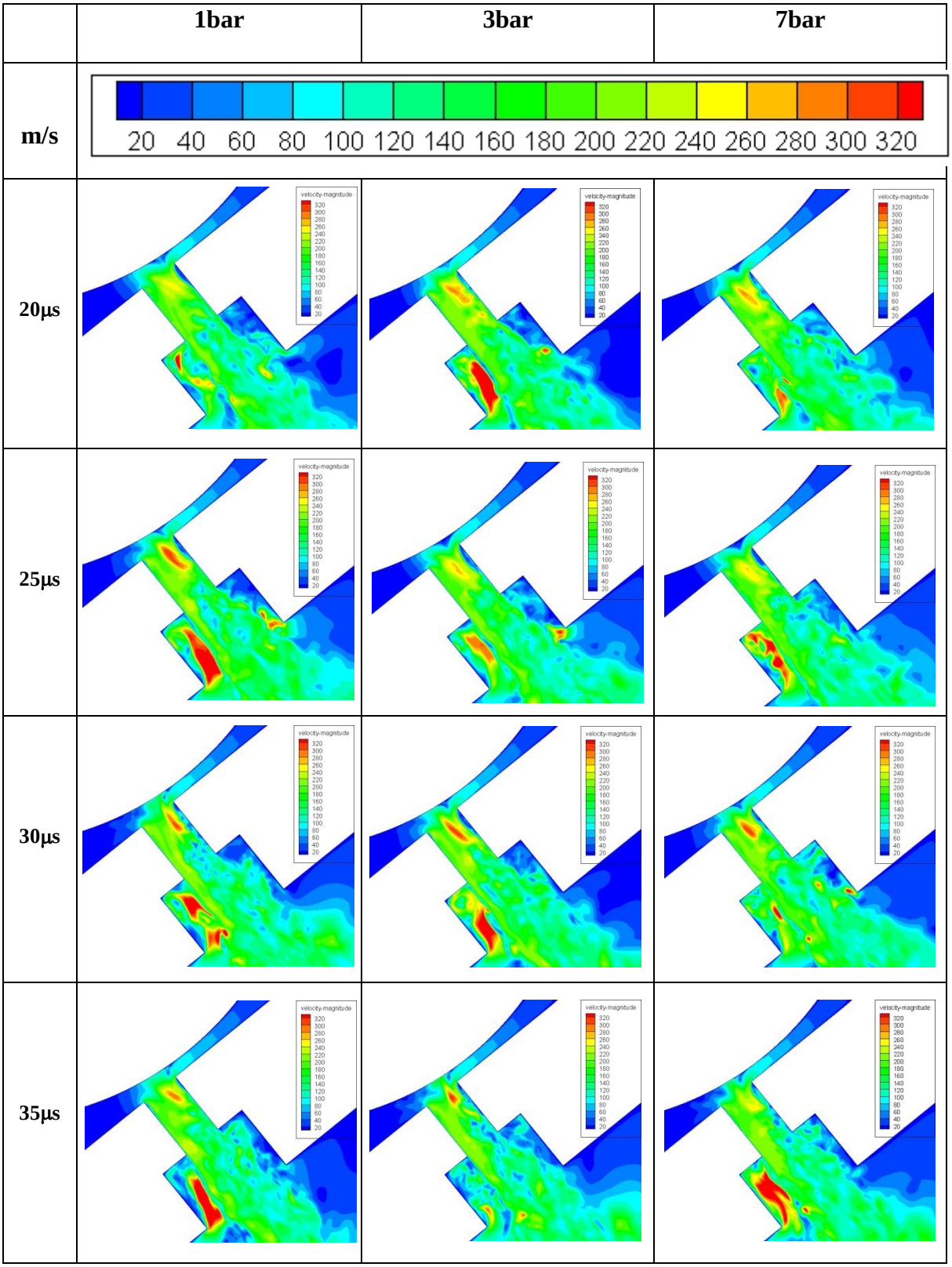

Figure 7.16 Distributions of velocity field at different flow time and ambient pressures

In Figure 7.17, it shows the distribution of streamline in the GDI nozzle at different ambient pressures at 25μs. On the left-hand side of the counterbore, the structure of the vortex strengthens when ambient pressure increases from 1 to 7 bar. Due to the opposite flow direction between liquid and air flow inside the counterbore, it decreases the field velocity at the counterbore exit.

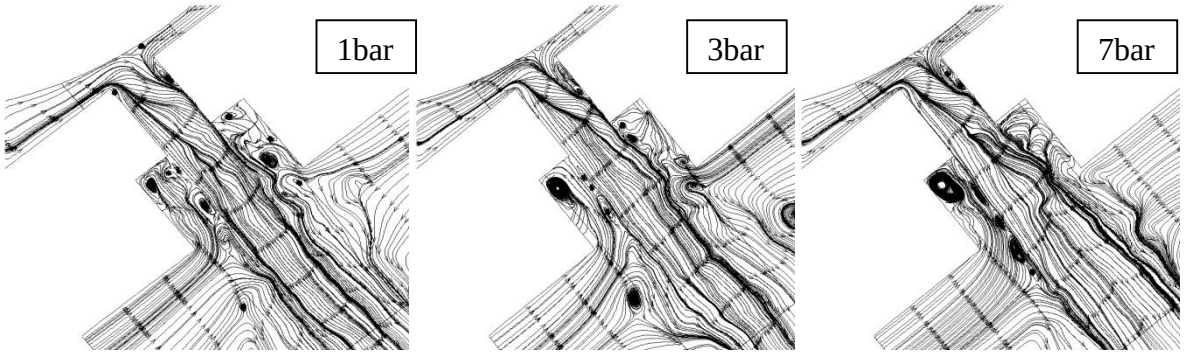

Figure 7.17 Distributions of streamline at different ambient pressures at 25 μs

The comparison of liquid breakup lengths at different ambient pressures is shown in Figure 7.18. Although the exit velocity is similar at the nozzle plane and decreases at the counterbore exit when ambient pressure increases, the results of liquid breakup length gradually decrease and even the exit velocity decreases when the ambient pressure increases which is an opposite trend to Figure 7.7. The increasing drag force (as in Figure 7.17) makes the liquid droplets take off from the liquid jet easier when the ambient density increases; which is why the liquid breakup length becomes shorter when the ambient pressure increases.

Furthermore, comparisons of the spray angle can be explained as well. In Figure 7.19, the spray angle at 7 bar ambient pressure has the biggest value (25.42°). The spray angle increases to 5.6% when the ambient pressure is raised from 1 to 3 bar and 17.2% from 1 to 7 bar. More detailed results are provided in Figure 7.20, presenting a central cutting plane of the distribution of liquid at a different flow time under different ambient pressures. From these images, it can

be observed that the liquid breakup length at a higher ambient pressure is shorter than the others and that the spray angle is larger.

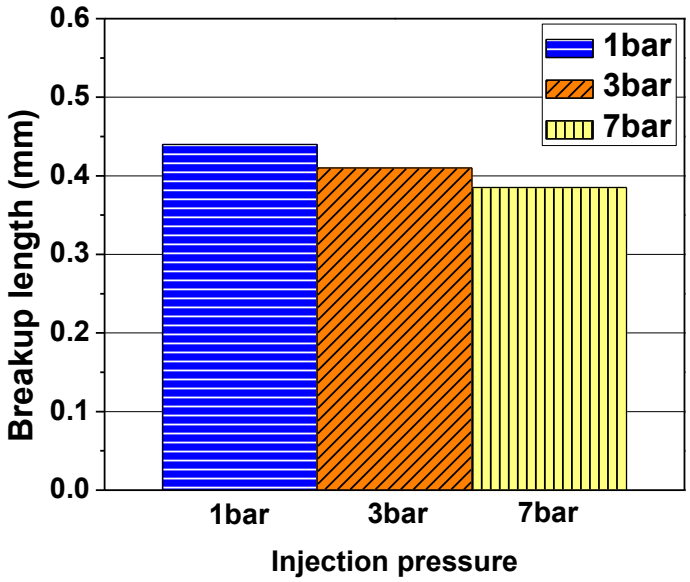

Figure 7.18 Comparison of liquid breakup length at different ambient pressures

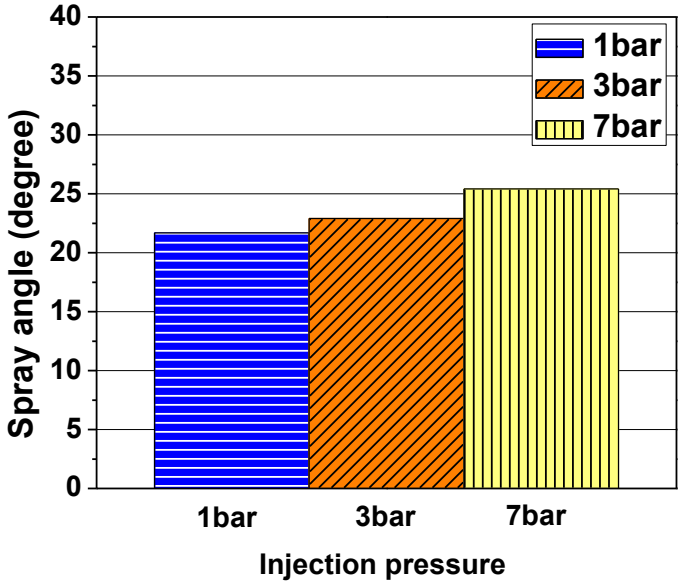

Figure 7.19 Comparison of liquid breakup length at different ambient pressures

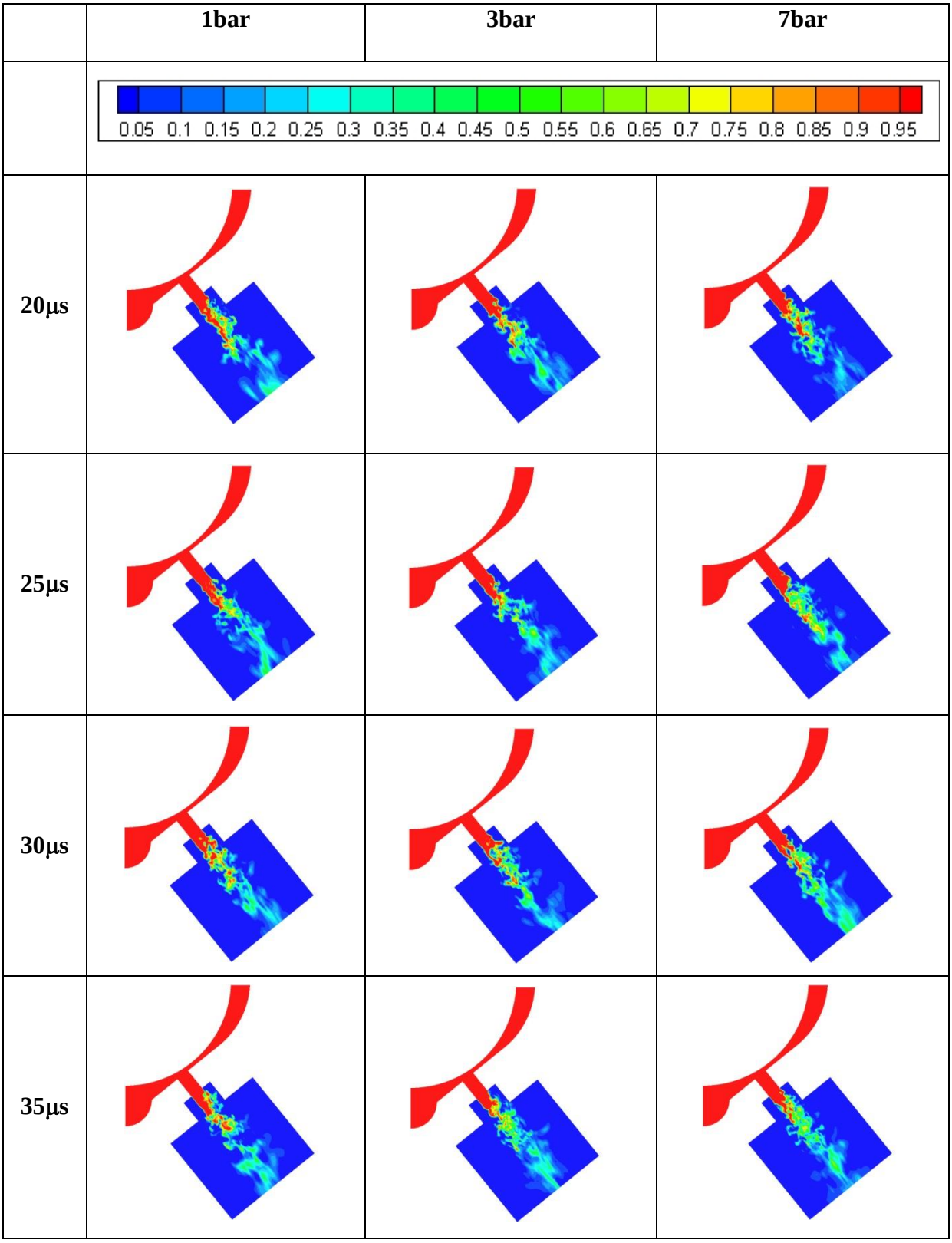

Figure 7.20 Distribution of liquid at different flow time and ambient pressures

The comparisons of average droplet diameters at different ambient pressures are shown in Figure 7.21. At the nozzle exit (plane A-A), the average droplet diameters for different ambient pressures are not affected by ambient pressure. However, the average droplet diameter at the counter-bore exit (plane B-B) dropped by 67 % and the influences of ambient pressure are significant. As mentioned previously, the higher drag force from the higher ambient pressure speeds up the liquid primary breakup process and causes a shorter breakup length. However, the average droplet diameter is larger at a higher ambient pressure because the droplet internal kinetic energy and velocity are decreased by the high ambient density. The downstream flow at planes C-C and D-D demonstrate a similar trend. Comparing the average droplet diameter between planes C-C and D-D, it can be seen that the droplet diameter decreases by 12.7 % at 1 bar, 7.2 % for 3 bar and 5.7 % for 7bar. From these results, it is observed that the increase of ambient pressure also slows down the droplet breakup speed.

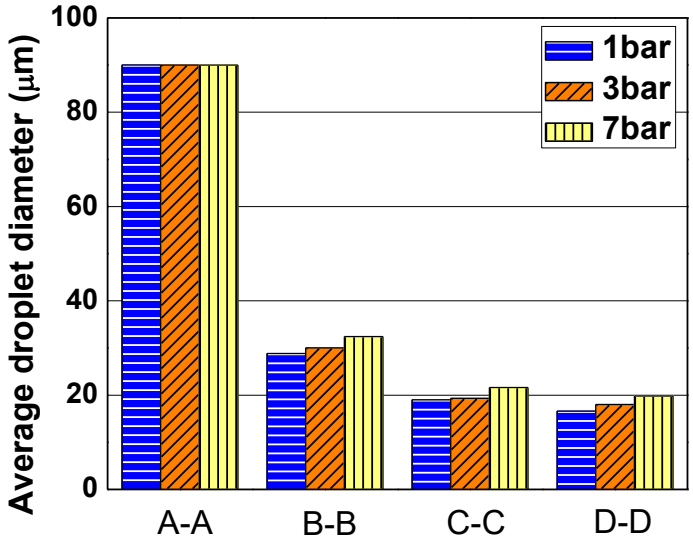

Figure 7.21 Average droplet diameters at different measuring planes at different ambient pressures

7.3 Modelling and Experiment of Secondary Breakup

In the previous sections, the spray characteristics at primary breakup regions were investigated by numerical methods due to the limitations of the experimental set-up. In this section, the more detailed spray characteristics in the secondary breakup region under different injection pressures and ambient pressures are studied by a high speed camera and the PDPA system. Moreover, the results from the optical methods are used to compare with the spray characteristics in the primary breakup process and validate the KIVA spray model to understand the comprehensive spray development.

7.3.1 Modelling and Experimental Conditions

In Table 7.2 are the testing conditions for the PDPA system and high speed images test.

Table 7.2 Testing conditions for PDPA system

	Test Conditions
Test Fuel	**Iso-octane**
Injection Pressure	**50, 100, 150 bar**
Ambient Pressure	**1bar, 3bar, 7bar**
Injection Duration	**1ms**

The testing injection pressure is examined by 50, 100 and 150 bar. The difference of injection pressure between this section and the previous section (nozzle flow simulation), at 200 bar cannot be investigated due to the experiment limitations of the fuel injection system. The ambient pressure is investigated by 1, 3 and 7 bar (the same testing conditions as CFD simulation from the previous section). The injection duration time of 1ms was chosen.

7.3.2 Spray Penetration Length and Spray Angle

The images of the spray development from the high speed camera at different injection pressures and ambient pressures are shown in Figure 7.22. From these comparisons of spray images, it can be observed that the different operating conditions directly change the spray penetration length and spray angle. By measuring the spray patterns, the detailed spray penetration length and spray angle are analysed and measured from high speed images. In Figure 7.23, the simulation results of the spray images from KIVA-3V at 0.8ms show an agreement of spray shape which compares with the high speed images.

	50bar-1bar	100bar-1bar	150bar-1bar	150bar-3bar	150bar-7bar
0.6ms	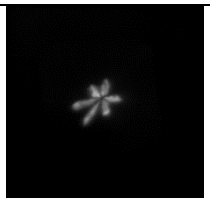	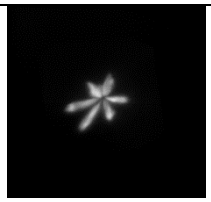	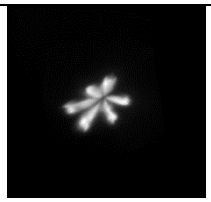	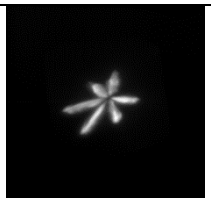	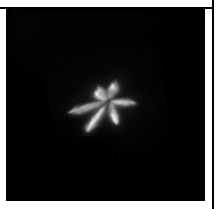
0.8ms	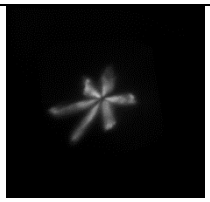	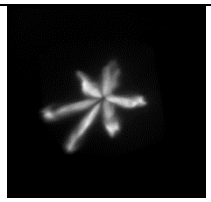	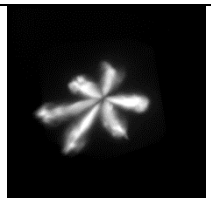	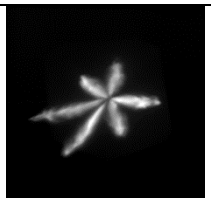	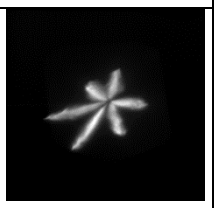
1.0ms	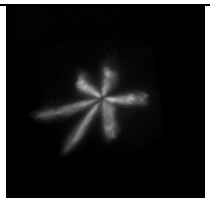	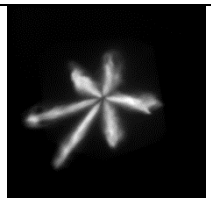	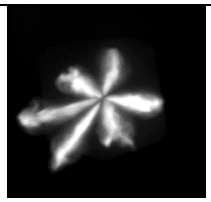	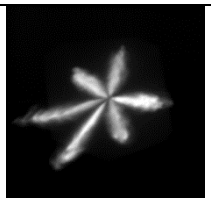	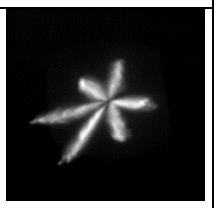
1.2ms	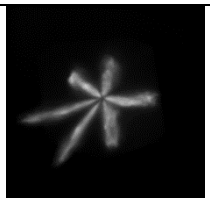	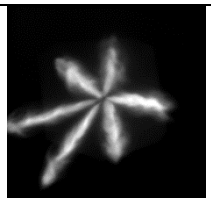	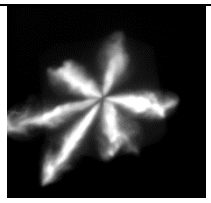	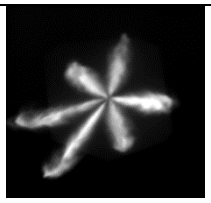	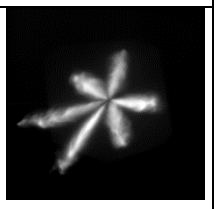

Figure 7.22 High speed images at different injection pressures and ambient pressures

	50bar-1bar	100bar-1bar	150bar-1bar	150bar-3bar	150bar-7bar
0.8ms	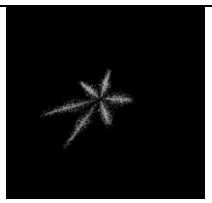	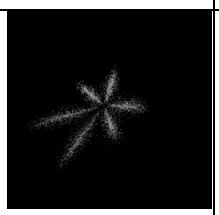	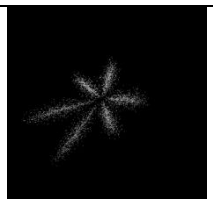	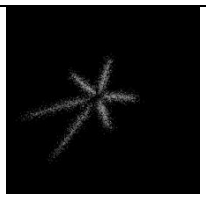	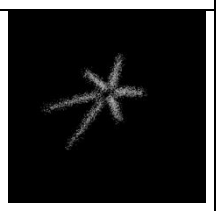

Figure 7.23 High speed images at different injection pressures and ambient pressures

In the previous chapter, the comparison of mass flow rate between the nozzle flow simulation and experimental results revealed that the effect of needle movement on mass flow rate is not significant, as shown in Figure 4.8. However, due to the transient needle lift in the real GDI nozzle, the injection velocity gradually increases when the nozzle needle gradually opens. The profile of mass flow rate during the injection time (1 ms) by using the Langrangian approach (KIVA3V) is shown in Figure 7.24. The profile of mass flow rate is established by calibrating the spray penetration length from experimental data. It can be observed that the injection mass flow rate (injection velocity) gradually increases and the area under the curve presents the total injection mass.

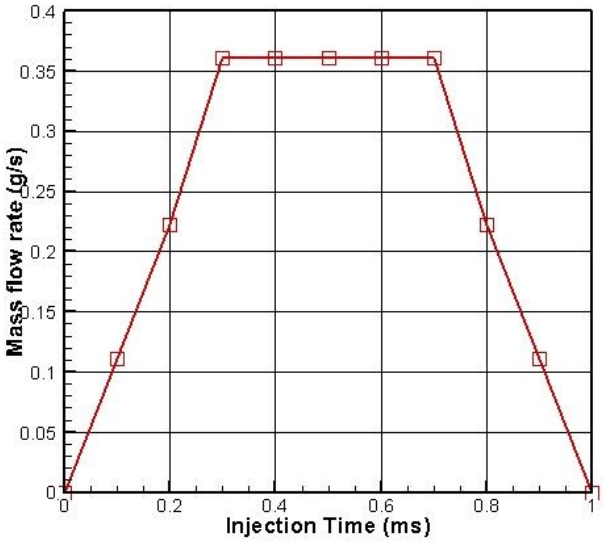

Figure 7.24 Profile of mass flow rate during the injection time

The calibration of the model parameters in the KIVA nozzle and spray model is based on the experimental data for 150 bar injection pressure and 1 bar back pressure. After the spray model is calibrated, the parameters of the nozzle and spray model are not changed for other conditions of injection and back pressure in spray modeling studies

The comparisons of spray penetration length for different injection pressures and ambient pressures are shown in Figure 7.25. From the previous results, different operating conditions are the main factors for determining the length of penetration. From Figure 7.25 (a), the differences of initial velocity can be found at an early injection time (between 0.35 and 0.45ms) from the spray penetration length. The 150 bar injection pressure has the longest spray penetration length than the other lower injection pressures. This can be illustrated by the nozzle exit velocity from the numerical results in Figure 7.3. To compare the final penetration length, the length of 150bar is higher by: 42.5 % than the 50 bar and 17.6% than the 100 bar. The effects of penetration at different ambient pressures are compared in Figure 7.25 (b). It illustrates that the differences between 1 and 3 bar are not significant in the early stage due to the ∇P between the nozzle inlet and exit being small. However, the ambient pressure still affects spray penetration after 0.55 ms because the downstream spray has more contact area to take on more ambient pressure. Furthermore, the simulation results from KIVA-3V show the comparisons of penetration length at different injection pressures and ambient pressures. For each testing condition, the CFD model shows an agreement with the experimental data.

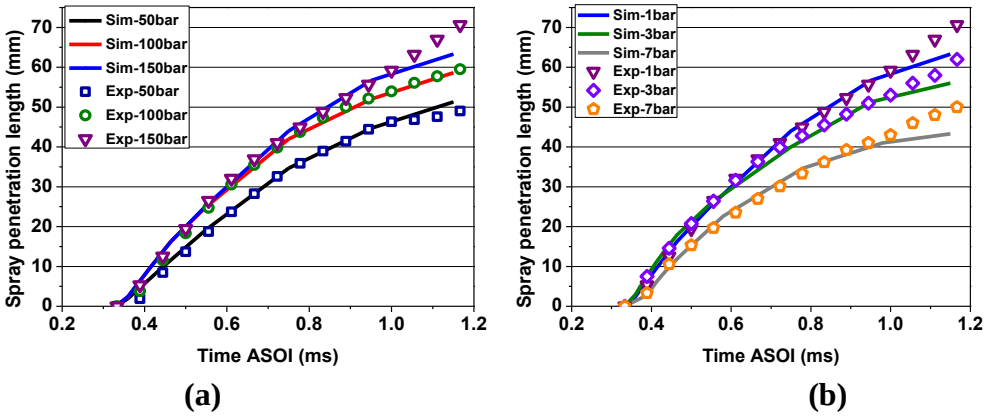

Figure 7.25 Influences of spray penetration length on (a) injection pressure (b) ambient pressure

The influences of injection pressure and ambient pressure on spray angles are clearly seen in Figure 7.26. The spray angle changes from 17.2° to 21.2° with the increase of injection pressure from 50 to 150 bar in Figure 7.26 (a). These results not only illustrate that the changes of injector pressure affect the development of penetration, but also alter the spray angle. The numerical results of the spray angle from the previous section are also compared with the high-speed images. The error between the experimental data and the CFD is around 1 to 5 % at different injection pressures. Figure 7.26 (b) shows the changes of spray angle at different ambient pressures. It can be seen that the spray angle increased by 11.9 % from 1 bar to 3 bar and by 14 % from 1bar to 7bar. The numerical results of the spray angle have similar trends to the high speed images. From Figures 7.7 and 7.18, the breakup length decreases (faster breakup process) when injection pressure increases and ambient pressure increases and then produces a larger spray angle.

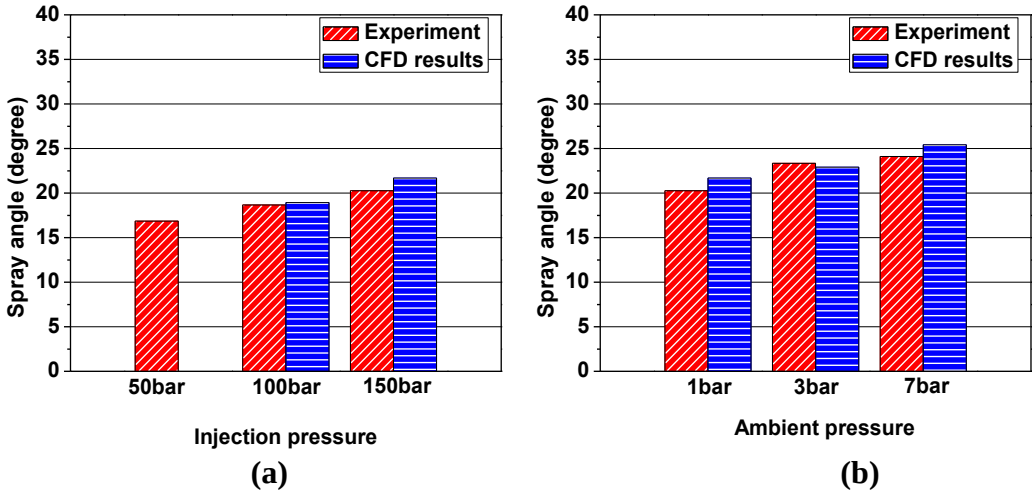

Figure 7.26 Influences of spray angle on (a) injection pressure and (b) ambient pressure

7.3.3 Droplet Size and Velocity at Different Injection and Ambient Pressures

The typical distributions of droplet velocity against time at the measuring point of 36.4 mm from the nozzle tip are shown in Figure 7.27. After fuel injection, the time for the spray to reach this measuring point is called the injection delay which is the sum of spray travelling time and solenoid delay time from the injector. The structure of this velocity profile can be separated into two parts: “main spray (head)” and “spray tail” (Tian 2010). In the region of the main spray, the head with high kinetic energy droplets show the obvious plateau and then the droplet velocity drops down to a low level in the spray tail region. In order to compare clearly the average velocity at different injection pressures and ambient pressures, the development of mean droplet velocity is presented in the red line which averages all droplet velocities at each time.

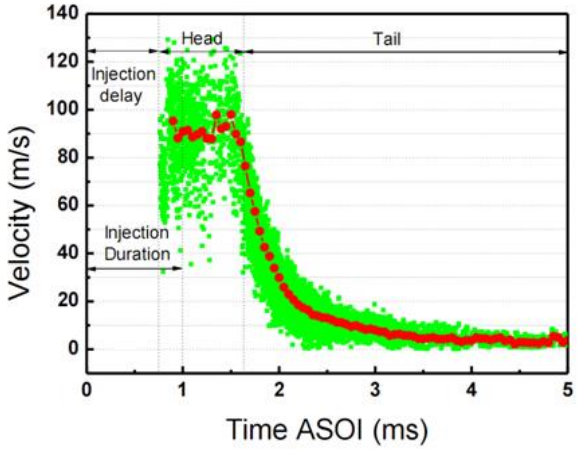

Figure 7.27 Distribution of droplet velocity data at 150bar injection pressure and ambient pressure at 36.4mm from the nozzle tip

Figure 7.28 shows the average droplet velocity under different injection pressures and ambient pressures at different measuring points (36.4 and 45.5 mm). Firstly, for the injection delay time, the time is, ostensibly, delayed by the decrease of injection pressure due to lower droplet velocity. Moreover, it is clearly seen that the average droplet velocity of 150 bar injection pressure can result in droplet achieving velocities of around 95 m/s and the velocity reducing to 58 m/s with 50 bar injection pressure in Figure 7.28 (a-1). The difference of droplet velocity between different measuring points can be observed as well. At the measuring point of 45.5 mm, the average droplet velocity of 150 bar is dropped from 95 m/s to 85 m/s from a measuring point of 36.4 mm in Figure 7.28 (a-1) and (a-2); as the drag force of the surrounding gases on the droplets increased resulting in lower droplet velocity. Unlike the unobvious trend in the spray penetration length between 1 bar and 3 bar ambient pressure in Figure 7.25.b, the average droplet velocity can be observed between 1 bar and 3 bar due to more drag force to the droplets, as displayed in Figure 6-30 (b-1).

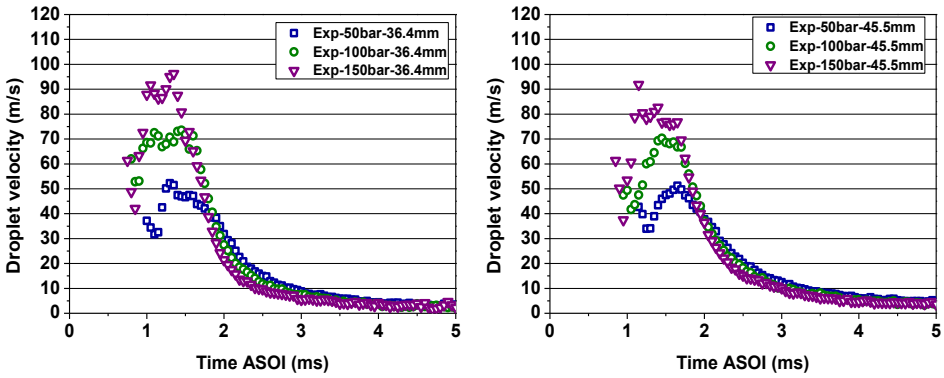

(a-1) 36.4mm (a-2) 45.5mm

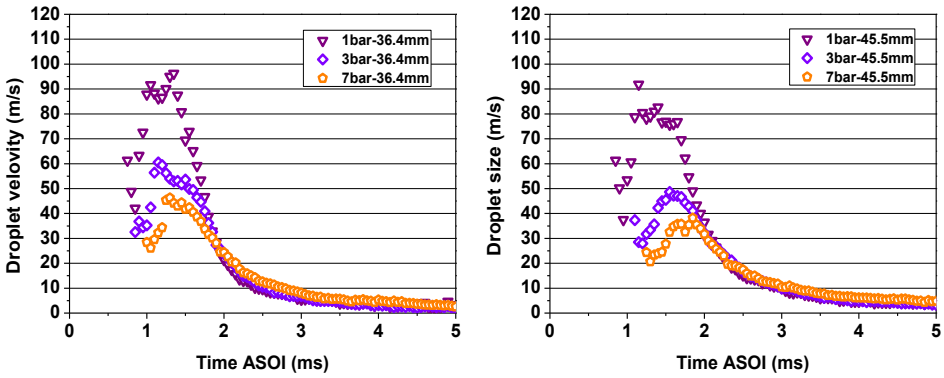

(b-1) 36.4mm (b-2) 45.5mm

Figure 7.28 Comparison of mean droplet velocity under different injection pressure and ambient pressures at 36.4mm and 45.5mm from the nozzle tip

The comparison of Figure 7.28 (b-1) and (b-2) and the effects of increasing ambient pressure are presented. To compare two measuring point positions at 36.4 and 45.5 mm, it can be seen that the average droplet velocity is dropped by 16 % for 3bar and 20% for 7bar. Furthermore, on comparing the influences of injection and ambient pressure on droplet velocity, it can be found that the drag force from the ambience can affect efficient droplet velocity rather than the droplet internal kinetic energy. Figure 7.29 shows the validations of the spray models with experimental droplet velocity at different injection and ambient pressures. The results from the CFD spray model show a similar trend of droplet velocity distribution and value to the PDPA data.

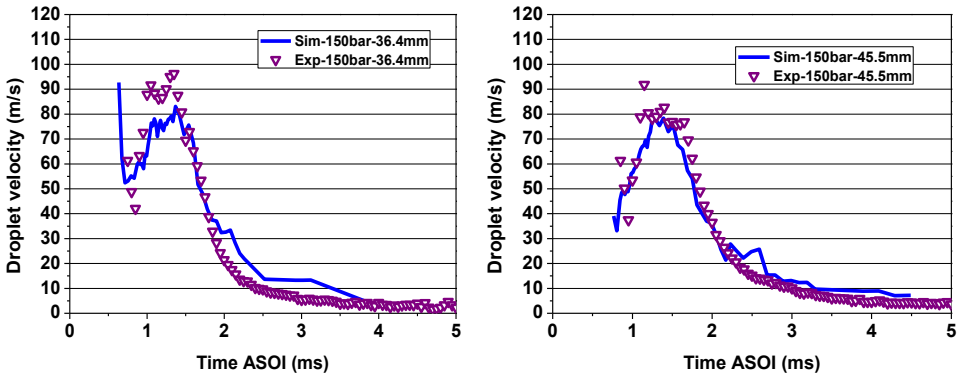

(a-1) 36.4mm (a-2) 45.5mm

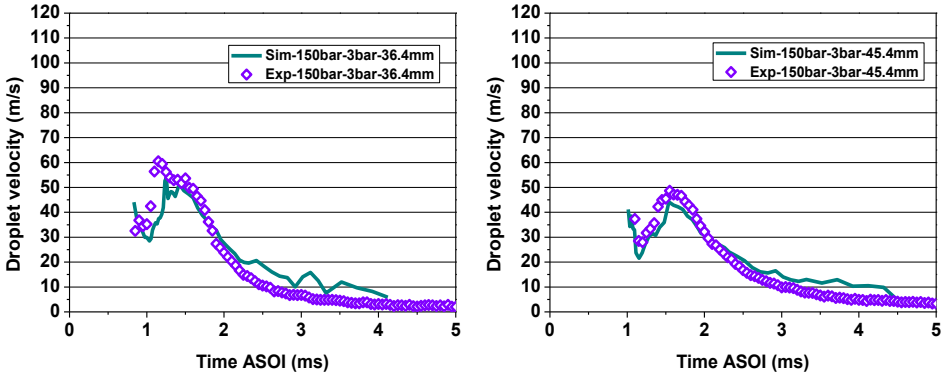

(b-1) 36.4mm (b-2) 45.5mm

Figure 7.29 CFD validation of mean droplet velocity at different injection and ambient pressures at 36.4mm and 45.5mm from the nozzle tip

The comparisons of Arithmetic Mean Diameter (AMD) for different injection pressures and ambient pressures at the measuring points 36.44 and 45.5mm from the nozzle are shown in Figure 7.30. The high injection pressure causes higher exit velocity from the nozzle which produces stronger turbulence (higher Weber number) rather than lower injection pressure. Due to these influences during the atomisation process, the AMD of the higher injection pressure was lower than the other two lower injection pressures. When discussing ambient pressure, to explain why the AMD is raised with increased ambient pressure, the liquid fuel jet turbulence level, Weber number and ambient drag force have to be considered.

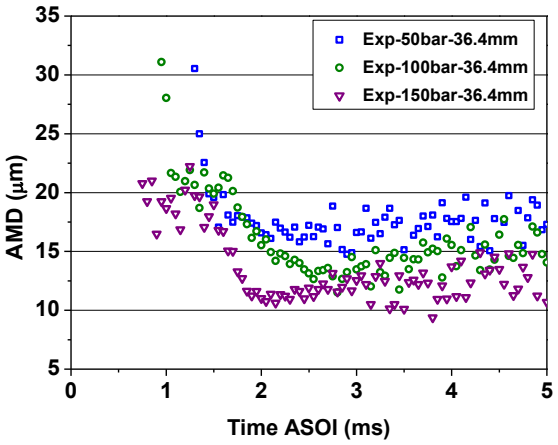

(a-1) 36.4mm

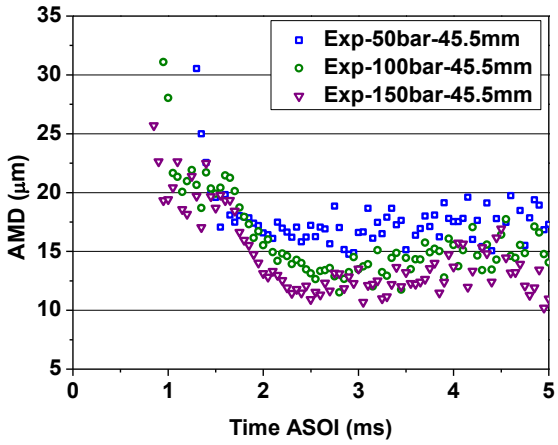

(a-2) 45.5mm

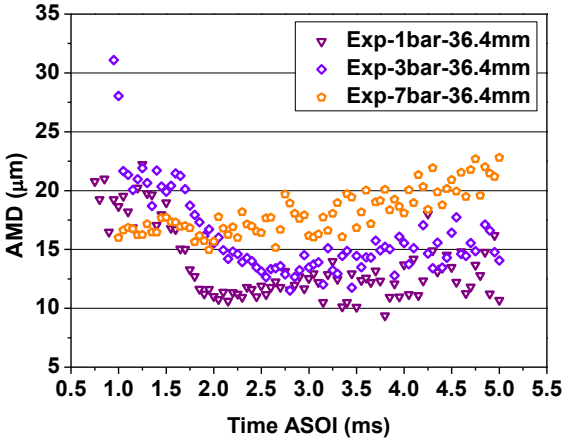

(b-1) 36.4mm

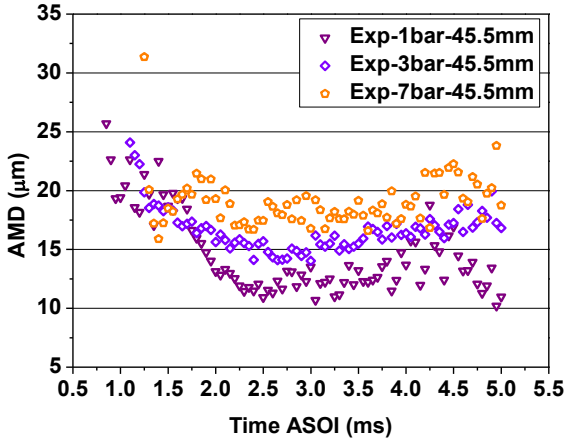

(b-2) 45.5mm

Figure 7.30 Comparison of mean droplet velocity under different injection pressure at (a) 36.4mm and (b) 45.5mm from the nozzle tip

The increased ambient pressure reduced the injection velocity and consequently reduced the *Re* and *We* which increased the AMD. Moreover, the increased ambient pressure raised the ambient density and consequently increased the drag force and shear force which tends to reduce the AMD. Since a larger AMD is observed with increased ambient pressure, it is concluded that the loss of droplet momentum from increased ambient pressure has a dominant effect in determining the AMD, rather than the drag force.

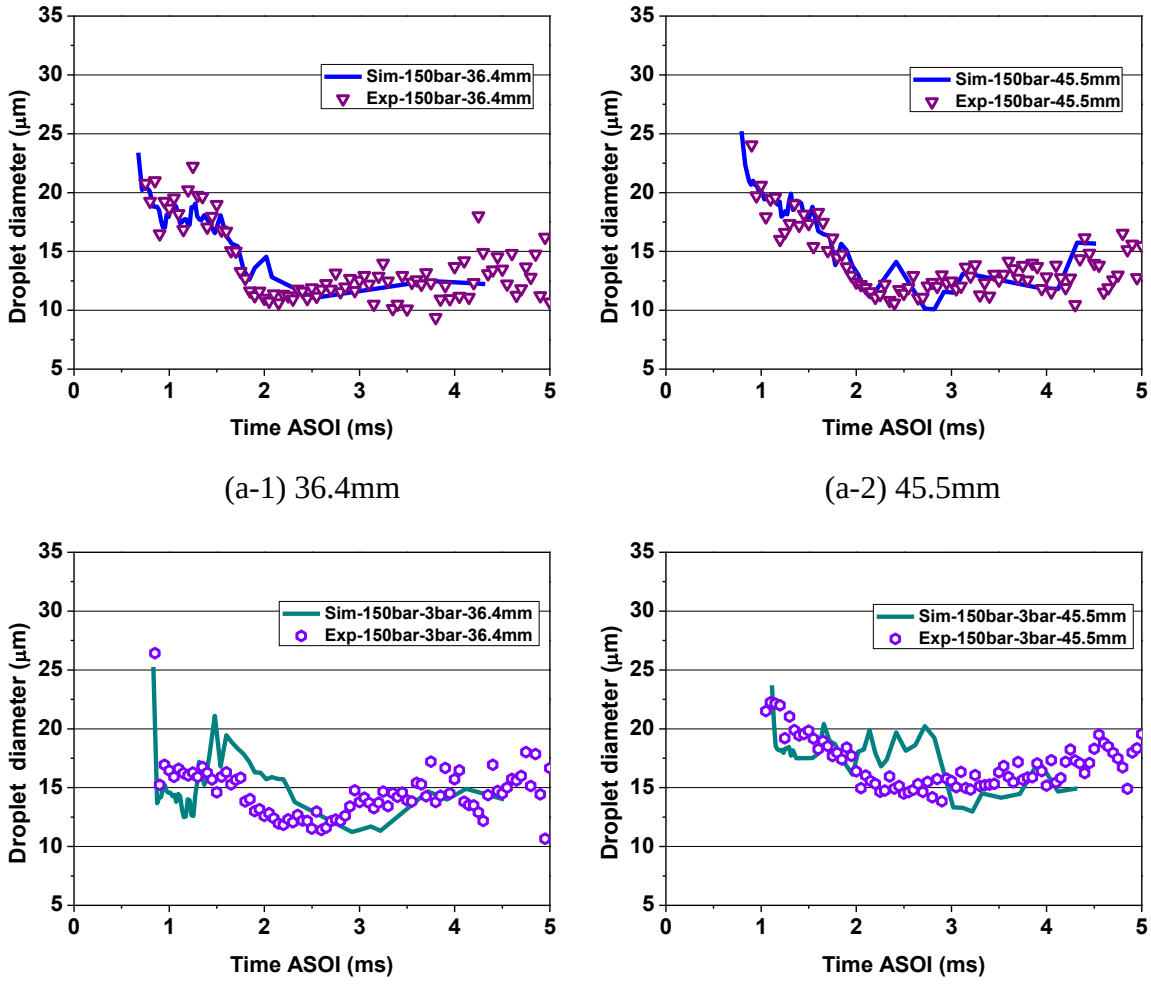

Figure 7.31 CFD validation of mean droplet velocity at different injection pressure at (a) 36.4mm and (b) 45.5mm from the nozzle tip

Figure 7.31 (a-1 and 2) presents the CFD validation of droplet size for 150bar injection pressure which show a strong agreement with the PDPA data at different measuring points. However, for the validation of ambient pressure, there are slight differences between the numerical results and the experimental data. The distributions of SMD under different injection pressures and ambient pressures at different measuring positions along the spray development are shown in Figure 7.32. The results indicates that the SMD increases when the measuring point moves downwards from 27.3 to 54.6 mm from the nozzle tip; the reason is that the droplet will evaporate during spray development. The quantity of droplets of different size is generated

after the liquid jet primary breakup and droplet secondary breakup. The droplets of a small size can evaporate easily compared with the larger droplets; this could cause the small droplets to disappear and the larger droplets would remain. This can explain why the SMD increased the spray downstream.

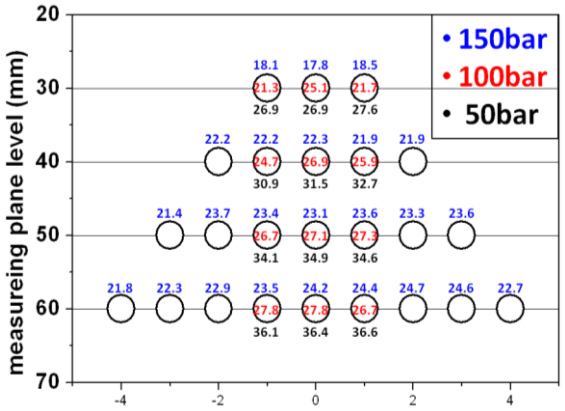

(a) Different injection pressures

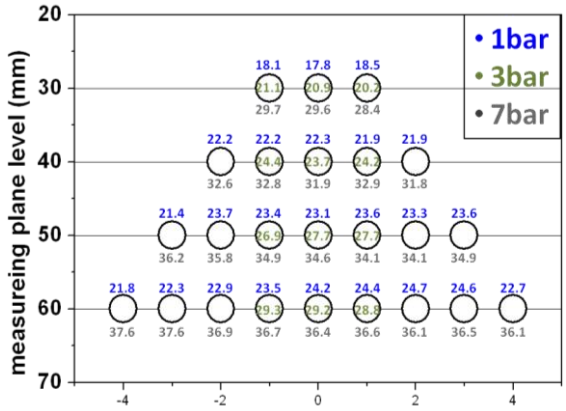

(b) Different ambient pressures

Figure 7.32 Distribution of SMD along spray development for (a) different injection pressures and (b) ambient pressures

7.4 Summary

This chapter separately investigates the changes of the spray characteristics under different injection pressures and ambient pressures in the near field and secondary breakup regions by numerical methods and optical methods. The spray characteristics in a primary breakup region from CFD methods show a similar trend to the experimental data and present some agreement

with experiments such as the spray angle. The numerical results in the primary breakup region not only show the detailed effects under different operating conditions but also prove the accuracy of the initial nozzle data for the spray models simulating the spray development. In these investigations, several key findings have been found which can add value and importance for future applications:

- Injection pressure has significant influence on the spray characteristics in the primary breakup region and secondary breakup region. Due to the high exit velocity from the higher injection pressure, the SMD decreased by around 23.6% from 50 to 100 bar and 33.5% to 150 bar.

- The influences of ambient pressure on the spray characteristics at the nozzle exit is insignificant. This is due to the liquid surface not being affected by ambient pressure at the beginning. However, when the liquid flows further down jet and the droplets would bear more drag force from ambient pressure.

- The liquid breakup length can be used to represent the speed of jet breakup which can be an important parameter to evaluate the spray angle. In higher injection pressure, the shorter liquid breakup length causes a larger spray angle. In higher ambient pressure, the lower exit velocity causes a larger spray angle because a higher drag force from higher ambient pressure makes the liquid droplets take off easier from the liquid jet.

- The distributions of the SMD at different injection pressures and ambient pressures all show a larger value in the far measuring positions. This is due to the disappearance of the small droplets which had been evaporated during the spray development.

Chapter 8

EFFECT OF FUEL PROPERTIES ON INCYLINDER SPRAY CHARACTERISTICS

This chapter investigates the microcosmic and macroscopic spray characteristics of DMF and ethanol in comparison to iso-octane by using numerical and experimental methods. The experimental methods such as a high speed camera and a PDPA system are used to examine the effects of fuel properties on spray characteristics such as cone angle, spray penetration length, droplet size and velocity. By using a numerical method, it further gives more insight into how fuel properties affect in-nozzle fuel flow and spray behaviours in the injectors' near-field region.

8.1 Introduction

In the past decade, due to the increasing consciousness of the energy crisis and the development of production methods, bio-fuels have gradually been promoted as an alternative fuel to gasoline, or as the addition to gasoline. These types of bio-fuels not only can improve the fuel economy but also decrease the environmental impact. Several investigations (Daniel 2012, Daniel 2012, Wang 2012) indicate that the CO_2 emissions of bio-fuel are lower than gasoline by around 15% and the use of bio-fuels increases engine operating time by up to 10%.

Several new generation bio-fuels such as DMF and ethanol are intensively investigated for their different fuel properties on the spray characteristics, engine performance and emissions..

DMF has been produced with a new catalytic strategy from glucose (Post 2002). The boiling point and energy density of DMF (365K and 37.8 MJ/L) are 20 degrees centigrade higher and 40% higher than ethanol (351 K and 24 MJ/L) respectively, giving it significant improvements on fuel economy and combustion. Ethanol is mainly used as a bio-fuel additive for gasoline which can be produced from corn, vegetables and other ethanol producing products. Due to the oxygen component of ethanol, it is helpful in reducing PM emissions.

This chapter investigates the effects of fuel properties on the spray characteristics in the nozzle flow, near field flow, secondary breakup region and engine flow field by using the CFD method and an experimental method respectively.

8.2 Fuel Properties and Experimental Conditions

The test conditions to investigate the effect of the different fuel properties on the spray characteristics are shown in Table 8.1. The test bio-fuels, DMF and ethanol, are examined and compared to iso-octane in order to understand the influences of different fuel properties on the spray behaviours.

Table 8.1 Testing conditions for numerical and experimental method

	Test Conditions
Test Fuel	**Iso-octane, DMF, Ethanol**
Injection Pressure	**150 bar**
Ambient Pressure	**1bar**
Injection Duration	**1 ms**

The injection pressure in the experimental and the numerical method uses 150 bar in 1bar ambient pressure. The injection duration in this test used is 1ms. In order to compare the spray characteristics of different bio-fuels, the fuel properties of iso-octane, DMF and ethanol are shown in Table 8.2. These fuel properties are used for the following comparison.

Table 8.2 Fuel properties of bio-fuels

	Iso-octane	**DMF**	**Ethanol**
Molecular Formula	C_8H_{18}	C_6H_8O	C_2H_6O
H/C Ratio	**2.25**	**1.333**	**3.0**
O/C Ratio	**0**	**0.167**	**0.5**
Density @293K (kg/m^{-3})	**702.6**	**889.7**	**789**
Molar Mass (g/mol)	**114.2**	**96.13**	**46.07**
Vapour Pressure@293K (pa)	**5500**	**4728**	**6539**
Viscosity@293K(k Pa s)	**$5.028x10^{-7}$**	**$6.503x10^{-7}$**	**$1.149x10^{-6}$**
SurfaceTension@293K (N/m)	**0.01816**	**0.02603**	**0.02406**

8.3 Modelling and Experimental Study of Spray Macro and Micro Parameters

8.3.1 Mass Flow Rate and Nozzle Exit Velocity

The comparisons of the mass flow rate for different bio-fuels at 150 bar injection pressure are examined by using the experimental method. These experimental data of the mass flow rate also provide a validation with a numerical model. Figure 4.8 presents the measured mass fuel flow rate for different bio-fuels at different injection durations. By using different injection durations, the experimental data can be examined for consistency and stability. The results show that the mass flow rate produce a similar value at different injection durations. From the

results, it can be found that DMF has the highest value of mass flow rate whereas iso-octane shows the lowest value. This discrepancy of the mass flow rate can be explained by that the mass flow rate is proportional to the fuel density, the density of DMF is the largest value (889.7 kg/m-3) while iso-octane has the smallest density (702.6 kg/m-3), as the volumetric flow rate remains roughly constant under the same injection pressure.

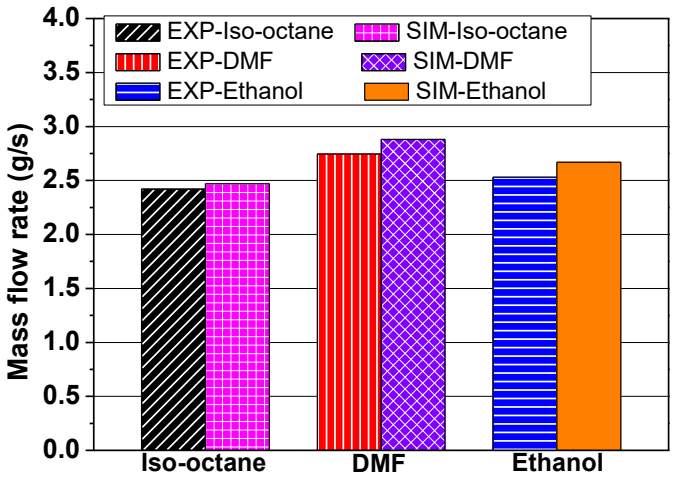

Figure 8.1 Comparison of mass flow rate between the experimental and numerical method

In Figure 8.1, the measured fuel flow rate is used to validate against the simulation results from the nozzle flow simulation by using ANSYS-Fluent. This can be used to examine the correctness and reliability of the nozzle geometrical design and the CFD modeling set up. From the comparison between the experiment and simulation, the difference is approximately 2.1% for iso-octane, 4.8% for DMF and 5.5% for ethanol respectively. This indicates the CFD nozzle model can accurately predict the mass flow rate with a real size GDI injector geometry, although that the slightly over-predicted flow rate is observed. This could be due to the simplification of the nozzle condition such as the nozzle wall friction or unknown cavitation effects inside the nozzle

The average exit velocity at the inner hole measuring plane A-A for different bio-fuels is shown in Figure 8.2. On the right-hand side, it shows the location of the measuring planes in nozzle geometry. From the comparison of the velocity, it shows that the highest exit velocity is observed from iso-octane (150 m/s) and the DMF has the lowest velocity (136 m/s); this is because of the heavier liquid mass (bigger liquid density) for DMF (889.7 kg/m-3), which slows down the nozzle exit velocity.

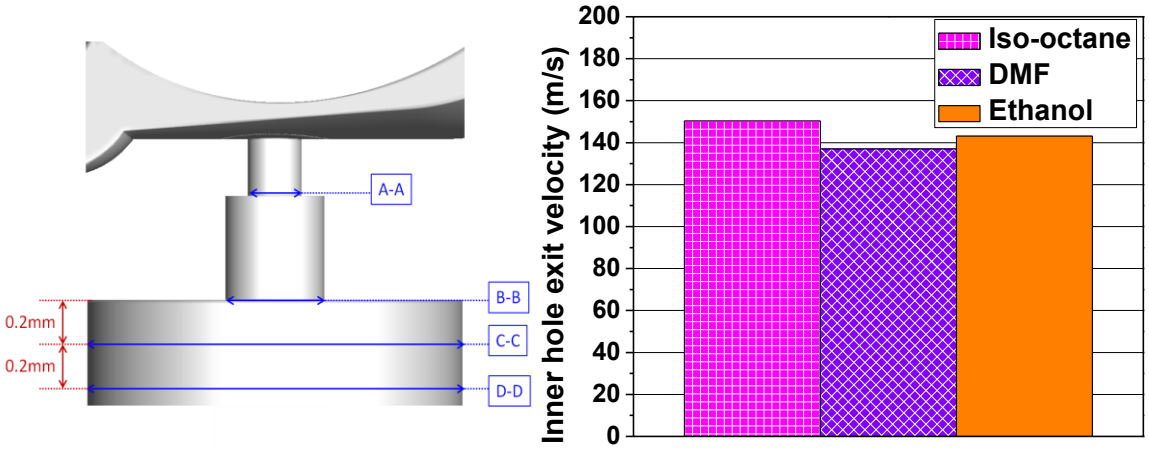

Figure 8.2 Comparison of average exit velocity at the inner hole exit plane A-A

However, due to the different fuel properties, it is better to use Reynolds (*Re*) number and Weber number (*We*) to present the intensity in the nozzle exit. The definition of *Re* and *We* numbers are expressed below

$$\mathrm{Re} = \frac{\rho_{air} V L}{\mu} \qquad \text{(Equation 8.1)}$$

$$\mathrm{We} = \frac{\rho_{liquid} V^2 L}{\sigma} \qquad \text{(Equation 8.2)}$$

Where ρ_{liquid} is the liquid density, ρ_{air} is the air density, V is the mean velocity, L is the characteristic length, here it is the hole diameter, σ is the liquid surface tension and μ is the dynamic viscosity of fluid.

The above definitions show respectively their physical meaning of *Re* and *We* number. Re number represents the intensity of turbulence level of fluid. For *We* number, it presents a measurement of the relative importance of the fluid's inertia compared to its surface tension. The comparison of the *Re* number for different bio-fuels is shown in Figure 8.3 (a). The iso-octane has the biggest *Re* number compared to the other bio-fuels. The *Re* number of ethanol has an obvious difference compared to the other two fuels; this is because of the larger viscosity of ethanol, resulting from the larger shear stress inside the fluid which then enhances the damping of velocity oscillation. The comparison of the *We* number in Figure 8.3 (b) shows a similar trend as in Figure 8.2. Iso-octane has the largest *We* number in these three different bio-fuels. According to the comparison of exit velocity, the *Re* and *We* for the three bio-fuels, it can be predicted that the atomisation of iso-octane will be more intensive. The DMF and ethanol still require more results and discussion.

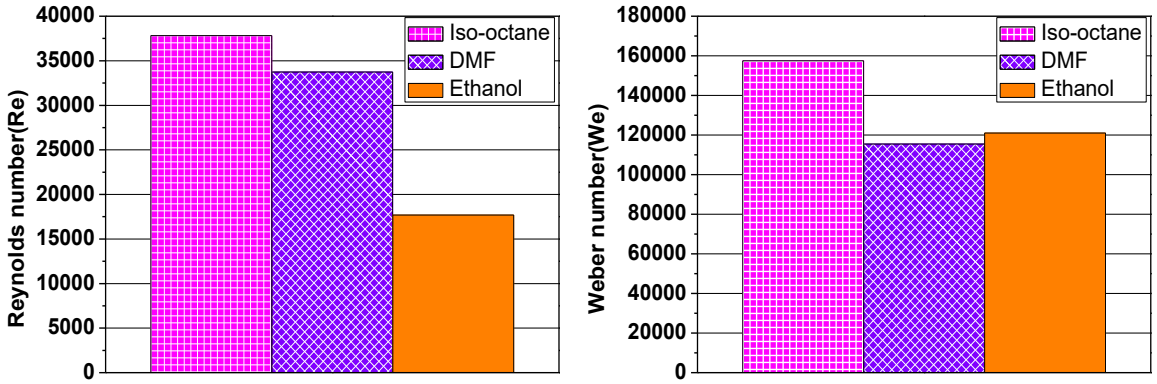

(a) Reynolds number **(b) Weber number**

Figure 8.3 Comparison of (a) Reynolds number and (b) Weber number for three bio-fuels

8.3.2 Spray Angle

In order to investigate the effects of the fuel properties for spray angle variations, the experimental and simulation results for different bio-fuels from using the high speed camera and KIVA3V are shown in Figure 8.4.

	0.2ms	**0.4ms**	**0.6ms**	**0.8ms**
Experiment Iso-octane	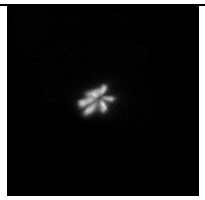	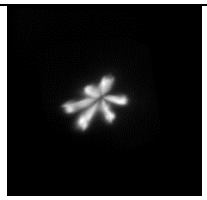	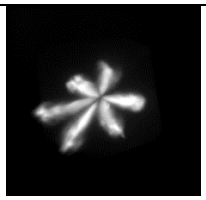	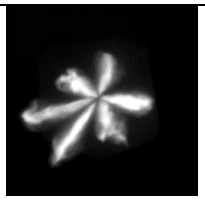
Simulation Iso-octane	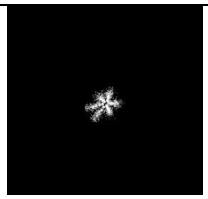	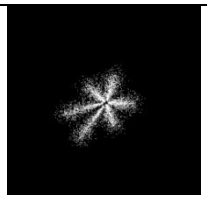	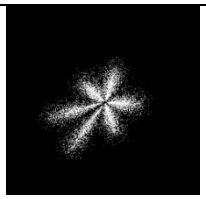	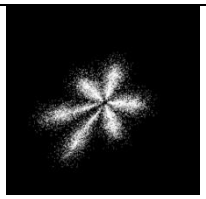
Experiment DMF	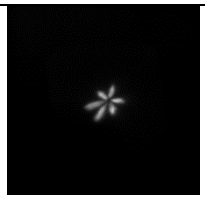	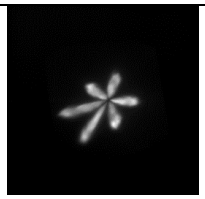	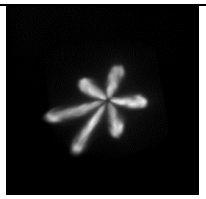	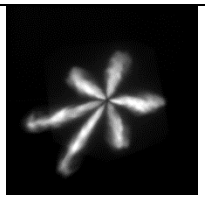
Simulation DMF	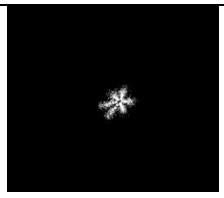	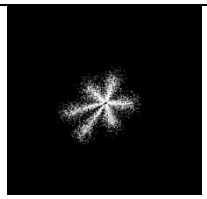	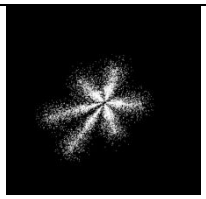	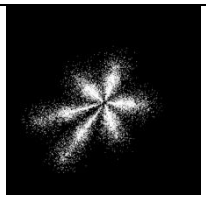
Experiment Ethanol	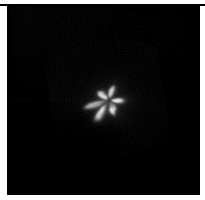	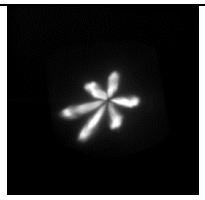	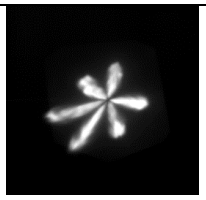	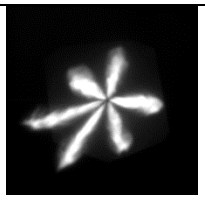
Simulation Ethanol	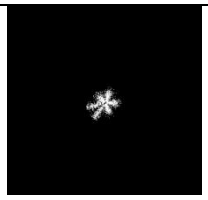	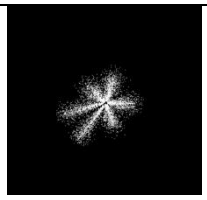	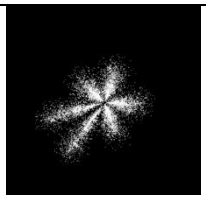	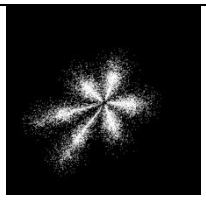

Figure 8.4 Experimental and simulation images of spray development for different bio-fuels

The simulated spray images from KIVA3V shows a reasonably good agreement in the spray development with the high speed photographs. From these images, it can be seen that the spray angle of DMF is obviously smaller than the cone of iso-octane and ethanol. In addition, iso-octane has the largest spray cone angle due to the higher *Re* and *We* numbers in Figure 8.3.

The comprehensive comparison between the experimental data and simulation results (from ANSYS-Fluent) of the spray cone angle is shown in Figures 8.5 and 8.6. It is clearly shown that the predicted spray cone angle agrees well with the measured ones, especially the same variation trend with different fuels. To compare DMF and ethanol, although the DMF has a higher *Re* number than ethanol in Figure8.3 (a), its spray angle is smaller than ethanol because the *We* number of DMF is smaller. This indicates that fuel surface tension force is a dominant factor in determining spray cone angle.

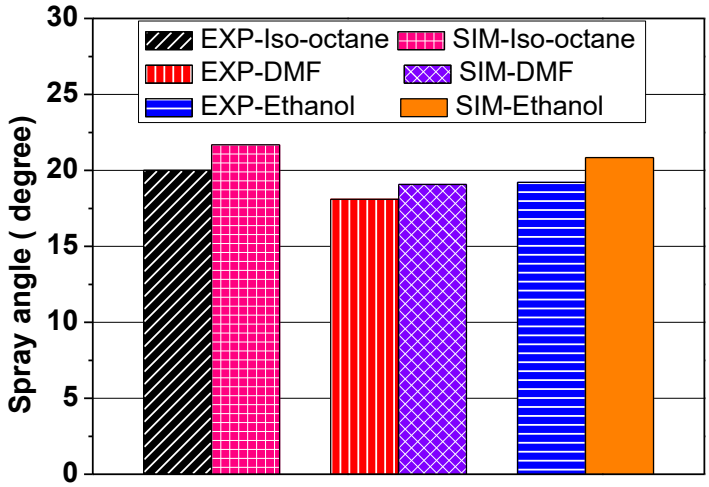

Figure 8.5 Comparison of spray angle between experimental and simulation data for different bio-fuels

Iso-octane	DMF	Ethanol
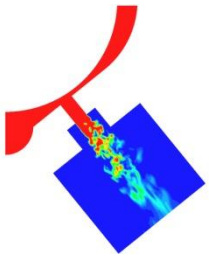	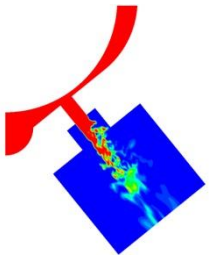	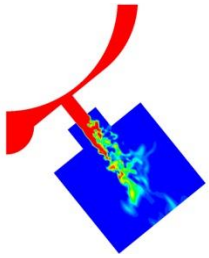

Figure 8.6 Distributions of liquid in GDI nozzle for different bio-fuel at 30μs

8.3.3 Spray Penetration and Liquid Breakup Length

Different fuel properties such as liquid density, surface tension, vapour pressure and viscosity not only affect spray cone angle but also result in different liquid penetration length. The comparison of penetration length is shown in Figure 8.7.

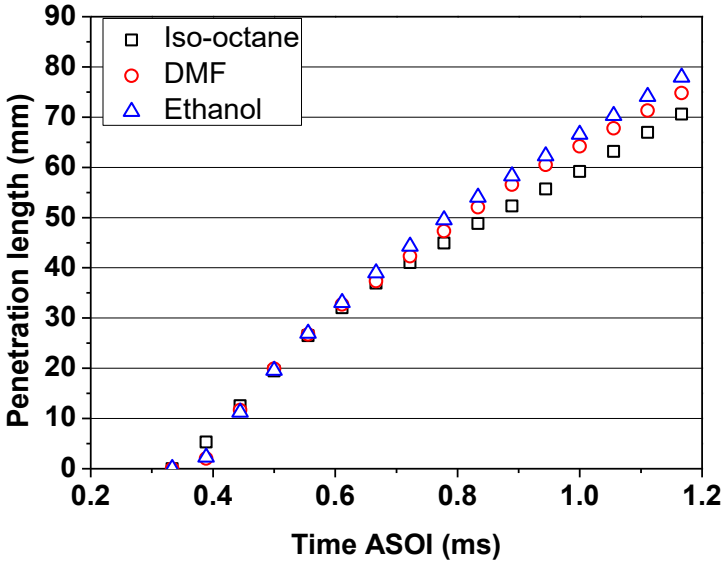

Figure 8.7 Comparison of penetration length for different bio-fuels

The shorter spray penetration length is observed with iso-octane as compared to DMF and ethanol fuels. This is due to the enhanced fuel atomization process associated with higher flow instability, as indicated by higher *Re* and *We* number. On the other hand, the comparison

between DMF and ethanol shows that the penetration length of ethanol is slightly longer than DMF by 3% at the end of an injection time of 1.0ms. The analysis on *Re*, *We* number and spray angle points out that the liquid viscosity might be the major factor in affecting the liquid penetration length, whilst the effect of the surface tension might be secondary, in general, higher Re number of flow, higher turbulence level. Therefore, higher liquid surface instability wave growth resulted from higher turbulence level in DMF fuel spray, most likely enhances the droplet secondary breakup process, leading to shorter penetration length, as compared to ethanol. Based on these penetration lengths of different bio-fuels, the numerical validation of the KIVA3V-spray models is shown in Figure 8.8. It shows a good agreement between the experimental and numerical penetration length.

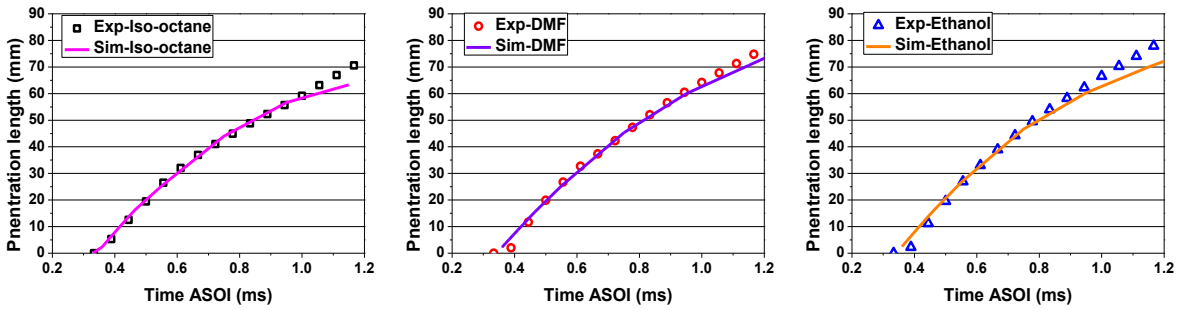

Figure 8.8 Numerical validation of different bio-fuels penetration length for KIVA3V

In the nozzle flow and near field flow, the liquid breakup length can be used to represent the intensity of fuel atomisation. The comparison of liquid breakup length for different bio-fuels by using ANSYS-Fluent is shown in Figure 8.9.

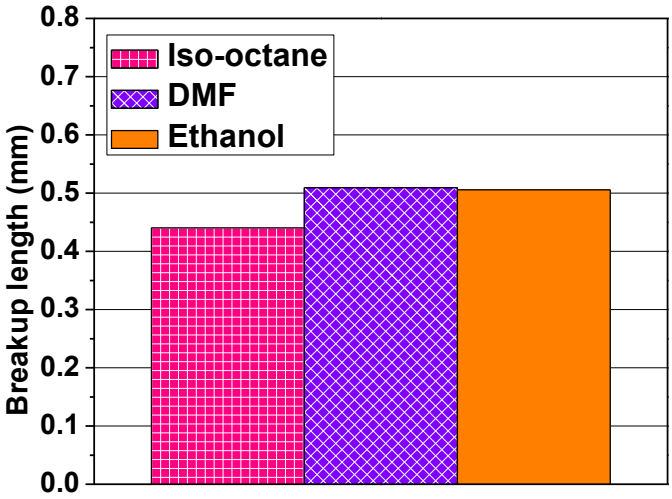

Figure 8.9 Comparison of liquid breakup length for different bio-fuels by using ANSYS-Fluent

As expected for iso-octane, it has the shortest liquid breakup length due the lowest both its liquid density, viscosity and surface tension among the three fuels. It seems that the combined effects of fuel viscosity and surface tension force possibly determines the liquid core length. As compared to DMF fuel, ethanol fuel has lower Re number due to higher viscosity, but it has slightly lower surface tension force. As a result, both effects actually leads to the similar intact core length between DMF and ethanol fuels as indicated in Figure 8.9.

8.3.4 Droplet Size and Velocity

In this section, the droplet size distribution is investigated for the primary and secondary breakup region respectively, by using numerical models and the PDPA measurement. The average droplet size in the primary breakup region is shown in Figure 8.10. The four different measuring cross planes inside the nozzle and the near-field as shown in Figure 8.10 are analyzed and are shown on the left side of Figure 8.10. The right side of Figure 8.10 points out the same average droplet size in the inner hole exit (A-A) for bio-fuels. Thus, ethanol shows

the largest average droplet size in the following planes: B-B, C-C and D-D because of the smallest *Re* number of ethanol from the inner hole exit. For iso-octane, as mentioned previously, the largest *Re* and *We* numbers result from the smallest average droplet size.

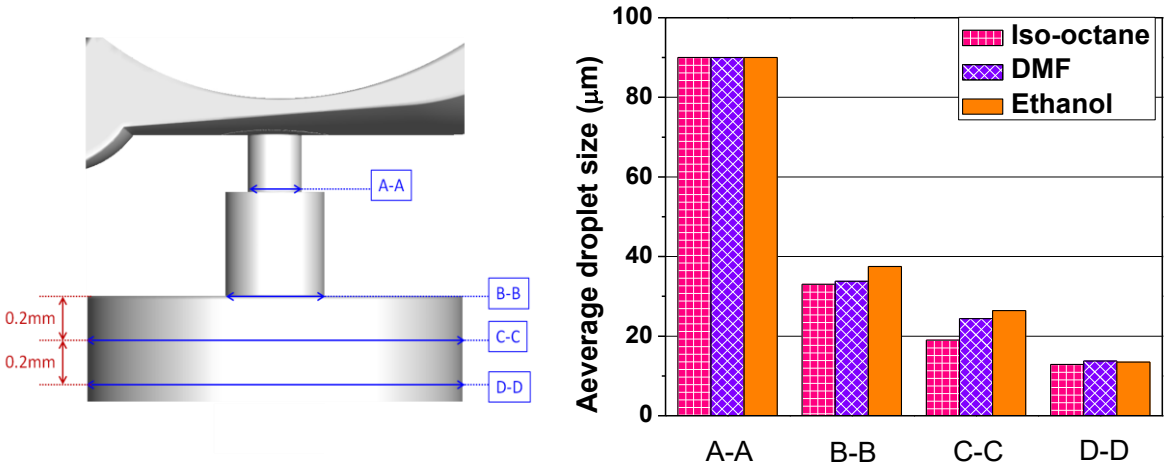

Figure 8.10 Comparison of average droplet size for bio-fuels at different measuring positions in the primary breakup region

The liquid distributions of iso-octane, DMF and ethanol at 30 μs after injection are shown in Figure 8.11. The distributions of droplet size for different bio-fuels at 40 and 50 mm from the nozzle tip under 150 bar injection pressure and 1bar ambient pressure are achieved by using the PDPA system as shown in Figure 8.12.

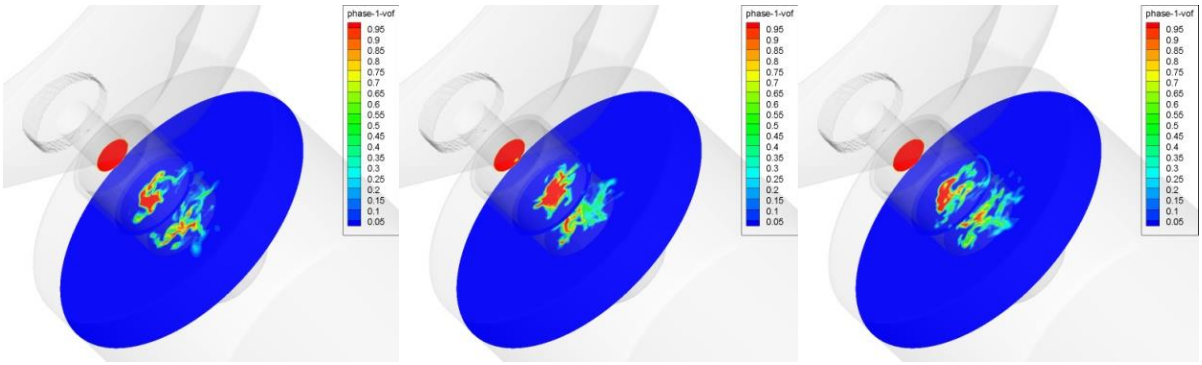

(a) Iso-octane **(b) DMF** **(c) Ethanol**

Figure 8.11 Distribution of liquid for bio-fuels at 30μs

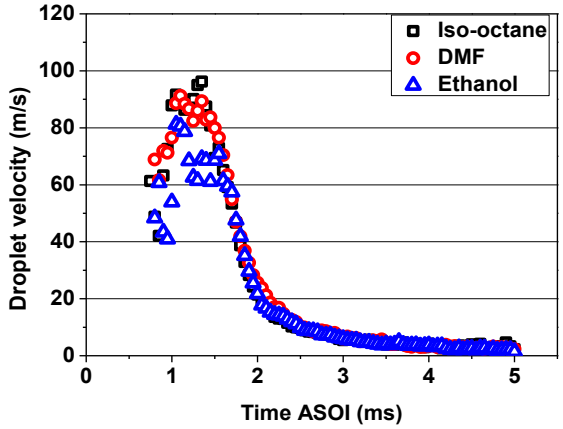

(a) Droplet velocity 40mm from nozzle

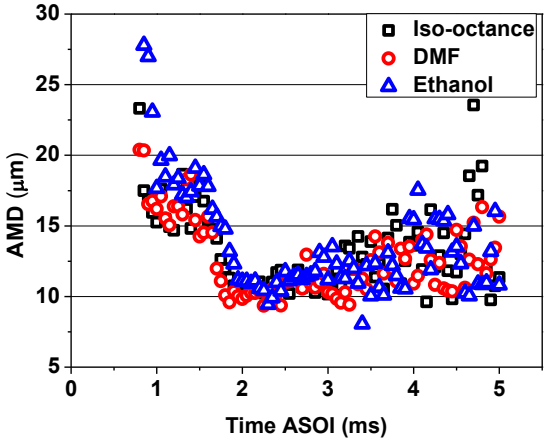

(b) AMD at 40mm from nozzle

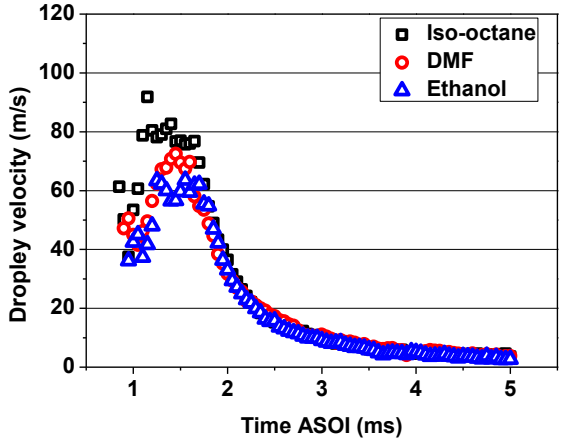

(b) Droplet velocity 50mm from nozzle

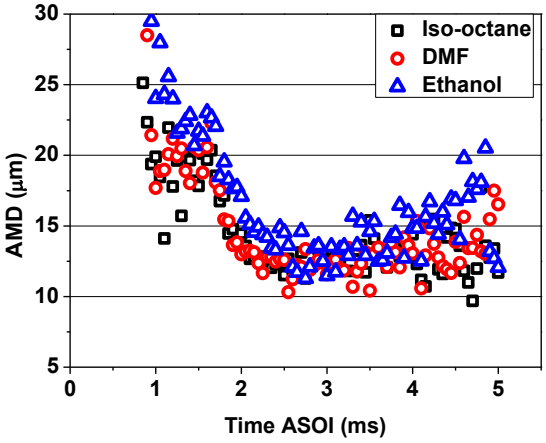

(d) AMD at 50mm from nozzle

Figure 8.12 Distribution of droplet velocity and size at 40 and 50mm from nozzle tip

At the measuring point of 40mm from the nozzle tip in Figure 8.12.(a), The droplet velocities for iso-octane and DMF fuels remain in the similar range, whilst ethanol droplet velocity is reduced by around 20%. The slower ethanol droplet velocity is consistent with the largest average droplet size being measured as shown in Figure. 8.12 (b). Another reason to cause this difference could be the higher latent heat of evaporation of ethanol which is shown in Figure 8.13. The higher latent heat of evaporation might cool down more on the ambient charge, thus increasing density and drag force.

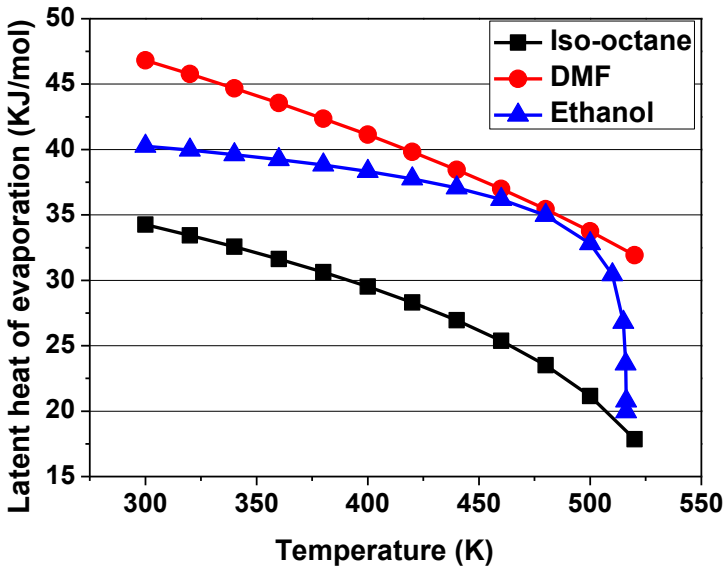

Figure 8.13 Comparison of latent heat of evaporation

At the following measuring point of 50 mm from the nozzle tip, iso-octane shows the highest droplet velocity and it is followed by DMF and ethanol in Figure 8.12 (c). In Figure 8.12.(d), ethanol still presents the largest AMD compared to distribution than the other two fuels. The difference between 40 and 50 mm is that the AMD of DMF becomes slightly larger than iso-octane. According to the experimental droplet size distribution and velocity, the spray models of KIVA3V are validated to examine its predictive capability. The validation of the droplet size and velocity between the experimental data and numerical results at 50mm from the nozzle tip are shown in Figure 8.14. It can be observed that there is a strong agreement between the experimental data and simulation results for DMF and ethanol.

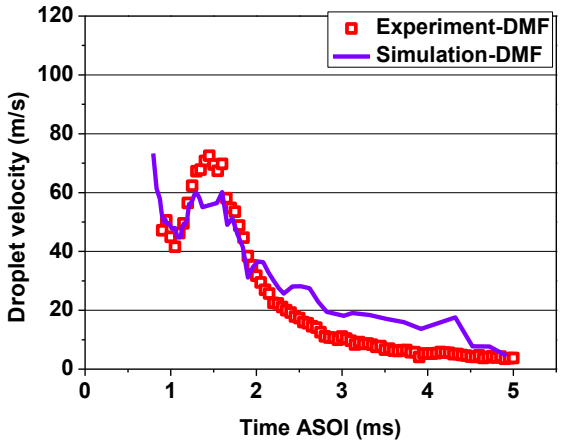

(a)Droplet velocity of DMF at 40mm from nozzle

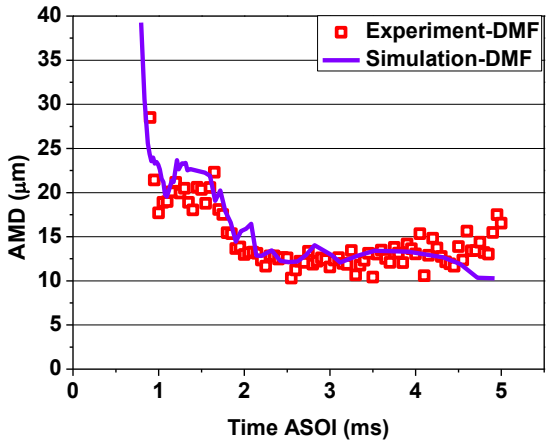

(b) AMD of DMF at 40mm from nozzle

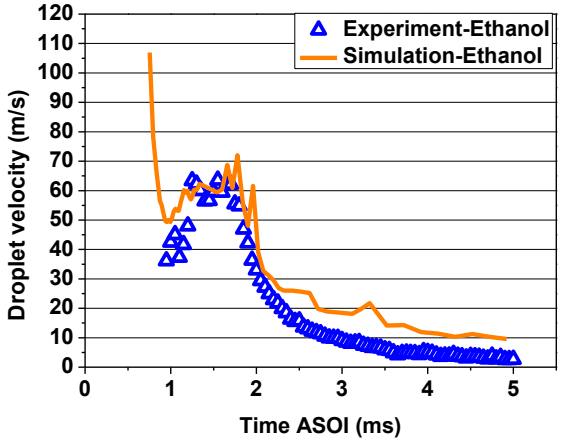

(c)Droplet velocity of ethanol at 50mm

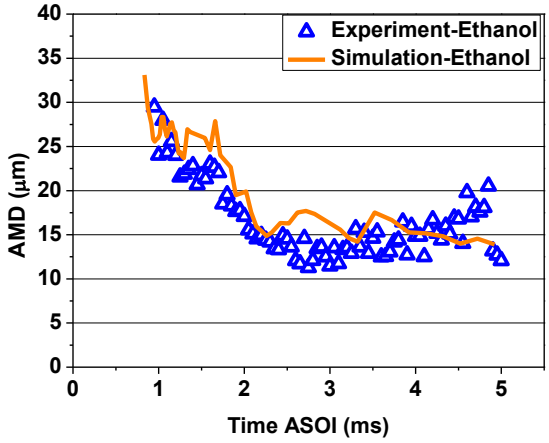

(d) AMD of ethanol at 50mm

Figure 8.14 Validation of experimental data and numerical results at 40 mm and 50 mm from nozzle

In order to investigate the detailed comparison of the droplet size between iso-octane, DMF and ethanol, the comparison of the SMD at different measuring positions is discussed in Figure 8.15. It is more obvious to observe that the SMD of ethanol is around 14% larger than iso-octane and DMF, is around 7% larger than iso-octane. More detail for the SMD distribution for bio-fuels at all the measuring points is shown in Figure 8.16.

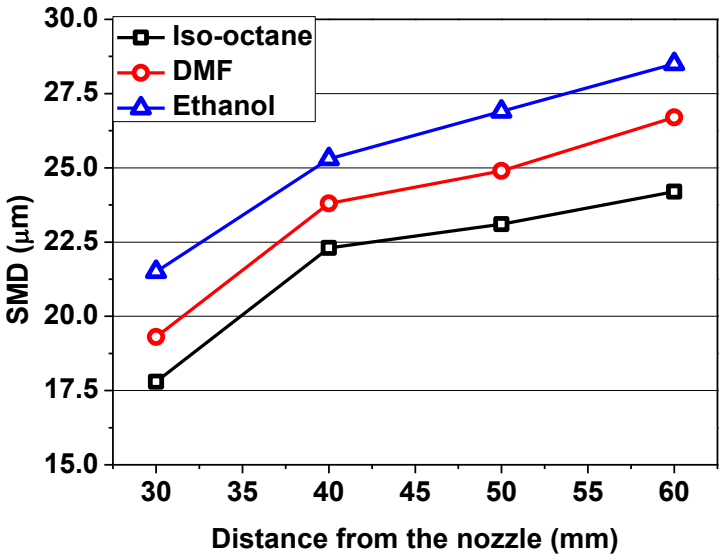

Figure 8.15 Comparison of the SMD for bio-fuels at different measuring positions

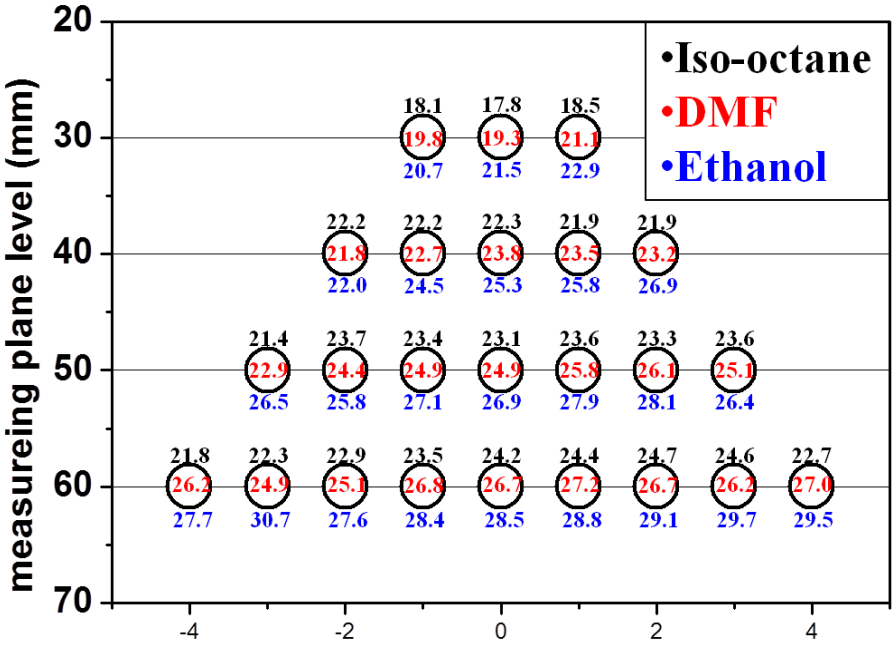

Figure 8.16 SMD distributions for bio-fuels at all measuring points

The detailed discussions of droplet size variation also relate to the *Re* and *We* number as shown in Figure 8.17. In Figure 8.17, iso-octane shows the highest *Re* and *We* numbers and results in stronger spray atomisation to cause the highest droplet velocity and smallest droplet size

distribution. For ethanol, due to having the smallest *We* number, it causes the largest droplet size in all the bio-fuels.

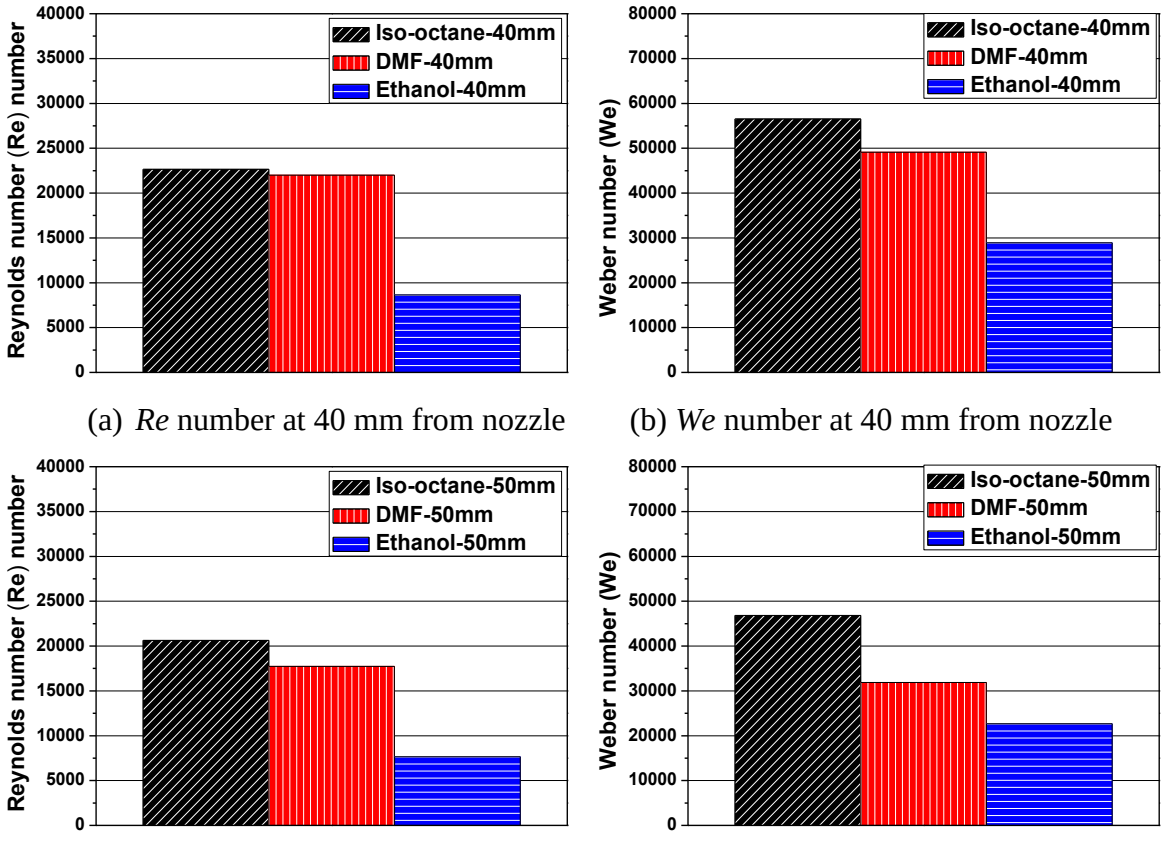

(a) *Re* number at 40 mm from nozzle (b) *We* number at 40 mm from nozzle

(c) *Re* number at 50 mm from nozzle (d) *We* number at 50 mm from nozzle

Figure 8.17 Comparison of Re and We number at different measuring planes

To compare the *Re* and *We* numbers in Figure 8.3 and 8.17, it can be observed that ethanol had the smallest *Re* number due to its higher liquid viscosity. For the *We* number, ethanol has a similar value to DMF at the inner hole exit (A-A). However, in the secondary breakup region, the *We* number of ethanol becomes obviously lower than that of DMF. The summary of above results illustrates that the liquid viscosity not only affects flow instability level, reflected by Re number, but also dominate the jet breakup behaviour in the primary breakup region. The higher liquid viscosity constrains the droplet detachment from the liquid jet in the primary breakup region. Subsequently, in the secondary breakup region, the droplet breakup is mainly

dominated by aerodynamical force. Thus, the We number (surface tension) becomes the dominant factor in deciding secondary breakup.

8.4 Mixture Distribution in a Stoichiometric Direct Injection Engine

8.4.1 Establishment of Engine Model

In this section, a numerical comparison of mixture distribution for different bio-fuels in the GDI engine is introduced to predict the efficiency of combustion and exhausts emissions. The engine model used in this study is based on the 4-valve single cylinder SI optical engine which has a similar engine configuration to a Jaguar 2.5L V6 GDI engine (Figure 8.18).

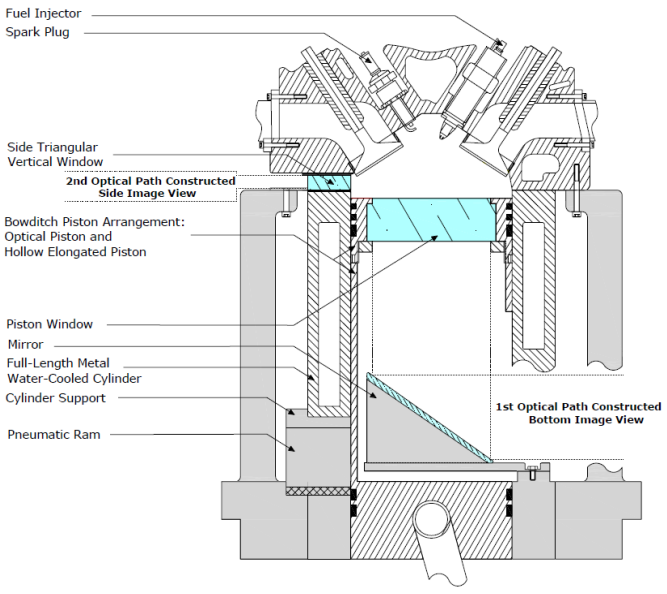

Figure 8.18 Schematic of the optical engine (Ma 2012)

According to the engine configuration in Figure 8.18, the three-dimensional optical engine geometry and mesh distribution are presented in Figure 8.19. In this numerical study, the mesh size is set to 2 mm which accords to the validation of the grid size in the engine simulation

from Beale (Beale and Reitz 1999). It points out that the usage of a 1 mm cell size can obtain independent grid results and an acceptable result on evaporated spray, as observed by using a 2 mm cell size (Juneja 2004). Therefore, in order to consider the balance between accuracy and computing efficiency, a 2 mm cell size is selected in this engine model setup. Moreover, the comparison of the spray images in the GDI engine model has been validated by Li (Li 2013, Li 2013) and it showed a strong agreement with the experimental images.

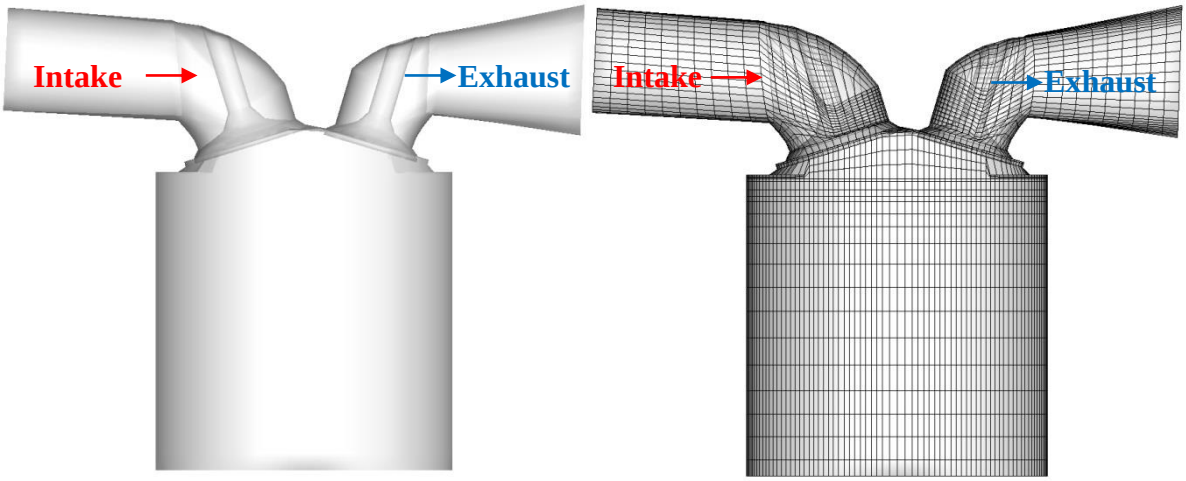

Figure 8.19 Schematic of the optical engine

8.4.2 Operating Conditions

The engine is operated at wide open throttle (WOT) and examined by 1500rpm. This investigation is simulated from the exhaust valve opening time (EVO) at 204 °CA BTDC as shown in Figure 8.20. The start time for the fuel injection is set to 80 °CA ATDC and the injection duration for each fuel is related to the stoichiometric ratio and the amount of inlet-air during the process of when the intake valve is opened and closed. This simulation finishes at to 340 °CA ATDC which is 10 °CA before ignition in order to understand the mixture distribution before the combustion. This takes place in order to have a reference for

comparisons, the same initial and boundary conditions are used for all the test runs. An intake pressure of 1.0 bar and an intake air temperature of 320 K are used. More details time for the intake and exhaust valve opening and closing time are shown in Table 8.3.

Table 8.3 shows the optical engine geometrical parameters and injection conditions. The injection pressure in this numerical study is fixed at 150 bar for iso-octane, DMF and ethanol which shows similar results to previous spray investigations. The spray patterns of the tested six-hole GDI injector are designated to two groups of three asymmetric holes in order to spread the fuel into the whole engine cylinder, as is shown in Figure 8.21.

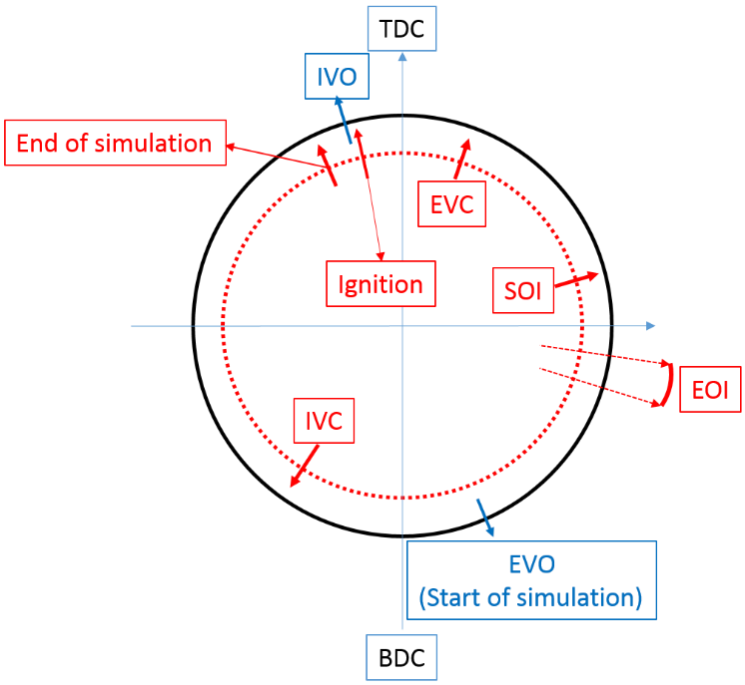

Figure 8.20 Operating time during engine cycle

Table 8.3 Engine and injection parameters

Displacement	0.56L		
Bore	89.0mm		
Stroke	90.3mm		
Connecting Rod	154mm		
Compression Ratio	11.3:1		
Intake Valve Open	16°CA BTDC		
Exhaust Valve Close	37 °CA ATDC		
Injector Type	6-hole solid cone		
Start of Injection	80 °CA ATDC		
Injection Pressure	150 bar		
Injection Fuel	Iso-octane	DMF	Ethanol
Injection Duration	24.5 °CA ATDC	29.3°CA ATDC	26.3°CA ATDC

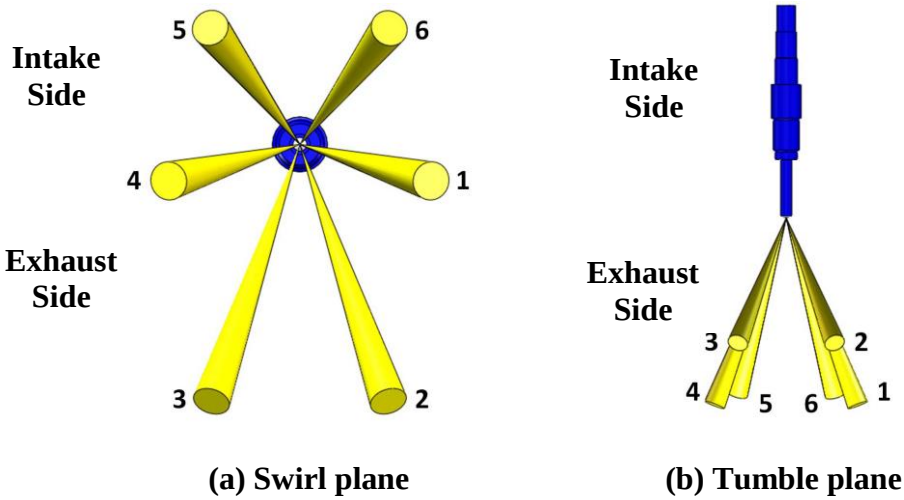

(a) Swirl plane **(b) Tumble plane**

Figure 8.21 Schematic of spray pattern in the thermal engine

8.4.3 Effects of Fuel Properties on the Mixture Distribution

In order to understand the spray development of different bio-fuels in the engine cycle, Figure 8.22 shows the numerical simulation of the spray images and velocity vector from a cut-away view in the engine cylinder at a different crank angle. It can be observed that the iso-octane shows the shortest penetration length at 86°CA ATDC (6°CA after SOI) when DMF and

ethanol attached to the piston wall. Moreover, Figure 8.22 presents the effects of intake-air on spray development in the engine cycle. In the GDI nozzle design, the spray pattern is assumed to be symmetrical to transfer the injection fuel into the whole engine cylinder. However, at 86°CA ATDC, the spray pattern on the right-hand side is obviously longer than the left-hand side. This is due to the intake air spread and the acceleration of the right-hand side spray pattern to be wider and longer than the left side.

From the distribution of the velocity vector in the cylinder field, the flow field presents a clockwise tumble flow from the right side to the left-hand side which caused the amount of droplets on the cylinder's left hand side to be higher than the right hand side after 120°CA ATDC, as in Figure 8.22. Due to the clockwise tumble flow in the engine cylinder, the liquid droplets which were attached to the cylinder wall and piston surface are gradually evaporated and transported, as illustrated by Figures 8.23 and 8.24. Figures 8.23 and 8.24 respectively show the liquid amount on the cylinder piston and wall for different bio-fuels. The parameter used in these figures has been normalized by total fuel mass, and the evaporation model is applied in this analysis. It can be observed that the liquid fuel amount of DMF on the cylinder piston (Figure 8.23) is obviously higher than ethanol and iso-octane although ethanol shows the higher penetration length in Figure 8.7. This may have resulted from the smaller spray angle and higher density of DMF (Figure 8.5 and Table 8.1), clearly being affected by intake air over ethanol. However, the amount of DMF decreases faster than ethanol after 240°CA ATDC due to the higher vapour pressure of ethanol which causes a slower evaporation process during the engine cycle. Moreover, due to the shorter spray penetration length and faster droplet evaporation of iso-octane, it results in the lowest amount of liquid attaching to the cylinder piston during the engine cycle.

	Iso-octane	DMF	Ethanol
82 °CA	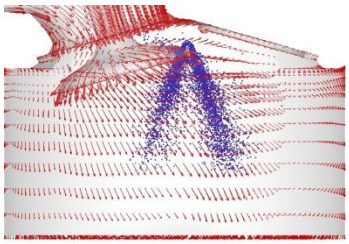	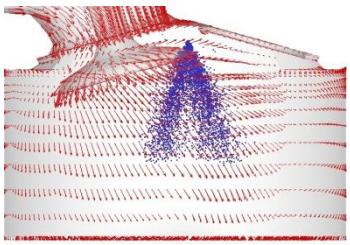	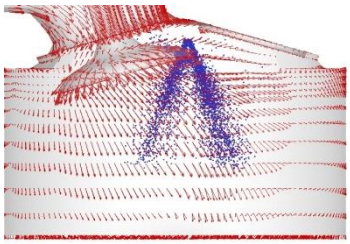
86 °CA	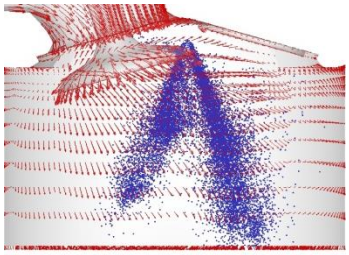	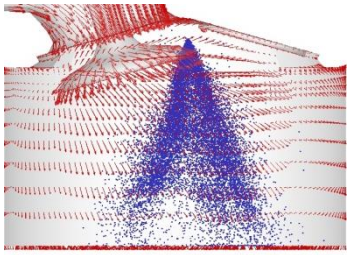	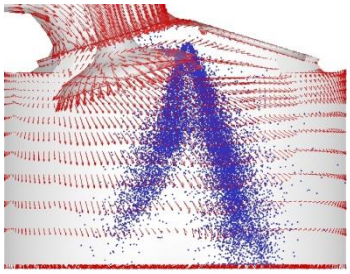
120 °CA	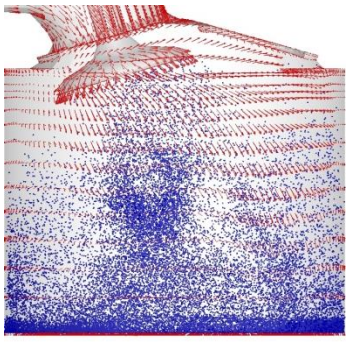	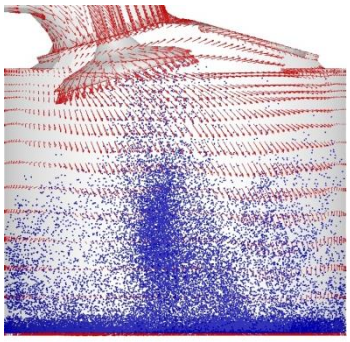	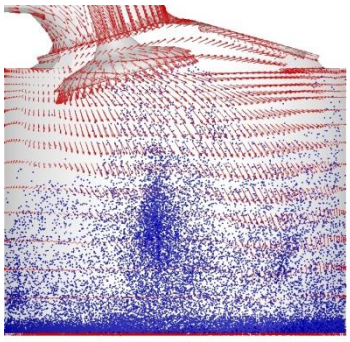

180°CA (BDC)	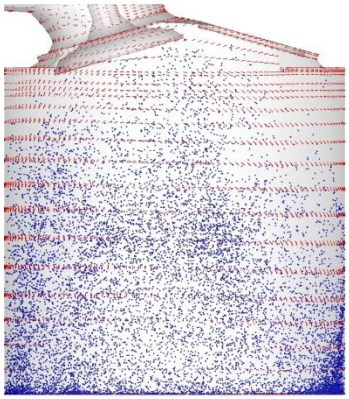	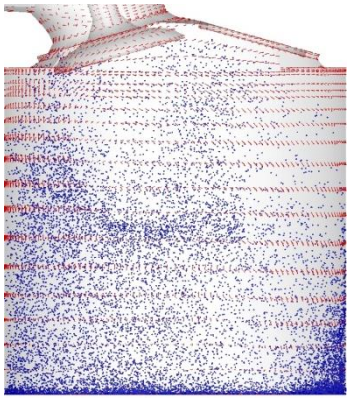	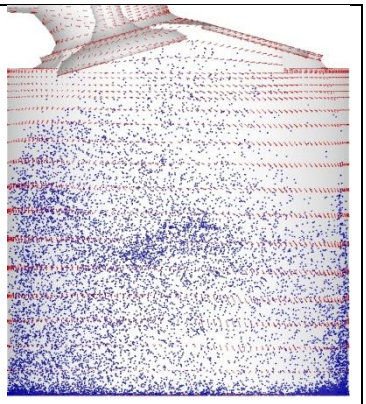
240°CA	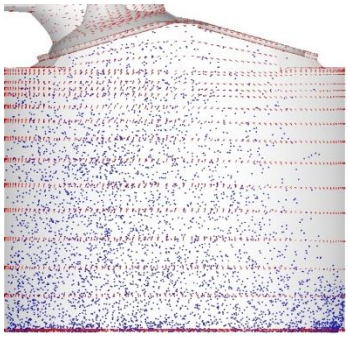	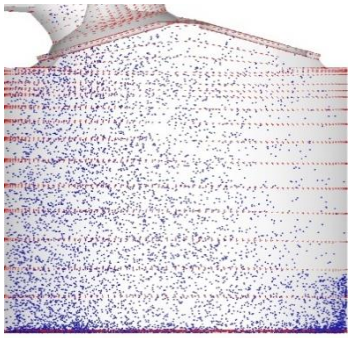	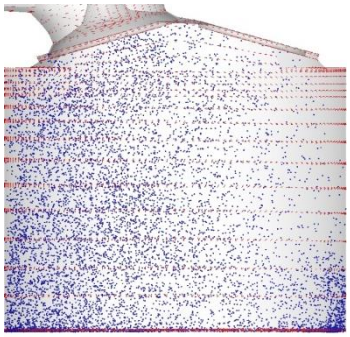
340°CA	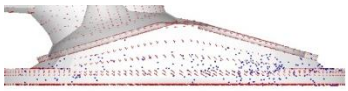	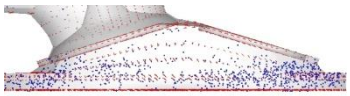	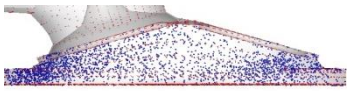

Figure 8.22 Distribution of droplets and air flow for different bio-fuels

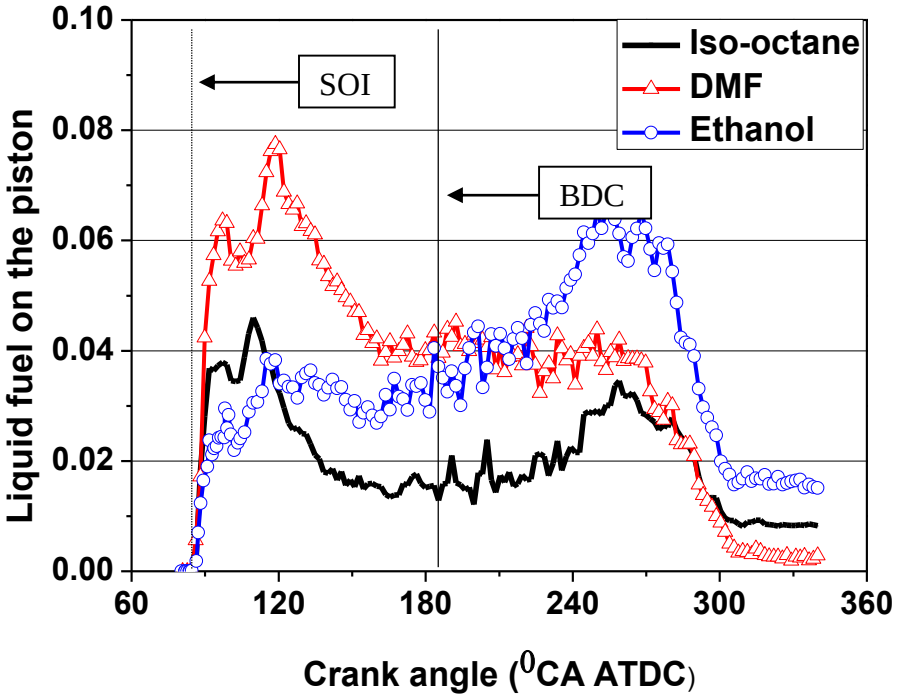

Figure 8.23 Comparison of liquid amount on the engine piston (fuel mass on cylinder piston was normalised by total fuel mass)

Figure 8.24 illustrates the comparison of liquid amount on the cylinder wall surface and shows the spray-wall impingement of ethanol which takes place earlier than DMF and iso-octane. This also illustrates that the bounce and splash of the spray-wall impingement (Figure 2.19) takes place for all the bio-fuels when the droplet impinges on the cylinder piston. Thus, the lower vapour pressure of iso-octane and DMF results in a faster droplet evaporation process than ethanol. Therefore, it causes a higher liquid amount of ethanol on the cylinder wall as shown in Figure 8.24. The increasing trend of ethanol on the cylinder wall is observed after 86°CA ATDC. This is due to the slower evaporation rate of ethanol which causes a higher amount of droplets to exist and attach on the cylinder wall during the engine compression process which can be found in Figure 8.22 at 340°CA ATDC.

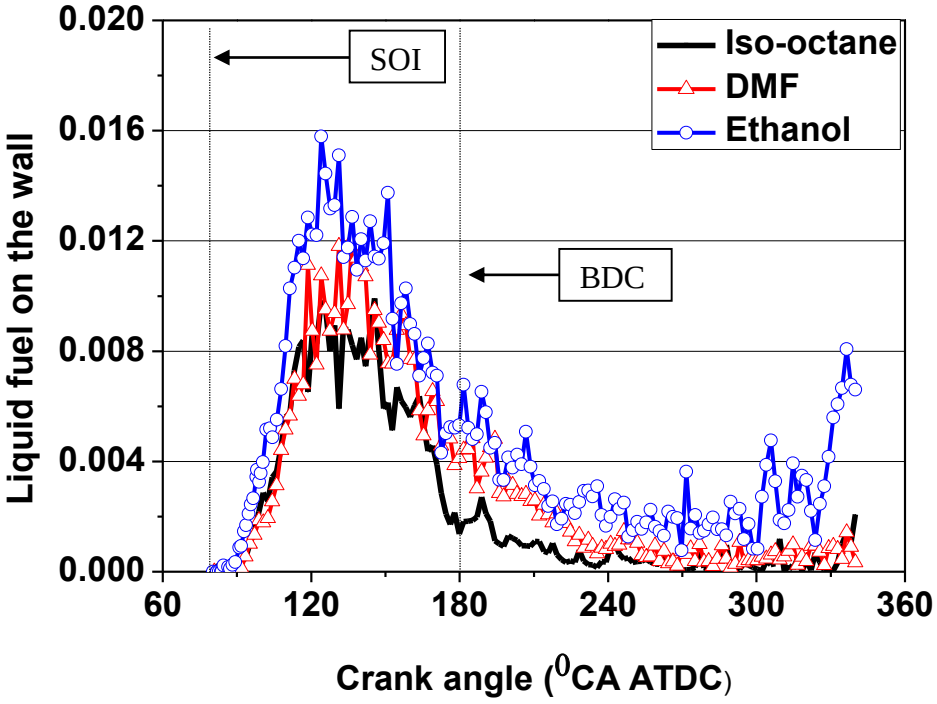

Figure 8.24 Comparison of liquid amount on the cylinder wall (fuel mass on cylinder wall was normalised by total fuel mass)

In the history of the vapour rate for different bio-fuels which is shown in Figure 8.25, the liquid evaporation rate during the engine cycle is presented. In Figure 8.23, the vapour rate is defined as below:

$$Vapor\ \ rate = \frac{Vapor_{total}}{Injection\ \ Fuel_{total}} \qquad \text{(Equation 8.1)}$$

When the liquid fuel injected into the engine cylinder, the high injection pressure causes droplet breakup and further evaporation. Moreover, due to the clockwise tumble flow, the liquid droplet on the cylinder wall and piston evaporate as shown in Figures 8.23 and 8.24. To compare the vapour rate of bio-fuels in Figure 8.25, the time for each bio-fuel, iso-octane, DMF and ethanol, to achieve 90% of fuel evaporation are respectively 240, 280, and 340 °CA ATDC.

It illustrates that the vapour rate of iso-octane shows a faster raised speed than the other two bio-fuels due to its lower vapour pressure. Moreover, it illustrates that DMF and ethanol need to take a longer time than iso-octane to complete the evaporation process before any further combustion process.

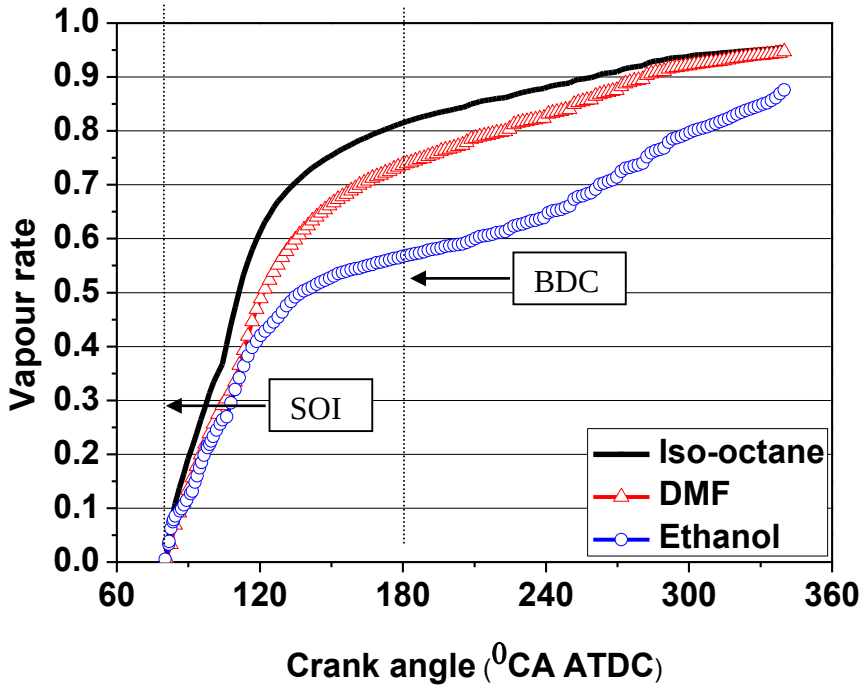

Figure 8.25 Comparison of evaporation rate for different bio-fuels

The distributions of equivalence ratio (ER) for different bio-fuels in the engine cylinder during the engine cycle were shown in Figure 8.26. At the 82 and 86 °CA ATDC, iso-octane already showed the higher value of ER around the spray jet during the injection process. Although the vapour pressure of DMF is lower than ethanol, the ethanol showed a higher ER distribution than DMF. This is due to the wider spray angle of ethanol which resulted in a faster evaporation process during the injection process (Figure 8.5).

However, after 120 °CA ATDC when the fuel injection stops, the DMF shows a richer mixture than the ethanol due to the lower vapour pressure causing faster liquid droplet evaporation on

the cylinder piston and wall. For the iso-octane, its faster vapor rate results in the richest mixture distribution. In the process of engine compression, due to the clockwise tumble flow in the engine flow field, the richer mixture distribution can be observed on the left side of the engine cylinder in all bio-fuel tests. Figure 8.27 shows the mixture distribution at the spark point plane from the bottom side at 340 °CA ATDC. In Figures 8.26 and 8.27 at 340 °CA ATDC (before ignition), iso-octane shows the richest mixture distribution around the spark plug area in which the ER value is around 1.03 and the DMF shows the a higher value (ER=0.8) than ethanol (ER=0.7). Moreover, for the overall mixture distribution in the engine cylinder at BDC, it shows that the mixture distribution of iso-octane is more homogenous than DMF and ethanol (Figure 8.26). Due to the clockwise tumble flow in the engine flow field, the unevaporated droplets of DMF and ethanol are transported to the left side near the engine head which are then attached on the cylinder wall. This causes a richer area, as observed near the engine head due to the more fuel evaporation from the liquid attachment on the cylinder wall and piston.

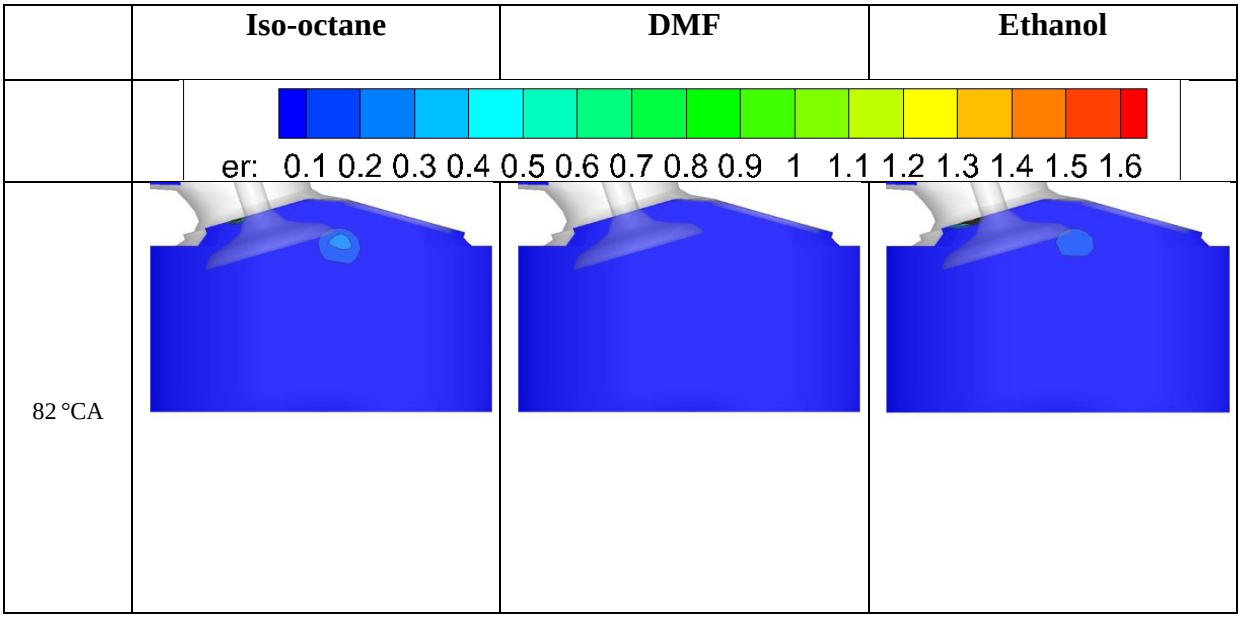

86 °CA	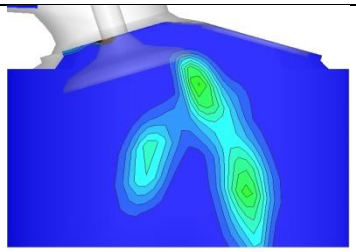	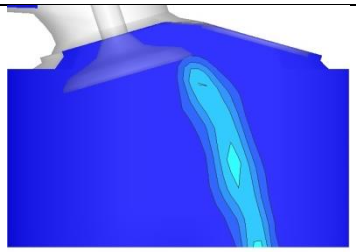	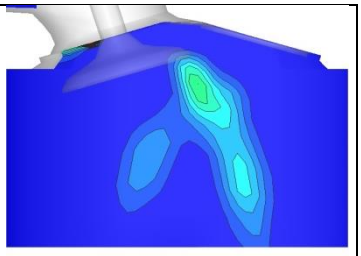
120 °CA	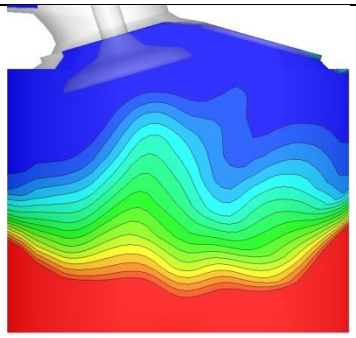	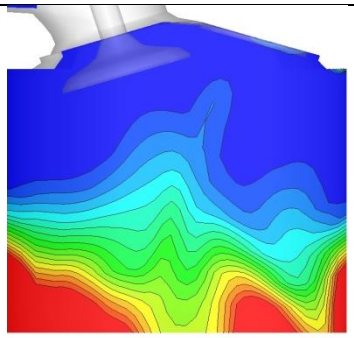	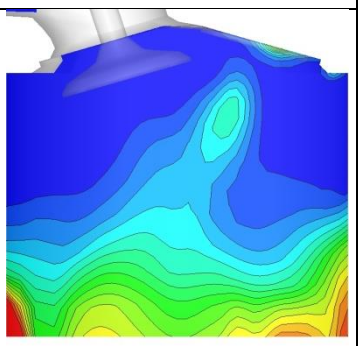
180°CA (BDC)	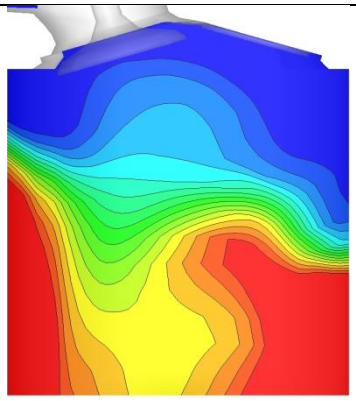	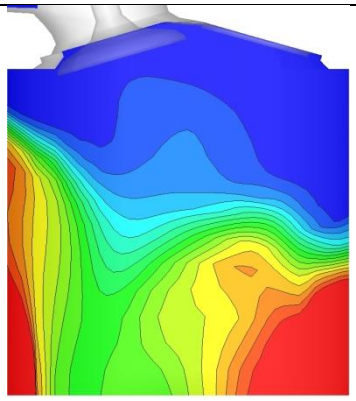	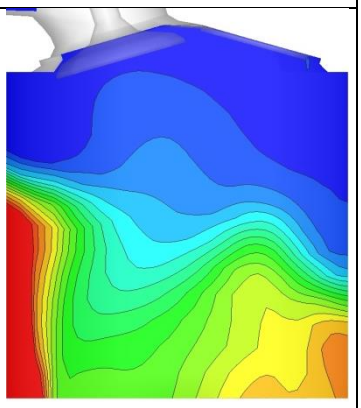
240°CA	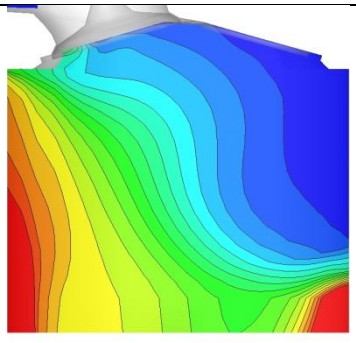	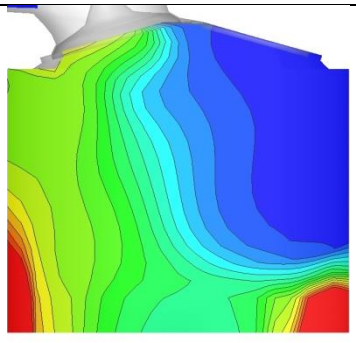	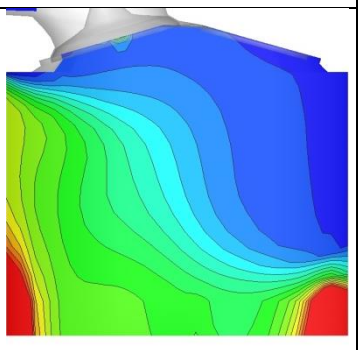

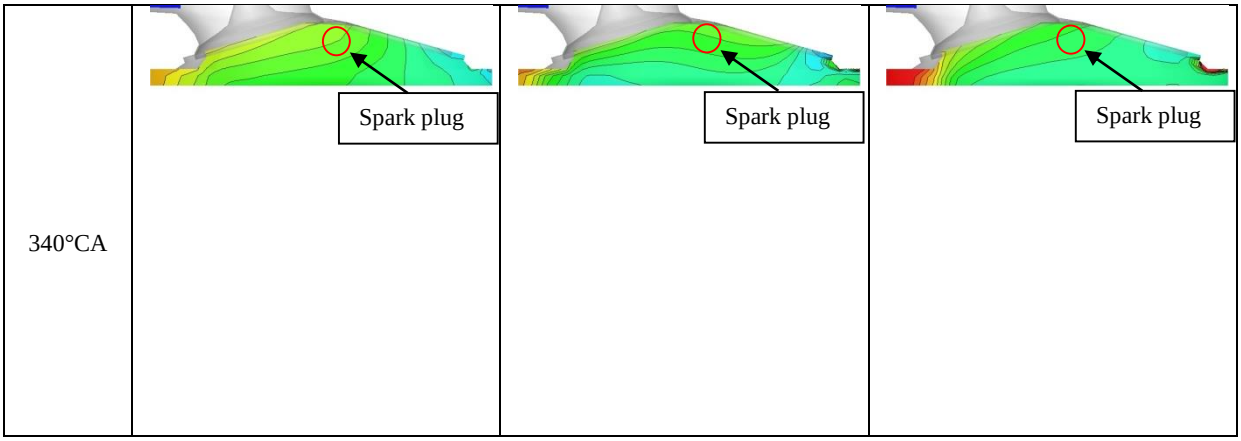

Figure 8.26 ER distribution of different bio-fuel during engine cycle

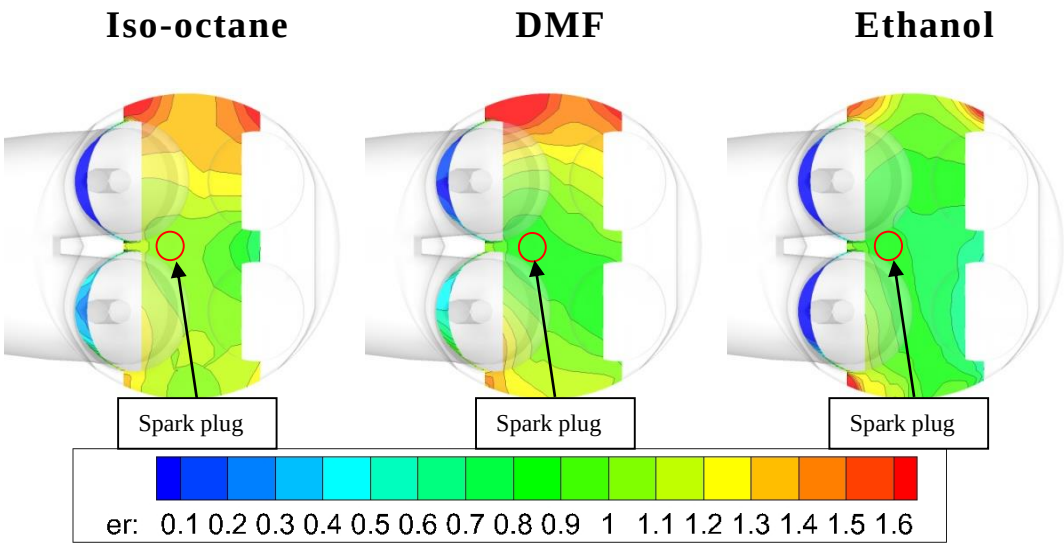

Figure 8.27 Comparison of ER distribution near spark point at 340 °CA ATDC

To quantify more detailed quality of mixture distribution, Figure 8.28 shows the comparison of distribution of temporal evolution of mixture volume using three different equivalence ratios ($0.5<\phi$, $0.5<\phi<1.5$ and $1.5<\phi$). From the overall trend of the all testing fuels, the percentage of dilute air/fuel mixing ($0.5<\phi$) gradually decreases and the percentage of ignitable air/fuel mixing ($0.5<\phi<1.5$) increases during the engine operating cycle. This is due to the injection fuel is gradually evaporated and then raise the percentage of rich mixture. The percentage of extra-rich mixture ($1.5<\phi$) gradually increases from the start of injection (ATDC 80 °) and

achieve the peak value at ATDC 140 °. This is due to the larger amount of liquid vapour is generated from the wetting position and wall which is due to the clockwise tumble flow in the engine flow field causes the faster fuel evaporation process, as in Figure 23 and 24. The comparison of ignitable air/fuel mixing (0.5< ϕ <1.5) between each testing fuel indicates iso-octane has the highest percentage and the ethanol shows the lowest percentage at the end of compression stroke (340°CA ATDC).

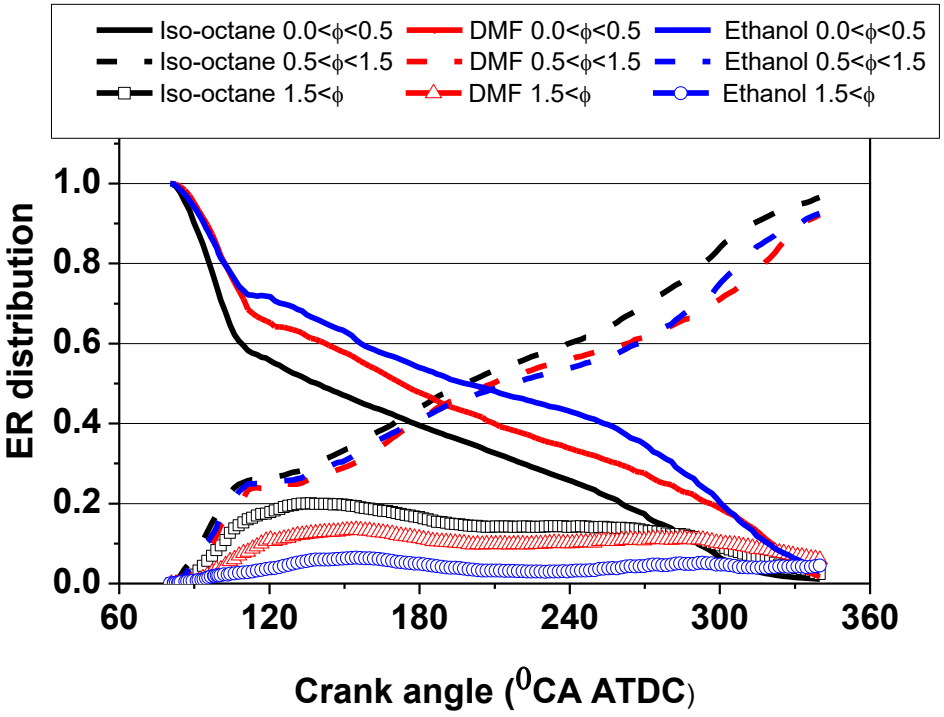

Figure 8.28 Percentages of the distribution of the equivalence ratio

8.5 Summary

This chapter mainly investigates the effects of fuel properties on spray characteristics in the primary and secondary breakup regions by using numerical and experimental methods. The three different bio-fuels, iso-octane, DMF and ethanol, were compared for their spray

characteristic at 150 bar and 1bar ambient pressure. These results not only provide more detailed information on the effects of fuel properties in the primary, secondary breakup process and engine cycle, but also validate the numerical spray models in KIVA3V. Several key findings for the effects of fuel properties from this investigation are shown as below:

- Although the largest mass flow rate is observed by using DMF, it also shows the lowest exit velocity in the nozzle's inner hole; which compares with the other two bio-fuels for the same conditions. This is due to the larger liquid density which slows down the liquid movement during the injection process.

- Another important parameter for spray characteristics which include liquid penetration length, droplet size and velocity is the viscosity of the liquid. For example, ethanol has the largest liquid viscosity in all the bio-fuel testing results as it has the smallest *Re* number. Moreover, from the investigation of the experimental and numerical methods, a higher liquid viscosity reveals a larger droplet size and droplet velocity.

- The surface tension of liquid shows increased obvious effects rather than liquid viscosity on the spray angle in the near field flow. In the variation of the spray angle, although DMF has a larger *Re* number than ethanol by 50%, the spray angle of DMF is still smaller than ethanol because the *We* number of ethanol is higher than DMF. This means that there is a stronger liquid atomisation for ethanol when the liquid jet leaves from the nozzle hole which then results in a larger spray angle.

- Although other fuel properties influence the spray characteristics, such as the fuel vapour pressure, this investigation shows that the density, viscosity and surface tension of the liquid are the major important factors to affect spray characteristic development. However,

in the engine cycle simulation, the ER distribution is strongly affected by the fuel vapour pressure due to its method of causing a different evaporation rate.

- The spray behaviours in the engine cylinder are strongly affected by the engine flow field and intake air. The intake air results in the longer penetration and wider spray angle on the right-hand side of the spray patterns. Moreover, the clockwise tumble flow in the engine flow field accelerates the fuel evaporation rate and directly affects the mixture distribution.

- The comparison of ER distribution during the engine cycle shows that the iso-octane presents the richest ER distribution near the spark plug region. On the other hand, the ER distribution of ethanol shows that the learn mixture near the area of the spark plug is due to its lower vapour pressure which causes the slower evaporation process.

Chapter 9

Conclusions and Recommendations

In this thesis, the detailed effects of different nozzle geometrical designs such as lift needle position , L/D ratio, r/D ratio and the counter-bore size on the spray characteristics in the nozzle near-flow field and far-flow field are investigated by using the Eulerian (ANSYS-Fluent) and Lagrangian (KIVA-3V) approaches. Moreover, the three different spray breakup models, KH-RT, KH-ACT-RT and MPI-CAB model, are compared for their calculation capability to simulate the different nozzle geometries and their breakup mechanisms. Furthermore, the improvement and accuracy of the coupling model between the nozzle flow data and KH-ACT-RT is examined. Subsequently, the spray characteristics of the different biofuels, iso-octane, ethanol and DMF, are examined by using numerical and experimental methods such as the PDPA system and a high speed camera in the different spray regimes in order to deeply understand the effects of fuel properties on the spray behaviours. Finally, the mixture distribution of different biofuels in the GDI engine is also analysed in order to predict their combustion efficiency.

9.1 Conclusions

- **Effect of Nozzle Geometry on the Spray Characteristics in the Near-Flow Field**

The GDI nozzle's geometrical design plays an important role in nozzle exit conditions such as mass flow rate, velocity and the spray characteristics in the nozzle near-field. As a result of the

detailed studies for nozzle flow and near-flow field, it has been found that it is difficult to observe this effect by experimental methods; therefore numerical study is used to investigate the effects of nozzle geometry on the spray characteristics in the near-flow field. The detailed variations of nozzle flow at different needle lift positions show its effects on mass flow rate change and the location of the recirculation zone. Increasing the r/D ratio can increase the nozzle exit velocity, mass flow rate and improve the recirculation inside the nozzle. However, a larger r/D ratio decreases the turbulent kinetic energy, which results in slowing down the spray atomisation. The influences of the nozzle L/D ratio show obvious differences on the spray characteristics in the primary breakup regime at high injection pressures. Moreover, the increased spray angle results in wall impingements inside the counter-bore cavity particularly for L/D=1; which can potentially lead to increased injector deposit build up. The effects of the counterbore size only show obvious overall adverse effects on the mass flow rate and jet breakup length when increasing the counter-bore diameter, due to the air recirculation effects inside the counterbore zone. The effects of deposit formation on the spray characteristics are also investigated which indicate the deposit accumulated inside the counterbore strongly affects the spray characteristics. However, although the spray characteristics are affected by deposit, less influence shows up on the mass flow rate (>1%). The mass flow rate will be changed when the deposit thickness covers the inner hole area.

- **Analysis of the Breakup Mechanism and Nozzle Geometry's` Effect in Far- Flow Field**

Spray breakup models are established by the different assumptions of the droplet breakup mechanisms. The KH-RT model which is the most common spray model to be used is compared with the KH-ACT-RT model to analyse the effect of different breakup mechanisms on the spray characteristics. The results indicate that the KH model has a higher value of SMD

than the KH-ACT-RT model under the same model setups due to uncompleted assumptions of the breakup mechanism of the KH-RT model. Also, the improvement of KH-ACT-RT is continuous. The coupling between the nozzle flow simulation and the KH-ACT-RT model presents more accurate results on the droplet mean diameter due to the correction of turbulent kinetic energy and dissipation rate value from the nozzle flow simulation. The analysis of the spray breakup mechanism during the spray development process points out the occurrence of the turbulence-induced breakup taking place earlier than the aerodynamically-induced; and then the aerodynamic force dominating the droplet breakup in the far-flow field (secondary breakup regime).

Another investigation also examines the effect of nozzle geometrical design such as r/D and L/D ratio in the secondary breakup regime. The KH-ACT-RT and MPI-CAB models indicate that a larger r/D ratio can increase the spray penetration length due to a higher exit velocity which result in the smaller droplet size and velocity in the secondary breakup regime. Lastly, the comparison of the KH-ACT-RT and MPI-CAB models points out that the great amount of small child droplets from KH-ACT-RT cause a more unstable trend and lower value in the droplet mean velocity.

- **Effect of Operating Conditions on the Spray Characteristics**

The effects of operating conditions such as injection pressure and ambient pressure in the near-flow and the far-flow field in the GDI injection system are intensively studied by numerical and experimental methods in order to understand the effects on the spray characteristics. The study points out the effect of the injection pressure is obvious on the spray characteristics in the primary and secondary breakup regimes. The effects from higher injection pressure cause the increase of the mass flow rate; spray penetration length and angle and the intensity of

droplet breakup. This is due to the higher nozzle exit velocity not only increasing the turbulent effects inside the droplet, but also producing a stronger vortex inside the counter-bore which results in a stronger disturbance on the liquid surface and then the generation of smaller droplets.

The influences of ambient pressure on spray characteristics at the nozzle exit ais not obvious, unlike injection pressure. The previous chapters point out that the spray characteristics are not obviously affected by ambient pressure in the near-flow field due to the complicated breakup mechanisms like turbulent effects. However, when the liquid flowed downwards, the liquid jet and droplets bear more drag force from the ambient pressure which then results in clearer differences.

By using the PDPA system and a high-speed camera, the detailed variations of spray characteristics under different operating conditions are used to validate the MPI-CAB model and to examine its limitations and accuracy. The validation results show that the MPI-CAB can provide a strong agreement with the experimental results at different injection and ambient pressures. The numerical and experimental studies not only present information about the effects of the operating condition on the spray characteristics, but also provide insight into the influences in the nozzle flow and near-flow field.

- **Effect of Fuel Properties on the Spray Characteristics**

The effects of fuel property on spray characteristics in the nozzle-near field, secondary breakup regime and engine cylinder are examined by using the present common market bio-fuel, iso-octane, DMF and ethanol, in this section. From the experimental measurements, it shows that DMF has the highest value of mass flow rate. However, the numerical nozzle simulation points

out that it has the slowest nozzle exit velocity. This is due to the highest liquid density value of DMF which slows down the liquid movement during the injection process.

In the nozzle near field, the liquid surface tension shows a dominant role over the spray characteristic by using the identification of *We* number. Another important parameter to affect the spray characteristics in the far-field flow is the liquid viscosity; for example, ethanol has the largest liquid viscosity of all the bio-fuels which results in the smallest Re number. A higher liquid viscosity reveals a larger droplet size and droplet velocity.

In the comparison of spray characteristics, the liquid vapour pressure shows unclear influences. This is due to the droplet breakup which is dominated by *We* and *Re* (liquid surface tension and viscosity) presenting a direct and obvious effect on the spray characteristics during the spray development. However, the comparison of ER distribution in the engine cylinder indicates that the liquid vapour pressure has a strong relationship with liquid evaporation rate which directly affects the mixture distribution.

9.2 Recommendations for Future Work

Nozzle Flow Simulation

The needle opening time (injection duration time) not only directly affects the spray characteristics but also affects the cavitation formation. The cavitation effect in the GDI nozzle is not as significant as the diesel nozzle due to the lower injection pressure of the GDI injection system. Thus, the cavitation effect is still intensively studied in the real gasoline nozzle simulation. This is because of the turbulent disturbance from the collapse of the vapour bubble also plays an important role in the droplet breakup mechanism. Therefore, more detailed

investigation of cavitation effects in the GDI nozzle still need to be carried out in the future.

Nozzle Near-Flow Field and Primary Breakup Regime

Due to the limitations of the experimental equipment, the detailed spray characteristics in the nozzle near-flow field and primary breakup regime can not be measured. Although the CFD approach can provide a prediction of the spray characteristics in the primary breakup, it is necessary to measure the spray behaviours in order to optimise the spray model. Thus, a high-power camera lens can catch the image of the liquid jet breakup in the nozzle near-flow field and the laser sheet drop-sizing (LSD) can measure the SMD distribution in the dense regions. By using the CFD approach, PDPA system and coupled with the new techniques, the clear variation of spray characteristics during the spray development can be presented.

Spray Model

In this work, the study of biofuels, iso-octane, DMF and ethanol, are the single component fuels which can be simulated by the current single-component evaporation model. However, the current market fuel is a mixture of gasoline with ethanol or DMF which cannot be simulated by using a single-component model. Thus, the implementation of the multi-component evaporation model can be used to continue further study of bio-fuels and their blending.

References

Ansys 14.5 Help.

"Energy Information Administration, Monthly Energy Review (May 2014), Tables 1.3, 2.1-2.6.".

"Energy Project (after John EDwards American Association of Petroleum Geologists); SRI Consulting.".
"http:// www.mie.utoronto.cal/labas/mfl/collision-seminar_files/frame.htm
".
"http://ourfiniteworld.com/2015/01/06/oil-and-the-economy-where-are-we-headed-in-2015-16/."
" Transportation, I.C.o.C., EU CO2 emission standards for passenger cars and light-commercial vehicles. 2015.".

"U.S. Energy Information Administration, International energy outlook 2014. US Energy Information Administration (EIA) Report Number: DOE/EIA-0484(2014).".

A. Lampa, U. F. (2013). "Large Eddy Simulation of the spray formation in confinements." International Journal of Heat and Fluid Flow 43(0142-727X): 26-34.

Abianeh, O. S., Chen, CP (2012). "A discrete multicomponent fuel evaporation model with liquid turbulence effects." International Journal of Heat and Mass Transfer 55(23): 6897-6907.

Abianeh, O. S., Chen, CP (2012). "Modelling of evaporation and dissolution of multicomponent oil droplet in shallow water." Advanced Computational Methods and Experiments in Heat Transfer XII 75: 231.

Alagumalai, A. (2014). "Internal combustion engines: Progress and prospects." Renewable and Sustainable Energy Reviews 38: 561-571.

Aleiferis, P. G., J. Serras-Pereira, A. Augoye, T. J. Davies, R. F. Cracknell and D. Richardson (2010). "Effect of fuel temperature on in-nozzle cavitation and spray formation of liquid hydrocarbons and alcohols from a real-size optical injector for direct-injection spark-ignition engines." International Journal of Heat and Mass Transfer 53(21–22): 4588-4606.

Amsden, A. A., P. O'rourke and T. Butler (1989). KIVA-II: A computer program for chemically reactive flows with sprays, Los Alamos National Lab., NM (USA).

Aoyama, T., Y. Hattori, J. i. Mizuta and Y. Sato (1996). An experimental study on premixed-charge compression ignition gasoline engine, SAE Technical paper.

Apte, S., M. Gorokhovski and P. Moin (2003). "LES of atomizing spray with stochastic modeling of secondary breakup." International Journal of Multiphase Flow 29(9): 1503-1522.

Arcoumanis, C., M. Gavaises and B. French (1997). Effect of fuel injection processes on the structure of diesel sprays, SAE Technical Paper.

Bai, C., Gosman, AD (1995). Development of methodology for spray impingement simulation, SAE Technical Paper.

Baumgarten, C. (2006). Mixture formation in internal combustion engines, Springer Science & Business Media.

Beale, J. C. and R. D. Reitz (1999). "Modeling spray atomization with the Kelvin-Helmholtz/Rayleigh-Taylor hybrid model." Atomization and sprays 9(6).

Befrui, B., G. Corbinelli, M. D'Onofrio and D. Varble (2011). GDI multi-hole injector internal flow and spray analysis, SAE Technical Paper.

Befrui, B., G. Corbinelli, P. Spiekermann, M. Shost and M.-C. Lai (2012). Large eddy simulation of GDi single-hole flow and near-field spray, SAE Technical Paper.

Befrui, B., D'Onofrio, Mario (2014). Primary Atomization of a GDi Multi-Hole Plume Using VOF-LES Method, SAE Technical Paper.

Bianchi, G. M. and P. Pelloni (1999). Modeling the Diesel Fuel Spray Breakup by Using a Hybrid Model, SAE International.

Boussinesq, J. (1877). "Théorie de l'écoulement tourbillant." Mem. Présentés par Divers Savants Acad. Sci. Inst. Fr 23(46-50): 6.5.

Butts, R. (2008). "Investigation of the effects of fuel properties on low temperature combustion in a highly dilute light duty diesel engine." University of Wisconsin-Madison.

Chiang, C., M. Raju and W. Sirignano (1992). "Numerical analysis of convecting, vaporizing fuel droplet with variable properties." International journal of heat and mass transfer 35(5): 1307-1324.

Christensen, M. and B. Johansson (2002). The Effect of In-Cylinder Flow and Turbulence on HCCI Operation, SAE International.

Clenci, A., G. Descombes, P. Podevin and V. Hara (2007). "Some aspects concerning the combination of downsizing with turbocharging, variable compression ratio, and variable intake valve lift." Proceedings of the Institution of Mechanical Engineers, Part D: Journal of Automobile Engineering 221(10): 1287-1294.

Crowe, C. (1982). "Review—numerical models for dilute gas-particle flows." Journal of Fluids Engineering 104(3): 297-303.

Daniel, R., C. Wang, H. Xu and G. Tian (2012). Effects of combustion phasing, injection timing, relative air-fuel ratio and variable valve timing on SI engine performance and emissions using 2, 5-dimethylfuran, SAE Technical Paper.
Daniel, R., C. Wang, H. Xu and G. Tian (2012). Split-Injection Strategies under Full-Load Using DMF, A New Biofuel Candidate, Compared to Ethanol in a GDI Engine, SAE Technical Paper.

De Villiers, E., A. Gosman and H. Weller (2004). Large eddy simulation of primary diesel spray atomization, SAE Technical Paper.

Delteil, J., S. Vincent, A. Erriguible and P. Subra-Paternault (2011). "Numerical investigations in Rayleigh breakup of round liquid jets with VOF methods." Computers & Fluids 50(1): 10-23.

Dwyer, H. A., P. Stapf and R. Maly (2000). "Unsteady vaporization and ignition of a three-dimensional droplet array." Combustion and flame 121(1): 181-194.

Estrade, J.-P., H. Carentz, G. Lavergne and Y. Biscos (1999). "Experimental investigation of dynamic binary collision of ethanol droplets–a model for droplet coalescence and bouncing." International Journal of Heat and Fluid Flow 20(5): 486-491.

Ferziger, J. H. and M. Perić (2002). Computational methods for fluid dynamics, Springer Berlin.

Fuster, D., A. Bagué, T. Boeck, L. Le Moyne, A. Leboissetier, S. Popinet, P. Ray, R. Scardovelli and S. Zaleski (2009). "Simulation of primary atomization with an octree adaptive mesh refinement and VOF method." International Journal of Multiphase Flow 35(6): 550-565.

Gavaises, M., C. Arcoumanis, H. Roth, Y. Choi and A. Theodorakakos (2004). Nozzle flow and spray characteristics from VCO diesel injector nozzles. Thermo-and Fluid Dynamic Processes in Diesel Engines 2, Springer: 31-48.

Gavaises, M., F. Villa, P. Koukouvinis, M. Marengo and J.-P. Franc (2015). "Visualisation and les simulation of cavitation cloud formation and collapse in an axisymmetric geometry." International Journal of Multiphase Flow 68: 14-26.

Georjon, T. L., Reitz, Rolf D (1999). "A drop-shattering collision model for multidimensional spray computations." Atomization and Sprays 9(3).

Giovanni, F., Alessandro di Gaeta, Angelo Palladino, Veniero Giglio (2013). "Common Rail System for GDI Engines."

Gorokhovski, M., Herrmann, Marcus (2008). "Modeling primary atomization." Annu. Rev. Fluid Mech. 40: 343-366.

Gosman, A., Johns, RJR (1980). Computer analysis of fuel-air mixing in direct-injection engines, SAE Technical Paper.

Gupta, H. N. (2012). Fundamentals of internal combustion engines, PHI Learning Pvt. Ltd.
Hannan, M., F. Azidin and A. Mohamed (2014). "Hybrid electric vehicles and their challenges: A review." Renewable and Sustainable Energy Reviews 29: 135-150.
He, Z., W. Zhong, Q. Wang, Z. Jiang and Z. Shao (2013). "Effect of nozzle geometrical and dynamic factors on cavitating and turbulent flow in a diesel multi-hole injector nozzle." International Journal of Thermal Sciences 70: 132-143.

Hiroyasu, H. and M. Arai (1990). Structures of fuel sprays in diesel engines, SAE Technical Paper.

Hirt, C. W., Nichols, Billy D (1981). "Volume of fluid (VOF) method for the dynamics of free boundaries." Journal of computational physics 39(1): 201-225.

Hsieh, K., Shuen, JS, YANG, VIGOR (1991). "Droplet vaporization in high-pressure environments I: Near critical conditions." Combustion Science and Technology 76(1-3): 111-132.

Huh, K. and A. Gosman (1991). A phenomenological model of diesel spray atomization. Proceedings of the international conference on multiphase flows.

IMechE. (2013). Internal Combustion Engines: Performance, Fuel Economy and Emissions, Elsevier Science.

Iwamoto, Y., K. Noma, O. Nakayama, T. Yamauchi and H. Ando (1997). Development of gasoline direct injection engine, SAE technical paper.

Jenny, P., D. Roekaerts and N. Beishuizen (2012). "Modeling of turbulent dilute spray combustion." Progress in Energy and Combustion Science 38(6): 846-887.

Jia, H., Gogos, G (1993). "High pressure droplet vaporization; effects of liquid-phase gas solubility." International journal of heat and mass transfer 36(18): 4419-4431.

Jia, M., Z. Peng, M. Xie and R. Stobart (2008). Evaluation of spray/wall interaction models under the conditions related to diesel HCCI engines, SAE Technical Paper.

Jiang, C., X. Ma, H. Xu and S. Richardson (2012). An optical study of DMF and ethanol combustion under dual-injection strategy, SAE Technical Paper.

Jiang, X., G. Siamas, K. Jagus and T. Karayiannis (2010). "Physical modelling and advanced simulations of gas–liquid two-phase jet flows in atomization and sprays." Progress in Energy and Combustion Science 36(2): 131-167.

Johansson, B. (1996). Cycle to Cycle Variations in S.I. Engines - The Effects of Fluid Flow and Gas Composition in the Vicinity of the Spark Plug on Early Combustion, SAE International.

Juneja, H., Y. Ra and R. D. Reitz (2004). Optimization of injection rate shape using active control of fuel injection, SAE Technical Paper.

Kalghatgi, G. (2015). "Developments in internal combustion engines and implications for combustion science and future transport fuels." Proceedings of the Combustion Institute 35(1): 101-115.

Kazour, J., B. Befrui, H. Husted, M. Raney and D. Varble (2014). Innovative Sprays and Particulate Reduction with GDi Injectors, SAE Technical Paper.

Kim, Y., Y. Kim, S. Jun, K. H. Lee, S. Rew, D. Lee and S. Park (2013). Strategies for particle emissions reduction from GDI engines, SAE Technical Paper.

Kolmogorov, A. N. (1941). The local structure of turbulence in incompressible viscous fluid for very large Reynolds numbers. Dokl. Akad. Nauk SSSR.

Launder, B., G. J. Reece and W. Rodi (1975). "Progress in the development of a Reynolds-stress turbulence closure." Journal of fluid mechanics 68(03): 537-566.

Launder, B. E., Spalding, DB (1974). "The numerical computation of turbulent flows." Computer methods in applied mechanics and engineering 3(2): 269-289.

Lee, C. S., Park, Sung Wook (2002). "An experimental and numerical study on fuel atomization characteristics of high-pressure diesel injection sprays." Fuel 81(18): 2417-2423.
Lefebvre, A. (1988). Atomization and sprays, CRC press.

Lei, Z., , Kai Hong Luoa, b, Wenjin Qinc, Ming Jiac, Shi Jin Shuaia, d (2015). "Large eddy simulation of spray and combustion characteristics with realistic chemistry and high-order numerical scheme under diesel engine-like conditions." Energy Conversion and Management 93: 377-387.

Li, H. (2013). CFD modelling study of sprays and combustion of gasoline and DMF in direct injection gasoline engines, University of Birmingham.

Li, H., X. Ma, T. PoWen, H. Xu, S.-J. Shuai and A. Ghafourian (2013). Numerical Study of DMF and Gasoline Spray and Mixture Preparation in a GDI Engine, SAE Technical Paper.

Liu, A. B., D. Mather and R. D. Reitz (1993). Modeling the effects of drop drag and breakup on fuel sprays, DTIC Document.

Ma, X., C. Jiang, H. Xu and S. Richardson (2012). In-cylinder optical study on combustion of DMF and DMF fuel blends, SAE Technical Paper.

Miesse, C. (1955). "Correlation of experimental data on the disintegration of liquid jets." Industrial & Engineering Chemistry 47(9): 1690-1701.

Mirshahi, M., J. M. Nouri, Y. Yan and M. Gavaises (2013). "Link between in-nozzle cavitation and jet spray in a gasoline multi-hole injector."

Munnannur, A., Reitz, Rolf D (2007). "A new predictive model for fragmenting and non-fragmenting binary droplet collisions." International journal of multiphase flow 33(8): 873-896.

Mwasilu, F., J. J. Justo, E.-K. Kim, T. D. Do and J.-W. Jung (2014). "Electric vehicles and smart grid interaction: A review on vehicle to grid and renewable energy sources integration." Renewable and Sustainable Energy Reviews 34: 501-516.
Naber, J., Reitz, Rolf D (1988). Modeling engine spray/wall impingement, SAE Technical Paper.

Naber, J. and D. L. Siebers (1996). Effects of gas density and vaporization on penetration and dispersion of diesel sprays, SAE technical paper.

Nishimura, A., Assanis, DN (2000). A model for primary diesel fuel atomization based on cavitation bubble collapse energy. Eight International Conference on Liquid Atomization and Spray Systems.

Nouri, J. M., S. Mackenzie, C. Gaskell and A. Dhunput (2012). Effect of viscosity, temperature and nozzle length-to-diameter ratio on internal flow and cavitation in a multi-hole injector. Fuel Systems for IC Engines, Woodhead Publishing: 265-278.

Nurick, W. (1976). "Orifice cavitation and its effect on spray mixing." Journal of fluids engineering 98(4): 681-687.

O'Rourke, P. J. (1981). Collective drop effects on vaporizing liquid sprays, Los Alamos National Lab., NM (USA).

O'Rourke, P. J., Amsden, AA (2000). A spray/wall interaction submodel for the KIVA-3 wall film model, SAE Technical Paper.

O'Rourke, P. J., Amsden, Anthony A (1987). The TAB method for numerical calculation of spray droplet breakup, SAE Technical Paper.

Obermeier, F. (1993). "Experimental and theoretical study of the influence of unsteady high frequency flow conditions on flow separation and cavitation within a nozzle and spray formation of fuel injectors under Diesel enginen conditions." IDEA Project, Subprogram FM 1.

Obermeier, F., Chaves, H (1992). Study of pressure fluctuations flows, separation and cavitation in the nozzle and their influence on spray formation. Proc. of the 6th Workshop of the IDEA Project.

Papageorgakis, G. and D. N. Assanis (1998). Optimizing gaseous fuel-air mixing in direct injection engines using an RNG based k-ε model, SAE Technical Paper.

Patel, V. C., W. Rodi and G. Scheuerer (1985). "Turbulence models for near-wall and low Reynolds number flows-a review." AIAA journal 23(9): 1308-1319.

Patterson, M. A. and R. D. Reitz (1998). Modeling the effects of fuel spray characteristics on diesel engine combustion and emission, SAE Technical Paper.

Payri, R., X. Margot and F. Salvador (2002). A numerical study of the influence of diesel nozzle geometry on the inner cavitating flow, SAE Technical Paper.

Popovac, M., Hanjalic, K (2007). "Compound wall treatment for RANS computation of complex turbulent flows and heat transfer." Flow, turbulence and combustion 78(2): 177-202.
Post, S. L., Abraham, John (2002). "Modeling the outcome of drop–drop collisions in Diesel sprays." International Journal of Multiphase Flow 28(6): 997-1019.

Qian, J., Law, CK (1997). "Regimes of coalescence and separation in droplet collision." Journal of Fluid Mechanics 331: 59-80.

Ra, Y., Reitz, Rolf D (2009). "A vaporization model for discrete multi-component fuel sprays." International Journal of Multiphase Flow 35(2): 101-117.

Ranz, W. E. (1959). On sprays and spraying, College of Engineering and Architecture.

Reitz, R. and F. Bracco (1982). "Mechanism of atomization of a liquid jet." Physics of Fluids (1958-1988) 25(10): 1730-1742.

Reitz, R. and F. Bracco (1986). "Mechanisms of breakup of round liquid jets." Encyclopedia of fluid mechanics 3: 233-249.

Reitz, R., Rutland, CJ (1995). "Development and testing of diesel engine CFD models." Progress in Energy and Combustion Science 21(2): 173-196.

Reitz, R. D. (1978). "Atomization and other breakup regimes of a liquid jet."

Reitz, R. D. (1996). "Computer modeling of sprays." Spray Technology Short Course, Pittsburgh, PA.

Reitz, R. D., Diwakar, R (1987). Structure of high-pressure fuel sprays, SAE Technical Paper.

Reynolds, O. (1894). "On the dynamical theory of incompressible viscous fluids and the determination of the criterion." Proceedings of the Royal Society of London 56(336-339): 40-45.

Reynolds, W. (1980). "Modeling of fluid motions in engines an introductory overview." Combustion Modeling in Reciprocating Engines, Plenum,(1980): 41-68
.
Rodi, W. (1993). Turbulence models and their application in hydraulics, CRC Press.

Román-Leshkov, Y., C. J. Barrett, Z. Y. Liu and J. A. Dumesic (2007). "Production of dimethylfuran for liquid fuels from biomass-derived carbohydrates." Nature 447(7147): 982-985.

Rutland, C. (2011). "Large-eddy simulations for internal combustion engines–a review." International Journal of Engine Research: 1468087411407248.

Samimi Abianeh, O., C. P. Chen and S. Mahalingam (2014). "Numerical modeling of multi-component fuel spray evaporation process." International Journal of Heat and Mass Transfer 69: 44-53.

Sanjosé, M., J. Senoner, F. Jaegle, B. Cuenot, S. Moreau and T. Poinsot (2011). "Fuel injection model for Euler–Euler and Euler–Lagrange large-eddy simulations of an evaporating spray inside an aeronautical combustor." International Journal of Multiphase Flow 37(5): 514-529.

Scussel, A. J., A. O. Simko and W. R. Wade (1978). The Ford PROCO Engine Update, SAE International.

Sementa, P., B. Maria Vaglieco and F. Catapano (2012). "Thermodynamic and optical characterizations of a high performance GDI engine operating in homogeneous and stratified charge mixture conditions fueled with gasoline and bio-ethanol." Fuel 96: 204-219.

Shost, M. A., M.-C. Lai, B. Befrui, P. Spiekermann and D. L. Varble (2014). GDi Nozzle Parameter Studies Using LES and Spray Imaging Methods, SAE Technical Paper.

Sieminski, A. (2013). "International energy outlook 2013." US Energy Information Administration (EIA) Report Number: DOE/EIA-0484.

Sirignano, W. A. (1993). "Fluid dynamics of sprays—1992 Freeman scholar lecture." Journal of fluids Engineering 115(3): 345-378.

Smith, A., Cebeci, Tuncer (1967). Numerical solution of the turbulent-boundary-layer equations, DTIC Document.

Smith, B. L., Bruno, Thomas J (2007). "Improvements in the measurement of distillation curves. 3. Application to gasoline and gasoline+ methanol mixtures." Industrial & engineering chemistry research 46(1): 297-309.

Som, S., Aggarwal, SK (2010). "Effects of primary breakup modeling on spray and combustion characteristics of compression ignition engines." Combustion and Flame 157(6): 1179-1193.

Som, S., A. Ramirez, S. Aggarwal, A. Kastengren, E. El-Hannouny, D. Longman, C. Powell and P. Senecal (2009). Development and validation of a primary breakup model for diesel engine applications, SAE Technical Paper.

Stefan, s. (2004). "Optical Diagnostics on FSI Transparent Engine." FISITA World Automotive Congress Barcelona.

Stiesch, G. (2003). Modeling engine spray and combustion processes, Springer Science & Business Media.

Su, T., P. Farrell and R. Nagarajan (1995). Nozzle effect on high pressure diesel injection, SAE Technical Paper.

Su, T., M. Patterson, R. D. Reitz and P. Farrell (1996). Experimental and numerical studies of high pressure multiple injection sprays, SAE Technical Paper.

Tamim, J., Hallett, WLH (1995). "A continuous thermodynamics model for multicomponent droplet vaporization." Chemical Engineering Science 50(18): 2933-2942.

Tanner, F. (1997). Liquid jet atomization and droplet breakup modeling of non-evaporating diesel fuel sprays, SAE Technical Paper.

Tennison, P. J., T. L. Georjon, P. V. Farrell and R. D. Reitz (1998). An experimental and numerical study of sprays from a common rail injection system for use in an HSDI diesel engine, SAE Technical Paper.

Tian, G., H. Li, H. Xu, Y. Li and M. Satish (2010). "spray characteristics study of DMF using phase doppler particle analyzer." SAE Int. J. Passeng. Cars-Mech. Syst 3(1): 948-958.

Torda, T. (1973). "Evaporation of drops and breakup of sprays." Astronautica Acta 18: 383-393.

Torres, D., O'rourke, PJ, Amsden, AA (2003). "Efficient multicomponent fuel algorithm." Combustion Theory and Modelling 7(1): 67-86.

Tu, P., C. Jiang, H. Ding, C. Li, H. Xu, A. Ghafourian and S.-j. Shuai (2014). Investigation on the Spray Characteristics of DMF-Isooctane Blends using PDPA, SAE Technical Paper.

von Kuensberg Sarre, C., S.-C. Kong and R. D. Reitz (1999). Modeling the effects of injector nozzle geometry on diesel sprays, SAE Technical Paper.

Waldheim, L., M. Monis and M. R. Verde Leal (2000). "Biomass power generation: Sugar cane bagasse and trash." Progress in thermochemical biomass conversion: 509-523.

Wang, C., R. Daniel and X. Ma (2012). Comparison of Gasoline (ULG), 2, 5-Dimethylfuran

(DMF) and Bio-Ethanol in a DISI Miller Cycle with Late Inlet Valve Closing Time, SAE

Technical Paper.

Wang, D. and F. L. Chia-fon (2005). Continuous multicomponent fuel film vaporization model for multidimensional engine modeling, SAE Technical Paper.

Wang, M., M. Wu and H. Huo (2007). "Life-cycle energy and greenhouse gas emission impacts of different corn ethanol plant types." Environmental Research Letters 2(2): 024001.

Wang, Y., L. Qiu, R. D. Reitz and R. Diwakar (2014). "Simulating cavitating liquid jets using a compressible and equilibrium two-phase flow solver." International Journal of Multiphase Flow 63: 52-67.

Watkins, A., Wang, DM (1990). A new model for diesel spray impaction on walls and comparison with experiment. COMODIA 90 Proceedings of International Symposium on Diagnostics and Modeling of Combustion in Internal Combustion Engines.

Wenjin Qina, Maozhao Xiea, , , Ming Jiaa, Tianyou Wangb, Daming Liub (2014). "Large eddy simulation of in-cylinder turbulent flows in a DISI gasoline engine." Applied Mathematical Modelling 38(24): 5967-5985.

Wesseling, J., J. Faber and M. Hekkert (2014). "How competitive forces sustain electric vehicle development." Technological Forecasting and Social Change 81: 154-164.

Wilcox, D. C. (1988). "Multiscale model for turbulent flows." AIAA journal 26(11): 1311-1320.

Wilcox, D. C. (1998). Turbulence modeling for CFD, DCW industries La Canada, CA.

Wilcox, D. C. (2008). "Formulation of the kw Turbulence Model Revisited." AIAA journal 46(11): 2823-2838.

Wu, X., Z. Huang, X. Wang, C. Jin, C. Tang, L. Wei and C. K. Law (2011). "Laminar burning velocities and flame instabilities of 2, 5-dimethylfuran–air mixtures at elevated pressures." Combustion and Flame 158(3): 539-546.

Yakhot, V., S. Orszag, S. Thangam, T. Gatski and C. Speziale (1992). "Development of turbulence models for shear flows by a double expansion technique." Physics of Fluids A: Fluid Dynamics (1989-1993) 4(7): 1510-1520.

Yakhot, V., Smith, Leslie M (1992). "The renormalization group, the ε-expansion and derivation of turbulence models." Journal of Scientific Computing 7(1): 35-61.

Yan, C. and S. K. Aggarwal (2006). "A high-pressure droplet model for spray simulations." Journal of engineering for gas turbines and power 128(3): 482-492.

Yokokawa, M., K. i. Itakura, A. Uno, T. Ishihara and Y. Kaneda (2002). 16.4-Tflops direct numerical simulation of turbulence by a Fourier spectral method on the Earth Simulator. Supercomputing, ACM/IEEE 2002 Conference, IEEE.

Zhao, H. (2010). 1 - Overview of gasoline direct injection engines. Advanced Direct Injection Combustion Engine Technologies and Development. H. Zhao, Woodhead Publishing. 1: 1-19.